A New Setup for Scaling Up Microlens-Based Individual-Atom Quantum Processors

Ein neuer Aufbau zur Skalierung von mikrolinsenbasierten Einzelatom-Quantenprozessoren
Zur Erlangung des Grades eines Doktors der Naturwissenschaften (Dr. rer. nat.)
Genehmigte Dissertation von Lars Pause aus Heppenheim
Tag der Einreichung: 8. Mai 2023, Tag der Prüfung: 5. Juni 2023

1. Gutachten: Prof. Dr. Gerhard Birkl
2. Gutachten: Prof. Dr. Thomas Walther
Darmstadt – Technische Universität Darmstadt

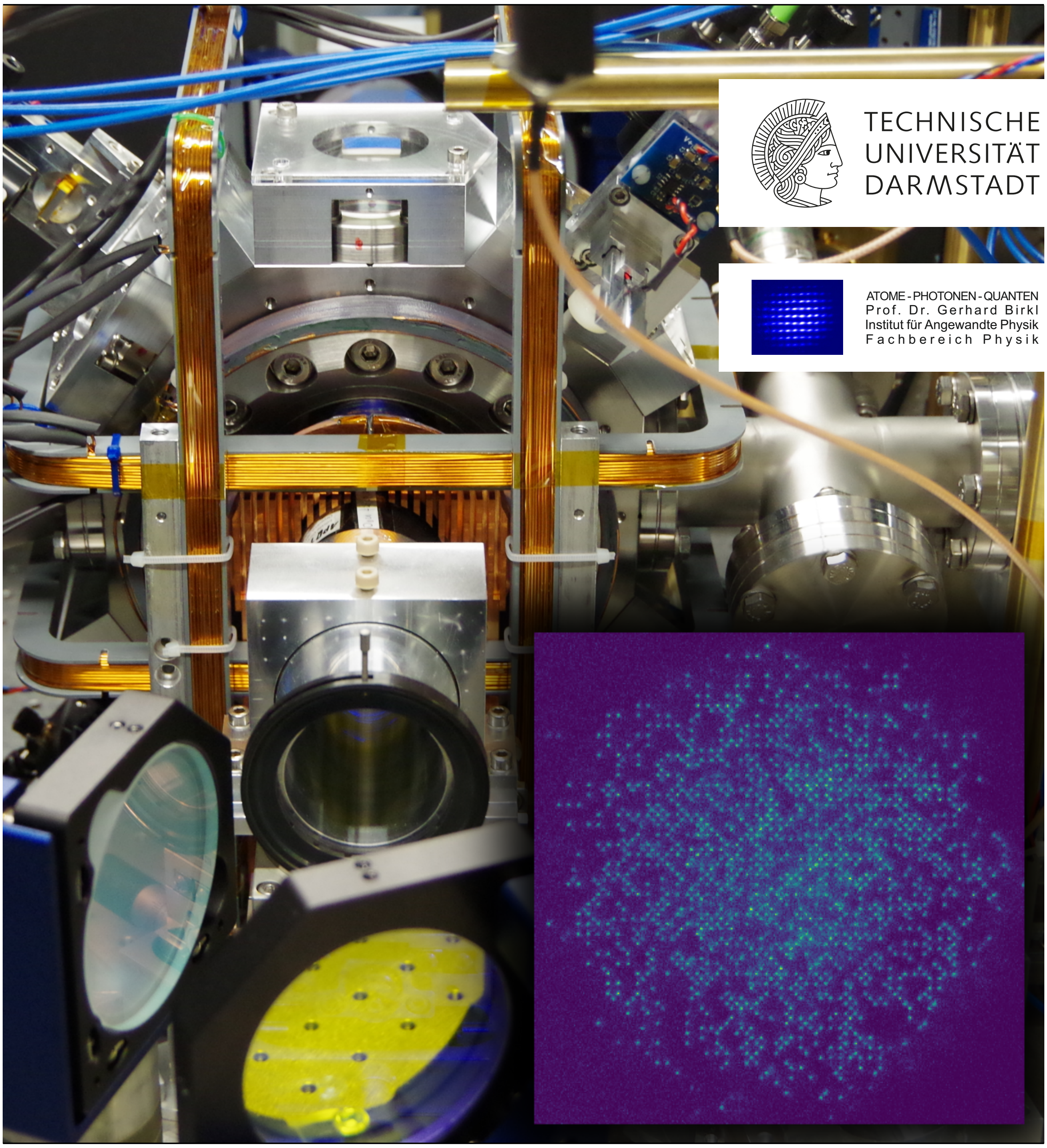

TECHNISCHE
UNIVERSITÄT
DARMSTADT

ATOME - PHOTONEN - QUANTEN
Prof. Dr. Gerhard Birkl
Institut für Angewandte Physik
Fachbereich Physik

A New Setup for Scaling Up Microlens-Based Individual-Atom Quantum Processors
Ein neuer Aufbau zur Skalierung von mikrolinsenbasierten Einzelatom-Quantenprozessoren

Accepted doctoral thesis by Lars Pause

1. Review: Prof. Dr. Gerhard Birkl
2. Review: Prof. Dr. Thomas Walther

Date of submission: May 8, 2023
Date of thesis defense: June 5, 2023

Darmstadt – Technische Universität Darmstadt

Bitte zitieren Sie dieses Dokument als:
URN: urn:nbn:de:tuda-tuprints-244463
URL: http://tuprints.ulb.tu-darmstadt.de/24446

Title image: Image of the experimental setup showing the central part of the vacuum chamber. The inset shows the fluorescence image of a single shot with 1305 detected single atoms using two interleaved arrays as described in chapter 5 and shown in Fig. 5.21.

Abstract

In current efforts, many platforms based e.g. on ions, neutral atoms, or superconducting qubits are being pursued with the goal to establish large-scale quantum devices for quantum computation and quantum simulation. Neutral atoms trapped in arrays of optical tweezers offer a versatile implementation in which the quantum system is well decoupled from its environment and the internal and external degrees of freedom of each individual atom can be precisely manipulated. Utilizing excitations of the atoms into Rydberg states enables interactions of selectable strengths thus allowing to perform gate operations or to implement spin Hamiltonians. As for all quantum processors, scaling up the system size is key for future progress.

In this work, a new experimental setup for trapping neutral 85Rb atoms in microlens-based tweezer arrays has been developed, addressing the challenge of scalability and demonstrating methods for enhancing the preparation of large-scale neutral atom quantum systems. A detailed introduction into the new setup and its essential elements is given. The design of a new vacuum chamber with versatile optical access allowing for different Rydberg excitation schemes used in state-of-the-art quantum experiments is presented. The experimental setup is controlled by a python-based experiment control-software which has been optimized to feature conditional control within an experimental cycle. Based on this new setup, large sets of individual atoms are prepared by loading the trap arrays from a laser-cooled cloud of neutral atoms which is the state-of-the-art procedure to provide a single-atom quantum processing platform.

For future quantum processing applications this procedure limits the data rate since the quantum operations have to be alternated with phases of laser cooling and trapping to compensate for unavoidable atom loss. In order to overcome these limitations a large-focus dipole trap providing a reservoir of laser-cooled atoms is introduced from which atoms are transported to the tweezer array using a single, movable tweezer. Utilizing an array of buffer traps, deterministic loading of a target structure with individual atoms from the cold-atom reservoir is demonstrated for the first time. Using solely reservoir atoms to load an empty trap array a cumulative success rate of 91.5(6) % for a defect-free target array is achieved. For a pre-loaded tweezer array an enhancement of the cumulative success rate from 62.1(6) % to 98.6(2) % is demonstrated. With this new method, it is possible to split the process of deterministic single-atom preparation into several functional units allowing for spatial separation as well as parallelized operation.

Implementing a new microscope objective with a higher numerical aperture of 0.385(5) in a modified optical setup allowed to reduce the volume of individual trapping sites and thereby reduce the necessary laser power for each individual trap. Utilizing this improvement together with the application of interleaved tweezer arrays based on multiple, individual laser beams, circumvented laser power limitations and for the first time enhanced the number of trapped individual atoms above 1000. With a single laser beam up to 600 individual atoms could be trapped in a quadratic trap array having a pitch of 5.17(2) µm. This number could be increased with the use of two interleaved arrays to an average of 1167(45) atoms. As this clearly demonstrates the scalability of microlens-based neutral atom platforms, approaches to deterministically arrange such large atom arrays and to further scale the system towards several thousand trapped atoms are outlined.

Zusammenfassung

Aktuell werden verschiedene Technologien, z.B. Ionen, neutrale Atome oder supraleitende Qubits, verwendet, um große Quantenprozessoren für Quantenberechnungen sowie Quantensimulationen zu entwickeln. Neutrale, in Registern von optischen Pinzetten gefangene, Atome stellen dabei eine vielseitige Plattform dar, bei der die Quantensysteme gut von ihrer Umgebung entkoppelt sowie ihre internen und externen Freiheitsgrade präzise manipuliert werden können. Durch die Anregung der Atome in Rydbergzustände können Wechselwirkungen wählbarer Stärke erreicht werden, welche die Durchführung von Gatteroperationen sowie die Implementierung von Spin-Hamiltonians erlauben. Für alle Formen von Quantenprozessoren ist dabei die Skalierbarkeit des Systems entscheidend für den zukünftigen Fortschritt.

In dieser Arbeit wurde ein neuer, experimenteller Aufbau zum Fangen neutraler ^{85}Rb-Atome in mikrolinsenbasierten Fallenregistern entwickelt, mit welchem die Herausforderung der Skalierbarkeit adressiert und neue Methoden zur Präparation großer Quantensysteme mit neutralen Atomen demonstriert werden. Es wird eine detaillierte Einführung in den neuen Aufbau und dessen wichtigste Elemente gegeben. Das Design der neuen Vakuumkammer mit vielfältigen optischen Zugängen, welche die gängigsten Schemata von Rydberganregungen ermöglichen, wird dargestellt. Der experimentelle Aufbau wird mit Hilfe einer Python-basierten Experimentsteuersoftware kontrolliert, welche für die konditionale Steuerung innerhalb eines Experimentzyklus weiterentwickelt wurde. Der neue Aufbau ermöglicht es aus einer Wolke von lasergekühlten Atomen große Systeme von Einzelatomen in Fallenregistern zu präparieren. Dies stellt das gängige Verfahren bei der Erzeugung von Einzelatomquantensystemen dar.

Für zukünftige Anwendungen begrenzt diese Technik jedoch die erreichbaren Datenraten, da Quantenoperationen mit Phasen des Fangens und Kühlens von Atomen abgewechselt werden müssen, um unvermeidbare Atomverluste auszugleichen. Zur Überwindung dieser Limitierung wird eine Dipolfalle mit großem Fallenvolumen genutzt, welche lasergekühlte Atome vorhält, die mit Hilfe einer optischen Pinzette entnommen werden. Unter Verwendung eines Registers von Pufferfallen kann damit erstmals das deterministische Laden einer Zielstruktur aus einem Reservoir kalter Atome demonstriert werden. Werden ausschließlich Reservoiratome zum Beladen des leeren Fallenregisters genutzt, kann eine kumulierte Erfolgswahrscheinlichkeit für eine defektfreie Zielstruktur von 91.5(6) % erreicht werden. Für ein vorgeladenes Register wird eine Erhöhung der Erfolgswahrscheinlichkeit von 62.1(6) % auf 98.6(2) % gezeigt. Mit dieser neuartigen Methode ist es möglich, den Prozess der Einzelatompräparation in mehrere, funktionale Einheiten zu zerlegen, welche räumlich getrennt und parallelisiert betrieben werden können.

Durch die Verwendung eines neuen Mikroskopobjektivs mit einer höheren numerischen Apertur von 0.385(5) in einem modifizierten optischen Aufbau war es möglich, das Volumen der einzelnen Fallenplätze und somit die benötigte Laserleistung für jede einzelne Falle zu reduzieren. Diese Verbesserung wurde mit verschachtelten, durch individuelle Laserstrahlen erzeugten Fallenregistern kombiniert. Dies reduziert laserleistungsbedingte Limitierungen und erhöht somit erstmalig die Zahl der gefangenen Einzelatome über 1000. Mittels eines einzelnen Laserstrahls können bis zu 600 Einzelatome in einem quadratischen Register mit 5.17(2) µm Fallenabstand gefangen werden. Darauf aufbauend wird durch die Verwendung von zwei verschachtelten Registern die Präparation von im Mittel 1167(45) Einzelatome demonstriert. Dies zeigt deutlich die Skalierbarkeit von mikrolinsenbasierten Neutralatomplattformen, weshalb darauffolgend Möglichkeiten zur deterministischen Anordnung großer Atomregister sowie zur weiteren Skalierung hin zu mehreren tausend Einzelatomen skizziert werden.

Contents

Appendix

Acronyms

AOD	acousto-optical deflector
AOM	acousto-optical modulator
BEC	Bose-Einstein condensate
CCD	charge-coupled device
CFS	chromatic focal shift
CPU	central processing unit
DDS	direct digital synthesis
DMA	direct memory access
DMD	digital micromirror device
DP	double-pass
DPSS	diode-pumped solid state
ECDL	external cavity diode laser
EMCCD	electron-multiplying charge-coupled device
EOM	electro-optical modulator
FIFO	first-in-first-out
FPGA	field-programmable gate array
GHZ	Greenberger-Horne-Zeilinger
GPIB	general purpose interface bus
GUI	graphical user interface
LSAP	linear sum assignment problem
MLA	microlens array
MOT	magneto-optical trap
MTS	modulation-transfer spectroscopy
NA	numerical aperture
NI	National Instruments
NPBS	non-polarizing beam splitter cube
PBS	polarizing beam splitter cube
PCB	printed circuit board
POP	physical-optics-propagation
PSF	point-spread function
ROI	region of interest
SBS	stimulated Brillouin scattering
SLM	spatial light modulator
SMF	single-mode fiber
SP	single-pass
SPI	serial peripheral interface
SSC	side-structure contrast
TA	tapered amplifier
TIA	transimpedance amplifier
Ti:Sa	titanium-sapphire
TOF	time-of-flight
TTR	tip, tilt, and rotation
UHV	ultra-high vacuum

1. Introduction

At the beginning of the 20th century the understanding of physics was fundamentally changed by experiments revealing and subsequent mathematical formulations describing what is nowadays known as quantum mechanics. It enabled the development of new pioneering technologies during the last century, e.g the laser, atomic clocks, and computer chips, which revolutionized our life. These innovations enabled further studies of quantum systems facilitating researchers to even better control and manipulate quantum systems. As a consequence, we currently consider ourselves to be part of a second quantum revolution in which technologies will be developed based on the fact that we are able to design man-made quantum states as needed for specific applications [1]. These quantum technologies comprise new paradigms for quantum information science including quantum communication and new devices for computation, simulation as well as for sensing and metrology [2]. There are several different intrinsic quantum systems, e.g. neutral atoms, nuclear spins, ions, and photons, as well as artificial quantum systems, e.g. superconducting circuits, quantum dots, and nitrogen-vacancies in diamonds, that can be utilized for quantum devices [3–10].

For the field of quantum computing, nuclear spins have been the first systems to demonstrate specific quantum algorithms, namely Grover's quantum search algorithm and Shor's quantum factoring algorithm, which in principle are able to outperform classical computers after sufficient scaling [11–14]. In the year 2000, DiVincenzo has outlined five requirements a physical system has to meet to be used for quantum computation [15]. Twelve years later, Cirac and Zoller added five similar criteria for the simulation of many-body quantum systems [16].

Following these criteria and due to the progress of research in atomic, molecular and optical physics during recent years, neutral atoms have become a well suited platform for quantum computing and simulation as outlined in detail by [17] and shortly summarized in the following. Groundbreaking experiments in laser cooling and trapping of atoms [18–21] paved the way to prepare single atoms, either in top-down approaches using the superfluid-Mott insulator transition of a Bose-Einstein condensate (BEC) in an optical lattice [22], or in bottom-up approaches where single atoms are trapped and individually arranged in arrays of optical tweezers [23–27]. These systems feature that neutral atoms of the same isotope are inherently indistinguishable, can be well isolated from their environment, and can be prepared in medium-sized systems of several hundred qubits. Furthermore, utilizing Rydberg excitations, digital quantum processing, using a universal set of quantum gates, as well as analog quantum simulation and processing, based on dipolar interactions to simulate different many-body Hamiltonians, has been demonstrated [3, 17, 28, 29].

For achieving advantage over classical computers for quantum computation as well as for quantum simulation, it is important to scale the quantum system to hundreds or even several thousand of individual qubits, which is challenging for all current platforms of quantum devices. For neutral atoms, the most advanced systems currently can provide several hundred atoms in roughly 1000 dipole traps utilizing different experimental techniques to create the tweezer arrays [30–33]. Systems based on spatial light modulators (SLMs) or digital micromirror devices (DMDs) offer a high flexibility in trap geometries but are damage-threshold-limited in terms of usable laser power [24, 26, 30]. Furthermore, the number of achievable high-quality traps is limited by the number of available pixels for wavefront variation. Acousto-optical deflectors (AODs) can be used both for red- as well as for blue-detuned traps in regular two-dimensional structures but are limited in terms of scalability by the number of usable distinct frequencies [23,34]. Other approaches are based on passive elements, such as projected Gaussian beams, microlens arrays or transmission masks [25,33,35]. Passive elements offer the advantage of handling high optical powers which make them extremely suitable for large-scale applications [33]. As microlens arrays (MLAs) with more than 10^5 lenslets are readily available they have enormous potential in terms of scalability as required for quantum simulators and quantum computers for real-world applications.

In this thesis, the microlens-based approach of creating trapping potentials for neutral atoms is used to develop a new setup for large-scale quantum information experiments. The here presented work was conducted in the research group of Prof. Dr. Gerhard Birkl within the QUIPS (**Qu**antum **I**nformation **P**rocessing **Systems**) project. The new setup is the third-generation QUIPS setup, also called QUIPS-C, and offers a platform for current as well as future state-of-the-art experiments. The capability of this new setup is demonstrated by conducting experiments to significantly scale up the system size of neutral atom quantum devices. A novel method for continuous supply of individual atoms utilizing a cold-atom reservoir is introduced. Furthermore, the combination of several microlens-based tweezer arrays is used to trap an unprecedented number of individual atoms. These topics are covered in the following chapters of this thesis which is structured as follows:

In **Chapter 2** an introduction into the physical concepts relevant for this thesis is given. It reviews the theory of neutral-atom trapping and single-atom preparation. Furthermore, parallelized creation of optical dipole-trap potentials with microlens arrays as well as their special features are discussed. At the end, a short overview about Rydberg atoms and their useful properties for quantum information processing is given.

Chapter 3 details the design and implementation of the new experimental setup developed during the course of this thesis. The vacuum chamber as well as additional equipment, such as the experiment control and laser systems, necessary to conduct quantum processing experiments will be introduced. This chapter concludes with the description of the experimental preparation of single atoms, being the bases for the following chapters.

Chapter 4 presents a new concept for the preparation of individual atoms by utilizing different, spatially separated modules enabling the parallelization of the state-of-the-art preparation process for large scale applications. The optical setup combining different types of dipole traps for the creation and interconnection of the functional units is introduced. Subsequently, results demonstrating the potential of the novel technique for continuous deterministic supply of single atoms are shown.

Scaling up the microlens-based approach of trap creation is the topic of **Chapter 5**. Utilizing a new microscope objective, a setup with interleaved tweezer arrays is introduced. Experimental results demonstrating the trapping of more than 1000 individual atoms are presented. Furthermore, the properties of the tweezer arrays are characterized and their limitations are discussed.

Chapter 6 summarizes the results of this thesis and gives an outlook on future applications as well as possible improvements to the current-state setup.

2. Theoretical concepts for trapping neutral atoms in microlens-based tweezer arrays

Neutral atoms are a promising platform for quantum computation as well as quantum simulation as mentioned in the previous chapter. In most state-of-the-art experiments, two different approaches are used to confine the atoms for quantum information experiments. Either laser-cooled neutral atoms are loaded into arrays of optical dipole traps, also called optical tweezers [36], or ultra-cold atoms are trapped in optical lattices [37]. Both approaches rely on trapping atoms due to the dipole force of a light field, but differ in the inter-atomic spacing between the atoms as well as in the time necessary to prepare the atom array [28]. While the distance between optical lattice sites is usually in the sub-micrometer regime, tweezer arrays typically feature a spacing of a few micrometers. Based on DiVincenzo's criteria, this is making single-site addressability available while suppressing interactions for neutral atoms in the ground state. In order to induce interactions, the atoms can be excited into states with a high principle quantum number n, so-called Rydberg states [38]. The interactions result from the extended wave function of Rydberg atoms due to the highly excited electron. Several fascinating experiments have demonstrated the capability of Rydberg atoms for quantum computation and quantum simulation in the past years [31, 32, 39–42].

In this chapter, the basic concepts necessary for dipole trapping of neutral atoms will be discussed, focusing on the architecture implemented in this thesis. The description will be limited to important relations and equations while citing adequate literature for further details. The first section summarizes the techniques necessary for preparing individual laser-cooled atoms based on atom-light interaction. Thereafter a more detailed introduction on principles and methods to create large-scale tweezer arrays is given. Finally, the properties of Rydberg atoms and possible excitation schemes into Rydberg states as utilized in state-of-the-art experiments will be briefly introduced.

2.1. Neutral atoms in optical dipole traps

Utilizing light to cool and trap neutral atoms enables scientists to use them as qubits in quantum information processing systems. Based on nobelprize-winning techniques developed in the 1970s and 1980s neutral atoms can be prepared in optical dipole traps ([20] and references therein). In this section basic equations describing the interaction between atoms and light fields will be introduced leading to the concept of optical dipole potentials. These principles are described thoroughly in literature such as [43–45], of which mainly [44] will be followed in this context. Combining these optical potentials with techniques to laser-cool and trap atoms as well as to singularize them enables the preparation of individual atoms as introduced in the second part of this section.

2.1.1. Atom-light interaction

In order to describe the interaction between an atom and a light field, we assume a two-level atom with ground state $|g\rangle$ and excited state $|e\rangle$ separated by the energy splitting $\Delta E = \hbar\omega_0$ where ω_0 is the resonance frequency of the corresponding transition and $\hbar$ the reduced Planck constant. In semiclassical theory, this atom interacts with a monochromatic light field described in its classical form by

$$\begin{aligned} \mathbf{E}(t) &= \frac{1}{2}\boldsymbol{\epsilon} E_0 \left(e^{-i\omega t} + e^{+i\omega t}\right) \\ &= \mathbf{E}_0^+ e^{-i\omega t} + \mathbf{E}_0^- e^{+i\omega t} \\ &= \mathbf{E}^+ + \mathbf{E}^- \end{aligned} \tag{2.1}$$

with angular frequency ω, unit polarization vector $\boldsymbol{\epsilon}$, and electric field amplitude E_0 at the location of the atom. This assumes that the wavelength λ of the light field is much longer than the size of the atom such that its spatial dependence can be omitted. Furthermore, the electric field has been separated into its positive and negative rotating terms for later derivations. The detuning between the light field and the atomic resonance is defined as $\Delta := \omega - \omega_0$.

The Hamiltonian operator of the atom and its dipole interaction with the field is given by

$$\hat{H} = \hat{H}_\mathrm{A} + \hat{H}_\mathrm{dip} = \hbar\omega_0 |e\rangle \langle e| - \hat{\mathbf{d}} \cdot \mathbf{E} \tag{2.2}$$

with dipole operator

$$\hat{\mathbf{d}} = -e\hat{\mathbf{r}} \tag{2.3}$$

The dipole operator couples the ground state $|g\rangle$ and the excited state $|e\rangle$ and can therefore be expressed in terms of these states. Using the atomic raising and lowering operators $\hat{\sigma} = |g\rangle \langle e|$ and $\hat{\sigma}^\dagger = |e\rangle \langle g|$, Eq. (2.2) can be rewritten as

$$\hat{H} = \hbar\omega_0(\hat{\sigma}^\dagger\hat{\sigma}) - \langle g| \hat{\mathbf{d}} |e\rangle (\hat{\sigma}^\dagger + \hat{\sigma}) \cdot \mathbf{E}. \tag{2.4}$$

It holds that $\hat{\sigma} \propto e^{-i\omega t}$ such that, comparable to the electric field, positive $\hat{\mathbf{d}}^+ \propto \hat{\sigma}$ and negative $\hat{\mathbf{d}}^- \propto \hat{\sigma}^\dagger$ rotating terms can be defined which enable the following rotating wave approximation of the dipole Hamiltonian

$$\begin{aligned} \hat{H}_\mathrm{dip} &= -\hat{\mathbf{d}}^+ \cdot \mathbf{E}^+ - \hat{\mathbf{d}}^+ \cdot \mathbf{E}^- - \hat{\mathbf{d}}^- \cdot \mathbf{E}^+ - \hat{\mathbf{d}}^- \cdot \mathbf{E}^- \\ &\approx -\hat{\mathbf{d}}^+ \cdot \mathbf{E}^- - \hat{\mathbf{d}}^- \cdot \mathbf{E}^+ \end{aligned} \tag{2.5}$$

where fast rotating terms $e^{\pm i(\omega+\omega_0)t}$ are neglected due to their zero average value on the time scale of the slowly oscillating terms $e^{\pm i\Delta t}$. It is in addition possible to transform into the frame of the laser field rotating with $e^{i\omega t}$ yielding an effective Hamiltonian given by

$$\hat{\mathcal{H}} = \hat{\mathcal{H}}_\mathrm{A} + \hat{\mathcal{H}}_\mathrm{dip} = -\hbar\Delta |e\rangle \langle e| + \frac{\hbar\Omega_0}{2}(\hat{\sigma}^\dagger + \hat{\sigma}) \tag{2.6}$$

with Rabi frequency

$$\Omega_0 = \frac{\langle g| \boldsymbol{\epsilon} \cdot \hat{\mathbf{d}} |e\rangle \cdot E_0}{\hbar} \tag{2.7}$$

characterizing the strength of the atom-field coupling. In the rotating frame, the states $|g\rangle$ and $|e\rangle$ are no longer eigenstates of the effective Hamiltonian $\hat{\mathcal{H}}$. Diagonalizing $\hat{\mathcal{H}}$, represented in the basis $\{|e\rangle, |g\rangle\}$ as

$$\hat{\mathcal{H}} = \hbar \begin{pmatrix} -\Delta & \frac{\Omega_0}{2} \\ \frac{\Omega_0}{2} & 0 \end{pmatrix}, \tag{2.8}$$

gives the new eigenvalues

$$E_\pm = -\frac{\hbar\Delta}{2} \mp \frac{\hbar\Omega}{2}. \tag{2.9}$$

Here, $\Omega := \sqrt{\Omega_0^2 + \Delta^2}$ is the generalized Rabi frequency. The corresponding eigenstates

$$\begin{aligned} |+\rangle &= \sin\theta\,|g\rangle + \cos\theta\,|e\rangle \\ |-\rangle &= \cos\theta\,|g\rangle - \sin\theta\,|e\rangle \end{aligned} \tag{2.10}$$

result from a rotation of the original eigenstates by a mixing angle

$$\tan 2\theta = -\frac{\Omega_0}{\Delta} \qquad \text{with} \qquad 0 \le \theta < \frac{\pi}{2}. \tag{2.11}$$

In the limit $\Omega_0, \Gamma \ll |\Delta|$ of far-detuned light-fields, with Γ as given in Eq. (2.14), the mixing angle is very small and $|-\rangle \approx |g\rangle$. The energy of the ground state is then shifted by

$$\Delta E = \frac{\hbar\Omega_0^2}{4\Delta} \tag{2.12}$$

due to the coupling. If a focused laser beam is considered, the electric field amplitude and, according to Eq. (2.7), the Rabi frequency are spatially dependent. For a negative detuned light field $\Delta < 0$ this results in a reduction of the energy proportional to the strength of the electric field leading to an attractive dipole potential. The potential depth can be written as

$$U_{\text{dip}}(r) = \frac{3\pi c^2}{2\omega_0^3}\frac{\Gamma}{\Delta} I(r) \tag{2.13}$$

where $I(r) = \epsilon_0 c \cdot |E(r)|/2$ and the spontaneous decay rate of the excited state

$$\Gamma = \frac{\omega_0^3}{3\pi\epsilon_0\hbar c^3}\left|\langle g|\,\hat{\mathbf{d}}\,|e\rangle\right|^2, \tag{2.14}$$

also known as natural linewidth, is introduced [45]; c is the speed of light and ϵ_0 the vacuum permittivity. The exact values of Γ for ^{85}Rb together with other important values are given in appendix A. The spontaneous decay of an excited state as quantified by Γ is a dissipative process which can be described together with the atom-light coupling through the optical Bloch equations [43, Chap. 2]. In the steady state, where excitation rate and decay rate are equal, the total scattering rate is given by

$$\Gamma_{\text{SC}} = \frac{\Gamma}{2}\frac{s_0}{1 + s_0 + (2\Delta/\Gamma)^2} \tag{2.15}$$

with saturation parameter $s_0 = I/I_{\text{sat}}$. The saturation intensity is

$$I_{\text{sat}} = \frac{\hbar\omega_0^3\Gamma}{12\pi c^2} \tag{2.16}$$

for the case of the cycling transition $|F=3,m_\text{F}=3\rangle \leftrightarrow |F=4,m_\text{F}=4\rangle$ and σ^+-polarized light [46].

This shows that for high laser intensities and small detunings, saturation effects occur which limit the maximum scattering rate to $\Gamma/2$. This regime will be used for laser cooling described in the next section. Optical dipole traps work with large detunings and it is assumed that $\Delta^2/\Gamma^2 \gg I/I_\text{sat}$. Then, the denominator in Eq. (2.15) can be approximated by $4\Delta^2/\Gamma^2$ resulting in a scattering rate given by

$$\Gamma_\text{SC} = \frac{3\pi c^2}{2\hbar\omega_0^3}\frac{\Gamma^2}{\Delta^2}I(\mathbf{r}) \tag{2.17}$$

As in optical dipole traps dissipative processes result in heating of the atoms, they need to be kept as low as possible. Looking at Eqs. (2.13) and (2.17) it is obvious that this can be achieved by increasing the intensity together with the detuning. This keeps the potential depth constant while decreasing the scattering rate.

As the derivations presented here assume a two-level system, it has to be pointed out that for a quantitative analysis of rubidium atoms the real level structure involving fine structure and hyperfine structure levels as well as the polarization of the laser field need to be taken into account. A better approximation taking the dominant rubidium transitions $|5S_{1/2}\rangle \leftrightarrow |5P_{1/2}\rangle$[1] and $|5S_{1/2}\rangle \leftrightarrow |5P_{3/2}\rangle$ into account can be found in [45] for both the scattering rate Γ_SC as well as the dipole potential U_dip. A detailed analysis also including the hyperfine structure is given in [47] and is followed for calculations of the scattering rate and the dipole potential in this thesis.

2.1.2. Laser cooling and single-atom preparation

For trapping atoms in the dipole potentials as introduced in the previous section, they have to be cooled to sufficiently low temperatures T such that their associated thermal kinetic energy $k_\text{B}T \ll U_\text{dip}(0) := U_0$ where k_B is the Boltzmann constant [48]. This can be achieved by two successive steps of laser-based cooling and trapping techniques: the magneto-optical trap (MOT) followed by sub-Doppler cooling in an optical molasses. The MOT has become the key technique for cold-atom experiments since its first experimental demonstration [49]. Using the radiative force of three pairs of counter-propagating laser beams in combination with a magnetic field gradient for spatial confinement, a cloud of cold atoms can be prepared at the intersection of the laser beams with the origin of the magnetic field gradient. At thermal equilibrium, where successive laser cooling as well as heating due to absorption and re-emission of photons balance, a minimal temperature, the so-called Doppler limit, given by

$$T_{Doppler} = \frac{\hbar\Gamma}{2k_\text{B}} \tag{2.18}$$

can be reached. For cooling on the D2-line of ^{85}Rb with $\Gamma = 2\pi \cdot 6.067\,\text{MHz}$, the Doppler limit is $T_{Doppler} = 146\,\mu\text{K}$.

However, taking the polarization of the laser beams as well as the different Zeeman sublevels of the hyperfine splitting into account, it can be derived that temperatures below this limit can be achieved [50]. In this phase no magnetic field gradient is present and no confinement is achieved which is why it is referred to as optical molasses. The theoretical lower boundary of

---

[1] In this work, as only rubidium states with spin quantum number $s = 1/2$ are used, the atomic term symbol $n^{2s+1}L_j$ is shortened by omitting the spin multiplicity $2s+1$.

the temperature achievable with the optical molasses corresponds to the recoil energy gained from the emission of a photon and is given by the recoil temperature [19]

$$T_{\text{recoil}} = \frac{(\hbar k)^2}{m k_{\text{B}}} \tag{2.19}$$

where m is the mass of the atom. For ^{85}Rb this limit is at a temperature $T_{\text{recoil}} = 370\,\text{nK}$. In experiments, typically temperatures one order of magnitude higher are reached, depending on the specific parameters used [19].

The laser-cooled atoms can be loaded into a dipole trap. The detailed experimental procedure used in this thesis is described in section 3.4. Loading the atoms into a dipole trap involves an interplay between the loading rate R, determined by the flux of atoms into the trap, and losses of atoms out of the trap. In the most simple case, if losses are assumed to be proportional to the atom number N described by a loss rate γ, the atom number follows a Poisson distribution and the equilibrium atom number is given by $\bar{N} = R/\gamma$. Tuning R such that $\bar{N} = 1$ the maximum possible probability for a single atom in the trap is 0.368. In reality, experiments in extremely small traps have shown however, that sub-Poissonian loading with $p(N = 1) \approx 0.5$ is possible [51]. The reason is that losses are in reality dependent on the specific loss mechanism: There are one-atom losses mainly due to collisions with background-gas atoms described by $-\gamma N$ and two-atom losses due to inelastic collisions of atoms described by $-\beta' N(N-1)$ [52].

The differential equation describing the atom number dynamics is therefore given by

$$\frac{\mathrm{d}N}{\mathrm{d}t} = R - \gamma N - \beta' N(N-1). \tag{2.20}$$

During trap loading, the two-body loss results from light-assisted collisions based predominantly on the mechanism of radiative escape with a loss rate coefficient [53]

$$\beta'_{\text{L}} = \frac{K I_{\text{M}}}{V} \frac{I_{\text{R}}}{I_{\text{R}} + a' I_{\text{M}}} \tag{2.21}$$

where K is a density dependent loss rate, I_{M} and I_{R} are the MOT and repumping laser intensities, and a' is a constant taking the relative pumping rates of MOT and repumping into account. For further calculations, a' is set to be 0.02 following [53]. The volume of the trap is given by

$$V = \pi w_0^2 z_{\text{R}} \ln\left(\frac{1}{1-\eta}\right) \sqrt{\frac{\eta}{1-\eta}} \tag{2.22}$$

with ratio $\eta = k_{\text{B}} T / |U_0|$, trap waist w_0 and Rayleigh range z_{R}. For measurements in chapter 5 η has been found to be around 0.4, which has been used for the simulations below. The dipole traps loaded with atoms in experiments described in this thesis have focal spot sizes between 0.9 µm for the smallest traps described in chapter 5 and up to 15.8 µm for the reservoir dipole trap in chapter 4. As $V \propto w_0^4$, the spot size w_0 strongly effects the trapping volume and therefore the two-body loss coefficient β'. For typical parameters used in the experiment (given and explained in Tab. 2.1) this results in $\beta' \approx 0.01$ for the reservoir dipole trap and $\beta' \approx 30$ for the array traps in chapter 4 as well as $\beta' \approx 1000$ for the smallest dipole traps used in chapter 5.

Using a Monte Carlo simulation, the equilibrium atom number resulting from Eq. (2.20) when atom losses equal out the gain of newly trapped atoms, the effect of different values β' can be modeled [54, 55]. Figure 2.1 depicts on the left side the number of atoms in a dipole trap as a function of the loading rate R for the experiment-relevant parameters of β'

Tab. 2.1.: Parameters used for Monte Carlo simulation shown in Fig. 2.1. The wavelength as well as the intensities for MOT and repumping light are based on experimental parameters used for experiments in chapters 4 and 5. γ is based on lifetime measurements with few imaging sections and η on release and recapture measurements as performed in chapter 5. K and a are values adopted from [53].

λ	I_M	I_R	K [53]	a' [53]	η	γ
$798\,\mathrm{nm}$	$0.022\,\mathrm{W/cm^2}$	$0.01\,\mathrm{W/cm^2}$	$1.1\times10^{-10}\,\mathrm{cm^5\,W^{-1}\,s^{-1}}$	0.02	0.4	2/s

showing a similar behavior as described in [47,52]. Looking at the average atom number $\bar{N}$ for $\beta' = 0.01$ it can be seen that for small loading rates R, one-body losses play the predominant role such that $\bar{N} \propto R/\gamma$. For high loading rates, $\bar{N}$ is large such that two-body collisions play the predominant role leading to $\bar{N} \propto \sqrt{\frac{R}{\beta'}}$. The boundary between both regimes is given by the critical atom number $N_\mathrm{c} = \gamma/\beta'$ corresponding to a critical loading rate $R_\mathrm{c} = \gamma^2/\beta'$. For $\beta' = 0.01$, corresponding to large N_c, a cross-over between both regimes is apparent by the change of the slope $\Delta\bar{N}/\Delta R$ comparing loading rates below and above R_c. The reason for the reduction of the slope for high loading rates is that two-body collisions further reduce the atom number.

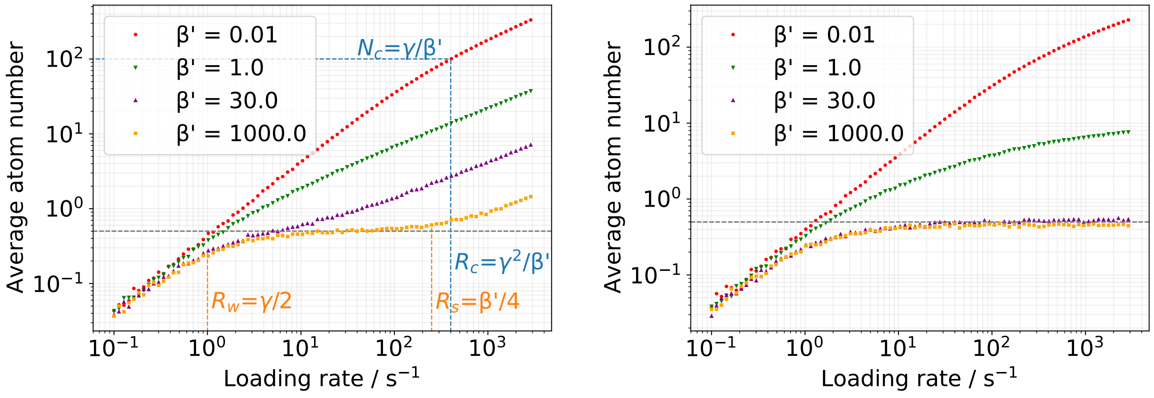

Fig. 2.1.: **Left:** Monte Carlo simulation showing the average atom number in a dipole trap during the loading process with respect to the loading rate R for different two-body loss rates β'. For $\beta' = 0.01\,\mathrm{s}^{-1}$ the critical loading rate R_c as well as the critical atom number N_c are given. For $\beta' = 1000\,\mathrm{s}^{-1}$ the boundaries of the blockade regime, R_w and R_s, are depicted. **Right:** Monte Carlo simulation showing the average atom number in a dipole trap after an exposure phase of $50\,\mathrm{ms}$ following the loading process. The atom number is again plotted with respect to the loading rate R for different two-body loss rates β'.

For large β' and intermediate loading rates, the average loading rate is constant over several orders of loading rates as the two-body-collisions are so strong that as soon as two atoms are inside the trap, they will be lost due to a collision. This is called the collisional blockade regime which is limited on the weak loading side by $R_\mathrm{w} = \gamma/2$ and on the strong loading side by $R_\mathrm{s} = \beta'/4$. Blockade appears only if $R_\mathrm{w} < R_\mathrm{s}$ and the average atom number for small R can by significantly reduced for high one-body loss rates as apparent from Fig. 2.1. For trap parameters as used in chapter 5, a constant filling fraction of typically 50 % to 60 % is directly achieved during the loading process. For larger traps, e.g. as in chapter 4, the collisional bloackade effect during loading is weaker such that the filling fraction during loading is still dependent on R. The loading phase is therefore followed by a so-called dummy imaging phase (see section 3.4) where no new atoms are loaded ($R = 0$) such that single-atom preparation is also achieved for larger trap volumes. The loading rate after a $50\,$ms imaging phase following the loading phase is shown on the right side of Fig. 2.1.

The increase above the model-based value of 50 % results from collisions where the energy is not high enough for both atoms to escape the trap as described and measured in [56, 57]. If tuning the laser parameters for collision-induced losses based on the principle of gray molasses, losses of only one atom can occur predominantly resulting in a measured single-atom loading efficiency of 80 % to 90 % as further described in [27, 58, 59]. This usually makes further laser systems or large frequency shifts necessary and is not further investigated in the scope of this thesis.

From the presented simulations, it is apparent, that traps with small trapping volumes, ideally below 1 µm need to be created inside the vacuum chamber to achieve single-atom loading already during the loading process. How these traps can be created and what techniques allow for a parallelized trap creation will be discussed in the following section. Before, a short discussion on loss mechanisms in a dipole trap follows.

2.1.3. Heating mechanisms in optical dipole traps

Having single atoms trapped in a dipole-trap potential, there can be different effects resulting in a loss of the atom which shall be summarized in the following.

Photon recoil heating

Due to the photon scattering processes of the atom, it gains $2E_\text{rec}$ of energy with each scattering process [45]. It has to be noted that this energy is distributed into different modes of motion (longitudinal or transversal) but here only the overall heating shall be considered. As scattering occurs at a rate of Γ_SC, the change in energy is given by

$$\frac{\mathrm{d}E}{\mathrm{d}t} = 2E_\text{rec} \cdot \Gamma_\text{SC}. \tag{2.23}$$

Knowing the rate of energy increase, a time constant can be deduced at which the atom will escape from the trap due to photon recoil heating [60]. The atom will be lost if its energy $E_\text{tot} = E_\text{init} + E_\text{gained}$, being its initial energy E_init and the gained energy E_gained, is larger than the potential depth U_0 of the trap. The time constant is therefore given by

$$\tau_\text{rec} = \frac{U_0 - E_\text{init}}{\frac{\mathrm{d}E}{\mathrm{d}t}} = \frac{U_0 - E_\text{init}}{2E_\text{rec} \cdot \Gamma_\text{SC}} \tag{2.24}$$

Heating due to technical noise

Heating can also occur due to technical noise of the trap laser exciting the atomic motion of the atom inside the trap. The increase of the average energy in a one-dimensional harmonic oscillator (regarding only a single axis of the trap) is given by

$$\frac{\mathrm{d}E}{\mathrm{d}t} = \Gamma_\text{noise} E \tag{2.25}$$

with rate constant

$$\Gamma_{\text{noise}} = \pi^2 \nu^2 S(2\nu), \tag{2.26}$$

where $\nu = \Omega_{\text{i,G}}/(2\pi)$ is the trap frequency of the trap as will be introduced in section 2.2.1 for Gaussian beams and $S(2\nu)$ is the one-sided power spectrum of the intensity noise at a frequency of 2ν (due to intensity noise only symmetric excitation is possible) [61]. Again, the atom will be lost from the trap if its energy is larger than the potential depth. The time constant can then be given by

$$\tau_{\text{noise}} = \frac{m w_{\text{r}}^2}{S(2\nu) \cdot U_0} \cdot \ln\left(\frac{U_0}{E_{\text{init}}}\right) \tag{2.27}$$

with radial beam waist w_{r} and mass m of the atom [62].

Atom loss due to background gas collisions

Atoms can also be lost from the trap due to collisions with the background gas which is at room temperature T_{room}. The lifetime due to background gas collisions is given by

$$\tau_{\text{back}} = \sqrt{\frac{\pi m k_{\text{B}} T_{\text{room}}}{8}} \cdot \frac{1}{\sigma p} \tag{2.28}$$

with vacuum pressure p, and scattering cross section σ [63]. In general, collisions of rubidium atoms with different types of background atoms need to be considered as they have different partial pressures and different scattering cross sections. According to [64], the scattering cross section of trapped rubidium atoms with background gas rubidium atoms is a factor of ten higher than for H_2 and He. Furthermore, rubidium atoms are injected into the chamber by dispensers which is why it is assumed that Rb-Rb collisions dominate the loss process. As the local rubidium pressure at the center of the vacuum chamber is higher than the measured vacuum pressure, p is taken as the vacuum pressure and the cross section is given by $\sigma_{\text{Rb}-\text{Rb}} = 2500\,\text{Å}^2$ [64] for an upper bound of the lifetime due to background gas collisions.

2.2. Microlens-based dipole-trap arrays

In the previous section 2.1 it was derived that a focused laser beam red-detuned to the corresponding atomic transition can act as a dipole trap for an atom. For the experiments in this thesis, dipole traps have been created using two slightly different methods. For the experiments described in chapters 4 and 5 the reservoir trap as well as the movable transport tweezer are created by focusing Gaussian laser beams while the dipole-trap arrays are created by reimaging the focal plane of a microlens array. As the beam radius of the laser beam illuminating the microlens array is up to a factor of 60 larger than the radius of the microlens, the incident light field can be assumed to be a plane wave. In the following sections it will therefore be discussed how focused Gaussian beams as well as focused plane-wave light fields can be described mathematically and what effects have to be taken into account when using microlens-based dipole-trap arrays.

2.2.1. Focused Gaussian laser beams

The ideal mode emerging from a single-mode fiber can be described by a Gaussian beam. Assuming an axially symmetric beam, its intensity distribution in radial direction $r = \sqrt{x^2 + y^2}$ and longitudinal direction z is given by [65, Chap. 13]

$$I_{\text{gauss}}(r, z) = I_0(0, z) \cdot \exp\left(-\frac{2r^2}{w^2(z)}\right) \tag{2.29}$$

with on-axis intensity

$$I_0(0, z) = \frac{2P}{\pi w^2(z)} \tag{2.30}$$

where P is the laser power of the Gaussian beam. The $1/e^2$ radius of the beam along z-direction is given by

$$w(z) = w_0 \sqrt{1 + \left(\frac{z}{z_{\text{R}}}\right)^2}. \tag{2.31}$$

with beam waist w_0 at $z = 0$. At the distance

$$z_{\text{R}} = \pi w_0^2 / \lambda, \tag{2.32}$$

the so-called Rayleigh range, the beam radius has increased by a factor of $\sqrt{2}$.

If a Gaussian beam is refocused by a thin lens of focal length f, the resulting beam is again Gaussian under the condition that diffraction due to truncation at the lens aperture can be neglected. This is valid if the truncation ratio

$$\epsilon = \frac{d}{2w} \tag{2.33}$$

is $\epsilon > 2$, where d is the aperture diameter of the focusing lens and w the beam radius on the lens [66, Chap. 25.3.3]. Given that the waist of the incident beam has a distance of s before the principal plane of the lens, the beam properties behind the lens are described by the following formulas [67]:

$$w_0' = m w_0 \tag{2.34}$$

$$z_{\text{R}}' = m^2 z_{\text{R}} \tag{2.35}$$

$$s' = f + m^2(s - f) \tag{2.36}$$

with magnification

$$m = \frac{f}{\sqrt{(s - f)^2 + z_{\text{R}}^2}}. \tag{2.37}$$

For a collimated laser beam where $s \approx 0$ and $z_{\text{R}} \gg f$ it holds that [68, Chap. 3]

$$w_0' = \frac{\lambda f}{\pi w_0} \qquad \text{and} \qquad s' = f \tag{2.38}$$

The larger the Gaussian beam is compared to d the more diffraction occurs. For $\epsilon < 2.5$ the resulting spot size can be calculated using an empirical approximation as given in [66, Chap. 25.3]:

$$w_0' = K_{1/\text{e}^2} \cdot \frac{2 \cdot f \cdot \lambda}{d} \tag{2.39}$$

with

$$K_{1/\mathrm{e}^2} = 0.8225 + \frac{0.3230}{(1/\epsilon - 0.2816)^{1.821}} - \frac{0.2660}{(1/\epsilon - 0.2816)^{1.891}}. \tag{2.40}$$

For $w_0 \gg d/2$, the Gaussian beam can be approximated as plane wave for which the intensity distribution and spot size will be derived in the following section.

Focusing down a Gaussian beam is a simple way to create a dipole potential as described in Eq. (2.13), from which follows that the maximal trap depth $U_0 \propto I_{\text{gauss}}(0,0)$. If the kinetic energy $k_{\text{B}}T$ of the atoms is significantly lower than U_0, the atoms occupy a volume close to the trap minimum and the Gaussian trapping potential in radial and longitudinal direction can be approximated by an harmonic oscillator

$$I_{\text{gauss}}(r,z) \approx I_0 \left(1 - \frac{2r^2}{w_0^2} - \frac{z^2}{z_{\text{R}}^2}\right) \tag{2.41}$$

The corresponding trap frequencies are given by

$$\omega_{\text{r,G}} = \sqrt{\frac{4U_0}{mw_0^2}} \qquad \text{and} \qquad \omega_{\text{z,G}} = \sqrt{\frac{2U_0}{mz_{\text{R}}^2}}. \tag{2.42}$$

2.2.2. Focused plane waves

When using microlenses to create large dipole-trap arrays, the incident wave is assumed to be a plane wave as described above. Therefore, a plane wave incident on a thin lens is considered creating a spherical wave front converging onto the focal point at distance f. The intensity distribution at the focal point is then given by [69, Chap. 8.8]

$$\begin{aligned} I(r,z) = I_0 \left(\frac{2}{u(z)}\right)^2 \cdot \Bigg[& \left(\sum_{s=0}^{\infty} (-1)^s \left(\frac{u(z)}{v(r)}\right)^{1+2s} J_{1+2s}(v_r)\right)^2 \\ & + \left(\sum_{s=0}^{\infty} (-1)^s \left(\frac{u(z)}{v(r)}\right)^{2+2s} J_{2+2s}(v(r))\right)^2 \Bigg]. \end{aligned} \tag{2.43}$$

where $J_n(x)$ are the Bessel functions of nth order and the origin of the coordinate system is at the focal point. Furthermore,

$$v(r) = k\left(\frac{d}{2f}\right) r \qquad \text{and} \qquad u(z) = k\left(\frac{d}{2f}\right)^2 z \tag{2.44}$$

with lens diameter d and wave vector $k = \frac{2\pi}{\lambda}$. In order to characterize the trapping potential for the atoms, the potential in the focal plane as well as along the optical axis is of interest. For these special cases Eq. (2.43) can be simplified to

$$I_{\text{P}}(r, z=0) = I_0 \left(\frac{2J_1(v(r))}{v(r)}\right)^2 \qquad \text{and} \qquad I_{\text{P}}(r=0, z) = I_0 \left(\frac{\sin(u(z)/4)}{u(z)/4}\right)^2. \tag{2.45}$$

The maximum intensity I_0 is given by

$$I_0 := I_{\text{P}}(0,0) = P\frac{\pi}{\lambda^2}\left(\frac{d}{2f}\right)^2. \tag{2.46}$$

Focused plane waves form the smallest possible spots, a so-called Airy-disc. From Eqs. (2.44) and (2.45) the radius

$$r_{\text{Airy},0} \approx 1.22\frac{\lambda f}{d} \tag{2.47}$$

where $I(r = r_{\text{Airy},0}, z = 0) = 0$ can be defined as a measure for the spot size. This represents the radius of the first dark ring of the Airy pattern. For beams measured in reality, $I(r)$ will never equal to zero and beams are often idealized as Gaussian beams. Therefore the Bessel waist

$$w_{\text{B}} \approx 0.67 \cdot r_{\text{Airy},0} = 0.82\frac{\lambda f}{d}, \tag{2.48}$$

the radius at which the intensity decreases to $1/e^2$ of the maximal intensity, is often used to compare the beam size with a Gaussian beam.

As for Gaussian beams, the trap frequencies for a dipole trap resulting from a focused plane wave can by derived from Eq. (2.45) using an harmonic approximation:

$$\omega_{r,P} = \frac{\sqrt{2}\pi}{\lambda}\frac{d}{2f}\sqrt{\frac{U_0}{m}} \quad \text{and} \quad \omega_{z,P} = \frac{\pi}{\sqrt{6}\lambda}\frac{d^2}{4 \cdot f^2}\sqrt{\frac{U_0}{m}} \tag{2.49}$$

Comparing Eq. (2.42) with (2.49) it can be seen that the same radial trap frequency as for a plane wave is achieved for a Gaussian beam with beam radius $w = d/(2\sqrt{2})$ at the position of the lens and the corresponding beam waist is given by

$$w_0 = \frac{2\sqrt{2}\lambda f}{\pi d} \tag{2.50}$$

under the assumption of no diffraction. In [70] the difference between both radial potentials under the assumptions of equal ω_r was further investigated showing a deviation of less than 2 % for the deeper half of the trapping potential. It is important to note that if the beam waist is used to deduce the trap frequency in longitudinal direction for a focused plane wave, a correction has to be included [70]. Under the condition of equal maximum intensity and equal radial trap frequency, the ratio between the longitudinal trap frequencies is

$$\frac{\omega_{z,G}}{\omega_{z,P}} = \sqrt{3} \approx 1.73 \tag{2.51}$$

Taking this transformation into account, a focused plane wave can be approximated using a focused Gaussian beam.

2.2.3. Diffraction effects of microlenses

In the previous section, a thin lens with focal length f was considered and the resulting intensity distribution was described. It was assumed that the focal length and thus the point of maximal intensity is solely determined by the refractive power of the lens. However, due to the diffraction at the small aperture of a microlens the effective focal length f_{e}, given by the length between the principal plane of the lens and the point of maximum intensity is modified as described in [71].

In geometrical optics, the focal length of a thin, plano-convex lens in vacuum is given by [68, Chap. 2]

$$f_{\text{g}} = \frac{\text{ROC}}{n-1} \tag{2.52}$$

where ROC is the radius of curvature of the lens and n is the refractive index of the lens material. In order to quantify, when diffraction at small apertures has to be taken into account, one can consider the Fresnel number

$$\mathrm{FN} = \frac{d^2}{4\lambda f_\mathrm{g}} \tag{2.53}$$

For FN > 3 the focal shift is smaller than 10 % of the focal length [71]. However, the MLAs used in this thesis have Fresnel numbers of $\mathrm{FN}_\mathrm{MLA1} = 0.71$ and $\mathrm{FN}_\mathrm{MLA2} = 1.61$. Therefore, it is expected that the maximum of the intensity distribution is shifted and that the intensity distribution along the optical axis as given in the previous section has to be modified. Following reference [71], the intensity distribution along the optical axis for a converging spherical wave is given by

$$I(f_\mathrm{g} + \Delta f) = I_0 \cdot \left(1 - \frac{u_N}{2\pi \cdot \mathrm{FN}}\right)^2 \cdot \left[\frac{\sin(u_N/4)}{u_N/4}\right]^2 \tag{2.54}$$

Here, the origin of the coordinate axis is at the plane of the aperture, Δf is the focal shift relative to the geometrical focal point and a modified variable

$$u_N = 2\pi \cdot \mathrm{FN} \cdot \frac{\Delta f / f_\mathrm{g}}{1 + (\Delta f / f_\mathrm{g})} \tag{2.55}$$

is introduced. The minima of the axial intensity distribution are found at $u_N = \pm 4m\pi$ with $m = 1, 2, 3, \ldots$ and the maxima are found at the root of the equation

$$\frac{\tan(u_N/4)}{u_N/4} = 1 - \frac{u_N}{2\pi \cdot \mathrm{FN}}, \qquad -2\pi < u_N < 0, \tag{2.56}$$

which can be evaluated numerically [72]. Using Eq. (2.55) the focal shift Δf can be calculated from the found root giving the effective focal length $f_\mathrm{e} = f_\mathrm{g} + \Delta f$.

Based on these equations, the theoretical focal shift has been calculated for MLAs with the same ROC $= 0.5$ mm but different aperture diameters as MLA2 ($d_\mathrm{MLA2} = 73\,\mu\mathrm{m}$). Furthermore, the calculations have been checked for validity against values given in [73]. In Fig. 2.2 the resulting dependence is shown together with a Zemax OpticStudio simulation using the physical-optics-propagation (POP) tool to compute the effective focal length [74]. It can be seen that the simulated maxima show variations in the transition part of the curve as at these values, computational variations have occurred depending on the boundary conditions of the simulation. For this reason two separate simulations (red and orange) with different boundary conditions have been performed. It can be seen that the simulated and the calculated focal lengths match well. Furthermore, the effective focal length of MLA2 is significantly lower than the geometrical focal length f_g expected from pure refraction. The resulting effective focal length f_e for both MLAs is given in Tab 2.2 (see section 2.2.5) together with other properties of the MLAs.

It is important to notice that this effect only shifts the intensity distribution resulting from diffraction at the aperture of the microlens and a changed interference of the single wavelets. The numerical aperture (NA) of the lens, defined as

$$\mathrm{NA} = n \cdot \sin\alpha, \tag{2.57}$$

where α is the maximum acceptance angle and n is the refractive index of the medium around the lens, is not affected.

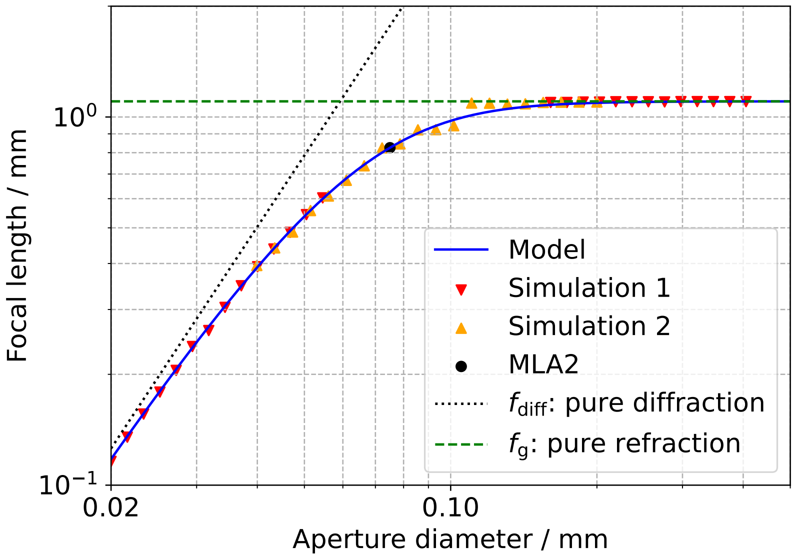

Fig. 2.2.: Model of the focal length of an MLA with same radius of curvature (ROC) but varying aperture diameter as MLA2 following the derivation in Eqs. (2.54) to (2.56) and references [71, 72]. The model is compared to the focal length determined using a Zemax OpticStudio physical-optics-propagation (POP) simulation of a single microlens (triangles), the geometric focal length f_{g} (green dashed line) resulting from Eq. (2.52), and the focal length resulting from pure diffraction (black dotted line) at an aperture given by $f_{\mathrm{diff}} = d^2/(4\lambda)$. The result for MLA2 is shown as a black dot.

2.2.4. Talbot effect for quadratic and hexagonal microlens arrays

If illuminating a microlens array with a coherent, monochromatic wave, the wavefront will be periodically modulated in the transverse directions by the lenslets. Due to Fresnel diffraction, self-images of the original structure appear at certain regular distances, the so-called integer Talbot planes, behind the microlens array [75]. However, there are not only exact copies of the original structure possible, but also fractional Talbot planes. It was already found by Lord Rayleigh at which distances exact self-images for a grating are created [76]. In [77] a derivation is given at which positions integer and fractional Talbot planes for arbitrary two-dimensional structures are found. Here, the derivation is limited to periodic structures with basis vectors $\vec{a}$ and $\vec{b}$ of equal length $a = b$, with a being used in the following as the pitch a_{MLA} of the MLA, which holds for the quadratic and hexagonal arrays that are used in this work as shown in Fig. 2.3. The positions of all fractional Talbot planes are given by

$$z_{Q+M/N} = \frac{\Theta a_{\mathrm{MLA}}^2}{\lambda}\left(Q + \frac{M}{N}\right) \tag{2.58}$$

where Q, M, N are natural numbers fulfilling the conditions $N > 0$ and $N > M \geq 0$. Here, $\Theta = 2 \cdot \sin^2 \gamma$ where γ is the angle between both basis vectors. In the following, the principle Talbot planes will be named as T_0 for the focal plane and $T_{\pm 1}$ for the first Talbot plane in each direction along the optical axis. Fractional Talbot planes are given by $T_{M/N} = \ldots, T_{1/3}, T_{1/2}, T_{2/3}, \ldots$.

In the limit of equal-length basis vectors, only quadratic ($\gamma = 90°$) and hexagonal structures

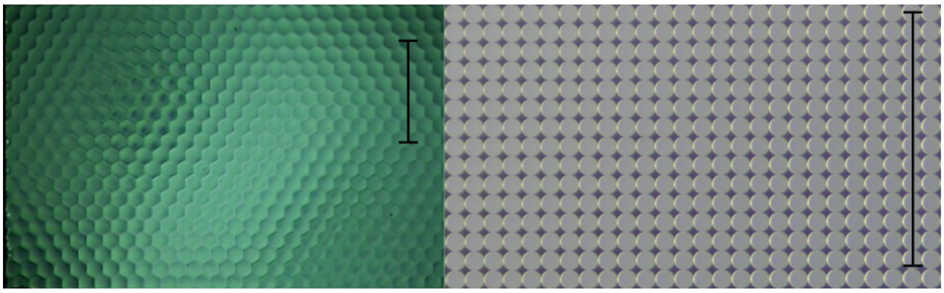

Fig. 2.3.: Images of the hexagonal (left) and the quadratic (right) MLA as used in this thesis. A scalebar of 1 mm is shown for comparison.

($\gamma = 60°$) are possible, resulting in the definition of the Talbot length z_T given by

$$z_\mathrm{T,quad} = \frac{2a_\mathrm{MLA}^2}{\lambda} \qquad \text{and} \qquad z_\mathrm{T,hex} = \frac{3a_\mathrm{MLA}^2}{2\lambda}. \tag{2.59}$$

For a quadratic MLA with 6×6 lenses it was investigated in [78] how the maximum intensity of the fractional Talbot planes for a small microlens array with $M/N < 1$ differs from the intensity in the focal plane. It was found, that especially the spots in the $T_{1/2}$ plane, being a self-image of the focal plane shifted by $a_\mathrm{MLA}/2$ along each basis vector, have a maximum intensity of 72 % compared to the focal plane T_0. In other fractional Talbot planes, the intensity is significantly lower. For principle Talbot planes T_0 and $T_{1/2}$ using the propagation of Gaussian beams, this is also investigated in [79] for a larger MLA illuminated with a Gaussian-shaped trapping laser having a beam waist of 17.5 pitches resulting in a maximum intensity for the $T_{1/2}$ plane of 96(2) %. Figure 2.4 (upper row) shows simulated light fields of different Talbot planes in the atom plane for a quadratic MLA as used in chapter 5 and introduced as MLA2 in the next section. For the fractional Talbot planes $T_{1/4}$ and $T_{3/4}$, these simulations differ slightly from the results in [78, 79] as the weaker intermediate spots show more aberrations resulting in an elliptical shape. It is expected that this results from aberration effects after reimaging due to the small pitch as similiar effects are observed in [80] where MLAs with a pitch of 10 µm are simulated.

For a quadratic as well as a hexagonal array similar simulations have been performed in [80]. In order to quantify the contrast of fractional Talbot planes the authors use the so-called Tamura-coefficient, a measure of the ratio between the standard deviation and the mean of the intensity distribution [81]. For a quadratic array this confirms the results in [78] and [79]. For a hexagonal array the simulations show that the contrast in the $T_{1/3}$ and the $T_{1/2}$ plane are relatively low and comparable to the $T_{1/4}$ plane of a quadratic array. However, the $T_{2/3}$ plane shows a contrast as high as in the T_1 plane.

Fig. 2.4 (lower row) shows simulated light fields of different Talbot planes in the atom plane for a hexagonal MLA with the same lens diameter and reimaging system as for the quadratic array above. The results do not confirm the higher intensity in the $T_{2/3}$ plane as shown in [81] but show that all fractional Talbot planes have comparable maximal intensities being approximately 1/3 of the T_0 plane. It has to be noted that for pronunciation of intermediate structures, each single image in Fig. 2.4 has its own colorbar scaling and the intensity variations between images are not visualized.

For the experiments presented in this thesis, the main attention has been put on trapping atoms in the focal plane. However, it has already been demonstrated that trapping in other

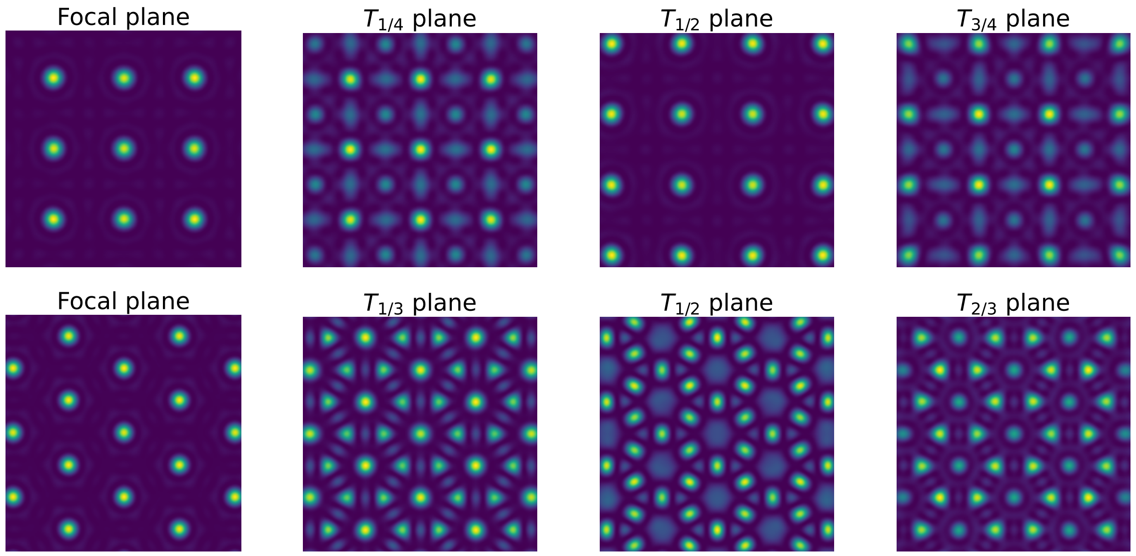

Fig. 2.4.: Simulation of the focal and fractional Talbot planes for a quadratic (upper row) and hexagonal (lower row) MLA after reimaging into the atom plane using the Zemax OpticStudio Huygens point-spread function (PSF) [74]. The lens properties of the microlenses are as in MLA2 (for details see Tab. 2.2 discussed in the next section). Each image has its own colorbar scaling.

Talbot planes is also possible [79]. If only one plane shall be used for trapping, the atoms trapped in other Talbot planes have to be removed. The procedure is explained in detail in section 3.4.3. Alternatively, the idea of using incoherent light has been demonstrated for similar systems in [33] to circumvent the creation of Talbot planes.

2.2.5. Experimental realization of microlens-based setups

Until now, only the spot size and structure in different planes directly behind an MLA have been discussed. Based on typical microlens arrays commercially available, the separation of focal spots is on the order of several 10 µm to 100 µm and therefore significantly larger than necessary for quantum information processing schemes based on Rydberg-mediated interactions [17]. Furthermore, the focal plane is usually only a few millimeter behind the principle plane of the microlens array. In order to avoid placing the MLA inside vacuum, the focal plane has to be reimaged into the vacuum chamber which, from an experimental side of view, has several advantages. First and foremost, it allows for easy rescaling of the trap separation as well as the spot size by choosing the matching reimaging optics. Furthermore, the microlens beam path can by superposed with other beams as used for atom rearrangement in this thesis. As the MLA is not inside the vacuum chamber, it can be easily exchanged.

Reimaging the focal plane is done by using an achromatic lens with focal length f_{AC} together with a microscope objective with focal length f_{Obj} as shown in Fig. 2.5. The focal plane of the achromatic lens is superposed with the desired Talbot-plane that shall be reimaged. This creates a collimated beam behind the achromatic lens which is propagated through the objective to produce an image at the working distance of the objective inside the vacuum chamber. The collimated beam is additionally more aberration-tolerant when using other optical elements along the beam path such as beam splitter cubes and dichroic mirrors for beam superposition

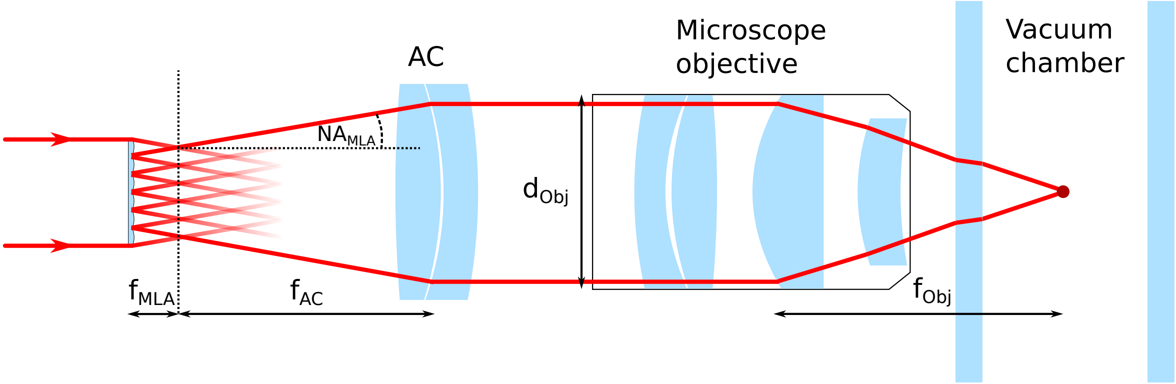

Fig. 2.5.: Schematic setup for reimaging of the focal plane of an MLA into the vacuum chamber using an achromatic lens with focal length f_{AC} and a microscope objective with aperture diameter of d_{Obj} and focal length f_{Obj}. Due to the multi-lens setup of the objectives, the focal length is only a useful measure for the magnification defined in Eq. (2.60) but is not equal to the working distance of the objective. The NA of the MLA in combination with the focal length of the achromatic lens define the beam size on the objective.

or separation. The magnification is given by

$$M = \left| \frac{f_{\mathrm{Obj}}}{f_{\mathrm{AC}}} \right| \tag{2.60}$$

and is on the order of 1/15 to 1/20 for systems used in this work. Depending on the exact magnification, waists in the single micrometer regime and trap pitches of several micrometers are achieved. The pitch in the atom plane inside the vacuum chamber is given by $a = M \cdot a_{\mathrm{MLA}}$. Each focus inside the vacuum chamber resembles a single dipole trap for the atoms. Due to the diffraction limit described in sections 2.2.1 and 2.2.2, the minimal spot size is limited by the NA of the objective as well as by the size of the collimated beam incident on the objective. For a fixed NA of the MLA, the beam size can be influenced by the focal length f_{AC} of the achromatic lens. The bigger f_{AC}, the larger is the beam incident on the objective (assuming the aperture of the achromatic lens is larger than the aperture of the objective). Although large beams will decrease the spot size, more intensity will be blocked by the aperture. Therefore, based on NA$_{\mathrm{MLA}}$, the focal length of the achromatic lens is usually chosen such that the geometrically determined beam diameter is as big as the aperture of the objective or slightly above.

In Tab. 2.2 the properties of the MLAs used in chapter 4 (MLA1) and chapter 5 (MLA2) as well as the expected parameters in the atom plane are given. For MLA1, an objective based on the design described in [82] with NA$_{\mathrm{Obj1}} \approx 0.27$ and an aperture diameter of roughly 20 mm is used. For MLA2 a new objective with NA$_{\mathrm{Obj2}} \approx 0.38$ is used whose properties are described in detail in section 5.1.1.

Tab. 2.2.: Properties of the MLAs as well as the traps created due to reimaging. The expected waist in the atom plane results from Eq. 2.48. Both MLAs are made of fused silica with MLA1 being made by aµs (APH-Q-161.5-R2.05) and MLA2 by Suess (19-0021). $f_{\mathrm{AC}} = 750\,\mathrm{mm}$ for both MLAs.

	d in µm	a_{MLA} in µm	ROC in mm	f_{g} in mm	f_{e} in mm	$\mathrm{NA}_{\mathrm{MLA}}$ in rad	f_{Obj} in mm	a in µm	w_0 in µm
MLA1	150	161.5	2.05	4.5	3.4	0.017	37.5	8.08	1.22
MLA2	73	75	0.5	1.1	0.83	0.033	52.9	5.29	0.86

2.3. Rydberg atoms

Neutral atoms in the ground state interact only if they are extremely close together such that collisions occur, e.g. two atoms in a single dipole trap as described in section 2.1.2. However, for quantum computing long-range interactions between atoms in different sites of the dipole-trap array are necessary. Those can be induced by exciting the atoms into so-called Rydberg states, which provide a controllable set of interactions. In the following, a brief introduction into Rydberg atoms as well as their possible excitation schemes will be given. This shall motivate why Rydberg atoms are considered for neutral atom interactions and especially what excitation pathways have to be considered to develop an experimental setup suitable for Rydberg-based experiments as described in chapter 3. Further details on Rydberg atoms and their implementation in quantum information processing can be found in [17, 83]

2.3.1. Properties of Rydberg atoms

In 1890 Johannes R. Rydberg found an empirical formula which very well described the series of spectral lines for different elements in the first three groups of the periodic table [84]. With the development of the atomic model by Niels Bohr, Rydberg's formula could be related to the binding energy E of the electron in a hydrogen atom described by

$$E = -\frac{R_{\mathrm{y}}^{*}}{n^2} \tag{2.61}$$

with Rydberg energy $R_{\mathrm{y}}^{*} \approx 13.6\,\mathrm{eV}$ and principal quantum number n [85, Chap. 3]. Today the term Rydberg atoms is used for atoms following the laws of Rydberg and Bohr. This holds for hydrogen as well as for alkali metals such as rubidium where the single valence electron is excited to a high principle quantum number. In the field of neutral-atom quantum-computing Rydberg atoms are assumed to have $n > 30$. In contrary to the hydrogen atom, the core of alkali metal atoms consists of the nucleus as well as closed electron shells which partly shield the positive charge of the nucleus. For low orbital angular momentum states (usually considered as $l \leq 4$), the valence electron can penetrate the inner electron shells and interact with the core electrons resulting in incomplete screening and an increase in the binding energy [28]. This can be taken into account by replacing n in Eq. (2.61) by the effective principle quantum number [38]

$$n^{*} = n - \delta_{\mathrm{n,l,j}} \tag{2.62}$$

where the quantum defect $\delta_{\mathrm{n,l,j}}$ can be determined based on the Rydberg-Ritz formula with empirically determined coefficients as found for ^{85}Rb in [86]. This and other properties

Tab. 2.3.: Scaling laws as a function of the effective principle quantum number n^* for the most important properties of Rydberg states. Adopted from [28, 38].

Property	Quantity	Scaling law
Binding energy	E_{n^*}	$(n^*)^{-2}$
Level spacing	$\lvert E_{n^*} - E_{n^*+1}\rvert$	$(n^*)^{-3}$
Radius	$\langle r\rangle$	$(n^*)^2$
Polarizability	α	$(n^*)^7$
Radiative lifetime	τ	$(n^*)^3$
Transition dipole moment $\lvert g\rangle \leftrightarrow \lvert nl\rangle$	$\lvert\langle nl\rvert - er\,\lvert g\rangle\rvert$	$(n^*)^{-3/2}$
Transition dipole moment $\lvert nl\rangle \leftrightarrow \lvert nl'\rangle$	$\lvert\langle nl\rvert - er\,\lvert nl'\rangle\rvert$	$(n^*)^2$
Resonant dipole-dipole interaction coefficient	C_3	$(n^*)^4$
van der Waals interaction coefficient	C_6	$(n^*)^{11}$

described next can be easily calculated using the Python-based *ARC*-library [87]. The energy of the Rydberg state is then denoted as E_{n^*}. From Eq. (2.61) it is obvious that the energy difference between neighboring Rydberg states decreases for higher lying Rydberg states scaling as $\left|\Delta E_{n^* \leftrightarrow (n^*+1)}\right| \propto (n^*)^{-3}$. It has to be noted that due to significant changes of $\delta_{\mathrm{n,l,j}}$ with l, the fine structure splitting is comparable to the energy difference of neighboring Rydberg states. Following Bohr's semi-classical atomic model, the atomic radius scales as

$$r = (n^*)^2 \cdot a_0 \tag{2.63}$$

with Bohr radius $a_0 = 0.529\,\text{Å}$ [85, Chap. 3] and thereby determines many other properties of Rydberg atoms as summarized by the scaling laws as given in Tab. 2.3. It is important to point out that these scaling laws are good to explain the behavior of Rydberg atom properties in general and to guide intuition. However, for exact calculations, the specific states and atomic species involved have to be taken into account.

Furthermore it has to be noted, that the lifetime of the state is not only determined by the spontaneous decay rate $\Gamma = 1/\tau$ but affected by decay through transitions between Rydberg states driven by black-body radiation. This is the case as the level spacing of Rydberg states is so small that the corresponding transition frequencies can be thermally populated. The induced decay rate is given by

$$\Gamma_{\mathrm{BBR}} = \frac{1}{\tau_{\mathrm{BBR}}} = \frac{A}{(n^*)^D[\exp\left(\frac{B}{(n^*)^C T}\right) - 1]} \tag{2.64}$$

with parameters A, B, C, D found in [88] for different alkali metals. The inverse of the resulting lifetime τ_{eff} is then given by

$$\Gamma_{\mathrm{eff}} = \frac{1}{\tau_{\mathrm{eff}}} = \frac{1}{\tau} + \frac{1}{\tau_{\mathrm{BBR}}}. \tag{2.65}$$

2.3.2. Excitation to Rydberg states

Following from the tight level spacing of Rydberg atoms, it is usually sufficient, to use a single laser tunable over several hundred GHz to address a wide range of Rydberg levels. For ^{85}Rb, the one-photon excitation from the ground state $\left|5S_{1/2}\right\rangle$ into some $|nP\rangle$ Rydberg state corresponds

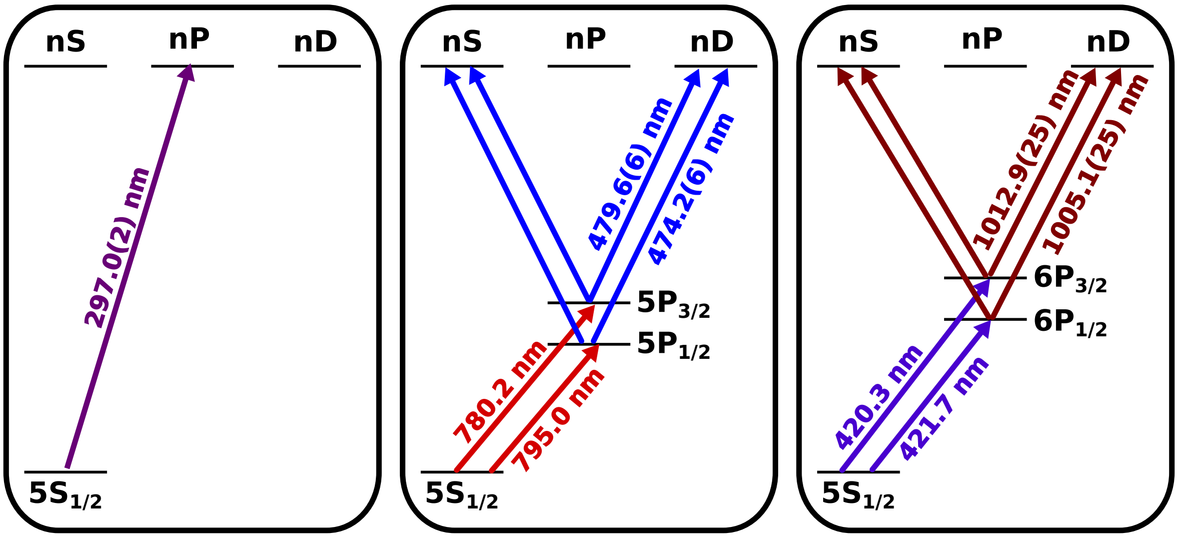

Fig. 2.6.: Possible one- and two-photon schemes for Rydberg excitation of ^{85}Rb atoms (references for three-photon excitations can be found in the text and are omitted here). For all transitions, no detuning is assumed and the wavelength for the upper transition is given for both nS and nD states although attached only to one of the arrows. The spread given in parentheses quantifies the wavelength range necessary such that states with $n = 50 \ldots 300$ can be excited. The energy shift for different angular momentum states is not taken into account for the drawing but for the wavelength values given. Data based on [46, 87, 89]

to a transition wavelength of 297.0(2) nm which would make excitation with a single laser possible as shown in Fig. 2.6 (left). This is maybe the most straight forward way for excitation, however, it is not always the best and easiest way. On the one hand, creating light at 297 nm is challenging and requires for example using single frequency doubling of a dye laser or two doubling steps of an amplified diode laser [90, 91]. Furthermore, there is a strong momentum transfer for a single-photon excitation which increases the Doppler sensitivity [92]. On the other hand, due to the direct excitation into the Rydberg state, no decoherence channels due to an intermediate state are present [93]. The most commonly used alternative is a two-photon transition utilizing the coupling to an intermediate state $|e\rangle$. The coupling of the ground state $|g\rangle$ and the intermediate state is given by the Rabi frequency Ω_{ge} whereas the coupling of the intermediate state and the Rydberg state $|r\rangle$ are given by the Rabi frequency Ω_{er}. In order to coherently excite the Rydberg state without populating the intermediate state, both laser fields are detuned by $\pm\Delta \gg \Omega_{\mathrm{i}}, \Gamma_{\mathrm{i}}$ from the respective transition such that the two photon resonance condition is fulfilled. Ω_{i} are the single-photon Rabi frequencies and Γ_{i} the transition line widths including all broadening mechanisms. When calculating the detuning, it is important to take the AC-Stark shift $\Delta_{\mathrm{AC}} \propto \Omega_{\mathrm{i}}^2/\Delta$ into account [94]. To achieve no shift in the transition frequency, it is important to have equal AC-Stark shifts and correspondingly equal Rabi frequencies which can be technically challenging as described below. Using adiabatic elimination of the intermediate level [95], the effective two-photon Rabi frequency is given by [44]

$$\Omega_{\mathrm{2Phot}} = \frac{\Omega_{\mathrm{ge}} \cdot \Omega_{\mathrm{er}}}{2\Delta} \tag{2.66}$$

for a single intermediate state. For rubidium, different excitation schemes are possible, using either the $|5P\rangle$ or the $|6P\rangle$ intermediate state. Two-photon transitions in general allow to excite into Rydberg $|nS\rangle$ and $|nD\rangle$ states (as shown in Fig. 2.6) while simultaneously reducing the complexity of the laser systems as the necessary transition frequencies are achievable with the direct or frequency doubled use of diode lasers. Furthermore, using counterpropagating laser beams, the Doppler broadening can be reduced. A commonly used path is the transition via the $|5P_{3/2}\rangle$ intermediate state whereas also transitions via the $|5P_{1/2}\rangle$ state are possible [25,96,97] (shown in Fig. 2.6 (center)). Due to the large dipole matrix element of the $|g\rangle \leftrightarrow |e\rangle$-transition compared to the $|e\rangle \leftrightarrow |r\rangle$-transition, the Rabi frequency in this case is always limited by the available laser power for the upper transition, especially if AC-Stark shifts shall be kept equal.

An alternative is therefore to use transitions via the $|6P\rangle$ states, especially the $|6P_{3/2}\rangle$ state, which reduces the dipole matrix element for the lower transition and increases it for the upper transition (shown in Fig. 2.6 (right)) [31,32]. Furthermore, high-power laser sources for the upper transition are easier for these transitions via the second resonance line (using $|6P\rangle$ states) than they are for the first resonance line (using $|5P\rangle$ states). Additionally, as the lifetime of the $|6P\rangle$ states are longer, the corresponding spontaneous decay rate is lower resulting in reduced decoherence due to spontaneous single-photon emission. The possible two-photon transition schemes are included into Fig. 2.6. Apart from two-photon transitions also three-photon transitions have been demonstrated which enable the sole use of diode lasers for the near-infrared and infrared transition wavelengths without the need for frequency doubling [98,99]. Furthermore, they allow for a complete recoil- and Doppler-free excitation of the atoms [92].

In this work, both possible two-photon transitions shall be taken into account for the design of the vacuum chamber as laser systems for both transitions are available in our group. The transition via the $|5P_{3/2}\rangle$ state has already been utilized in [25] while the laser system for the transition via the $|6P_{3/2}\rangle$ state is currently under development.

With excitation schemes at hand to excite ground state atoms into the Rydberg state, the remarkable properties of Rydberg atoms as detailed in section 2.3.1 can be utilized to implement dipole-dipole interactions between them. This offers a broad range of applications both in the field of quantum computing as well as in the field of quantum simulation. In the last years, two- and multi-qubit gates [34,39,100–105], the entanglement of several atoms into so-called Greenberger-Horne-Zeilinger (GHZ) states [106], the implementation of Ising- and XY-models [107–111] as well as topological phases [41], to just name a few, have been demonstrated. A detailed introduction into the interactions of Rydberg atoms in different interaction regimes as well as an overview of possible multi-qubit manipulations and realizable many-body Hamiltonians is given in [17].

2.4. Conclusion

This chapter discussed the theoretical concepts for trapping neutral atoms in optical dipole traps and introduced important knowledge about the light fields used to scale the trap creation with the help of microlens arrays. Based on the fundamental techniques of laser cooling and trapping, the preparation of single atoms was discussed and mechanisms causing atom loss in dipole traps were reviewed. The intensity distributions of focused Gaussian beams and plane waves as used for dipole trapping in this thesis have been discussed and special effects of microlens-based trap creation have been pointed out. Furthermore, a short introduction into the extraordinary properties of Rydberg atoms was given and possible excitation schemes were discussed.

3. A new setup for quantum experiments with rubidium atoms

Tweezer-based neutral-atom experiments have emerged from small atom ensembles trapped in small numbers of optical dipole traps or single atoms trapped in a single dipole trap [51, 112]. During the past years the technology has evolved to single-atom experiments where up to 500 atoms at several hundred trapping sites can be prepared, manipulated and, using Rydberg excitations, brought into interaction [31, 33, 113, 114]. In order to build a basis for a future quantum technology platform, an experimental setup needs to be developed allowing for current as well as future state-of-the-art quantum experiments. Based on the design of current neutral-atom quantum-technology platforms as well as experience gained in performing neutral-atom experiments in our group, some key requirements for the new setup have been defined [115]:

- **Versatile optical access:** With increasing complexity of experiments, more possibilities for optical access are necessary. Overlapping laser beams using a dichroic mirror or a polarizing beam splitter cube (PBS) is limited for light with separated wavelengths or specific polarization which is why different possibilities to optically address the quantum system are important. This especially includes the optical coatings as state-of-the-art experiments use different one- and two-photon transitions for Rydberg-mediated gate operations and simulations. Low-loss optical access for these excitation schemes need to be available for future experiments.

- **High long-term stability:** Quantum technology platforms need to be robust and experiments need to run stable without interruptions. Furthermore, effort for maintenance should be as low as possible. Long beam paths have been critical in the past, which is why new technical solutions shall be included to reduce beam path lengths wherever possible with reasonable effort.

- **High-NA optical access for trap creation and imaging:** The waists of the optical tweezers inside the vacuum chamber are limited by the NA of the microscope objective used for reimaging. Increasing the NA of the microscope objective will result in smaller trap sizes such that less laser power is needed for a single trap. Furthermore, tweezer arrays can be made more compact and thus increase the number of traps per area.

Based on these requirements, the design of a new experimental setup optimized for Rydberg experiments in large-scale optical tweezer arrays has been developed. In this chapter the key elements of the experimental setup built during this thesis will be presented. At first the vacuum chamber with its central part, the science chamber, as well as its most important components will be introduced. Next, the experimental control system used to conduct the experiments is described and an overview of the used laser systems is given. Furthermore, the standard procedure to prepare single atoms from a cold atom cloud is explained, being the basis of the experiments described in subsequent chapters. The details of the respective setups used in this thesis are described in the corresponding chapters 4, where a single large dipole trap is used in combination with a hexagonal dipole-trap array, and chapter 5, where three interleaved large-scale quadratic arrays are used. Both setups create dipole-trap structures based on microlens arrays as described in section 2.2 in general terms.

3.1. Design of the vacuum chamber

Based on the experience with previous experimental setups in the Atoms-Photons-Quanta group at TU Darmstadt the design of the vacuum chamber including all its electrical and optical attachments has been governed by the following design guidelines:

- Compact but versatile vacuum chamber with two large viewports for high-NA optical access and several other viewports for MOT and other auxiliary beams.
- Two independent ultra-high vacuum (UHV) pumps attached to the vacuum chamber as close as possible to the science chamber without limiting the optical access.
- Fiber collimators mounted close to the vacuum chamber should be used wherever possible in order to increase the mechanical stability and reduce the length of the beam paths.
- Optical viewport coatings with low losses for current state-of-the-art Rydberg experiments.
- Independent sets of magnetic field coils for magnetic field compensation and quantization field creation.

The full setup of the vacuum chamber based on these guidelines is shown in Fig. 3.1. The different components are described in the following sections whereas the respective microscope objectives are presented with the corresponding optical setups in chapters 4 and 5. In order to separate the atomic fluorescence light used for imaging the atoms from the trapping light, a dichroic mirror is used. Details on the dichroic mirror as well as an the general setup for detection of the atomic fluorescence are given in section 3.4.2.

3.1.1. Vacuum chamber

Vacuum glass cells are one possibility allowing for good optical access with high-NA microscope objectives. However, as anti-reflection coating for vacuum glass cells on the inside and outside is challenging, here a custom-made, flat, octagonal-like chamber with two CF100 re-entrant viewports is used. Four of the octagonal faces are equipped with large CF40 viewports to allow for good optical access from top and bottom as well as from the sides. The remaining four octagonal faces are split into three tilted faces with one CF16 viewport each. This increases the versatility as viewports can be equipped with different coatings or be exchanged by electrical feedthroughs if necessary. The vacuum in the chamber is maintained using an ion getter pump (Agilent Vaclon Plus 20 Noble Diode) running steadily and a titan sublimation pump (Thermionics Laboratory, Inc.; SB-1020) where one filament is heated for roughly one minute on a monthly basis. The pressure is continuously monitored using pressure gauge 1 (Balzers IKR 270) giving a pressure of $7.0(5)\times10^{-10}$ mbar. Pressure gauge 2 (Balzers IKR 070) can be used to intermittently check the vacuum pressure closer to the science part of the chamber and is measuring a pressure of $1.3(1)\times10^{-9}$ mbar. The estimated pressure in the vacuum chamber is therefore assumed to be on the order of $1.0(5)\times10^{-9}$ mbar. Rubidium is supplied to the center of the chamber by two rubidium metal dispensers (SAES) positioned below the

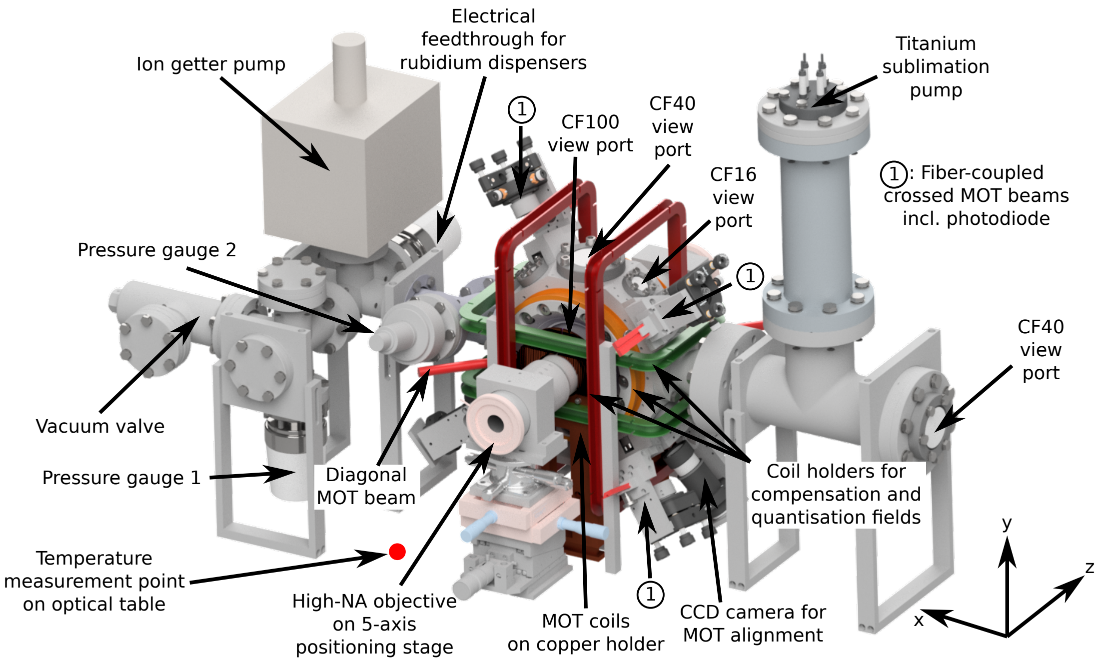

Fig. 3.1.: Front view of the vacuum chamber in its most recent setup with the high-NA microscope objectives as used for experiments described in chapter 5. On the left side, all vacuum components are of CF40-standard holding pressure gauges, the ion getter pump, the rubidium dispensers as well as the vacuum valve. The right side uses CF63 vacuum components being attached to the main chamber by a conical adapter to increase the pumping speed of the titan sublimation pump. The MOT coils are wound in anti-Helmholtz configuration onto two all-copper holders (with slit on top to avoid eddy currents) mounted in front of the CF100 viewports. The coil holders for magnetic field compensation and quantization fields are shown in orange, green and red. A high-NA microscope objective is mounted in front of each CF100 viewport. For laser cooling and trapping six MOT beams are used: Two beams, called ’diagonal MOT beams’, enter the chamber through the CF100 viewports under an angle of 47.3(5)° relative to the optical axis of the microscope objective (z-axis); The other four, called ’crossed MOT beams’, form a cross with an angle of 14.78° relative to the x-y-plane and enter through CF16 viewports on the diagonals of the vacuum chamber.

Tab. 3.1.: Typical wavelengths used in ^{85}Rb Rydberg experiments. Rydberg levels from n=50 to n=300 are considered.

Transition	Purpose	Wavelength
$\lvert 5S_{1/2}\rangle \Leftrightarrow \lvert 5P_{1/2}\rangle$	State manipulation on D1 line	795.0 nm
$\lvert 5S_{1/2}\rangle \Leftrightarrow \lvert 5P_{3/2}\rangle$	State manipulation on D2 line	780.2 nm
-	Dipole trapping	796 nm to 805 nm
$\lvert 5S_{1/2}\rangle \Leftrightarrow \lvert 6P_{1/2}\rangle$ or $\lvert 6P_{3/2}\rangle$	Rydberg excitation	420.3 nm and 421.7 nm
$\lvert 5P_{1/2}\rangle \Leftrightarrow \lvert nS\rangle$ or $\lvert nD\rangle$	Rydberg excitation	473.7 nm to 474.8 nm
$\lvert 5P_{3/2}\rangle \Leftrightarrow \lvert nS\rangle$ or $\lvert nD\rangle$	Rydberg excitation	479.1 nm to 480.2 nm
$\lvert 6P_{1/2}\rangle \Leftrightarrow \lvert nS\rangle$ or $\lvert nD\rangle$	Rydberg excitation	1002.6 nm to 1007.5 nm
$\lvert 6P_{3/2}\rangle \Leftrightarrow \lvert nS\rangle$ or $\lvert nD\rangle$	Rydberg excitation	1010.4 nm to 1015.4 nm

ion getter pump in the 5-way-cross leaving approximately 10(1) mm of optical access above and below the optical axis. The vacuum chamber is sealed after rough pumping using an all metal valve (MKS UHV-40-ACC-EVLN).

3.1.2. Optical viewports

Following the design guidelines, three different types of viewports are used:

- Custom-made CF100 re-entrant viewports with glass thickness of 6.35 mm and a coated viewing area of 75 mm diameter (made by MPF products). The mounted windows have a separation of 39 mm between the inner surfaces. The windows are anti-reflection coated for an angle of incidence of 0° to 45° within a wavelength range from 420 nm to 480 nm and from 780 nm to 1050 nm.
- CF40 (4 pieces) and CF16 (10 pieces) viewports (DUV grade; MPF products) with an anti-reflection coating made by Laseroptik GmbH for an angle of incidence of 0° resulting in a reflectivity per surface below 1 % for 420 nm to 480 nm and 780 nm to 815 nm as well as less than 2 % for 815 nm to 1200 nm. Two CF16 windows of the vacuum chamber are uncoated for possible UV access in future. One of these is currently used for MOT monitoring.

As the large CF100 viewports are the main optical access to the vacuum chamber allowing for high-quality imaging on the one hand and the creation of large-scale arrays of optical tweezers or single-site addressability with micrometer-sized waists on the other hand, the coating needs to cover as many of the standard wavelengths in ^{85}Rb-experiments as possible. An overview of the involved wavelengths is given in Tab. 3.1.

Additional information on the transmission through the viewports together with the coating curves can be found in section C.1.

3.1.3. Magnetic field coils

In order to achieve a good preparation of cold neutral atoms, using a MOT phase to cool and trap the atoms as well as a subsequent molasses phase for sub-Doppler cooling, it is important to control the magnetic field gradient for atom trapping as well as to compensate any other magnetic fields. External magnetic fields such as the earth's magnetic field as well as fields from the ion getter pump and other devices can shift the zero point of the gradient field away from the intersection point of the laser beams reducing the trapping performance. Furthermore, an uncompensated magnetic field offset can result in an undefined magnetic quantization axis affecting optical pumping mechanisms. Therefore a pair of gradient field coils was designed, built and characterized for the MOT gradient field and three splitted pairs of homogeneous field coils for field compensation and magnetic bias fields to define a quantization axis.

The magnetic field of each coil can be theoretically calculated using Biot-Savarts law [116]. For thin wires the magnetic field $\mathbf{B}(\mathbf{r}_\mathrm{a})$ at position $\mathbf{r}_\mathrm{a}$ is calculated using

$$\mathbf{B}(\mathbf{r}_\mathrm{a}) = -\frac{\mu_0}{4\pi} \cdot I \cdot \int \frac{\mathbf{e}_\mathrm{ab} \times \mathrm{d}\mathbf{s}}{r_\mathrm{ab}^2} \tag{3.1}$$

with current I along the wire segment $\mathrm{d}\mathbf{s}$, vector $\mathbf{r}_\mathrm{ab}$ from $\mathbf{r}_\mathrm{a}$ to $\mathbf{r}_\mathrm{b}$ with unit vector $\mathbf{e}_\mathrm{ab}$ and length r_ab as well as $\mathrm{d}s$ being the infinitesimal piece of wire at position $\mathbf{r}_\mathrm{b}$. In order to calculate the magnetic field of a coil at position $\mathbf{r}_\mathrm{a}$, the coil is modeled using linear pieces of wire with current I flowing from $\mathbf{r}_1$ to $\mathbf{r}_2$ as shown in Fig. 3.2.
Equation 3.1 can then be simplified to

$$\begin{aligned} \mathbf{B}(\mathbf{r}_\mathrm{a}) &= \tfrac{\mu_0 I}{4\pi R} \int_{\alpha_1}^{\alpha_2} \cos(\alpha)\mathrm{d}\alpha \cdot \mathbf{e}_t \\ &= \tfrac{\mu_0 I}{4\pi R} \left[\sin(\alpha_2) - \sin(\alpha_1)\right] \mathbf{e}_t \end{aligned} \tag{3.2}$$

with $\mathbf{R}$ being the vector from $\mathbf{r}_\mathrm{a}$ perpendicular to the axis of the wire $\mathbf{e}_\mathrm{wire}$ (unit vector from $\mathbf{r}_1$ to $\mathbf{r}_2$; same direction as current I) and

$$\begin{aligned} \mathbf{r}_\mathrm{wire} &= \mathbf{r}_2 - \mathbf{r}_1 = \mathbf{e}_\mathrm{wire} \cdot |\mathbf{r}_2 - \mathbf{r}_1| \\ \mathbf{e}_t &= \mathbf{e}_R \times \mathbf{e}_\mathrm{wire} \end{aligned} \tag{3.3}$$

For a rectangular coil, each side of a winding is modeled as a single, straight wire piece whereas for a circular coil, one loop is approximated by a 32-sided polygon[1]. The magnetic field vectors of all pieces of a coil add up to the total magnetic field.

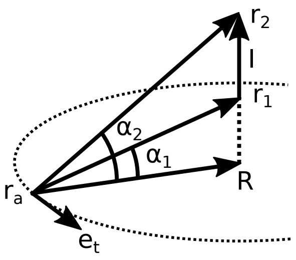

Fig. 3.2.: For calculating the magnetic field at $\mathbf{r}_\mathrm{a}$ resulting from a straight wire between $\mathbf{r}_1$ to $\mathbf{r}_2$ one can use the integration from α_1 to α_2 as described in Eq. (3.2)

.

Gradient field of magneto-optical trap

For the gradient field of the MOT, there are several constraints influencing the possible design: First of all, the achievable gradient of the coils should be around 20 G/cm, a value which has been used in several groups for 3D-MOTs [47, 117]. Simultaneously, the current needs to be low enough to not heat the coils above 50 °C. This limit is set to reduce thermal effects close to the vacuum chamber and for safety reasons (no overheating possible). Furthermore, the optical access should not be diminished by the coils. In order to reduce complexity coils inside the vacuum chamber where not considered.

From these constraints two options result: Either the gradient field coils can be placed around the CF-100 flange or around the microscope objective using a coil with a triangular cross section such that the diagonal MOT beam is not constrained. A gradient field coil around the vacuum flange would have direct thermal contact to the chamber and eddy currents are

---

[1] The deviation to a circular loop is below 0.2 % and therefore smaller than any uncertainty accumulated during winding.

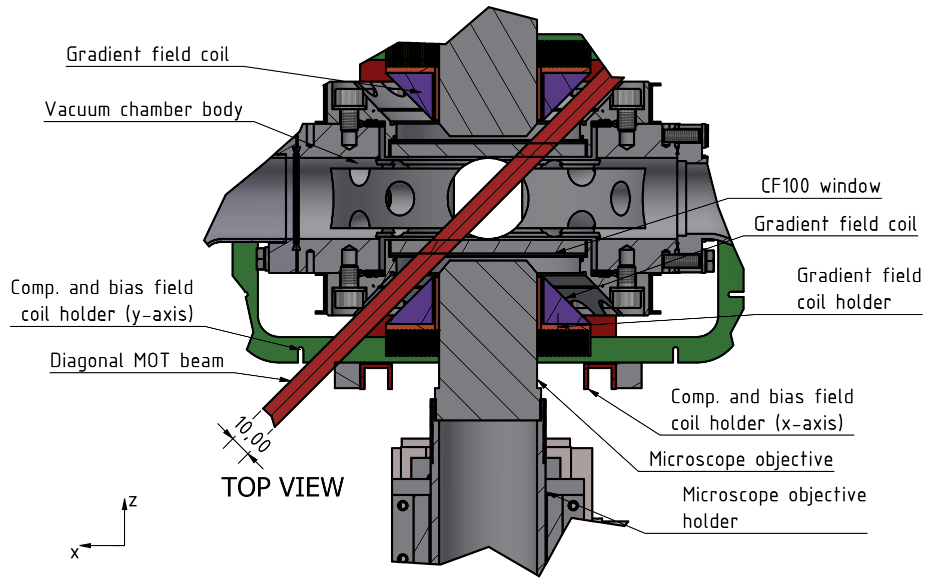

Fig. 3.3.: A cross sectional view from the top of the vacuum chamber: The gradient field coil is shown in purple and the gradient field coil holder in copper brown. Inside the copper holder there is the cross section of the microscope objective shown in shaded grey (no lenses depicted). Between the CF100 flange and the gradient field coil is space for a diagonal MOT beam approximately 10 mm in diameter.

directly induced in the flange itself. Using a gradient field coil around the microscope objective will enable us to reduce eddy currents by slitting the holder but will also heat the optics more. It was decided to use coils around the microscope objective mounted on a copper holder with cooling fins for heat dissipation which leaves space for compensation field coils around the flange. The coil holder has a cut parallel to the symmetry axis of the coil to reduce eddy currents (see appendix B for a drawing). A cross section through the vacuum chamber and attached parts is shown in Fig. 3.3. The gradient field coils are wound onto the holder while covering them in thermally conductive epoxy (Electrolube ER2220). A total of 165 windings fit on the holder resulting in a measured magnetic field gradient of 4.45(5) G/(A cm) along the coils symmetry axis and of 2.18(5) G/(A cm) perpendicular to the symmetry axis. Based on the theoretical winding configuration gradients of 4.36 G/(A cm) along the coils symmetry axis and 2.17 G/(A cm) perpendicular to it were expected; the deviation results from the fact that the exact positioning of each individual winding of the coil cannot be resembled in the theoretical calculation leading to slight deviations. The resistance of the coil is 1.22(2) Ω for a current of 1 A and 1.28(2) Ω for a current of 5 A. With a steady current of 5 A it heats up to approximately 45 °C. On a measurement point (see Fig. 3.1) placed close to the vacuum chamber on the experimental table a temperature change of 1.1(1) K can be observed. The heating of the rubidium dispensers results in a temperature change of 0.4 K. In between experimental runs the experiment is therefore kept in a ”keep warm”-cycle. This is continuously switching the magnetic field at a similar rate as during experimental cycles to keep the experimental table in a thermal equilibrium state.

Tab. 3.2.: Magnetic field strength for compensation and bias field coils attached to the vacuum chamber. The coordinate system definition is shown in Fig. 3.1. All resistances have been measured at a current of 1 A. The used currents for compensation fields were predetermined from measurements with a hall sensor on both sides of the vacuum chamber. Tuning of the compensation fields has been used to position the MOT relative to the trap arrays for optimal loading. A measurement of the residual magnetic field based on a two-photon Raman process as described in [119] has not yet been performed.

Coil pair (windings)	B-field (meas.) in G/A	B-field (calc.) in G/A	Resistance in Ω	Current I used in Exp. in A
Comp. x (19)	1.6(1)	1.61	0.8	0.68
Bias x (59)	4.8(1)	4.86	2.4	not used
Comp. y (17)	1.8(1)	1.79	0.5	0.0
Bias y (64)	6.65(10)	6.74	1.5	not used
Comp. z (19)	2.2(1)	2.11	0,7	0.23
Bias z (59)	6.3(1)	6.29	2.0	not used

Compensation and quantization fields

For the layout of the coils for the compensation and bias magnetic fields it is important to know the strength of the magnetic fields that have to be compensated and the strength of the quantization fields necessary for experiments. In Darmstadt the earth's magnetic field has a magnitude of 0.487 G [118][2] and up to 2 G are expected to result from the ion getter pump at the center of the vacuum chamber. For all three coil pairs there is a space-limited capacity of roughly 80 windings. Since roughly 20 windings are expected to result in a magnetic field of approximately 2 G/A, the coils were split into roughly 20 windings for magnetic field compensation and 60 windings for bias fields. This enables the use of the compensation fields with a moderate current of 1 A while allowing for the creation of bias fields with 5 G/A to 6 G/A. The measured and calculated magnetic fields at the center of the vacuum chamber for all coils and axes are given in Tab. 3.2. The corresponding measured and calculated magnetic fields along the coil axes can be found in appendix B.

3.1.4. Attachments to the vacuum chamber for stable optical access

As described at the beginning of this chapter, long beam paths for e.g. the MOT beams can be a limitation for continuous, stable operation of the experiments. The more complex experiments get, the more pieces need to work perfectly together such that every single part with a high long-term stability reduces the amount of time for maintenance. It was therefore intended to reduce the maintenance for the MOT compared to the previous setup. In order to achieve this the corresponding beams should be as large as possible and mounted as close as possible to the chamber such that MOT optimization using beam steering is not necessary after an optimal alignment.

The vacuum chamber was therefore equipped with 3 to 6 threaded holes around each CF16 and CF40 flange to attach custom optic holders to it. For each flange, an adapter with a viewport cut-out mounted directly onto the vacuum chamber was designed, acting as an

---

[2] The components of the magnetic field in Darmstadt are: North: 0.2 G, East:0.01 G, Vertical: 0.45 G and the y-axis of the optical table is oriented along the north-west direction.

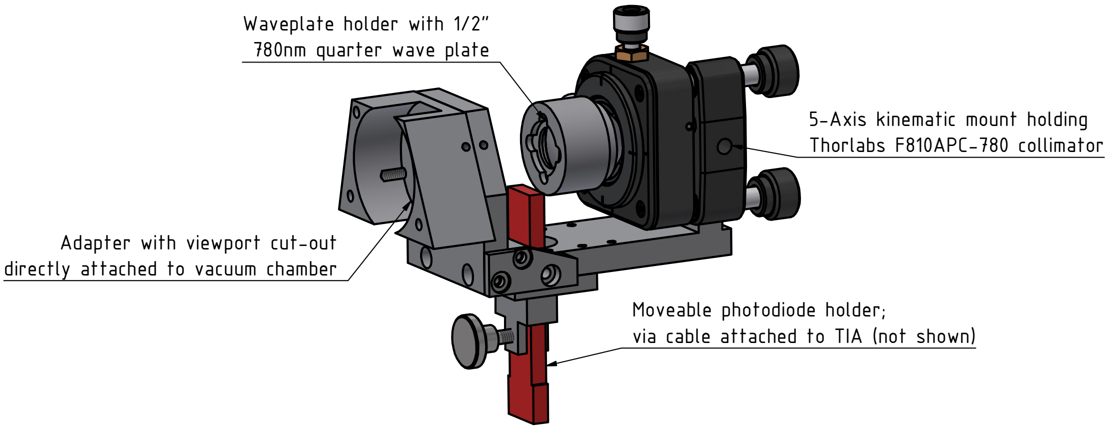

Fig. 3.4.: Vacuum chamber attachment for a fiber-coupled MOT beam. The adapter directly mounted onto the chamber is acting as the interface for any opt-mechanical attachment and is not intended to be removed. The collimator (Thorlabs F810APC-780) in its 5-axis kinematic mount (Thorlabs K5X1) is attached to the adapter via an aluminum angle guaranteeing a centered beam relative to the vacuum viewport. The mounting also holds a movable photodiode (OEC S-100CL) connected to a transimpedance amplifier (TIA) to measure the laser power of each MOT beam.

interface for any future optical holder. This ensures protection of the vacuum viewports as well as reducing the risk of wearout for the threads directly drilled into the metal body of the vacuum chamber.

At the current stage of the experiment, the four crossed MOT beams are directly attached to the vacuum chamber while the diagonal MOT beams originate from collimators (Thorlabs F810APC-780) on aluminum posts close to the vacuum chamber. The mounting of one of the MOT beams including the vacuum chamber attachments is shown in Fig. 3.4. Each collimator mount was pre-assembled by fiber-coupling the laser beam to it using a polarization-maintaining fiber (Thorlabs P3-780PM-FC) and mounting a quarter waveplate (FOCtek 780 nm True Zero order) onto the collimator [3]. In order to check the laser output power of the fiber, a photodiode (OEC S-100CL) connected to a transimpedance amplifier is attached to the mount. Checking the laser output power on a monthly basis and in case optimizing the fiber coupling efficiency is usually sufficient to achieve stable MOT trapping, beam position readjustments are not necessary. However, it was observed that polarization changes in the fiber can result in a force imbalance of the MOT. It is therefore important to reduce changes in the fiber position and to keep a constant temperature on the experiment table. Another possibility would be to clean the polarization after the collimator using a polarizing beam splitter cube combined with active laser power stabilization. This was not implemented due to space restrictions.

On two of the CF16 viewports, charge-coupled device (CCD) cameras for MOT observation are attached to the vacuum chamber by replacing the kinematic mount by a lens tube mount (Thorlabs SM1TC).

---

[3] The crossed MOT beams (cooling and repumping beams) are all right-handed circularly polarized whereas the two diagonal beams are left-handed circularly polarized with respect to the direction of beam propagation.

3.2. Experiment control system for neutral-atom experiments

In order to perform cold atom experiments, all parameters of the hardware (light fields, magnetic fields, cameras, and many more) need to by orchestrated precisely. On the hardware-side, the major challenge is to synchronise hardware triggers and voltage changes down to sub-microsecond timescales over a typical experiment period of up to a few seconds. On the software-side, it is important to use software working perfectly together with the available hardware. Furthermore, it is beneficial for the operator of the experiment to be able to plan, execute as well as analyze experiments as efficient as possible. In the following sections, an overview of the implemented software and hardware will be given.

3.2.1. Introduction to experiment control software `labscript-suite`

For the experiments described in this thesis the experiment control software `labscript-suite` is used [120]. It was developed at Monash University (Victoria, Australia) for BEC experiments and is described in detail in [121]. Here a short overview of its main functions and the interaction with hardware shall be given. Custom adaptions made to the `labscript-suite` are described in subsequent sections.

The `labscript-suite` is an open-source experiment control software including programs for experiment preparation, execution, and analysis in python-based packages. The strength of the `labscript-suite` is that it combines scripted experiment logic with experiment parameters that can be manipulated in a graphical user interface (GUI). The complete data flow within the `labscript-suite` package and its interplay with the experiment-specific hardware currently used is shown in Fig. 3.5.

To start, the user writes an experiment script describing the logic of the experiment and, within the GUI of `runmanager`, defines the parameters used within the experiment script. In `runmanager`, the information is saved in a shot file and send to a background process utilizing the `labscript` package. `labscript` is a software library providing common functions to control various types of hardware. With these functions the experiment script and the experimental parameters are compiled with the help of the `labscript-devices` plugins into hardware instructions which are also saved to the shot file. The labscript-device plugins provide device-specific commands to compile `labscript`-code into hardware instructions. Furthermore, they incorporate classes to communicate with the hardware itself and to manually control the device via a GUI.

After compilation, `runmanager` sends the shot file to `BLACS`. `BLACS` is responsible for shot execution and hardware control. On the one hand, `BLACS` offers GUI-based manual control over the hardware. On the other hand, it manages the execution of experiment shots sent from `runmanager` by organizing them in a queue. Upon execution, `BLACS` disables manual control and uses the hardware instructions of the first shot file in the queue to program all devices and put them into a buffered execution mode. After programming is finished, `BLACS` sends a start command to the master clock of the experiment. The master clock triggers the output changes of all devices attached to it. The specialty of the `labscript-suite` is that it relies on variable frequency clocks, so-called pseudoclocks, which send a trigger to attached devices only if an output change on any of the devices shall occur. This drastically reduces the amount of instructions on each device compared to a fixed-frequency clock, as for each trigger an instruction has to be saved on the attached devices. After the master clock has finished its last trigger event, it sends a finished statement back to `BLACS` and `BLACS` coordinates saving

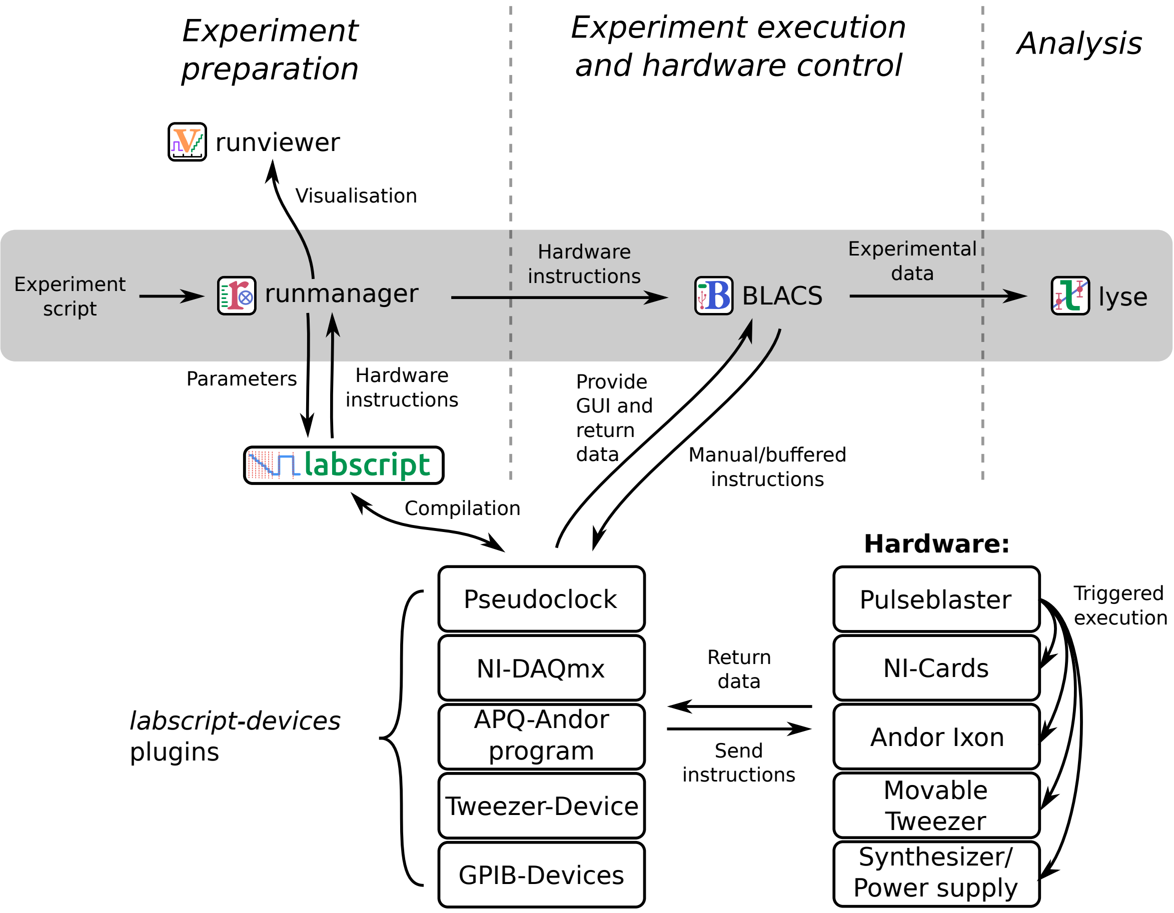

Fig. 3.5.: Overview of the software and hardware used for experiment control. The `labscript-suite` software provides programs for all stages of an experiment: preparation, execution including manual hardware control, and data analysis. Arrows indicate how information is passed between the different components of the experiment control system.

the acquired data to the shot file.

The shot file now contains all relevant information of the complete experiment and immediately, or at any later time, be analyzed using `lyse`. If the operator needs to plan experimental cycles or analyze the parameters and timings of the experiment script without executing the experiment in reality, the `runviewer` can be used. `runviewer` is a visualization program able to analyze the hardware instructions and turn them into ”output value-vs-time” graphs for each device output of the experiment. It can be directly fed from the runmanager or already compiled shots can be loaded by hand.

3.2.2. Experiment-specific hardware and software for experiment control

The hardware used in the experimental setup builds on five main components as shown in Fig. 3.5:

- The master pseudoclock Pulseblaster PB24-100-4k-PCIe.

- National Instruments (NI) cards PCI-6713, PCI-6534 and PCI-6259 to generate analog and digital output signals as well as acquiring analog signals for experiment control.
- Andor electron-multiplying charge-coupled device (EMCCD) camera (IXON DV887DCS-UV (X-1441) used in chapter 4 or IXON DU-888U3-CS0-EXF (X-13700) used in chapter 5 with custom-developed camera software.
- A custom Tweezer controller for the movable tweezer.
- Several general purpose interface bus (GPIB)-controlled devices such as synthesizers for RF-frequencies as well as a Keysight HP662xA power supply for magnetic field coils.

The open-source `labscript-suite` project provides device plugins for some of these devices (e.g. the Pulseblaster as well as NI-cards). However, in some cases, modifications for experiment-specific tasks have been necessary which is why the currently used device plugins for the Pulseblaster, the NI cards as well as the GPIB-controlled devices can be found in the ”APQ-devices”-branch of our GitHub-repository [122]. For controlling the camera and the movable, optical tweezer, external programs communicating with the `labscript-suite` via the local network are used. More details on these programs are described in the following sections. Furthermore, during this thesis, an Arduino-based `labscript-devices` plugin for controlling an AD9910 direct digital synthesizer (DDS) has been developed. The system can be used as triggerable radio-frequency source providing frequency switching on a microsecond timescale. It has mainly been used as standalone device for the characterization of acousto-optical deflectors and is currently not included in the main experimental setup. The details of its characterization and implementation can be found in appendix F.

Implementation of the camera system

Core of the data acquisition in most individual-atom experiments is an EMCCD camera used to detect the fluorescence of the atoms inside the vacuum chamber as described in section 3.4.2. The camera program in our lab is thereby not only responsible for controlling the camera and saving the acquired images but also does a live-analyses of images during the experimental sequence to provide the single-atom trap occupation for atom rearrangements. Here an overview of the camera program is given. Further details on the camera program can be found in [123].

Figure 3.6 shows a screenshot of the camera GUI during a measurement with one tweezer array as described in chapter 5. It provides a large-scale life view of the most recent acquired image on the left side as well as different hardware and software control parameters for the camera and the acquired data on the right side of the GUI.

The hardware specific camera settings are found in the left column (A) facilitating the definition of all important control parameters of the camera when operating it manually. During an experiment those parameters are defined in the experiment script. The right column offers most importantly functions for grid analysis in the top part (B) and for setting a region of interest (ROI) as well as custom levels defining the colorbar range in the bottom part (C).

The ROI allows the user to define which rectangular area of the camera is of interest and shall be read out. Making this region as small as possible reduces the readout time. For better visual analysis of images, especially when optimizing the magneto-optical trap, a custom levels setting has been included. This enables the user to set custom thresholds for the image’s colorbar facilitating the recognition of intensity changes.

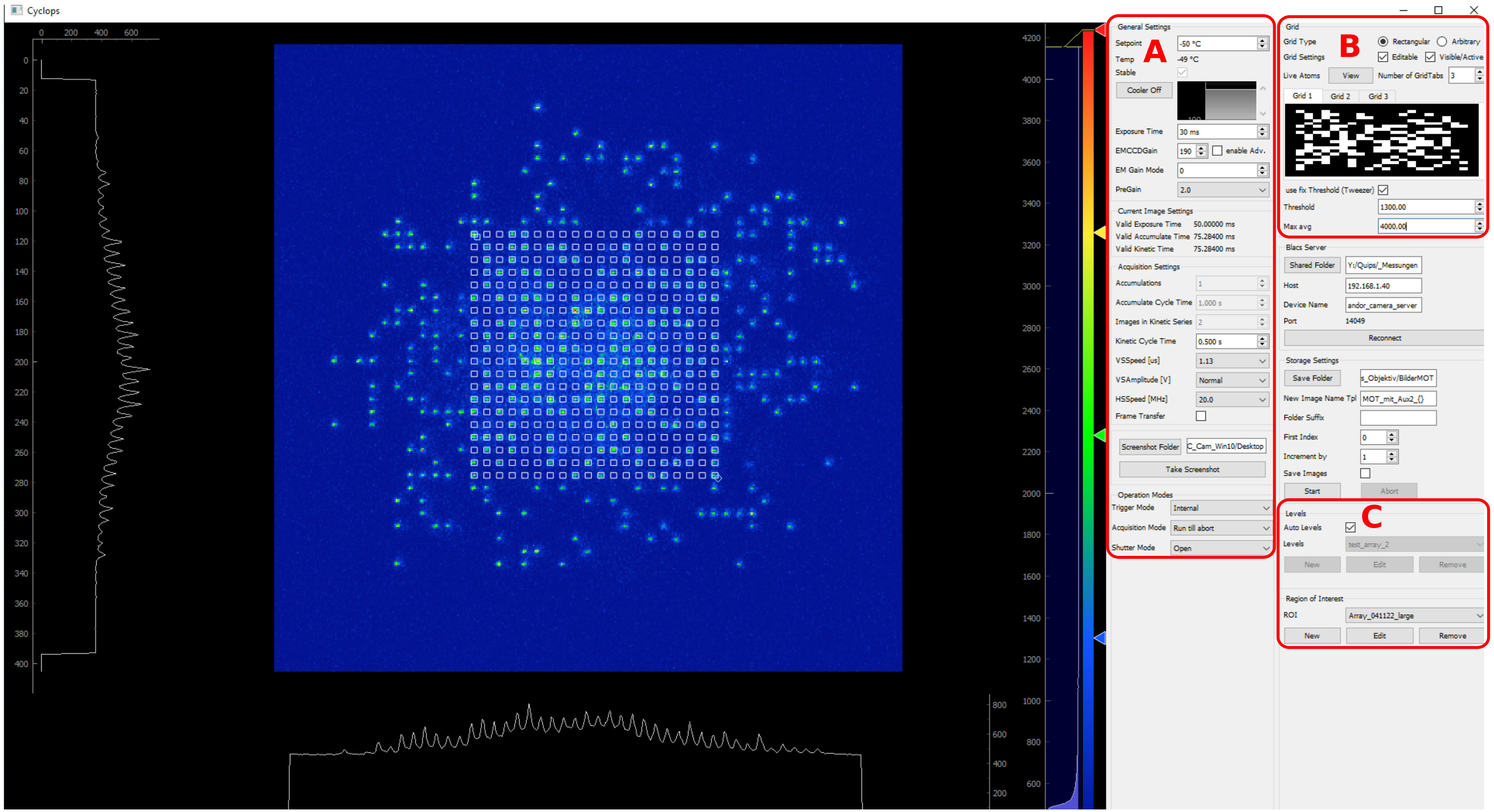

General Settings
Setpoint: -50 °C
Temp: -49 °C
Stable: ☑
Cooler Off
Exposure Time: 30 ms
EMCCDGain: 190 ☐ enable Adv.
EM Gain Mode: 0
PreGain: 2.0

Current Image Settings
Valid Exposure Time 50.00000 ms
Valid Accumulate Time 75.28400 ms
Valid Kinetic Time 75.28400 ms

Acquisition Settings
Accumulations: 1
Accumulate Cycle Time: 1,000 s
Images in Kinetic Series: 2
Kinetic Cycle Time: 0,500 s
VSSpeed [us]: 1.13
VSAmplitude [V]: Normal
HSSpeed [MHz]: 20.0
Frame Transfer: ☐

Screenshot Folder: C_Cam_Win10/Desktop
Take Screenshot

Operation Modes
Trigger Mode: Internal
Acquisition Mode: Run till abort
Shutter Mode: Open

Grid
Grid Type: ● Rectangular ○ Arbitrary
Grid Settings: ☑ Editable ☑ Visible/Active
Live Atoms: View
Number of GridTabs: 3
Grid 1 | Grid 2 | Grid 3
use fix Threshold (Tweezer) ☑
Threshold: 1300,00
Max avg: 4000,00

Blacs Server
Shared Folder: Y:/Quips/_Messungen
Host: 192.168.1.40
Device Name: andor_camera_server
Port: 14049
Reconnect

Storage Settings
Save Folder: s_Objektiv/BilderMOT
New Image Name Tpl: MOT_mit_Aux2_{}
Folder Suffix:
First Index: 0
Increment by: 1
Save Images: ☐
Start | Abort

Levels
Auto Levels: ☑
Levels: test_array_2
New | Edit | Remove

Region of Interest
ROI: Array_041122_large
New | Edit | Remove

Fig. 3.6.: Screenshot of the camera program during an experimental cycle. The left part shows the most recent acquired image including cuts along both axes and one currently activated grid (Grid 1) for single atom analyses. The right side offers parameter settings for manual control of the camera (A), a user-defined region of interest as well as a custom colorbar range called 'levels' (C), and, most importantly, a live view of the trap occupation of the currently active grids (B).

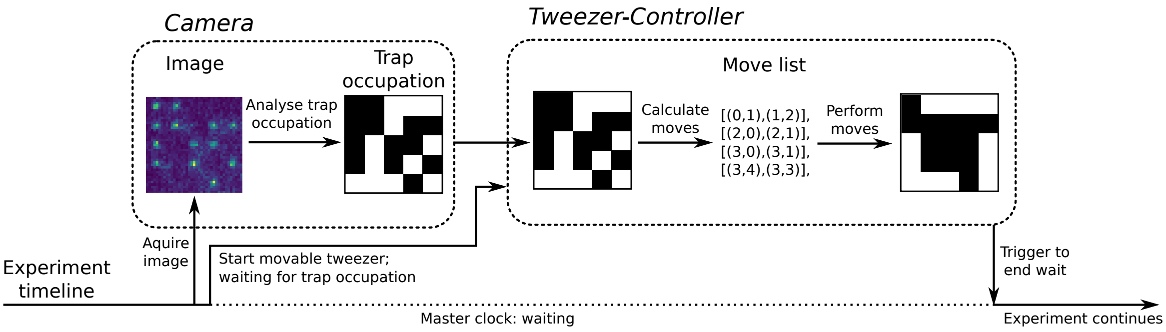

Fig. 3.7.: Flowchart illustrating the experimental timeline when using the wait-functionality of `labscript` while rearranging atoms.

For single-atom grid analysis, the camera program includes several features. For a single dipole-trap array, a rectangular grid of boxes, variable in size and spacing, can be generated. The grid is stored to the experiment file during measurements and is used for image analysis later on. Furthermore, it offers the possibility for a live analysis of the current image. If ”use fix threshold” is checked, the mean signal in each box is compared to the user-defined threshold below. This results in a boolean trap occupation as shown in the upper left of Fig. 3.6. If ”use fix threshold” is unchecked, it uses image masks generated from previous analyses to calculate the trap occupation as described in section 3.4.2. Apart from calculating and visualizing the current trap occupation, the camera program also provides this information to other devices such as the movable tweezer and the grid jumper described in the following sections. For the experiments described in chapter 5, the program was extended to allow for several grids, one for each tweezer array used in the experiment. As for large, interleaved grids recognition in such a small window is difficult, the live atom occupation can be shown in an extra pop-up window if necessary.

Atom rearrangements using `labscript` waits

The `labscript-suite` provides a ”wait” feature to hold the pseudoclock until a parameter or condition is met. This is done by stopping the master clock until an external trigger ends the wait and the master clock resumes the hardware-triggered execution. The intended use in `labscript` is for example to guarantee a constant MOT filling by ending a wait during the MOT phase when a predefined fluorescence threshold is exceeded. During one experimental cycle, several waits can be used.

The wait-functionality is used to hand-over part of the hardware control to another device, namely the movable tweezer, for the period of atom rearrangement. The process is shown in Fig. 3.7 leaving aside the details of the sorting algorithm which will be described in section 5.2.3. After the camera is triggered to take a fluorescence image of the tweezer array, the tweezer controller is activated. When the camera has read out the acquired image and analyzed the trap occupation, this information is handed over to the waiting tweezer controller. The tweezer controller calculates the necessary moves to fill the target structure and performs those moves. After the tweezer controller has finished, it sends a trigger signal back to the master clock ending the wait and the rest of the experimental cycle continues hardware-triggered by the master-clock. Due to the use of waits, the rearrangement time is as short as possible. However, there is another limit currently restricting the functionality for experiments based on deterministic

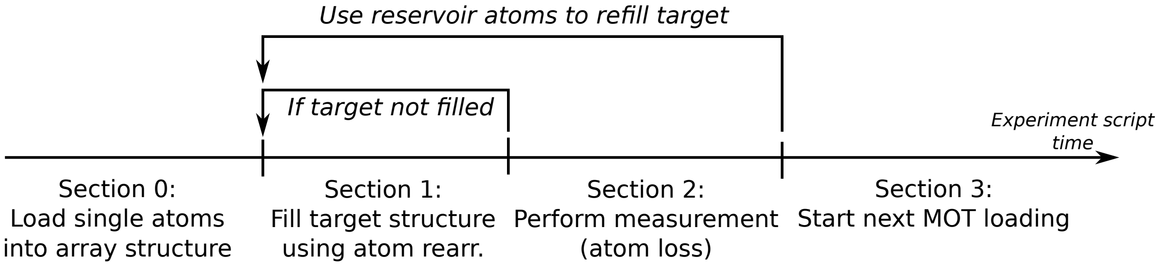

Fig. 3.8.: Timeline of the experiment script with two jump decisions. The aim is to rebuild a target structure as often as possible to perform an experiment on the defect-free target structure. The experimental sequence starts with initial single-atom loading (section 0). Then the target structure is filled by atom rearrangement until it is defect-free (section 1). At the end of each refill cycle (a single cycle is as described in Fig. 3.7), the jump condition is checked, repeating section 1 if the target structure is not defect-free. Otherwise the measurement (section 2) is performed. The measurement is assumed to use loss-based detection schemes such that a second experiment cycle without MOT loading can only be performed by refilling the target structure from reservoir atoms. After a fixed number of measurements or if not enough reservoir atoms are left, the experimental cycle is finished by starting a new MOT loading phase (section 3).

assembly of atoms: As atom assembly is not perfect, defects after one rearrangement cycle are inevitable. Therefore several rearrangement cycles as described above are performed. Due to atom loss it can not be guaranteed, that after the final pre-scheduled cycle the target structure is achieved. Therefore it would be advantageous to restart the rearrangement if losses occurred or to continue with the planned sequence if the target structure is defect-free. This demands for in-time conditional control over the experimental sequence.

3.2.3. Conditional control

The `labscript-suite` builds on shot-based experiments where all instructions for one experimental cycle are pre-loaded onto the hardware devices and stepped though based on a master clock. Therefore, the functionality of conditional control is not included. In general it would therefore be necessary to change the experimental control system to a field-programmable gate array (FPGA)-based system such as ARTIQ [124, 125]. ARTIQ offers first-in-first-out (FIFO) buffers whose execution is timed using a precise FPGA-based clock. As the buffers can be filled while the experiment is running, conditional control is possible. The downside of ARTIQ is that it requires a completely new hardware system as well as the portation of currently used experiment scripts into a completely new software environment. In the context of this thesis it was investigated whether conditional control can also be implemented within the `labscript-suite`. If the building blocks of the experiment are predetermined as it is the case for the atom rearrangement, the different blocks can in principle be pre-compiled and loaded in time onto the hardware. When implementing this, there are mainly two issues that have to be taken into account. On the one hand, the process of reloading new instructions onto the hardware has to be short enough to avoid loosing the trapped atoms during this time. On the other hand, during instruction reloading, no hardware-triggered timing is possible and all devices are in some steady state. It has to be ensured, that this steady state is compatible with the experiment timeline.

We developed the concept of splitting the experiment into several deterministic sections. Sections are separated by jump decision points and jump destination points. At a jump decision point it is decided, whether a jump to the corresponding jump destination point is performed or not. It is also possible to use several jump decision points and corresponding jump destination points. Using the atom rearrangement process as an example, the corresponding experiment timeline is shown in Fig. 3.8.

The functionality of splitting an experiment script into different sections and compiling them separately into hardware instructions is implemented into the `labscript`-module being responsible for compilation as described in section 3.2.1. Furthermore, some process needs to be responsible for deciding, whether a jump is performed or not. This is done by the jump controller which is implemented as `labscript-devices` plugin. The jump controller is in charge of the chronology of the sections. It sends all devices the instruction which section needs to be loaded next. Furthermore, it starts the hardware-triggered execution once all devices have loaded the new hardware instructions. At the end of a section, the jump controller evaluates if the jump condition is met and, depending on the result, sends the new load instruction to the devices. If the last section of the experiment script is finished, the jump controller hands over to the general labscript controller responsible for transitioning all devices to their manual states and loading the next experiment. Further details on the explicit software implementation can be found in [126].

Deciding, whether a jump condition is met or not and reprogramming the devices inevitably takes time. It is therefore important to evaluate how much additional time is added to the experimental sequence when using conditional jumps. For a typical experiment as performed in chapter 4 with a small scale tweezer array the average time between two sections is 90(10) ms. The time interval is composed of 40 ms for image readout and image transfer, 15 ms for image evaluation and up to 35 ms for reprogramming the devices. A reprogramming time of less than 100 ms is fast compared to the standard `labscript` reprogramming time between shots and allows a demonstration of the resorting concept as presented in section 4.2.3 after having introduced the experimental setup. However, it also shows the limitations of the process itself: Reprogramming of the devices can be reduced from 30 ms to almost 0 ms using another experimental control system, e.g. ARTIQ. However, it is even more important to acquire and analyze the image as fast as possible offering to save additional 30 ms to 40 ms.

3.3. Overview of laser systems

In this section, a general overview of the laser systems used in QUIPS-C, as shown in Fig. 3.9, is given. The laser systems which are necessary for dipole-trap based neutral-atom quantum platforms can be divided by their function into two main categories. On the one hand, laser systems for cold atom preparation and state manipulation are necessary. They are shown on the left hand side of Fig. 3.9 and their application is described in detail in section 3.4. On the other hand, the laser systems for the generation of dipole-trap structures are shown on the right hand side of Fig. 3.9 and their usage is described in detail in chapters 4 and 5. The laser systems based on external cavity diode laser (ECDL) and especially their laser stabilizations were set up and characterized in [127].

For dipole trapping, several laser systems have been used during this thesis. The reservoir trap used for the experiments described in chapter 4 is supplied by an ECDL used as seed laser for a tapered amplifier (TA). All ECDL lasers used in this thesis are based on an interference filter for wavelength selection in the external cavity as described in [129]. In combination with

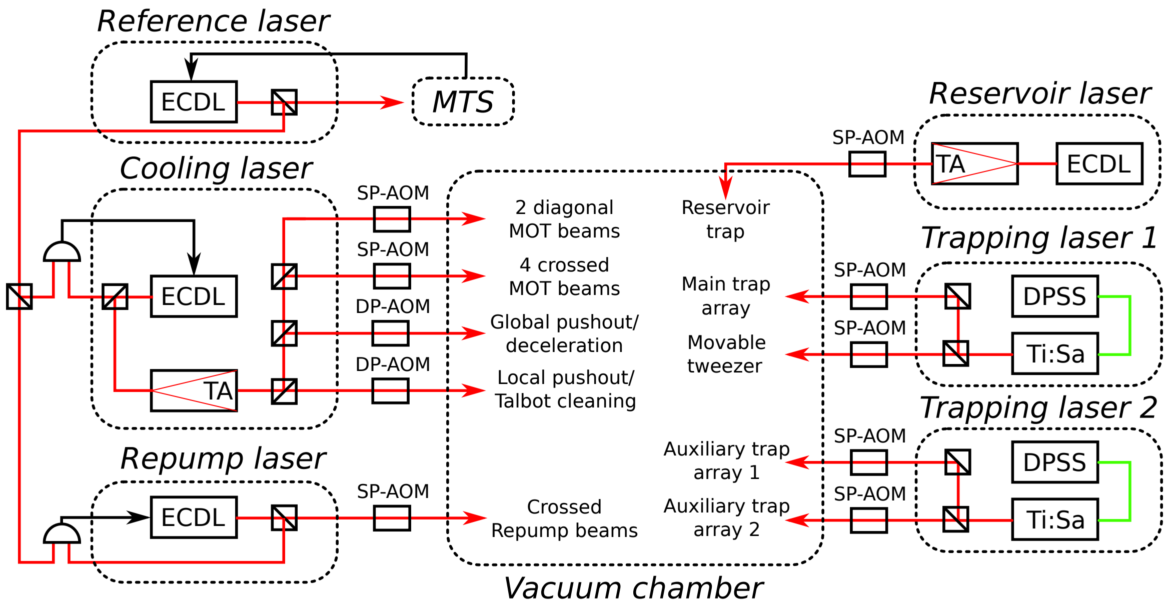

Fig. 3.9.: Schematic overview of all laser systems used. On the left side, the laser systems for preparation of cold atoms and fluorescence imaging are shown. The reference laser, an ECDL, is stabilized to a spectroscopic reference using modulation-transfer spectroscopy (MTS) [128]. All other lasers are offset-locked relative to it. On the right side all laser systems for dipole trapping are depicted. For the reservoir trap an ECDL-seeded tapered amplifier (TA) is used. As trapping laser 1 a Coherent 899-01 Titanium:Sapphire(Ti:Sa) ring laser pumped by a Verdi-V18 (Coherent) diode-pumped solid state (DPSS) laser is used for experiments described in chapter 4. For experiments described in chapter 5 two Matisse Ti:Sa (Sirah Lasertechnik) each pumped by a Millennia DPSS laser (Spectra Physics) were included as trapping laser systems. For fast switching single-pass (SP) acousto-optical modulators (AOMs) are used while for simultaneous frequency and amplitude switching AOMs in double-pass (DP) configuration are used.

a stable laser diode current driver and a temperature stabilization for the diode as well as for the housing this enables a long-term mode-hop-free operation. Using a 3 W TA chip (*DILAS TA-0795-3000*) more than 750 mW of laser power are available after a single-mode fiber. For all tweezer arrays as well as for the movable tweezer, titanium-sapphire (Ti:Sa) ring-laser systems pumped by diode-pumped solid state (DPSS) lasers are used. In chapter 4 this is a *Coherent Verdi V18* in combination with a *Coherent 889-01* providing up to 500 mW of laser power out of an optical fiber. The laser power hereby is limited due to stimulated Brillouin scattering in the fiber as the transport length is more than 20 m. At a later stage, new laser systems (*Spectra Physics Millennia 25* in combination with *Sirah Matisse C*) were available enabling us to use a total of more than 8 W after fiber coupling for up to four trapping beams creating large-scale dipole trap arrays as described in chapter 5.

The heart of the laser systems for cold-atom preparation and state manipulation is an ECDL, i.e. reference laser, stabilized onto a spectroscopic reference using modulation transfer spectroscopy [128]. It has a long-term linewidth of approximately 100 kHz over several weeks and a short-term linewidth of 52(1) kHz [130]. All other ECDLs are stabilized relative to the reference laser using offset-locking techniques with a linewidth of approximately 250 kHz and therefore well below the natural linewidth $\Gamma = 2\pi \cdot 6.066\,\text{MHz}$ of the $|5S_{1/2}\rangle \leftrightarrow |5P_{3/2}\rangle$-

transition [46]. The frequency offset of the cooling laser is determined by the required frequency offset for the MOT cooling beams as in their beam path only an acousto-optical modulator (AOM) in single-pass configuration is used for switching. The light for decelerating the atoms and cleaning unused Talbot planes as described in the following sections is switched and shifted using an AOM in double-pass configuration to allow for frequency changes of approximately $\pm 30\,\mathrm{MHz}$. Using matching AOM-frequencies this enables us to use a single ECDL amplified by a TA as light source for eight different beam paths entering the vacuum chamber. For the repumping laser a separate ECDL is used to achieve the necessary frequency offset of approximately 3035 MHz, the hyperfine splitting of the $|5^2S_{1/2}\rangle$ ground state. For offset locking of our ECDL lasers as well as for intensity stabilization of all lasers we use servo electronics based on the STEMlab platform which is described in detail in [130].

3.4. Preparation of individual atoms from a cold atom cloud

In order to be able to prepare clouds of cold ^{85}Rb atoms and load them into arrays of optical dipole traps, the components of the setup introduced in the previous sections need to be combined. In this section, the general experimental procedure for these two steps is described, being the basis for the experiments presented in chapter 4 and 5. The corresponding theoretical concepts have been outlined in section 2.1. For an efficient transfer of atoms into dipole-trap arrays, the atoms evaporated from heated dispensers have to be cooled and the size of the atom cloud has to match the size of the target structure that is to be filled. To achieve this, the cold atom cloud is prepared in MOT and molasses stages and the atoms are then transferred into the dipole-trap structures. The timeline for the different experimental components involved is shown in Fig. 3.10.

3.4.1. Preparation of a cold atom cloud

Cooling of the atoms starts with a deceleration beam that enters the vacuum chamber through a CF40 viewport on the side of the titanium sublimation pump (see Fig. 3.1). It is counter-propagating the atoms released from a rubidium dispenser heated by a current of 3.0 A to 3.5 A. To efficiently slow down the atoms, the deceleration beam uses an intensity of $6.7(6)I_{\mathrm{sat}}$ and a detuning of -3.5Γ relative to the $|5S_{1/2}, F=3\rangle \leftrightarrow |5P_{3/2}, F=4\rangle$-transition[4]. During the final stage of deceleration, the atoms are cooled and trapped in the center of the vacuum chamber using a magnetic field gradient along the z-axis of 17.8(2) G/cm and six MOT beams. The four crossed beams have an intensity of $22(2)I_{\mathrm{sat}}$ per beam while the two diagonal beams have an intensity of $30(3)I_{\mathrm{sat}}$. All MOT beams usually have a detuning of -2Γ relative to the $|5S_{1/2}, F=3\rangle \leftrightarrow |5P_{3/2}, F=4\rangle$-transition. For some measurements in chapter 5, a slight increase in the atom number has been observed when reducing the detuning to -1.7Γ.

Although the hyperfine splitting between the $|5P_{3/2}, F=3\rangle$ state and $|5P_{3/2}, F=4\rangle$ state is $2\pi \cdot 120.6\,\mathrm{MHz}$, there is a finite possibility for atoms to be exited into the $|5P_{3/2}, F=3\rangle$ state due to the off-resonance excitation probability of the Lorentz profile. From here spontaneous emission into the $|5S_{1/2}, F=2\rangle$ ground state is possible. Therefore a repumping laser is necessary to bring the atoms back into the cooling cycle. The repump laser is detuned by -0.2Γ from the $|5S_{1/2}, F=2\rangle \leftrightarrow |5P_{3/2}, F=3\rangle$-transition and the light is coupled through the same

---

[4] For the cooling transition of ^{85}Rb ($|5S_{1/2}, F=3, m_{\mathrm{F}}=3\rangle \leftrightarrow |5P_{3/2}, F=4, m_{\mathrm{F}}=4\rangle$) with σ^+-polarized light, $I_{\mathrm{sat}} = 1.67\,\mathrm{mW/cm^2}$ [46].

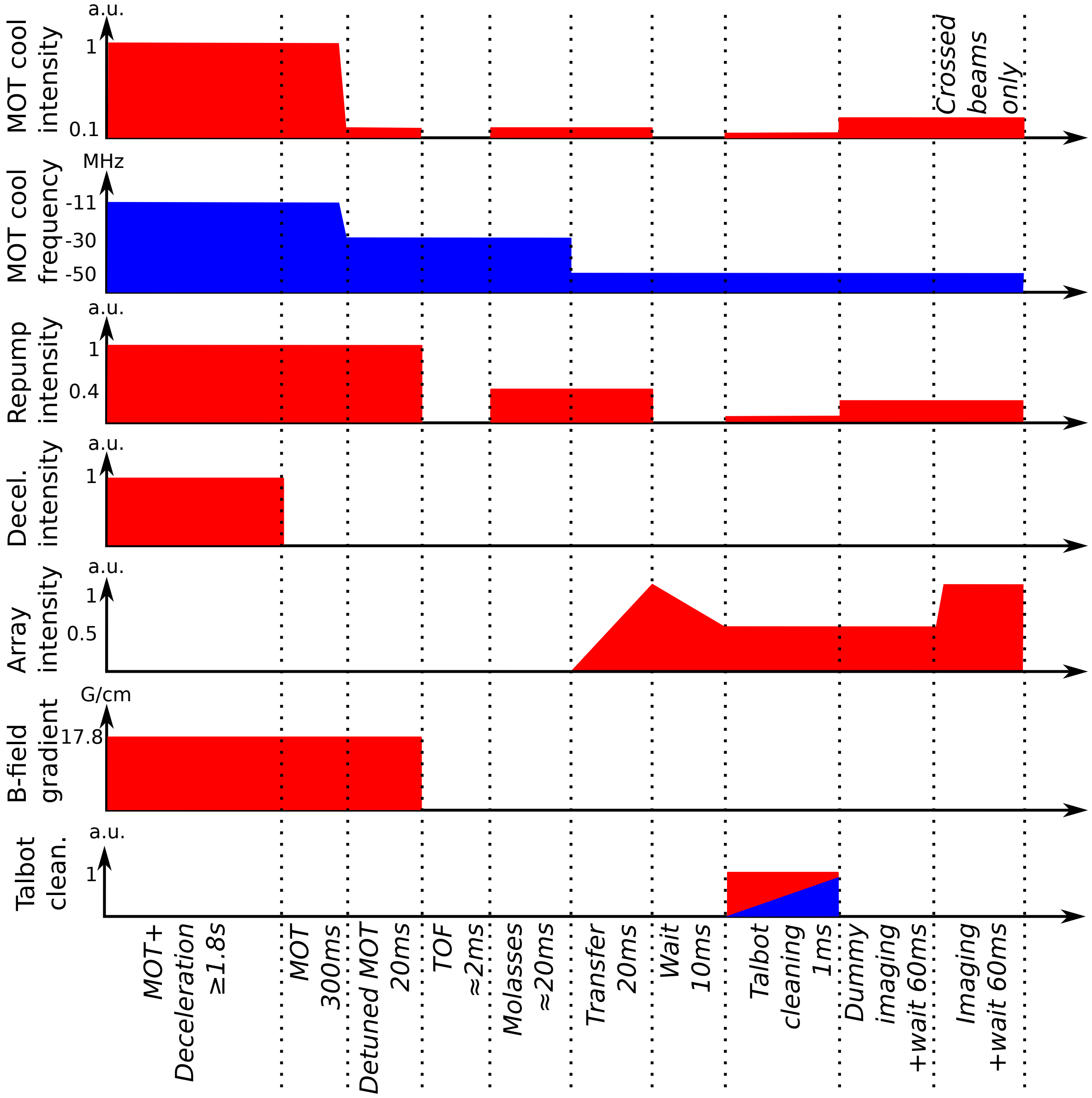

Fig. 3.10.: Timeline of the different parameters (intensities in red; detunings in blue) used for single atom preparation. MOT cool int.: Intensity of the crossed and diagonal MOT light; MOT cool freq.: Frequency of the cooling laser light relative to the cooling transition. Repump int.: Relative repump intensity; Repumping light is only used via the crossed MOT beams and the detuning is fixed at -0.2Γ relative to the repump transition (not depicted). Decel. int.: Relative intensity of the deceleration beam counterpropagating the atoms evaporated from the dispensers. Array int.: Intensity of the main array as used in chapter 5. B-field gradient: Magnetic field gradient from the MOT coils along the z-axis. Talbot clean.: Intensity (constant) and detuning (linearly ramped) of the laser beam used to clean the unused Talbot planes. a.u.: arbitrary units.

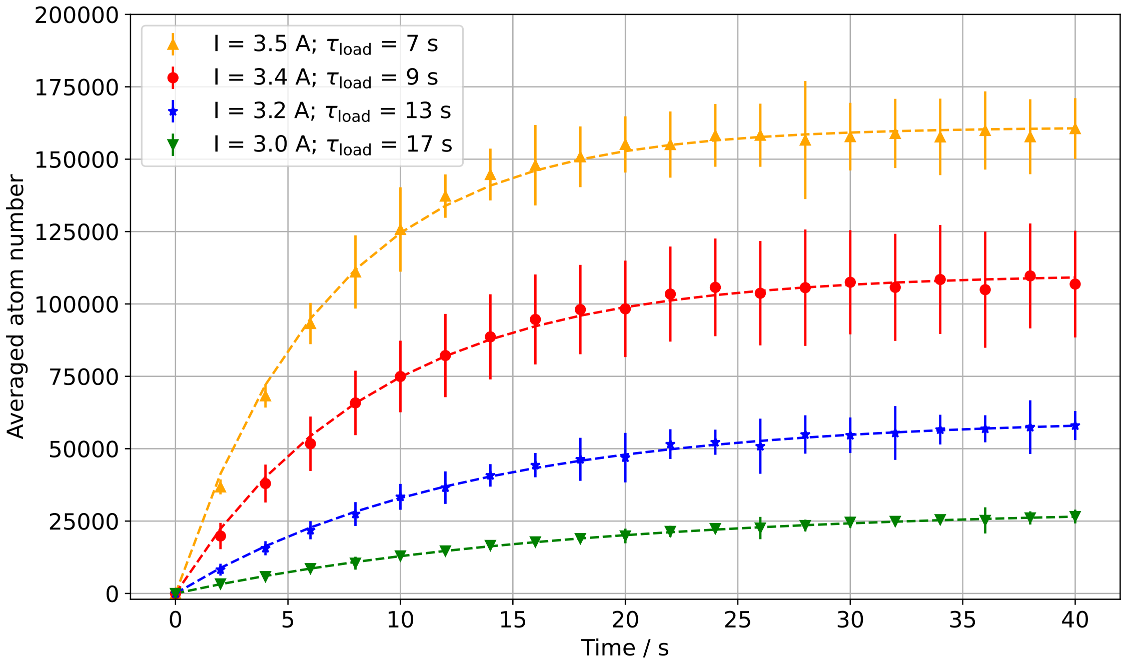

Fig. 3.11.: MOT loading curves for different dispenser currents I in a range as used during experiments presented in this thesis. τ_{load} is the 1/e loading time.

fiber as the crossed MOT beams. During the MOT phase, the repumping light, circularly polarized the same way as the corresponding cooling beams, is incident on the atoms with a peak intensity of $1.5(1)I_{\text{sat}}$ per beam. At the end of this phase, taking usually 1.8 s to 5 s, the deceleration beam is turned off as its radiation pressure shifts the atom cloud off-center. The 1/e loading time of the MOT as well as the number of atoms in the MOT depend on the dispenser current as shown in Fig. 3.11. A higher dispenser current decreases the 1/e loading time while simultaneously increasing the available number of atoms. The atom density is roughly 1×10^8 atoms/cm^3 such that the MOT is not density-limited due to rescattering of the trapping light [131].

During the following MOT phase of 300 ms without deceleration beam, the MOT settles in its new equilibrium position. At this stage, the MOT has a typical diameter of 100 µm to 150 µm and a temperature of 450(50) µK. This results from high laser intensities and small detuning.

In order to measure the temperature of the atom cloud images of the atom cloud are taken after different time-of-flight (TOF) intervals. Due to the thermal velocity distribution of the atoms, the cloud expands as long as no cooling force is acting on it. From the expansion, the average temperature T of the atoms with mass m can be calculated using [132]:

$$\sigma_{\mathrm{i}}^2(t) = \sigma_{\mathrm{i}}^2(t=0) + \frac{k_{\mathrm{B}}T}{m}t^2. \tag{3.4}$$

$\sigma_{\mathrm{i}}(t)$ and $\sigma_{\mathrm{i}}(t=0)$ are the final and initial width of the atom distribution along axis i.

After the MOT phase without deceleration beam, a phase of detuned MOT with 20 ms duration leads over to the molasses phase lasting 10 ms to 20 ms cooling the atom cloud to a temperature of 15(5) µK. During the detuned-MOT phase, the cooling laser intensity is reduced to 1/10 of the MOT intensity and the detuning is increased to -5Γ. For the molasses phase the magnetic field is turned off while keeping the laser parameters as in the detuned-MOT phase. In between the detuned-MOT phase and the molasses phase there is a TOF period with all lasers turned off lasting up to 2 ms to match the size of the atom cloud to the size of the target array. This enables optimizing the loading efficiency. It has been empirically determined that with this detuned-MOT phase, although the magnetic field is still turned on, a temperature decrease down to 30 µK to 40 µK is possible. Due to the lower atom temperature, the size of the atom distribution is less sensitive to the length of the TOF-phase enabling a better matching of the size of the atom cloud to the target array size.

Testing a chirped beam for deceleration

The deceleration beam currently used to slow down the atoms emitted from the dispensers uses a constant detuning of -3.5Γ as described above. It has also been tested, if chirping the deceleration beam can be used in the current setup to increase the atom number. When using a chirped laser beam, the detuning of the laser frequency is swept to keep the laser frequency resonant to the atomic transition during the process of deceleration. This is necessary as due to deceleration of the atoms, the Doppler shift $\delta(t) = -\mathbf{k} \cdot \mathbf{v}(t)$ changes with decreasing velocity $\mathbf{v}$ of the atoms. The transition frequency in the inertial frame of the lab is therefore given as $\omega_{0,\text{lab}} = \omega_0 - \mathbf{k} \cdot \mathbf{v}(t)$. The technique was demonstrated in [133] and is used in our group to slow down an atomic beam created in a Rb-oven used for a BEC-experiment [134].

For the laser cooling process described above, it was investigated if a chirped laser beam is more efficient than a static frequency detuning to slow down the atoms. It was found that the highest loading efficiency is achieved with a frequency sweep from -12Γ to $-\Gamma$ at a rate of 1050 kHz with the same laser intensity as for the static case. The atom number is then not significantly higher than in the static case resulting in 5(5) % more atoms on average. As the frequency of the laser is detuned using a double-pass (DP)-AOM (see Fig. 3.9), the maximum frequency detuning is limited to -12Γ. Furthermore, the laser beam illuminates all atoms coming from the rubidium dispensers, especially those already trapped inside the MOT. It is assumed, that this is the main reason why chirping does not improve the atom number as the MOT is continuously influence by the chirped laser. In the BEC experiment, for example, the chirp beam is used slightly above the MOT such that slowed atoms fall into the MOT region due to gravitation but the chirping does not influence the already trapped atoms.

3.4.2. Single-atom detection using fluorescence imaging

The cold atom cloud is the starting point for further experiments in optical dipole traps. To efficiently load the atoms into the dipole traps, the atom cloud is superposed with a single dipole trap or a trap array, then the trap intensity is ramped up from 0 to its final transfer intensity over a period of 20 ms. The exact final transfer intensity is different for the experiments described in chapters 4 and 5 but corresponds to the maximum trap depth given therein. During this transfer phase, the frequency of the cooling lasers is set to -8.2Γ and its intensity to $1.7(1)I_{\text{sat}}$ for the crossed MOT beams and $2.2(1)I_{\text{sat}}$ for the diagonal MOT beams. For small trapping volumes light-assisted collisions due to the red-detuned cooling light, as described in section 2.1.2, are used to prepare individual atoms in the dipole traps. As shown in Fig. 3.10, between the transfer of the atoms followed by a short waiting time and the imaging, two other stages are performed. Their use becomes apparent after having introduced the fluorescence imaging which is described next.

As the loading probability is only between 50 % and 60 %, it is necessary to be able to detect if a specific trap is occupied or not. For this purpose the fluorescence signal of the atom is acquired by irradiating the atoms for typically 50 ms with the four crossed MOT beams. During this phase cooling light with $4.4(1)I_{\mathrm{sat}}$ for the crossed MOT beams and a detuning of -8.2Γ relative to the cooling transition as well as repumping light with an intensity of $0.75(5)I_{\mathrm{sat}}$ per beam and a detuning of -0.2Γ is used. Experiments with down to 30 ms imaging time have shown only a small reduction in single-atom detection fidelity. The diagonal MOT beams are not used during imaging as light reflected from the vacuum viewports through the microscope objective onto the EMCCD camera causes a strong background signal. Improvements are already planned in order to implement continuous cooling in all three dimensions during imaging. For this purpose light at 795 nm close to the D1-line of rubidium could be used.

As the large CF100 viewports are the main optical access to the vacuum chamber, they allow not only for the creation of large-scale arrays of optical tweezers with micrometer-size waists but also enable to collect as much fluorescence light from the atoms as possible to facilitate high-quality fluorescence imaging. For this purpose high-NA microscope objectives are used. As those microscope objectives differ for the measurements described in chapter 4 and chapter 5 and are therefore described in the corresponding section. The limited high-NA optical access demands first and foremost for splitting the fluorescence light from other laser beams used for trap creation or single-site addressability. In this section, the general setup for fluorescence imaging as well as the image processing to detect single atoms will be described.

Imaging beam path and dichroic mirror

For splitting the fluorescence light of the atoms from the trapping light beam path, a dichroic mirror at an angle of 22.5° is used. The mirror is coated to reflect 95 % of the fluorescence light at 780 nm and to transmit 95 % of light at 795 nm. Furthermore, high transmission is given for Rydberg wavelengths around 420 nm, 480 nm, 1005 nm, and 1013 nm. Transmission and reflection are intended to be close to 95 %, not 100 %, to allow the coupling of laser light for low-power applications via a second beam path. In order to achieve similar transmission values at both s- and p-polarization it is not possible to use a 45° angle of reflection which is why the dichroic mirror is designed for use at an angle of incidence of 22.5°. Further explanations are found together with the coating curves of the dichroic mirror as well as measurements testing its performance in appendix C.2.

The schematic setup for fluorescence imaging is shown in Fig. 3.12. After separating the fluorescence light via the dichroic mirror, a high-reflectivity mirror is used to propagate the fluorescence light into the imaging beam path where it is imaged onto an EMCCD camera via an achromatic lens. In order to minimize stray light, the beam path is encapsulated in black cardboard after the achromatic lens and two laser line filters transmitting only light at 780 nm (Semrock SEM-LL01-780-25) are mounted onto the camera. For the experiments presented in this thesis, two different EMCCD camera models were used as described together with the other hardware components in section 3.2.2.

Fluorescence-image processing for single-atom detection

For distinguishing an occupied from an unoccupied trap, the fluorescence signal captured be the camera has to be analyzed. The general idea is to compare the fluorescence signal captured from a single trap with a predetermined threshold value. If the fluorescence signal is above the threshold value one atom is assumed to be inside the trap, while for a fluorescence

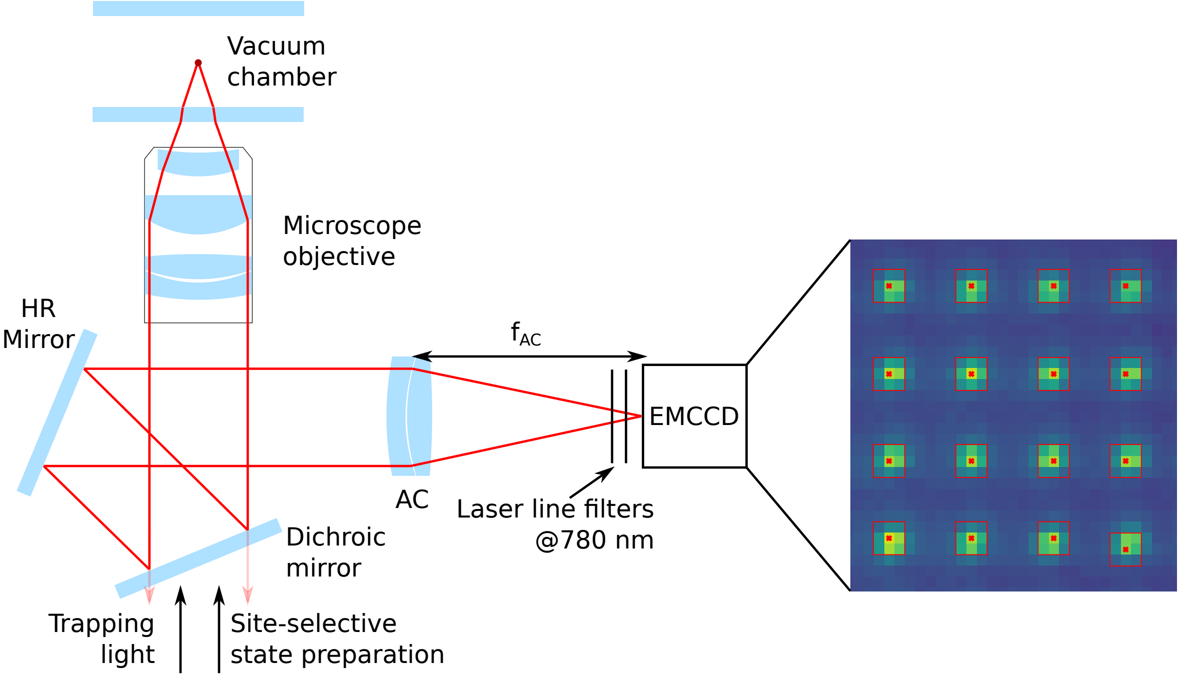

Fig. 3.12.: Fluorescence light from ^{85}Rb atoms in the MOT or in dipole traps is captured by the microscope objective. In order to separate the fluorescence light from the trapping light beam path, the dichroic mirror reflects 95 % at 780 nm and transmits trapping light as well as light for state preparation between 420 nm and 480 nm as well as above 795 nm. The fluorescence light is imaged with an achromatic lens onto an EMCCD camera (shown on the right with analysis mask as used in chapter 5). HR: high-reflectivity.

signal below the threshold value the trap is assumed to be empty. To be able to evaluate a fluorescence image, it is therefore necessary to know which camera pixels correspond to which trap and to determine an optimal threshold value for each trap such that false determinations of trap occupations are minimized. Based on several hundred repetitions of an atom-trapping experiment, an averaged fluorescence image as shown on the right side in Fig. 3.12 is calculated. From this averaged image a mask is determined, assigning the camera pixels to the different traps. For evaluations used in chapter 4, the mask for each individual trap was determined from a two-dimensional Gaussian approximation to the fluorescence signal. An approximation to each individual trap is time-consuming and therefore in chapter 5, the mask determination was simplified. By analyzing the single-atom detection fidelity as described below for different mask sizes the best mask size was found to be a 3×3 pixel mask for the fluorescence imaging setup in chapter 5. From the averaged fluorescence image the highest intensity pixel (red cross in Fig. 3.12) and around this pixel a mask (red square in Fig. 3.12) for each trap is determined and the 3×3-pixel mask around it is assigned to the corresponding trap.

Based on these masks, the mean fluorescence signal for each trap in each individual image is determined. These fluorescence signal values for each trap are plotted into a histogram as shown for a section of traps in Fig. 3.13. It can be clearly seen that each histogram shows two distinct peaks corresponding to zero atoms or one atom inside the trap. The histogram is approximated using the sum of two Gaussian distributions. The normalized area under each Gaussian distribution corresponds to the relative number of zero-atom and one-atom events, respectively, and their ratio determines the loading efficiency of each individual trap. The

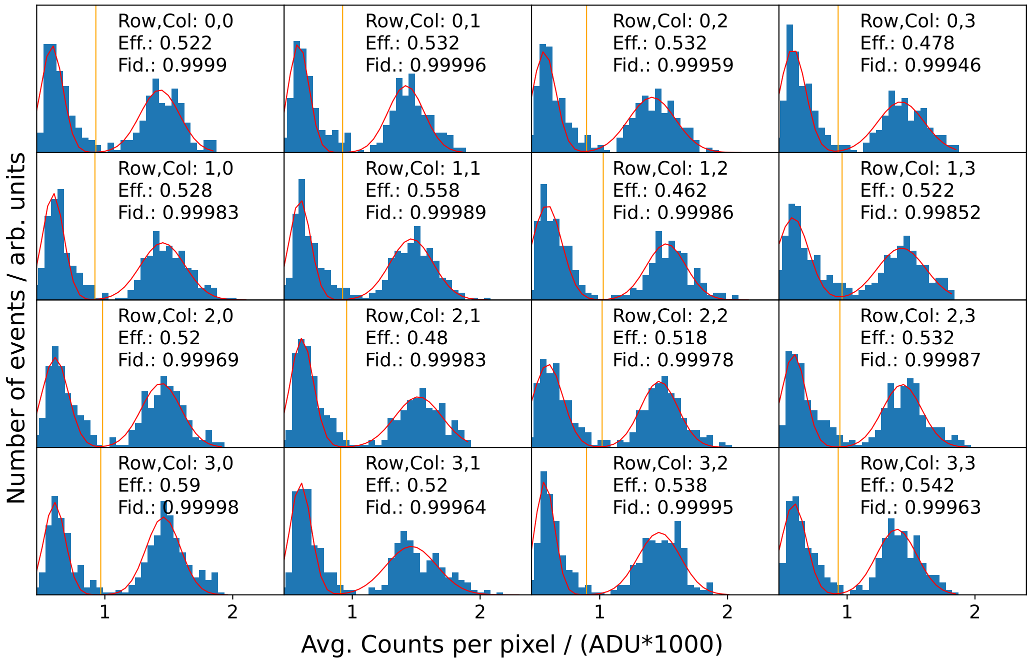

Fig. 3.13.: Histogram for 16 traps in the center of the array showing the number of occurrences of a certain mean fluorescence signal (in Analogue to Digital Units (ADU) of the camera) detected by the 3×3 pixels of the respective trap. The two peaks correspond to the zero-atom events (lower signal) and one-atom events (higher signal). The dark count level of the camera (camera shutter closed) is at 490(19) ADU. The optimal threshold (orange line) to distinguish between zero-atom and one-atom events is found using the approximation of the distribution by Gaussian functions (red) as described in the text.

optimal threshold is found by maximizing the fidelity $\mathcal{F}$ given by

$$\mathcal{F} = 1 - \frac{1}{2}(\epsilon_0 + \epsilon_1) \tag{3.5}$$

where ϵ_0 (ϵ_1) is the probability to falsely assigning a zero-atom (one-atom) event to be a one-atom (zero-atom) event [47]. It has to be noted, that the histogram shown in Fig. 3.13 is from the inner traps taken during a measurement as described in chapter 5. It can be seen that, for example for trap (1,3), the zero-atom peak is distorted and non-Gaussian which results from atoms in other structures that could not be removed with the procedure described next. As events of this type lying above the determined threshold value are rare, the introduced error estimated to be below 1 percent.

The mask as well as the corresponding threshold values are saved for each trap and are used for further post-processing of atom occupations. Furthermore, these results are handed over to the camera program to be able to perform an in-situ analyses of the acquired images. The camera program determines a boolean array of the trap occupation directly after receiving the image from the camera and provides this array to other programs as described in section 3.2.2.

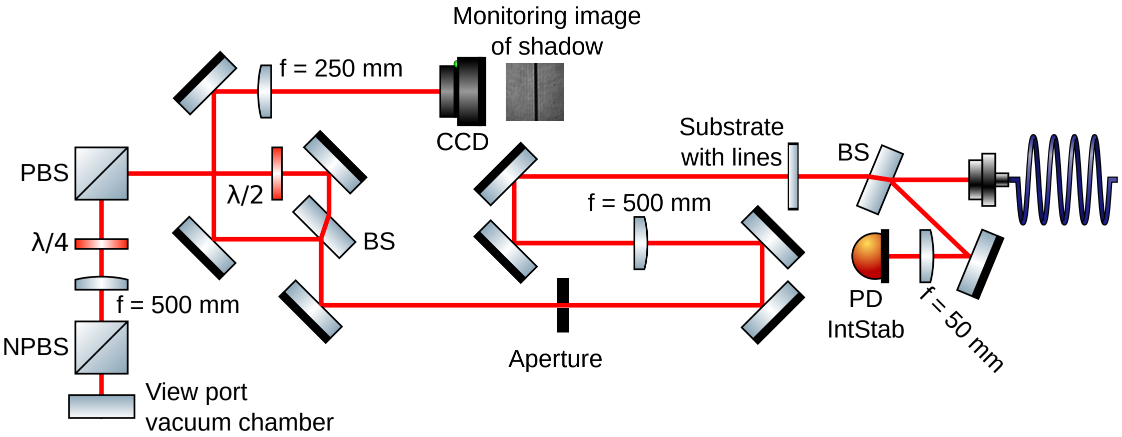

Fig. 3.14.: Optical setup (not drawn to scale) used to clean unused Talbot planes. A substrate with lines (30 µm, 40 µm, 60 µm, 80 µm, 100 µm, 150 µm, and 200 µm) is imaged into the vacuum chamber using a 4f imaging system with two 500 mm lenses. Beam samplers (BS) are used for intensity stabilization (IntStab) via a photodiode (PD) as well as for shadow monitoring. Schematic created using [135].

3.4.3. Single-atom preparation in a microlens-based setup

When loading the atoms into a microlens-generated dipole-trap array, all Talbot planes overlapping with the volume of the atom cloud during the molasses are loaded with atoms. However, using fluorescence imaging, only those atoms in the focal plane of the microscope objective are focused onto the camera. All other atoms cause a background signal reducing the discriminability between zero- and one-atom events. Atoms in the currently unused Talbot planes as well as atoms weakly trapped in intermediate structures therefore have to be removed.

Talbot cleaning

Cleaning the Talbot planes is achieved by heating the corresponding atoms out of their traps. This is done by illuminating the atoms along the direction parallel to the array plane (x-y-plane) with a laser beam larger in diameter than the atom cloud, right-handed circularly polarized, and near-resonant to the $|5S_{1/2}, F = 3\rangle \leftrightarrow |5P_{3/2}, F = 4\rangle$ cooling-transition. As this would heat all atoms out of their traps, a shadow is imprinted onto the laser beam protecting the atoms in the array plane. This is done by using a 4f imaging system to image a thin line with a width of 60 µm printed on a substrate into the vacuum chamber as shown in Fig. 3.14. The substrate has several lines with thickness 30 µm, 40 µm, 60 µm, 80 µm, 100 µm, 150 µm, and 200 µm, respectively, imprinted onto it. To allow for the use of different lines if the Talbot distance of the trapping planes change, the substrate is mounted onto a translation stage. Furthermore, a non-polarizing beam splitter cube (NPBS) is placed in front of the vacuum chamber to provide optical access for additional laser beams entering the vacuum chamber along this beam path. It can be used as a second monitoring path as well. For efficient heating, the laser is activated with a peak intensity of $0.35\ I_{\text{sat}}$ for 1 ms during which its frequency is linearly swept from 1.65Γ to 0Γ blue-detuned relative to the cooling transition. Atoms in the lower hyperfine ground state are pumped back as during the MOT phase using the repump laser with an intensity of $0.50(5)I_{\text{sat}}$ per beam and a detuning of -0.2Γ as during the MOT phase.

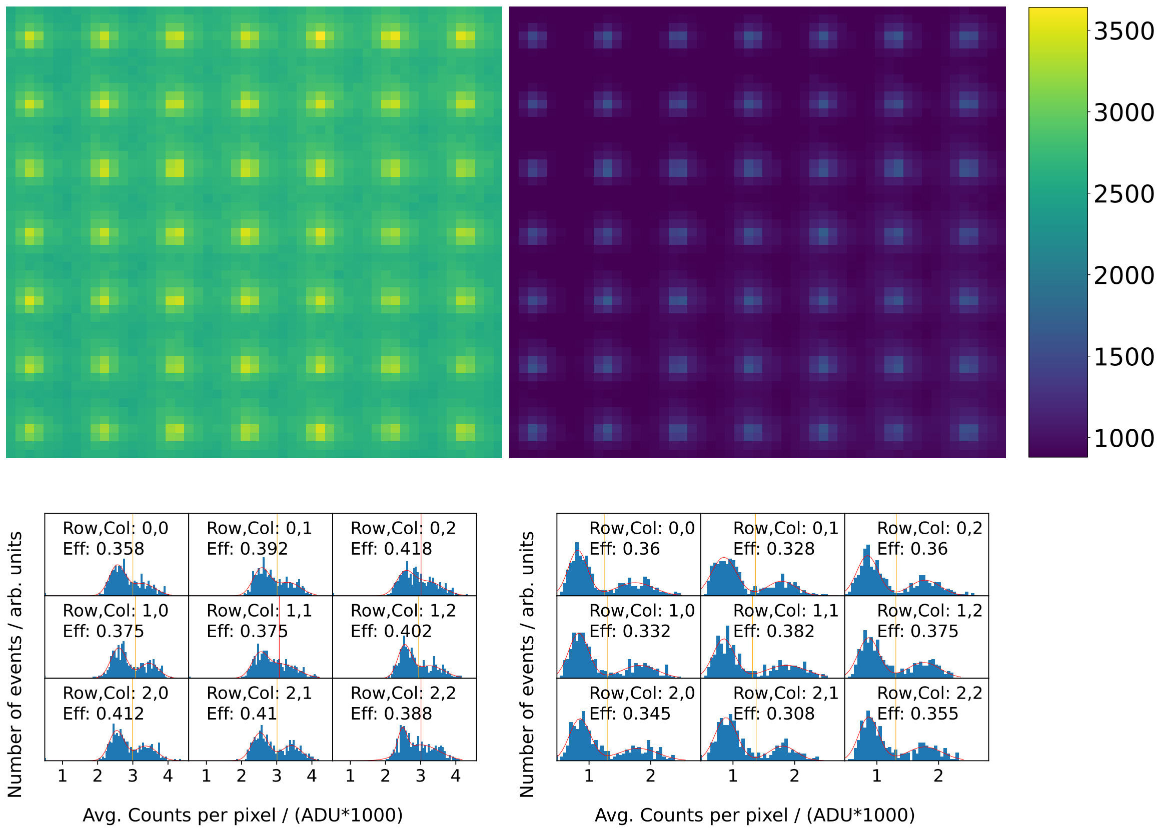

Fig. 3.15.: **Top:** Averaged fluorescence image of 400 realizations of atoms loaded into one trap array as described in chapter 5 (only a section of 7×7 traps is shown). The left image shows a measurement without Talbot cleaning resulting in an extremely high background signal. In the measurement shown in the right image, Talbot cleaning was used to significantly reduce the background signal. The same colorbar scaling is used for both images. **Bottom:** The corresponding histograms for the inner 3×3 array is depicted visualizing the reduction in background signal as well as the better separation of both peaks.

Figure 3.15, showing an averaged fluorescence image of 400 experimental realizations (top), illustrates the effect of cleaning the Talbot planes. Defining a contrast

$$\mathcal{K} = \frac{I_{\text{max}} - I_{\text{min}}}{I_{\text{mean}}} \tag{3.6}$$

quantifies a contrast increase from $\mathcal{K} = 0.5$ without Talbot cleaning to $\mathcal{K} = 2.0$ with Talbot cleaning. I_{max} (I_{min}) is the highest (lowest) pixel value in the averaged image and I_{mean} the average pixel value of the whole image. Without cleaning, the background signal from atoms trapped in other Talbot planes increases the overall level of detected photons making the single-atom detection more ambiguous. This effect is also clearly visible in the histograms shown in Fig. 3.15 (bottom) where the lower boundary of the signal is strongly reduced by the Talbot cleaning resulting in an improved discrimination of zero- and one-atom signals. Further optimizing the parameters for preparation and imaging leads to histograms as shown in Fig. 3.13.

To further improve the discrimination between zero- and one-atom events, a 50 ms phase with a cooling light intensity of $4.4(1)I_{\text{sat}}$ for the crossed MOT beams, $6.0(1)I_{\text{sat}}$ for the diagonal MOT beams, and $0.75(5)I_{\text{sat}}$ for the repumping light is used. This process is comparable to the following imaging phase and therefore called *dummy imaging*. Due to the atom-light interaction, weakly trapped atoms, which would be lost during the following imaging process, are removed, thus improving the single-atom detection.

3.5. Conclusion

In this chapter, the new vacuum chamber design was introduced and discussed. Based on the demands formulated at the beginning of this chapter, new ideas have been implemented to create a versatile experimental platform for future experiments. The design considerations have been explained and the properties of the vacuum chamber and its corresponding parts have been introduced. Furthermore, the experimental control system as well as its prospects for conditional control have been outlined. In combination with the laser system, these components are the foundation for further experiments. In the final section, the utilization of all parts to prepare and detect single atoms from a cold atom cloud has been explained. This will be the basis for the experiments presented in the following two chapters.

4. Reservoir-based deterministic supply of single atoms

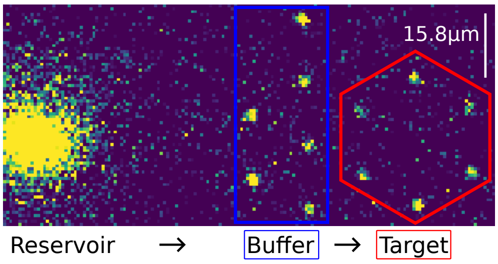

Fig. 4.1.: Single-shot fluorescence image of an atom ensemble in the reservoir dipole-trap (left) and individual atoms in the hexagonal tweezer array (right). Within the hexagonal tweezer array, the blue frame defines the buffer-trap section and the red frame defines the target structure, respectively. Reservoir, buffer, and target traps are interconnected by a movable tweezer (not visible as turned off during imaging) which is capable of rearranging atoms between all three units. The image is taken after four rearrangement sequences as described in detail in section 4.2 and shows a fully filled target structure.

The experimental setup described in the previous sections lays the foundation for a quantum processing platform with extended capabilities. Loading the dipole-trap structure from an optical molasses is a perfect way to load large arrays with filling fractions of roughly 50 % to 60 % based on collisional blockade as described in section 2.1.2. This is the easiest and most prevalent technique for dipole-trap loading. However, a filling fraction of up to 60 % still requires subsequent rearrangements to achieve defect-free filling. Furthermore it limits the total number of available atoms per experimental cycle to approximately half of the total number of available traps. Utilizing the principle of gray molasses even higher loading rates of more than 80 % in a 100-site register have been demonstrated for alkali metals and more than 90 % for alkali earth metals [27, 136, 137], thus increasing the number of available atoms and making successful defect-free assembly more probable.

However, the number of initially loaded atoms is still finite such that atom loss due to imperfections in the rearrangement process or due to loss-induced detection schemes utilized for qubit readout make renewed atom loading necessary after each experimental cycle. For a quantum processing platform this alternation between dipole loading and computational sequences intrinsically limits the achievable data rate. Therefore, a novel technique is presented in this chapter to decouple the preparation of individual atoms in optical tweezers from the supply of laser-cooled atoms: Deterministic loading of a target dipole-trap structure with single atoms from a spatially separated, large dipole-trap reservoir is demonstrated by utilizing intermediate buffer traps as shown in Fig. 4.1. Combining this technique with the molasses-based loading of trap arrays in the prove-of-principle experiments of this thesis, furthermore allows to increase the number of available atoms and thereby improving the probability for achieving defect-free filling. In a future perspective, this paves the way to continuous supply of qubits for quantum processors compensating losses during computational sequences.

In this chapter, the setup providing a single, large reservoir trap as well as a small-scale tweezer array will be explained. Subsequently, the deterministic preparation of target structures from an atom reservoir, including experiments utilizing conditional control, is demonstrated.

4.1. Dipole-trap setup

In order to demonstrate deterministic supply of individual atoms from a cold-atom reservoir into arrays of dipole traps, a small scale tweezer array in combination with a movable tweezer and a large reservoir dipole-trap are utilized. The movable tweezer interconnects the reservoir with the trap array as well as the different trapping sites within the array. For this purpose, a setup based on an MLA (MLA1 as described in section 2.2.5) complemented by a single movable tweezer for atom transport as shown in Fig. 4.2 (top) is combined with an additional setup for a single, large dipole trap (Fig. 4.2 (bottom)).

To allow for a dynamic manipulation of the light field illuminating each single lenslet of the array, a DMD (DLP LightCrafter from Texas Instruments) is used. The micromirror array incorporates 608 × 684 quadratic mirrors with a pitch of 7.64 µm along the mirror edges on a total area of 6.57 mm × 3.70 mm. The tilt angle of each mirror can be individually set to one of two distinct orientations having an angle of ±12° relative to the DMD surface. The DMD is illuminated with a Gaussian laser beam having a $1/e^2$-radius of $1.2(1)$ mm at an angle of incidence of $\alpha \approx 26°$ and a wavelength of $\lambda = 796.51(1)$ nm. This ensures the highest diffraction efficiency as the diffraction pattern of the DMD (blazed grating) best overlaps with the maximum of the single slit envelope of the tilted mirrors at an angle of $\alpha \approx 24°$. The DMD is reimaged onto the microlens array using a telescope consisting of two achromatic doublets with focal lengths of 50 mm and 30 mm which results in roughly 875 mirrors illuminating one lenslet. An achromatic lens with focal length of 750 mm and a microscope objective with a focal length of 37.5(10) mm are used to reimage the focal plane of the MLA into the vacuum chamber as described in section 2.2.5.

Using a movable optical tweezer, atoms can be rearranged within the array structure and transferred between the reservoir and the trap array. The movable tweezer is based on a collimated beam with $1/e^2$-radius of $1.5(1)$ mm propagating through an AOD (AA DTSXY-400-800 from AA Opto Electronic) that deflects the beam in two axes and has a scanning angle of $(44\,\mathrm{mrad})^2$. An achromatic doublet with a focal length of 60 mm focuses the beam to translate the deflection angle into a x-y-translation. The focal plane is reimaged into the vacuum chamber using an achromatic doublet with a focal length of 400 mm and the microscope objective. The movable tweezer beam and the trap-array beam are overlapped before propagating though the microscope objective. The spot size of the movable tweezer inside the vacuum chamber is 2.2(1) µm ($1/e^2$-radius) and the scanning range is roughly 250 µm in each dimension. Both, the laser beam for the array as well as for the movable tweezer have a wavelength of 796.5 nm as they are sourced from the same laser (see section 3.3).

The resulting light field of the trap structure is shown in Fig. 4.3 (left). The image is taken by reimaging the light field inside the vacuum chamber onto a CCD camera outside the vacuum chamber as shown in Fig. 4.2 (lower part). For this purpose, a second microscope objective with the same properties as the one used for the array traps as well as an achromatic lens with a focal length of 400 mm are used behind the vacuum chamber. Based on this image, the measured spot size of the array traps has an average waist of 1.97(12) µm and a pitch of 7.9(1) µm inside the vacuum chamber. The spot size is significantly larger than values measured in offline setups [138]. The main reason is a suspected non-perfect alignment of the beam path into the vacuum chamber. As the matching of DMD, MLA and microscope objective is extremely sensitive, in situ optimization was only successful to a limited extent. Furthermore, the reimaging with an objective of the same kind can increase the determined spot size due to aberrations resulting from misalignment of both objectives relative to each other.

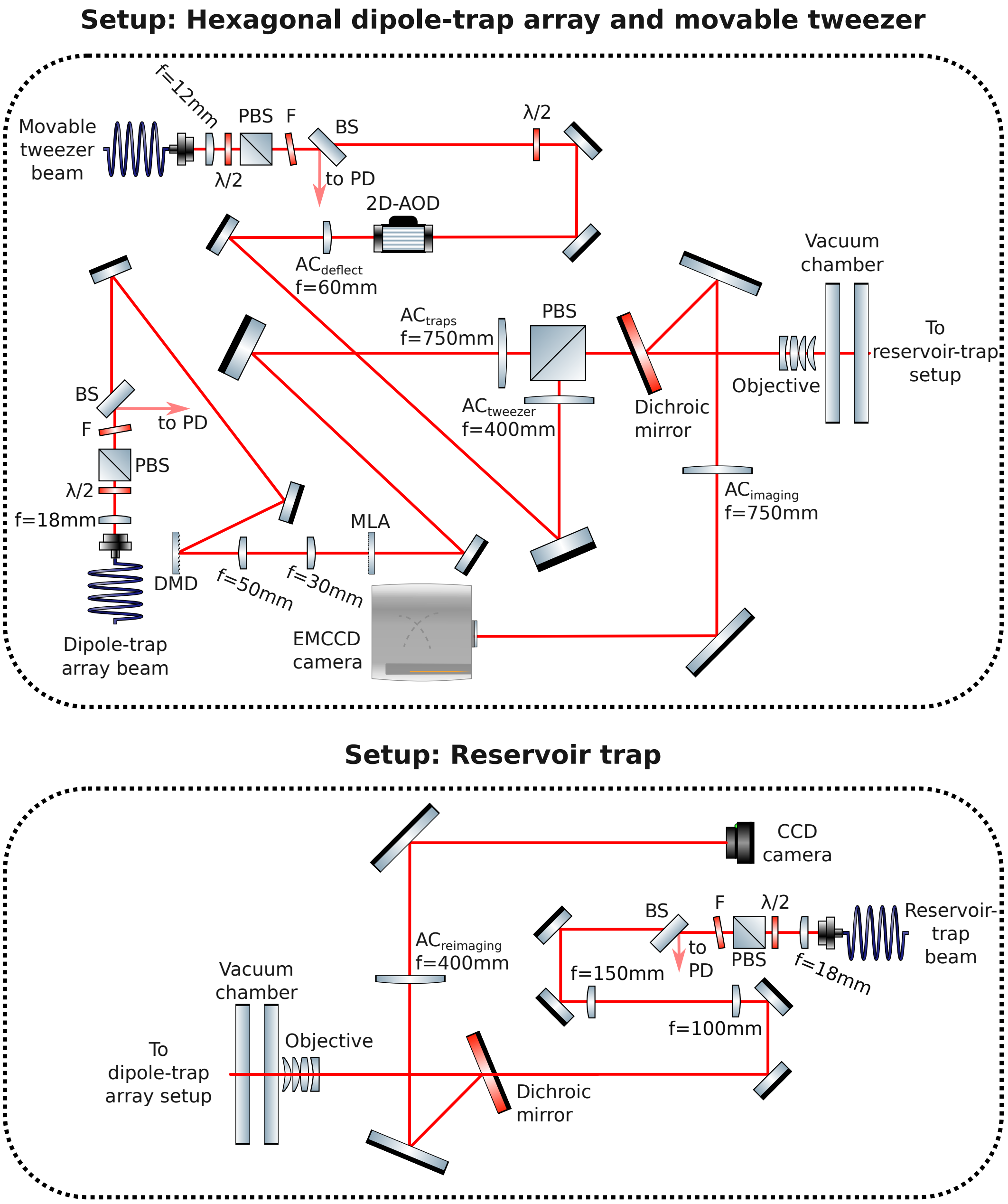
Setup: Hexagonal dipole-trap array and movable tweezer

Setup: Reservoir trap

Fig. 4.2.: **Top**: Setup for hexagonal dipole-trap arrays combined with a movable tweezer for atom transport. The top beam path is used as movable tweezer utilizing a two-dimensional AOD. The beam path starting at the bottom left creates the hexagonal dipole-trap array using a DMD for single-site addressability. The bottommost beam path is for fluorescence imaging. To the right of this setup, on the other side of the vacuum chamber follows the setup for reimaging and for the reservoir trap which is shown in the bottom part of this figure.
Bottom: Setup for a reservoir trap and for reimaging the dipole-trap array. The uppermost beam path is for reimaging the dipole-trap array together with the movable tweezer which is used for calibration purposes. The reservoir trap beam path starts at the right side.
All beams are intensity stabilized using a beam sampler (BS) coupling out a small fraction of light which is focused onto a photodiode (PD). Components: AC: achromatic lens; F: RazorEdge Filter (see chapter D). Schematic created using [135].

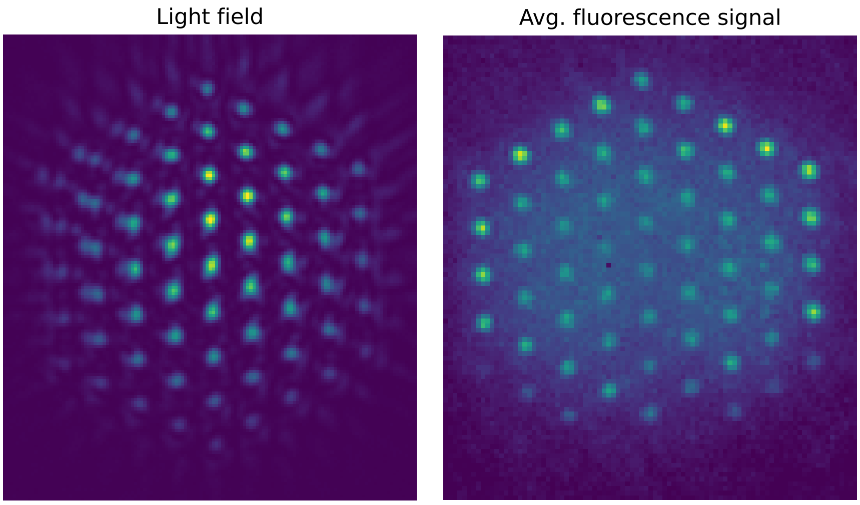

Fig. 4.3.: Light field of the dipole-trap array after reimaging (left) and corresponding averaged fluorescence image of single atoms trapped in the array structure (right). The Gaussian intensity profile of the illuminating beam is visible as the beam profile is not adjusted for uniform trap depth with the DMD for this image. Due to non-optimal imaging, the trap structure, especially at the edges, is distorted.

4.1.1. DMD-based trap manipulation

Utilizing the DMD, it is possible to modify the light field incident onto the MLA. The surface of the DMD is directly imaged onto the surface of the MLA such that arbitrary aperture structures can be generated on the microlens array. This allows to turn off all those mirrors of the DMD which would illuminate structures at the boundaries between neighboring microlenses as it was applied in Fig. 4.3. It is also possible to turn off specific traps of the underlying hexagonal grid. This was used to create a hexagonal sub-array with doubled pitch by turning off all other lenslets as depicted in Fig. 4.4 which reduced the background fluorescence signal of atoms trapped in intermediate structures. Additionally, individual lenslets of the double-pitch array are turned off to achieve the trap structures used in the following sections.

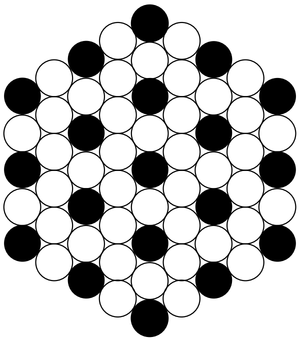

Fig. 4.4.: Used double-pitch array structure (filled black circles) resulting from turning off intermediate traps (non-filled black circles).

Furthermore, the fact that each individual lens is illuminated by typically 875 mirrors, the laser power illuminating each microlens can be controlled individually by disabling a certain fraction of the mirrors [138]. As the tweezer array inside the vacuum chamber is assumed to be distorted, a spot-specific adjustment of the trap intensity was not suitable at that stage. Therefore, the central part of the Gaussian light field illuminating the MLA was lowered to a flat-top profile using the DMD. This matches the trap depth of the inner most trap to the surrounding six traps resulting in an uniformly strong single-atom fluorescence signal. For all traps used in the following sections, this reduces the variation of the single-site trap depths to 25 % resulting in a typical trap depth of $U_{\mathrm{array}}/k_{\mathrm{B}} = 600(200)$ µK.

4.1.2. Reservoir for cold rubidium atoms

In order to decouple the supply of laser cooled atoms from the loading process of tweezer arrays, a reservoir of cold neutral atoms is necessary. In the experiments described in this chapter, a large-volume optical dipole trap acting as reservoir trap is used for this purpose. The reservoir trap is created using a collimated laser beam at a wavelength of 798.8 nm which is focused into the vacuum chamber using the second microscope objective used in parallel for monitoring the array light field (see Fig. 4.2 (bottom)). Using two lenses with focal lengths of 150 mm and 100 mm, the beam radius of the outcoupled beam is adjusted such that the resulting trap has a spot size of 14.6(1) µm ($1/e^2$-radius) inside the vacuum chamber. The typical trap depth used during the experiments is $U_\mathrm{R}/k_\mathrm{B} = 600(200)\,\mu\mathrm{K}$, matching the trap depth of the array.

4.2. Deterministic preparation of target structures from an atom reservoir

The experimental setup described above can be used to deterministically supply individual atoms from the atom reservoir into target structures [139]. At first, the principle is demonstrated by only loading the reservoir trap and filling the empty target structure. In the second section, the enhancement of the loading efficiency of pre-filled dipole-trap arrays is analyzed for the implemented setup.

4.2.1. Filling empty target structures exclusively from a reservoir trap

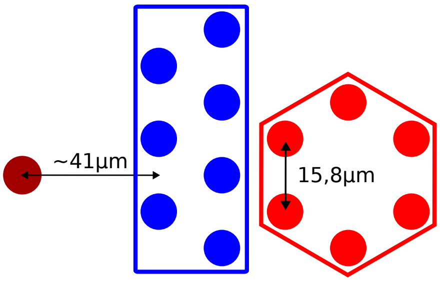

Fig. 4.5.: Dipole-trap configuration for experiments presented in section 4.2. Buffer traps are marked in blue, target traps are marked in red. The reservoir trap is marked in dark red.

In order to demonstrate deterministic supply of atoms from an atom reservoir, a trap structure with a doubled-pitch of 15.8(2) µm as shown in Fig. 4.5 is used. The reservoir trap (dark red) is positioned with a lateral distance of 41 µm to the closest row of the trap array. Within the array structure, a target area (red) of 6 trapping sites as well as a buffer area (blue) of seven trapping sites are defined.

Based on the loading procedure described in section 3.4, the reservoir trap is loaded with approximately 80 atoms while the array traps are turned off. Using fluorescence imaging, the resulting starting situation with an empty trap array and a filled reservoir is confirmed. If by chance, an atom is captured during imaging from the background gas, the shot is discarded in post-processing. In order to fill the trap array, the atoms in the reservoir are extracted with the movable tweezer. When directly filling the complete target structure, deterministic supply of single atoms is not possible. The reason is that with the movable tweezer a small ensemble of atoms is extracted from the reservoir trap which has to be reduced to zero or one atom using light-assisted collisions. Filling the target sites directly would therefore result in a similar loading efficiency as when loading them from an optical molasses directly. It is desired to deterministically fill the target structure. Therefore, only part of the whole trap array, i.e. the buffer structure, is filled directly from the reservoir resulting in a filling fraction

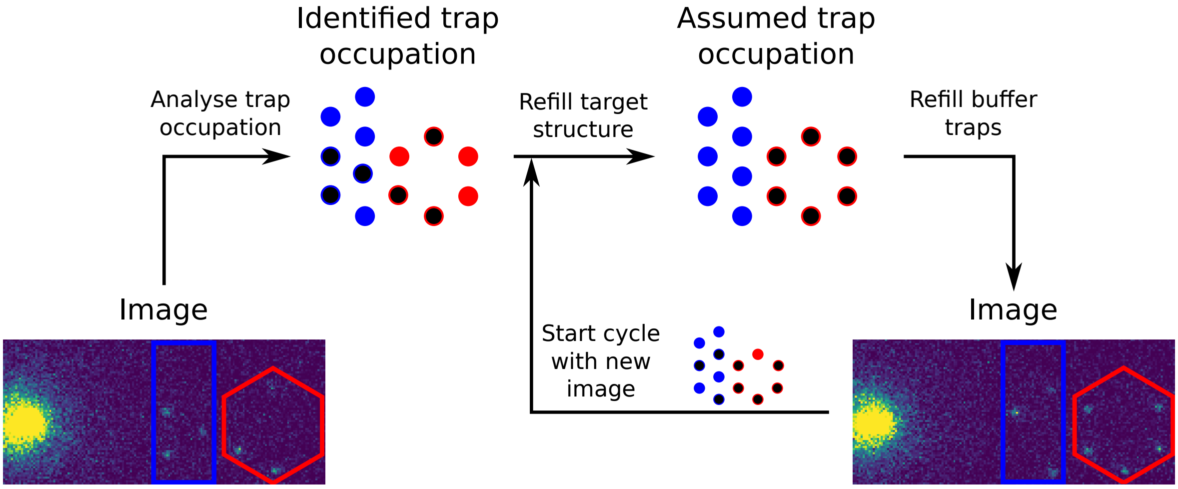

Fig. 4.6.: Experimental cycle refilling target traps (red) from buffer traps (blue) and subsequently refilling buffer traps from reservoir. Atoms occupying a trap are shown as black dots. From the initial image, the trap occupation is analyzed and the target traps are deterministically filled from the buffer traps. The resulting trap configuration is assumed to be known and the corresponding empty buffer traps are refilled from the reservoir with a maximum of 60 % efficiency. Afterwards an image is taken to detect the real trap occupation used for the next cycle. In the shown example, an atom was detected in the top target trap in the first image. This atom was lost in between the imaging phases and will be refilled in the next cycle using one of the three new buffer atoms.

of up to 60 % within the buffer region depending on the atom density in the reservoir. Using successive cooling during the transfer process as well as fluorescence imaging, single atoms are prepared in the buffer traps at known trap sites. These individual atoms can then be used to deterministically fill the target structure by utilizing the movable tweezer again to rearrange single atoms from the buffer traps to the target traps. For full knowledge over the current trap occupation, it would be necessary to image the atoms after the loading process from the reservoir as well as after the rearrangement process between buffer and target traps.

In order to reduce the time-consuming phases of imaging, an experimental cycle as shown in Fig. 4.6 is used, performing the rearrangement of atoms between buffer and target traps before reloading the buffer structure. After imaging the trap occupation, the first step is to use the currently filled buffer traps to fill the target structure using a shortest-move heuristic sorting algorithm as described in section 5.2.3. For extracting an atom, the movable tweezer is ramped up to a trap depth of $U_{\mathrm{T1}}/k_{\mathrm{B}} = 1.6(4)$ mK. The intensity ramp takes 130 µs each and the move is performed within 310 µs. The transport efficiency currently is 75.3(9) %.

The second step is to reload the buffer structure from the atom reservoir. As the initial buffer occupation as well as the performed moves to refill the target structure are known, the current occupation of the buffer traps after the first sorting step can be calculated. This circumvents renewed fluorescence imaging. To refill empty buffer traps, the movable tweezer is overlapped with the center of the reservoir trap, ramped up to a trap depth of $U_{\mathrm{T2}}/k_{\mathrm{B}} = 0.8(2)$ mK and moved to a position of an empty buffer site where the atoms are released by ramping down the movable tweezer. The movement timings are as the ones described in step one. During the movement process, the molasses lasers are used with the same detuning and have the intensity as during the molasses phase to achieve single-atom preparation based on light-

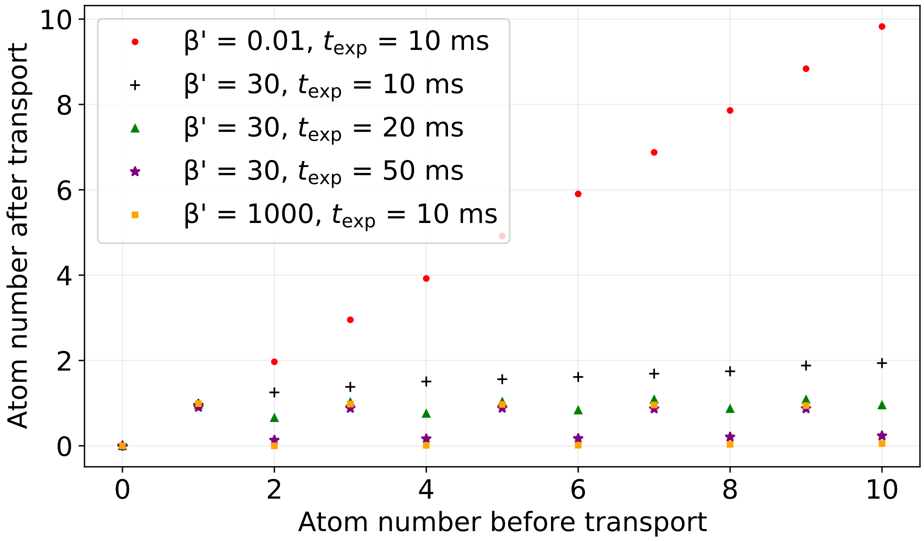

Fig. 4.7.: Simulation of the atom number due to light-assisted collisions and one-body losses during a cooling phase of 10 ms for different β'. A value of $\beta' = 0.01$ corresponds to the reservoir trap and $\beta' = 30$ corresponds to the buffer and target traps. Furthermore, for the movable tweezer ($\beta' \approx 30$) the atom number for different lengths of the cooling phase is shown.

assisted collisions as described in section 2.1.2. The new trap occupation is detected using fluorescence imaging and a new cycle can start. One cycle typically takes 230 ms of which roughly 130 ms are used for image acquisition and readout. The rest of the time is necessary to process the image, calculate the moves and perform the two rearrangement steps. For comparison, the trapping lifetime of the atoms in the array is 10.0(5) s independent of whether they are loaded from the molasses or from the reservoir trap into the array.

The continuous cooling of the atoms during the transport and imaging phases, utilized for single-atom preparation of the atoms transferred from the reservoir to the buffer traps, also induces light-assisted collisions and corresponding atom loss in the reservoir trap. The loss rate in the reservoir trap is given by $\beta' \approx 0.01$ whereas the loss rate in the movable tweezer or the buffer traps is $\beta' \approx 30$. The process of atom extraction under these conditions is modeled for a time span of 10 ms using a Monte-Carlo simulation of Eq. (2.20) as described in section 2.1.2. Furthermore, for $\beta' \approx 30$ the atom number after 20 ms and 50 ms is shown. For all loss rates and exposure times t_{exp}, the final atom number in the trap in relation to the initial atom number n is plotted for the range of one to ten atoms as shown in Fig. 4.7. To complement the behavior values for $\beta' = 1000$ as used in section 2.1.2 are added in the simulation.

It can be seen that single-atom preparation is not fully completed after 10 ms in the trapping volume of the movable tweezer or a buffer trap ($\beta' = 30$), as for traps with an initially even number of atoms the average trap occupation (black plus) is not zero. However, for even smaller traps ($\beta' = 1000$) single-atom preparation is completed. When simulating a cooling time of 20 ms, the average atom number for an even number of initial atoms in the trap is already below 1. For a cooling time of 50 ms the simulation shows complete single-atom preparation. Although a single transport process takes less than 1 ms for an individual atom, several transport processes and a small waiting time after atom transport for imaging to start guarantee that a minimal cooling time before imaging of 10 ms. This could in principle mean that more than one atom is inside the buffer trap when imaging starts. After imaging, which takes 100 ms, single-atom preparation inside the buffer trap is guaranteed. In the experiment no evidence was found that incomplete single-atom preparation would limit the single-atom detection fidelity. Furthermore, Fig. 4.7 shows that there is almost no loss of atoms in the reservoir trap due to light-assisted two-body collisions as the trapping volume due to the low loss coefficient β'.

Figure 4.8 shows the atom-by-atom composition of a hexagonal target structure based on the rearrangement cycle described above. Starting with a filled reservoir trap loaded from the optical molasses (Frame 0), the reservoir is used to fill the buffer structure (Frame 1). As all buffer traps are empty during the first loading cycle, no rearrangement between buffer traps and target traps is performed. From frame 2 onward, the repetitive experimental cycle as shown in Fig. 4.6 is used to fill the target structure in clock-wise direction atom-by-atom. Experimentally this is achieved by increasing the target structure one-by-one between subsequent images.

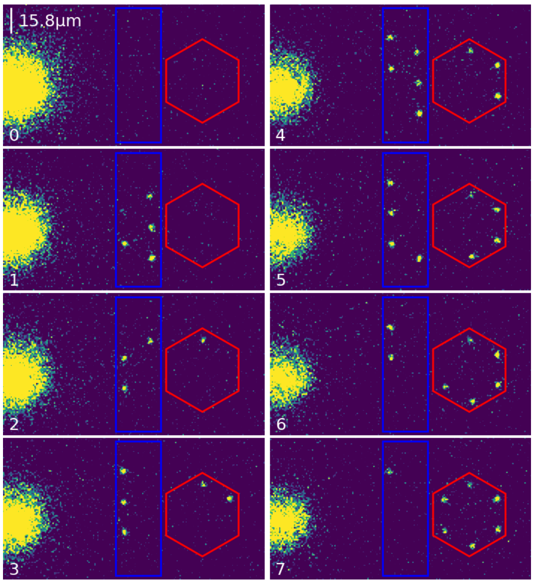

Fig. 4.8.: Image series demonstrating the composition of an increasing target structure (marked red). At first, only the reservoir trap is loaded from an optical molasses (Frame 0). Next, the buffer traps are filled from the reservoir (Frame 1). The subsequent images show the clockwise atom-by-atom loading of the target structure starting with the top trap.

In general, the aim is to fill the desired target structure as fast as possible. Therefore, measurements with the full hexagon defined as target structure right from the beginning have been performed and the cumulative success rate p_{fa} for a fully filled target structure has been evaluated. The cumulative success rate states in which percentage of experimental realizations the target structure has been achieved in at least one of the resorting cycles. This takes the functionality of conditional control, as described in section 3.2.3, into account without the increased experiment time due to hardware reprogramming. The course of the cumulated sucess rate after the nth rearrangement cycle is shown as blue circles in Fig. 4.9. After 8 rearrangement cycles a fully filled target structure is achieved with 86.8(7) % probability, while a maximum of $p_{\mathrm{fa}} = 91.5(6)$ % is achieved for 15 rearrangements.

As the target traps are refilled by using the available buffer atoms, Fig. 4.9 also shows the percentage of filled buffer traps after each rearrangement cycle. Initially, buffer and target traps are empty as only the reservoir is loaded with atoms. During the first rearrangement, atoms are loaded into an empty buffer structure from a fully filled reservoir trap. At this stage, a loading efficiency of 59.6(4) % is achieved. Later on, the percentage of filled buffer traps decreases as atoms are used for filling the target traps. Simultaneously the reloading of buffer traps is less efficient as the atom density in the reservoir trap is reduced due to atom extraction and heating of the atoms. This can be seen from the correlated decrease of the normalized reservoir fluorescence, shown as red crosses, and the fraction of filled buffer traps, shown as green triangles in Fig. 4.9. During the first rearrangements, the reservoir fluorescence decreases significantly due to the extraction of atoms from the reservoir. The time constant for atom number reduction of the reservoir is reduced to 1/4th as compared to a reservoir without extraction.

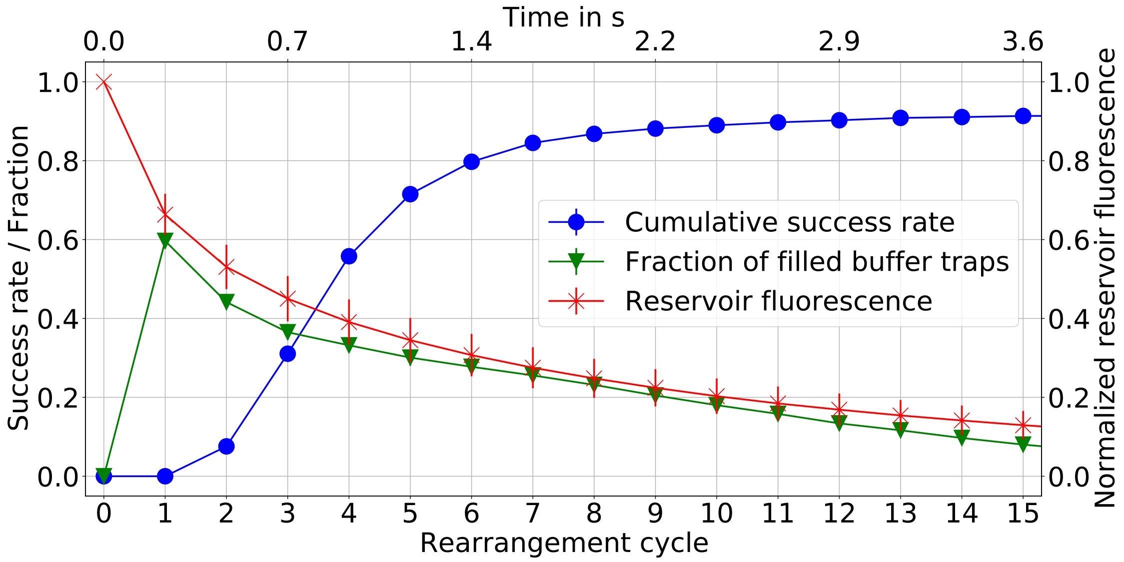

Fig. 4.9.: Analysis of the reservoir-based reloading of an empty target structure (6-site hexagon) using multiple rearrangements. Blue dots: Cumulated success rate of a deterministically filled target structure. Green triangles: Average fraction of available buffer atoms. Red crosses: Normalized reservoir fluorescence corresponding to the atom number inside the reservoir. Data is based on more than 2500 experimental repetitions. For the normalized reservoir signal, the uncertainty is given by the standard deviation and for the two other signals by the 1σ-confidence interval (error bars smaller than the size of the data points).

These results show that one limitation of the current setup is the relatively small reservoir trap. During the first reloading cycle, the reloading probability is limited by the single-atom preparation efficiency whereas for subsequent rearrangements the limitation is the atom density in the reservoir. In principle, the atom number in the reservoir could be increased by deepening the reservoir potential. As the trap depths influences the extraction process the initial reservoir trap depth was experimentally chosen as deep as possible to trap a large number of atoms but shallow enough to effectively extract atoms from the reservoir. If the reservoir trap is too deep, a deeper movable tweezer has to be used for atom extraction resulting in an increased atom loss in the reservoir trap due to atom extraction. Currently, we prepare on average 10(2) atoms in the buffer structure, which can be increased to a steady fraction of 60 % of the number of buffer traps utilizing constant refilling of the reservoir such that atom loss in the reservoir is not a limiting factor.

Furthermore, the transport efficiency of 75.3(9) % accounts for a not inconsiderable amount of losses during atom transport. However, optimizing the transport process should allow to achieve efficiencies above 98 % as described by [31, 140].

4.2.2. Enhancing the loading efficiency of prefilled array structures

With the demonstration of the deterministic preparation of individual atoms into an empty trap array, it is obvious that the reservoir can also be used to enhance the loading efficiency of prefilled array traps. With the large dipole trap, an atom reservoir is available which

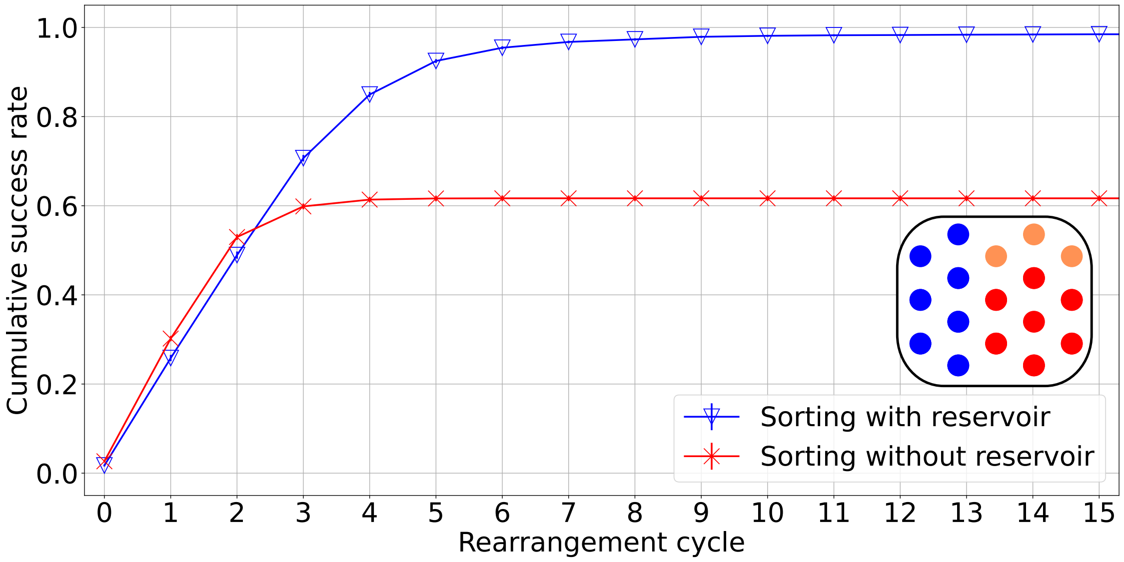

Fig. 4.10.: Enhancement of the cumulative success rate due to buffer atoms loaded from the reservoir. The trap structure (6-site hexagon and central trap) is shown in the inset: Blue traps are used as buffer traps, red traps are used as target traps and orange traps are only used for initial loading.

can compensate for atom losses due to heating, background-gas collisions, loss-based state detection or non-perfect atom transport. In experiments where atoms are exclusively loaded into a tweezer array, excess atoms in the whole array act as a reservoir of individual atoms as described for example in [31, 113, 140]. For this reason, in chapter 5 a setup to drastically increase the number of available reservoir atoms is presented.

Here, we want to investigate on a small scale, what effect the presented reservoir has on the loading efficiency. For comparison we use a 17-site trap structure which is loaded with individual atoms as described in section 3.4. In the first measurement series, the reservoir trap is loaded in parallel with the array and in the second measurement series the reservoir trap is turned off. The cumulative success rate after the nth rearrangement cycle is shown in Fig. 4.10 for both settings. The used trap structure is shown in the inset of Fig. 4.10 with buffer traps marked blue and target traps marked red; Orange traps are only used for initial loading.

For loading the 17-site trap structure, an average of 8(2) individual atoms are detected. Only in 2.7 % of the experiments, the target structure (6-site hexagon plus central trap) is completely filled after loading. This can be strongly improved by rearranging the atoms resulting in a cumulative success rate of roughly 60 % after three rearrangements (red crosses). Up to the second rearrangement the cumulative success rate is limited by the transport efficiency whereas for further rearrangements the limit is the low number of available atoms. The benefit of an external reservoir is visible in the second measurement (blue triangles). During the first two rearrangements the limit is, as before, the transport efficiency. For further rearrangements the higher available atom number increases the achievable cumulative success rate. Due to excess atoms loaded from the external reservoir, the cumulative success rate increases to a maximum of 98.6(2) % for 10 or more rearrangements.

4.2.3. Demonstrating conditional control within the `labscript-suite` architecture

As described in section 3.2.3, investigations were made regarding the implementation of conditional control within the `labscript-suite`. Based on the setup introduced in this chapter, the functionality of conditional control is demonstrated for a small target structure of a triangle of three atoms as shown in Fig. 4.11. The experimental cycle is as shown in the timeline in the top of Fig. 4.11. After loading the reservoir as well as the array structure with single atoms (section 0), there are two sections after which conditional control is used. In section 1 atoms are rearranged to fill the target structure and buffer traps are refilled from the reservoir. After section 1, conditional control is used to check the occupation of the target structure. If the target structure is not completely filled after section 1, this section is repeated. If a full target structure is achieved, section 2 follows where a loss-induced measurement is simulated by removing all atoms from the target structure. After section 2, by default, section 1 is started again to load the target structure. However, after section 1 and 2 conditional control checks if a termination condition (e.g. a maximum number of images) is fulfilled in which case section 3 would be started, thus ending the current experiment by starting a new MOT-loading phase.

The corresponding images of a single experimental run are shown in the bottom of Fig. 4.11. Initially, the reservoir as well as the tweezer array are loaded with atoms (individual atoms in the case of the tweezer array) during section 0. Based on the first image (Frame 0) the trap occupation is determined and the necessary rearrangements to fill the target structure and refill buffer traps are performed (section 1). The new trap occupation is imaged (frame 1) and as the target structure is fully occupied, a measurement (section 2) is simulated by removing all atoms from the target structure. The resulting trap occupation (Frame 2) is analyzed again and as the terminating condition (maximum of 21 images) is not fulfilled, the target structure is refilled with available buffer atoms (again section 1). As the refill process is successful (Frame 3), the process of cleaning and refilling is repeated. This results in a fully filled target structures in frames 5 after which a measurement is simulated as described above. In frame 6 only one buffer atom is available such that completely filling the empty target structure is not possible. In the next image (frame 7) it is detected that the target structure is not completely filled and another refill process is performed. Following frame 8, again a measurement is simulated. In the following, refilling atoms from the reservoir has a low probability due to the few atoms left in the reservoir, therefore section 1 is repeatedly performed and it takes several tries to load atoms into the buffer traps which are subsequently used to fill the target structure. The experiment is aborted after 21 images due to the termination condition.

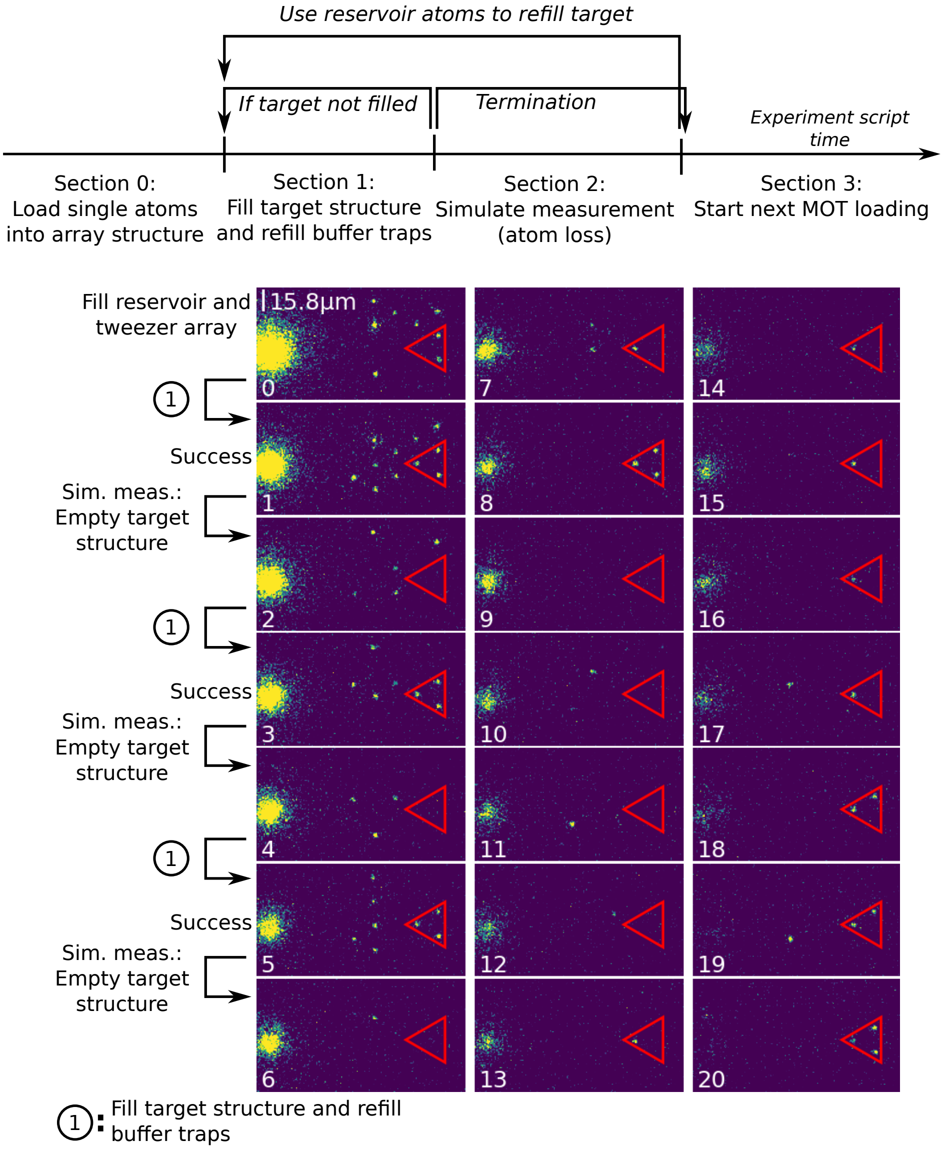

Fig. 4.11.: Experimental cycle of 21 atom rearrangements demonstrating the implementation of conditional control. The target structure is a triangle of three atoms. Using surrounding atoms in buffer traps as well as reloading buffer traps from atoms in the reservoir trap, rearrangements are performed to fill the target structure. If the target structure is successfully filled, a loss-based measurement is simulated by removing all atoms from the target structure. If the target structure is not completely filled, another rearrangement is performed. The decisions made by conditional control for the first column of images are shown in the left side of the figure. Further decisions made in the following frames are described in the text.

4.3. Conclusion

In this chapter, a novel method has been presented which allows to separate the provisioning of laser-cooled atoms from the single-atom preparation in tweezer arrays. Laser-cooled atoms are provided in a large reservoir trap from which small ensembles of atoms are repeatedly extracted. Single atoms are prepared from these ensembles and stored in the buffer trap region of the tweezer array. Using the atoms in the buffer traps, a deterministic supply of individual atoms into empty target traps is achieved. Both the setup for the reservoir trap as well as for the tweezer array in combination with the movable tweezer have been introduced. It has been shown on a small scale how the new concept can be used both to fill completely empty target structures or to enhance the filling of preloaded tweezer arrays. In the final section, the setup has been used to demonstrate conditional control within the `labscript-suite` framework.

The novel concept is the basis for future large-scale implementations as it splits the experimental process of deterministic single-atom loading into several functional units which enable spatial separation as well as parallel operation. One unit, e.g. a MOT/Molasses setup, continuously prepares laser-cooled atoms. A second unit provides those laser-cooled atoms in a reservoir such as the reservoir dipole-trap in the experiments described in this chapter. The connection between both units is possible by adopting one of two recently demonstrated techniques: Atoms can be transported over a long distance from a continuous MOT into the reservoir trap [141], or the reservoir trap can be continuously supplied with cold atoms as demonstrated even for a BEC in [142]. Continuous refilling of the reservoir trap circumvents the reduction of available reservoir atoms as shown in Fig. 4.9 such that a steady refill probability of 60 % for the buffer traps is available. Furthermore, it is possible to increase the reservoir size by utilizing the micro-optical parallelization of traps. Using different microlens and reimaging parameters, several reservoirs can be easily achieved as shown in reference [112]. The third unit are the buffer traps providing individual atoms for the fourth unit, the target array. As proven in this chapter, movable tweezers can be used to connect the dipole-trap units paving the way to a continuously operating quantum computer based on neutral atoms. This allows for a spatial separation as well as for a parallelization of the operation.

5. Large scale tweezer arrays for trapping more than 1000 individual atoms

For applicable quantum technology platforms, scalability is a demanding challenge as already introduced in chapter 1. In microlens-based trap-array setups scalability is an intrinsic feature as several thousand foci are readily available when illuminating the MLA with a large-scale laser beam. An explicit example is MLA2 given in Tab. 2.2 which has a size of $10\,\mathrm{mm} \times 12\,\mathrm{mm}$ making more than 20000 identical microlenses available. One of the challenges arising from such large arrays is the illumination with enough laser power. Additionally, with an increasing trap-array size, high-quality reimaging into the vacuum chamber becomes more demanding. These challenges are addressed in this chapter resulting in three interleaved dipole-trap arrays that are used for single-atom trapping. In the following, the new setup is introduced and the implementation of a 1000-atom-array is demonstrated. Furthermore, observed limitations as well as possible solutions are discussed.

5.1. Setup with three interleaved dipole-trap arrays and a movable tweezer

In large tweezer-array setups, usually a single laser is used for trap-array creation [25, 31, 32]. As the trap depth is proportional to the laser power within the focal spot (assuming a fixed spot size and detuning), the number of realizable trapping sites with sufficient trap depth is proportional to the available laser power as given by Eqs. (2.13) and (2.30). However, laser power from a single laser source is limited by different factors: Maximum output power of the available laser source, transmission threshold of the optical fiber (limited by stimulated Brillouin scattering (SBS) or damage threshold of the fiber), and the laser damage threshold of optical components (especially SLMs). In the microlens-based setups in our group, the first two aspects are the predominant ones. For shifting these limitations to significantly larger array sizes, a new setup was designed which enables the use of multiple laser sources in parallel. A related idea has recently been demonstrated in the group of Mark Saffman by using two different laser beams for the creation of blue-detuned traps [143].

In this section a setup utilizing three interleaved dipole-trap arrays fed by three independent laser beam paths is presented. A new high-NA microscope objective has been used for creating spot sizes down to the sub-micrometer regime thereby reducing the necessary laser power to achieve the same peak intensity in each focal spot. At first, a detailed analysis of its performance is given. Then the optical setup is introduced and the achieved trap structures are discussed.

5.1.1. High-NA microscope objective for array reimaging and fluorescence imaging

For the experiments in this chapter, a new high-NA microscope objective designed and fabricated by Lens-Optics GmbH has been available. The main features of the new objective are a high

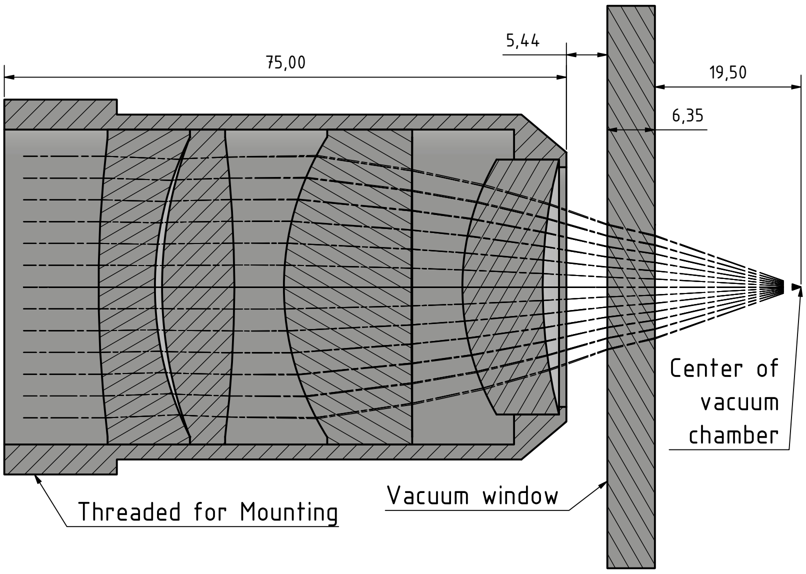

Fig. 5.1.: Schematic of the high-NA objective together with the window of the vacuum chamber. Important dimensions as well as some geometric rays of a collimated beam are shown. The design was made by Lens-Optics GmbH. All measures are given in mm.

NA, the best possible achromatic performance for different Rydberg wavelengths, and a large field of view. The schematic of the final design is shown in Fig. 5.1.

The microscope objective consists of four spherical lenses where the lens closest to the vacuum chamber has a smaller radius compared to the other three. This allows a narrowed objective housing close to the vacuum chamber as the space is needed for the diagonal MOT beams. The design is optimized for a vacuum window made from fused silica with a thickness of 6.35 mm. The lenses are anti-reflection coated for the relevant wavelengths given in Tab. 3.1 resulting in a guaranteed total transmission above 92 % for 420 nm and above 94 % for all other wavelengths given therein. For dipole trapping and fluorescence imaging at 780 nm to 800 nm a transmission of 98.0(5) % was measured. The microscope objective has a free aperture of 39.5(5) mm and an effective focal length of 52.90(5) mm for the trapping wavelength of 797(1) nm. The NA is given by 0.385(5), calculated from a Zemax OpticStudio simulation using the angle of incidence of the marginal rays. As the NA is slightly wavelength dependent, the uncertainty takes all wavelengths of interest into account. The field of view inside the vacuum chamber is stated to be at least 200 µm×200 µm.

For site-specific two-photon Rydberg excitation of the atoms trapped in the dipole-trap arrays, it is advantageous to have a minimal focal shift between different wavelengths. The microscope objective was therefore designed to have a low chromatic focal shift (CFS) between the trapping wavelengths at 797(1) nm and the Rydberg wavelengths at 420 nm and 480 nm. Figure 5.2 shows the CFS relative to a trapping wavelength of 797 nm. The objective has no CFS for 796.5(15) nm and 425.6(3) nm. For the Rydberg wavelengths at 421(1) nm, the CFS is 7(2) µm, whereas for the Rydberg wavelengths at 480(1) nm, the CFS is −48(2) µm relative to the trapping wavelength.

Illuminating the objective with a plane, uniform wavefront (assuming a point source at

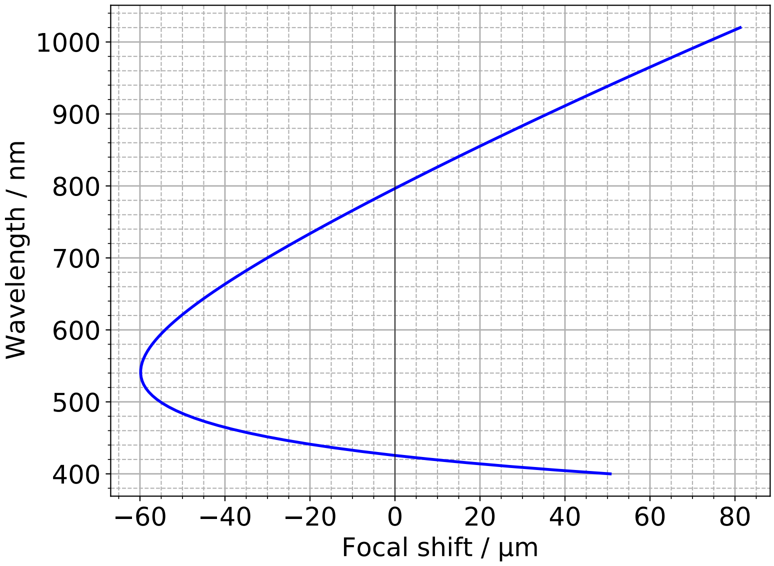

Fig. 5.2.: Chromatic focal shift (CFS) of a single spot relative to the reference wavelength of 797 nm plotted for the interesting wavelength range for Rydberg excitations between 420 nm and 1015 nm. For specific focal shift values at important wavelengths see text. The CFS is calculated using the corresponding Zemax OpticStudio tool which is based on paraxial ray tracing [74].

infinite distance) allows to evaluate its performance in creating small spots and its robustness against misalignment of optical components. Due to diffraction of the light at the aperture of the objective, an Airy-disc is created in the far-field from the lens as described in section 2.2.2. The resulting intensity distribution is given by Eq. (2.45). Optical systems working close to this theoretical limit are called diffraction-limited. The intensity distribution at the image plane of a lens system resulting from a point source is also called the point-spread function (PSF) [144, Chap. 1.2]. In order to quantify how close the system is working to the theoretical limit, the maximum amplitude $I_{\text{real}}(r=0)$ of the PSF of a real system can be compared with the theoretical amplitude $I_{\text{ideal}}(r=0)$ of an ideal system as given by Eq. (2.46). The ratio between both, given as

$$S = \frac{I_{\text{real}}(r=0)}{I_{\text{ideal}}(r=0)}, \tag{5.1}$$

is called the Strehl ratio [145]. A Strehl ratio above 0.8 is generally considered as diffraction-limited performance.

To evaluate the performance of the microscope objective, a plane wave was propagated through the objective using the Huygens PSF tool from Zemax OpticStudio simulating the PSF at the focal plane. For this, the wavefront in the object space is decomposed into single point sources radiating spherical waves. The ray for each point source is traced to the image plane and the complex amplitude of the wave is calculated at the image plane. The resulting amplitude distribution is given by the complex sum of all single wavefronts. The even more realistic physical-optics-propagation (POP) tool cannot be used here as the NA of the objective is too large with the consequence that the simulations get too computation-intensive. The POP tool is based on wavefront propagation from one surface to the next and is not using ray-based propagation. For further explanations see [74].

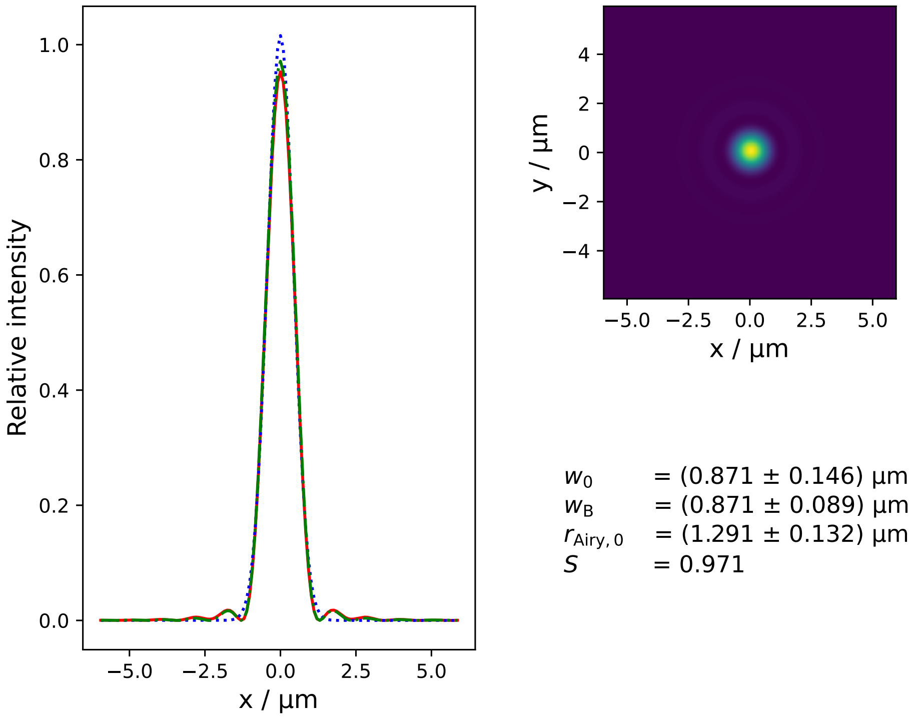

Fig. 5.3.: Focal spot simulated in Zemax OpticStudio using the Huygens PSF with the high-NA objective being illuminated by a uniform, plane wave. On the left, the cross-section along the x-axis is shown: Red: Intensity variation resulting from the simulation; Dotted blue: Approximation of a Gaussian function to the data; Dot-dashed green: Approximation of a Bessel function of first order to the data. On the right side, the 2D-intensity distribution in the focal plane is shown and spot sizes w_0, w_B, and $r_{\mathrm{Airy},0}$ as well as the Strehl ratio S deduced from the data on the left are given below.

In Fig. 5.3 the focal spot created for a plane wave with wavelength 795 nm is shown. The parameter summary for different wavelengths is given in Tab. 5.1, where a wavelength of 795 nm is used to quantify the results for both the D1-line of rubidium as well as for the trapping wavelengths of 797(1) nm. The waist w_0 is determined from a Gaussian approximation to the intensity distribution whereas w_B and $r_{\mathrm{Airy},0}$ are based on Eqs. (2.47) and (2.48). The Strehl ratio of all spots is above 0.95 showing that spots for all wavelengths are diffraction-limited, but an exact comparison between different wavelengths is not possible due to a too coarse sampling with 1 µm resolution along the direction of propagation.

For 795 nm, not only the spot size resulting from a uniform illumination of the objective is given but also using a Gaussian intensity distribution. The uniform illumination resembles the optimal performance of the objective, however the real beams used a best modeled as Gaussian beam and therefore will have a Gaussian intensity distribution (The non-plane wavefront cannot be modeled here). As described in section 2.2, the achromatic lens used to reimage the focal plane of the MLA is therefore matched with the NA of the used MLA. Using $\mathrm{NA}_{\mathrm{MLA2}} = 0.034$ of the MLA as given in Tab. 2.2, a beam radius ($1/e^2$ intensity radius) of 25.5 mm on the

Tab. 5.1.: Spot size in the atom plane at the center of the vacuum chamber and corresponding Rayleigh range z_R calculated from w_0 using Eq. (2.32) given for different wavelengths λ using uniform illumination of the microscope objective. For 795 nm also the spot size resulting from a illumination with Gaussian intensity distribution is given (see text for details). Different simulations using the Huygens PSF analysis from Zemax OpticStudio were performed sampling the spot along the direction of propagation in steps of 1 µm. The data is based on the respective simulation with highest peak intensity. The distance l' between the last lens surface and the vacuum chamber window is given, quantifying the focal shift. Uncertainties for spot sizes result from the approximation of the corresponding functions to the simulated intensity distribution.

λ in nm	l' in mm	w_0 in µm	w_B in µm	$r_{\mathrm{Airy},0}$ in µm	z_R in µm	Strehl ratio
420	8.638	$0.459(78)$	$0.458(47)$	$0.679(70)$	$1.58(53)$	0.955
480	8.578	$0.523(86)$	$0.522(52)$	$0.774(78)$	$1.85(60)$	0.984
780	8.613	$0.854(143)$	$0.853(87)$	$1.265(129)$	$2.94(98)$	0.975
795	8.618	$0.871(146)$	$0.871(89)$	$1.291(132)$	$3.0(10)$	0.971
795, Gauss	8.618	$0.926(147)$	$0.926(90)$	$1.373(133)$	$3.4(11)$	0.968
1015	8.695	$1.114(187)$	$1.113(113)$	$1.650(168)$	$3.8(13)$	0.973

achromatic lens is expected. As the achromatic lens collimates the beam, it is assumed that the beam radius at the microscope objective is the same as at the achromatic lens. This means, that the radial spot size of the Gaussian intensity distribution illuminating the objective is also $w = 25.5$ mm while the upper bound of the free aperture of the objective is 40 mm in diameter. This corresponds to an apodization factor $G = (d/2)^2/w^2 = 0.615$ following the definition of the normalized intensity distribution in the Zemax OpticStudio manual [74]

$$I(\rho) = \exp\left(-2G\rho^2\right) \tag{5.2}$$

with normalized pupil coordinate $\rho = r/(d/2)$ and free aperture diameter d. Simulating the spot size using a Gaussian intensity distribution with apodization factor G reveals a spot size roughly 5 % larger than with uniform illumination, also showing diffraction effects from the aperture of the objective. As apparent from the results described in section 5.1.3, the simulated spot size of a plane wave can be seen as a lower bound for achievable spot sizes. The smallest individual spots were observed to be slightly smaller than expected from the simulation with a Gaussian intensity distribution.

In the experimental setup, the microscope objective is mounted in front of the vacuum window. The alignment of window and objective relative to each other as well as relative to the incident beam influences the imaging quality as the vacuum window in combination with the microscope objective are part of the imaging optics and the window can therefore be thought as a fifth lens. In order to simulate non-perfect alignment in the real setup, it was investigated how tilts and shifts of the objective and the vacuum window relative to the optical beam path effect the spot quality. Details of this analysis have been performed in [146]. The general finding is that a tilt relative to the optical axis of up to 0.2° is acceptable for all optical components and wavelength above 480 nm, for 420 nm only a tilt of less than 0.1° guarantees diffraction-limited performance. Larger wavelengths are in general less sensitive. For tilts larger than these boundaries, the spot is not diffraction-limited. For lateral shifts of

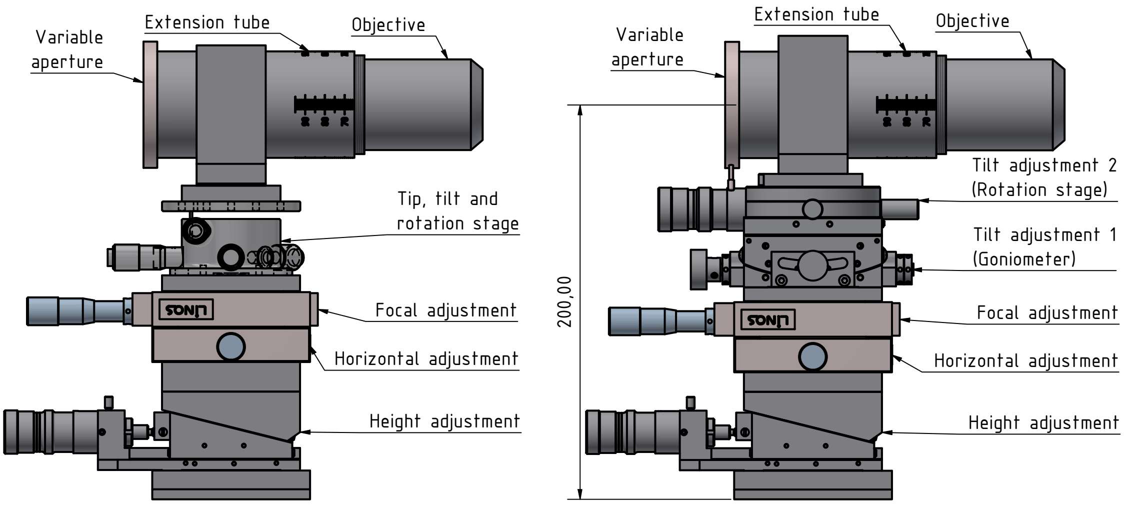

Fig. 5.4.: Two versions of optical mountings for the high-NA objective. **Left (Version a)**: Mounting platform using a tip, tilt, and rotation (TTR) stage; **Right (Version b)**: Mounting platform using a goniometer in combination with a rotation stage for tilting the objective. The lower part including x-, y- and z-positioners are the same for both mounts. An engraved scale on the extension tube is used as measure to calculate the distance between the front of the objective and the vacuum chamber. Measure given in mm.

the objective relative to the beam path, the impact is smaller. For up to 2 mm of shift of the objective, the increase in spot size is calculated to be less than 10 %.

From these results it is obvious that for optimizing the position of the objective relative to the vacuum chamber, five degrees of freedom are required: Two degrees of freedom for lateral positioning relative to the incident laser beam, one degree of freedom for adjusting the position of the focal plane and two degrees of freedom to tilt the objective around two independent axis perpendicular to the beam path. To allow for all of these adjustments, two versions of mounts for the positioning of the objective have been designed and are shown in Fig. 5.4. Both versions allow for the adjustment of all five degrees of freedom. Version a) was the one designed first and is based on a tip, tilt, and rotation (TTR) stage from Thorlabs (TTR001). During the adjustments, it became apparent that the adjustment using the TTR stage is more difficult for small angular deviations as the screws for tilting are spring-loaded and show too much hysteresis. Therefore version b) was designed which has improved options for tilting. Due to limited availability of parts at the time of integration into the experiment, only version a) was available when integrating the setup into the experiment. Version b) could later be used to easily exchange the reimaging setup on the other side of the vacuum chamber (see also Fig. 5.8). Exchanging the objective mount for trap creation would have made a complete readjustment necessary. As a good adjustment has been found with version a), the change to version b) is scheduled in combination with other major beam line modifications at a later stage.

In the simulations described above, a plane wave with uniform or Gaussian apodization was used. However, in the real setup, the focal spots of the microlens array are reimaged into the vacuum chamber using an achromatic lens in combination with the microscope objective. Therefore, the reimage of a focal spot with an achromatic lens and the objective were analyzed investigating how different focal lengths of the achromatic lens affect the quality of the reimaged focal spot. The simulations show that the achromatic lens needs to have a focal length of 300 mm at minimum, as for shorter focal lengths the reimaged focal spot is not diffraction-limited anymore due to spherical aberrations. Further simulations were performed together with the microlens array and are discussed at the end of the next section after introducing the new microlens setup.

5.1.2. Optical setup

As mentioned in the introduction, the goal of the new optical setup is to increase the number of trapping sites by overcoming the power limitations resulting from a single laser beam illuminating an MLA. For increasing the available number of trapping sites inside the vacuum chamber, different options utilizing multiple laser beams have been evaluated which shall be introduced briefly, including a discussion of their advantages and disadvantages:

- **Overlap two laser beams with perpendicular polarization using a PBS:** This allows to double the laser power in the single overlapped beam after the PBS used for dipole trapping. Furthermore, the technique is relatively simple and each single high-power laser beam can be well adjusted to achieve good imaging quality. Even working with different wavelengths is possible, such that deeper traps with less detuning can be added to farther detuned traps during loading. The disadvantage is that the trap structure and the interatomic spacing of the microlens-based grid is fixed. Furthermore, the resulting light field includes two orthogonal polarizations thus limiting the use of polarization sensitive optics [143].

- **Overlap two laser beams with different wavelengths using a dichroic mirror:** This idea is similar to the first option but limited in the use of different wavelengths. The wavelength difference has to be large enough to merge them with high-quality dichroic mirrors resulting in a wavelength difference of typically more than 1 nm. Furthermore, overlapping with a dichroic mirror is restrictive in the use of wavelengths as tuning the cutoff wavelength is possible by angle-tuning the filter but requires the readjustment of the reflected beam path. The advantage is, that both laser beams can have the same polarization.

- **Increase the number of traps by irradiating a microlens array under different angles of incidence:** Instead of increasing the total laser power within a single beam, smaller scale arrays can be interleaved by using different angles of incidence. For this method, the pitch of the traps has to be large enough so that the individual dipole-trap potentials are still distinct after interleaving two arrays. Furthermore, the angle of incidence reduces the reimaging quality of the traps into the vacuum chamber and increases losses on apertures as the light travels further off-axis. On the other hand, the resulting trap structure is compact and independent of polarization and wavelength.

From testing the new high-NA objective in offline setups as well as simulating its performance in Zemax OpticStudio, it became obvious that a straight laser beam path with normal incidence is necessary to achieve the best quality traps. However, small angles of incidence are possible to implement interleaved trap arrays with a single MLA.

In order to achieve a versatile trap geometry the decision was made to use a single straight beam path with one MLA creating the main array. This path is overlapped with two interleaved

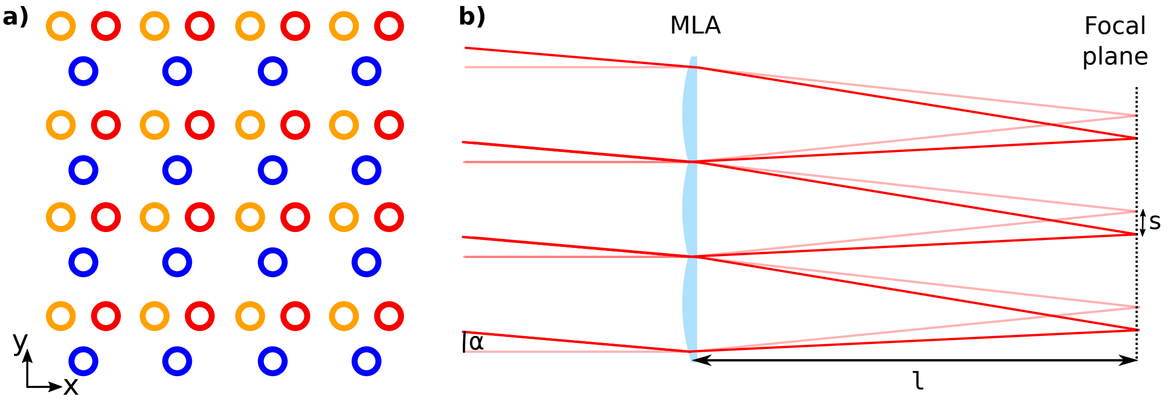

Fig. 5.5.: **a)** Interleaved trap pattern of the main array (blue) and two auxillary arrays (red and yellow). The MLA of the auxiliary arrays can be moved in the x-y-plane whereas the MLA of the main array can be moved along the z-axis to match the focal planes of both MLAs. **b)** Illustration of the focal shift resulting from a collimated laser beam incident under an angle α onto an MLA. The amplitude of the shift s is dependent on length l between the MLA and the considered plane (here focal plane) as given by Eq. (5.3). Images adopted from [147].

trap arrays from a second MLA, referred to as auxiliary array 1 and auxiliary array 2 using a PBS. The resulting trap pattern is shown in Fig. 5.5 a). The position of the auxiliary arrays can be adjusted arbitrarily with respect to the main array using two translation stages and the separation between the auxiliary arrays is defined by the angle of incidence.

Adjusting the separation between the auxiliary arrays

For achieving a separation of half a pitch between both auxiliary arrays, each individual auxiliary array has to be shifted by a quarter pitch to either side, which can be done in the focal or any Talbot plane. The relation between the angle of incidence α of the laser beam onto the MLA and the shift s of the focal spot in the corresponding Talbot plane is illustrated in Fig. 5.5 b) and given by

$$s = l \cdot \tan(\alpha) \tag{5.3}$$

As the used MLA is a square pattern of lenses, the Talbot length z_T is given by Eq. (2.59). Identical copies of the focal plane are therefore found at $l = f + n \cdot z_\mathrm{T}/2$ with $n \in \mathbb{N}$. For the focal plane, this results in an angle of incidence of $\pm 0.976°$ whereas for the $\mathrm{T}_{1/2}$-plane, the angle of incidence would be $\pm 0.131°$. It shall be noted that for future setups using Talbot planes, larger angles resulting in a shift of $1/4 + n \cdot 1/2$ are possible which can be used as a compromise between long beam paths for overlapping the beams and small angles for highest spot quality.

When planning the desired setup and choosing the plane to work in, the space requirement for beam steering and superposition before illuminating the MLA has to be taken into account. The two beams can best be superposed by using D-shaped mirrors. Due to the beam size incident onto the MLA, in the following denoted as $w_\mathrm{inc,MLA}$, there needs to be a presumed minimal distance from the beam center to any edge of optical elements of $1.5 \cdot w_\mathrm{inc,MLA}$ limiting the cropped fraction to 1×10^{-3} of the incident laser power. Small angles of incidence therefore demand for a long beam path in front of the MLA to be able to overlap the laser beams. The distance d_SP, being the minimal distance between the D-shaped mirrors and the MLA, is given

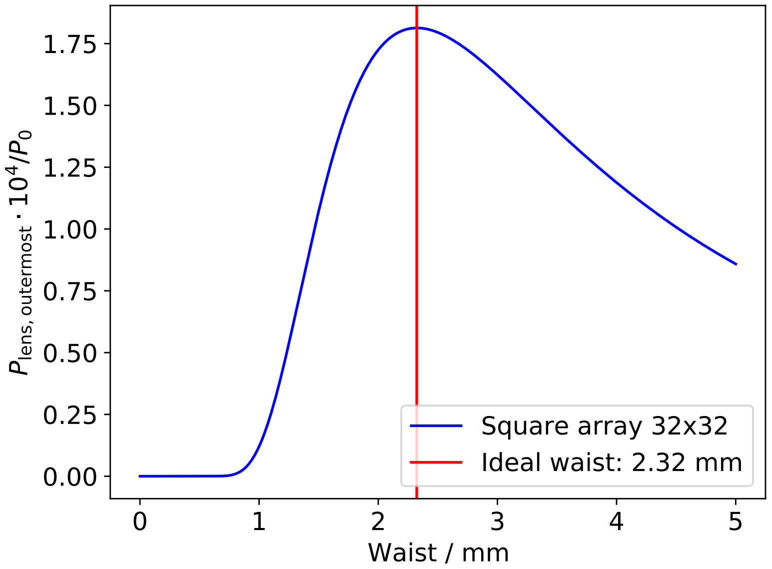

Fig. 5.6.: Relative laser power in the outermost trap of a 32×32 trap array using MLA2 plotted versus the beam radius of the incident beam. The optimal beam size yielding the highest relative laser power is found to be 2.32 mm. Based on similar analysis in [147]

by

$$d_{\mathrm{SP}} = \frac{3}{2}\frac{w_{\mathrm{inc,MLA}}}{\tan(\alpha)} \approx \frac{3}{2}\frac{w_{\mathrm{inc,MLA}}}{\alpha}. \tag{5.4}$$

Optimal beam size

The beam size $w_{\mathrm{inc,MLA}}$ depends on the available laser power. Increasing the beam size will enlarge the number of traps but also lower the relative intensity of the traps compared to the total laser power incident onto the MLA. The aim is to have a quadratic working area of roughly 1000 traps meaning an array of size 32×32 traps when using MLA2. Plotting the relative laser power in the outermost trap versus the waist of the laser beam incident on the MLA, as shown in Fig. 5.6, yields an ideal waist of $w_{\mathrm{inc,MLA}} = 2.32\,\mathrm{mm}$. In this case, the outermost trap of the 32×32 grid has 39 % of the trap depth of the innermost trap.

Using a triplet collimator (TC25APC-780) and a fiber patch cable (P3-780PM-FC) manufactured by Thorlabs results in a collimated beam radius of 2.4 mm matching well the desired beam size. As all arrays should have comparable beam sizes and the quality of collimation for fixed fiber collimators such as the TC25APC is strongly dependent on the exact pair of fiber and collimator, individual collimator-fiber pairs were tested in order to find the best matching pairs with the least divergence and the least variation of divergences between the beams.

Simulating the effect of tilted beams on the spot size

Knowing the beam size used in Eq. (5.4) it is obvious that small angles on the one hand result in long beam paths in front of the MLA occupying a lot of space. On the other hand, small angles cause less aberrations. The MLA in this setup, MLA2, has a focal length (determined using only geometrical optics) of $f_{\mathrm{MLA2}} = 1.10\,\mathrm{mm}$ resulting in an angle of $0.97°$ and a distance

Tab. 5.2.: Spot size w_i and pitch a_i given for focal and Talbot plane at 0° angle of incidence and for focal plane at 0.97° angle of incidence. For angles of incidence different from 0°, also the shift s as determined with the simulation is given. For the simulation, a microlens array of 9 by 9 lenses was used. Ignoring traps that are affected by calculation errors due to boundary effects, the waists given are determined as mean and standard deviation of 2D-Gaussian approximations to the single spot intensity distributions. The pitch is determined from mean and standard deviation of the distances between the spot locations. The shift s_x and the side-structure contrast (SSC) are only calculated for the central spot, therefore no uncertainty is given. Spot analysis based on [148].

Angle of incidence, analysed plane	w_x in µm	w_y in µm	a_x in µm	a_y in µm	s_x in µm	SSC
0°, focal plane	0.84(1)	0.84(1)	5.19(2)	5.19(2)	-	0.03
0°, $\mathrm{T}_{1/2}$ plane	0.84(1)	0.84(1)	5.23(2)	5.23(2)	-	0.04
0.97°, focal plane	0.83(1)	1.02(3)	5.19(1)	5.18(3)	1.28	0.07

of $21\,$cm for interleaved arrays in the focal plane or an angle of $0.13°$ and a distance of $153\,$cm for interleaved arrays in the Talbot plane $T_{1/2}$.

Simulating the Huygens PSF of the dipole-trap array inside the vacuum chamber results in spot sizes of the single-trap foci and pitches between the foci as given in Tab. 5.2. It can be seen that tilting the plane of incidence of the beam in the x-dimension relative to the MLA will result in aberrations which increase the spot size. However, not only the spot size is increased, but also the side structures of the spot change. In Fig. 5.7 the simulation of the central spot is shown for a straight as well as for a tilted beam. For straight incidence onto the MLA, a symmetrical structure with an Airy disk around the focus is visible. Illuminating the MLA under an angle creates asymmetric side structures as the Airy disc as well as the quadratic structures are distorted. These side structures can potentially trap atoms if the created optical potential is deep enough. This is especially problematic for side structures which are in the same plane as the array we are working with, as the atoms therein cannot be eliminated with the cleaning procedure described in section 3.4.3. We therefore evaluate the side structures with respect to the focal spot by defining a side-structure contrast (SSC) as the ratio between the maximal intensity outside the focal spot (outside the first Airy minimum) relative to the maximum intensity of the focal spot:

$$SSC = \frac{I_{\text{max(outside,Airy)}}}{I_{\text{max(inside,Airy)}}} \tag{5.5}$$

Implemented optical setup

As the Zemax OpticStudio simulations imply that an angle of up to 1° is acceptable and as the space on the laser board for three interleaved beam paths is limited, the arrays were interleaved in the focal plane with a measured angle of incidence of 0.985(15)°. The implemented optical setup is shown in Fig. 5.8.

The three interleaved trap arrays are created using three separate beams, coupled out of three individual optical fibers utilizing triplet collimators (Thorlabs TC25APC-780) with focal length of 25 mm. This allows the usage of three individual laser sources thus decreasing the power requirement of a single laser system including the optical fiber. The general setup of

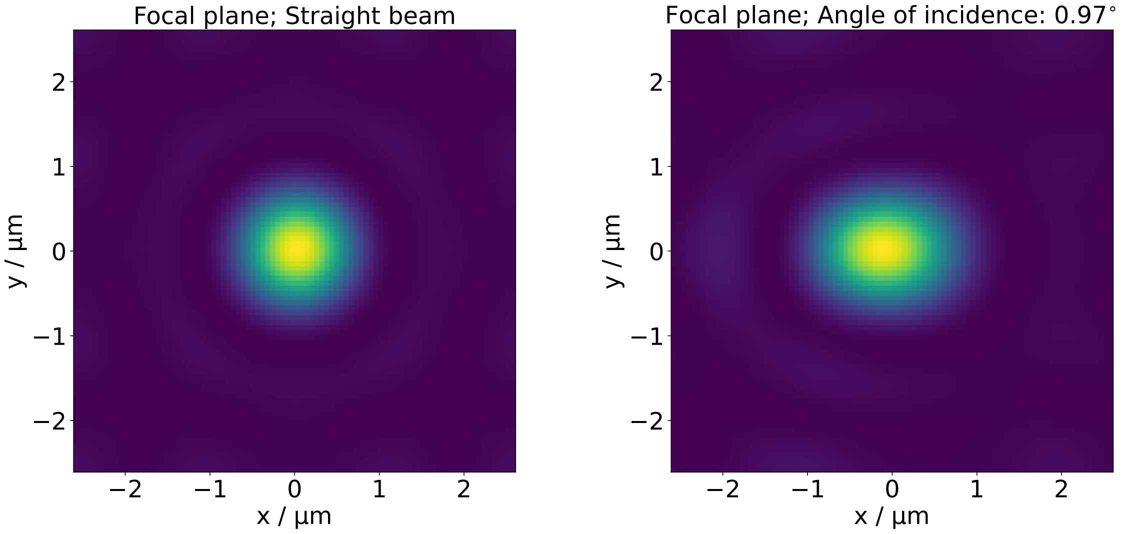

Fig. 5.7.: Simulation of a single spot in the focal plane for light with angles of incidence of 0° and 0.97° relative to the normal vector of the MLA. The left side shows the single central spot for the straight beam whereas the right side shows the spot of the beam tilted in the x-direction.

each beam path is as described in section 2.2. The MLA array is irradiated by the collimated laser beam creating an array of focal points which are reimaged into the vacuum chamber using an achromatic lens and a high-NA microscope objective. As the high-NA microscope objective together with the vacuum chamber window is sensitive to beam misalignments, we use a straight beam path to create the main dipole-trap array. This simplifies the positioning of the setup relative to the objective and the vacuum chamber. Two auxiliary arrays are created by illuminating a second MLA with two skew laser beams. Their beam path is overlapped with the beam path of the main array before reimaging into the vacuum chamber using a PBS in combination with a half-wave plate in the auxiliary beam paths.

To allow for defect-free assembly of the atoms inside the vacuum chamber, a movable tweezer is used. Based on a two-dimensional AOD, the collimated laser beam is deflected. This deflection is converted into a movable focal spot using an achromatic lens with 60 mm focal length. To reimage the focal spot an achromatic lens with a focal length of 750 mm is used together with the objective to reimage the focal spot into the vacuum chamber. The beam path is overlapped with the array beam paths using a NPBS with 90 % transmission and 10 % reflectance. As the movable tweezer only needs low laser power, these in proportion high losses are acceptable since the absolute losses remain small. To simplify the positioning of the whole setup, a guiding beam is overlapped with all beam paths using a second NPBS with the same properties as the first one. This provides another optical access for later applications. The complete optical setup was assembled offline on two separate laser breadboards attached to each other with tight fittings, which allows for easier transport and reproducible alignment on the experimental table. Furthermore, the offline setup could be optimized using the new objective together with a glass substrate of 6 mm thickness (Edmund Optics 36956) mimicking the vacuum window. Using a microscope objective (Linos G038724000), called analysis objective in the following, with a NA of 0.65 together with a CCD camera, the created trap arrays are analyzed. The use of an analysis objective to directly image the plane inside the vacuum chamber in the offline setup circumvents possible distortion resulting from a non-

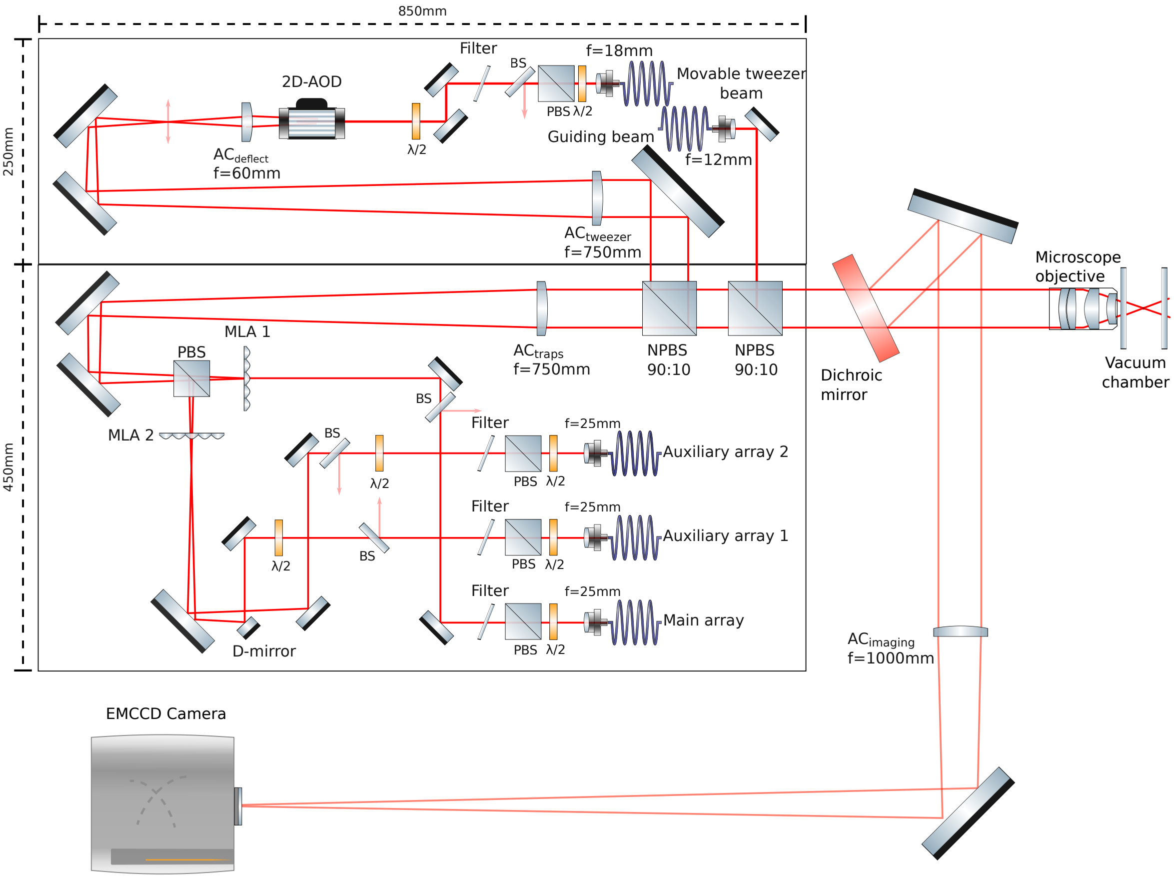

Fig. 5.8.: Setup for three interleaved dipole-trap arrays combined with a movable tweezer. At the top left, the two-piece laser breadboard containing the setup for the movable tweezer and a guiding beam (top) as well as the interleaved dipole-trap arrays (bottom) is shown. On the right and bottom side, the fluorescence imaging beam path as well as part of the vacuum chamber is visible. The reimaging beam path on the other side of the vacuum chamber is not shown. It follows the same setup as shown in Fig. 4.2 but is utilizing an achromatic lens with 750 mm focal length with the new microscope objectives used for the experiments described in this chapter. All beams are intensity stabilized using a beam sampler (BS) coupling out a small fraction of laser light which is focused onto a photodiode (PD) (not shown). AC: achromatic lens; The microscope objective visible in this image is mounted with the TTR-stage as shown in Fig. 5.4 whereas the opposite objective (not shown) uses the goniometer-based mount. Schematic created using [135].

Tab. 5.3.: Measured spot sizes and trap separations (pitch) measured in the offline setup for all three trap arrays. To quantify distortion, the aspect ratio between the long and the short axis of the spots is given. Furthermore, the SSC is given for the deepest trap (see text for explanation). Spot analysis based on [148]; Measurement done during [149].

	Main array	Auxiliary array 1	Auxiliary array 2	Movable tweezer
Average pitch in µm	5.16(1)	5.16(2)	5.17(2)	-
Average larger waist in µm	0.94(3)	1.20(5)	1.12(5)	0.97
Average smaller waist in µm	0.87(3)	0.98(5)	0.95(5)	0.81
Average mean waist in µm	0.90(2)	1.09(7)	1.03(6)	0.89
Average aspect ratio	1.09(5)	1.22(8)	1.19(4)	1.20
SSC deepest trap	0.14	0.21	0.18	0.16
No. of detected spots	726	649	827	1

perfectly aligned second reimaging objective (same as the one used for creating the trap arrays). However, in the real experimental setup the use of an analysis objective is not possible due to its short focal distance. Therefore, the use of two identical microscope objectives on both sides of the vacuum chamber is the only option. The setup of the reimaging path is the same as described in Fig. 4.2 but with an achromatic lens with a focal length of 750 mm. This results in further distortions from a misalignment of the microscope objectives relative to each other making optimization and calibration of the trap arrays in the vacuum chamber setup more difficult and increasing the uncertainty of analyzing the spot structure inside the vacuum chamber.

5.1.3. Achieved spot sizes and discussion of limitations

To quantify the achievable spot size, the offline setup was optimized in the same way as it is possible in the experimental setup: The glass substrate mimicking the vacuum chamber is fixed and we position the microscope objective as well as the array setup relative to the fixed substrate. As only a single laser source was available in the offline setup, all three trap arrays were imaged individually and the normalized intensity was added to create the resulting trap structure as depicted in Fig. 5.9. In the real setup, the beam paths are supplied by trapping lasers 1 and 2 as shown in Fig. 3.9 and beam paths from the same laser use opposite diffraction orders for the single-pass switching-AOM to circumvent low-frequency interference. As only low laser power for a single movable tweezer is needed, the movable tweezer is supplied together with the main array from trapping laser 1. This allows for larger detunings and a total laser power of more than 4 W from a single fiber supplying the main array. The two auxiliary arrays are supplied by the second Ti:Sa system and therefore equally share the available laser power. In the merged figure, individual, dark traps with low or even zero intensity are visible which can be backtracked to single, irremovable dust particles or imperfections on the MLA. To reduce aberrations, the curved surface of the MLA is the first surface to be hit by the trapping laser beam. This results in the focal spot of the microlens being created close to the plane surface of the substrate, such that small imperfections on this surface have a higher effect on the focal spot.

Using [148], the spots of the different trap arrays as well as of the movable tweezer are

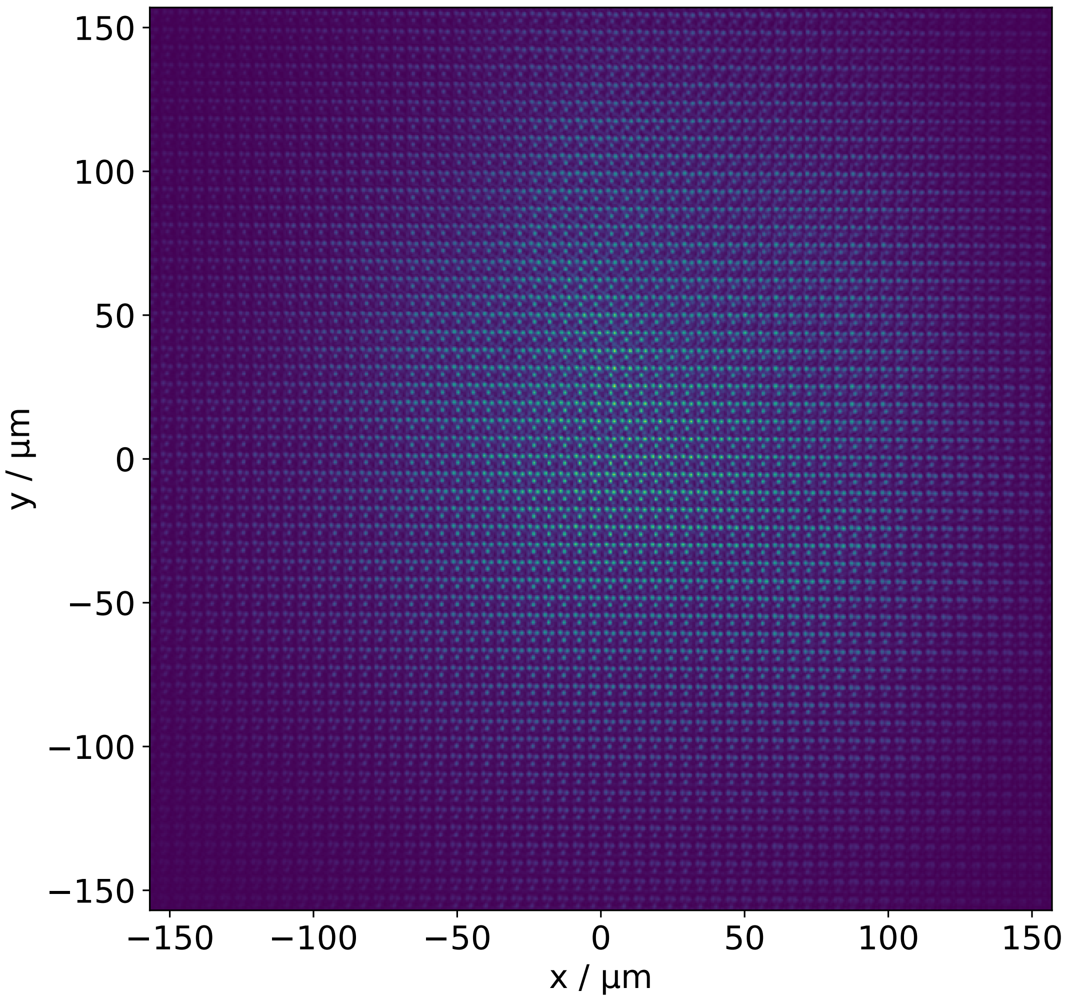

Fig. 5.9.: Overlapped light field of all three dipole-trap arrays making roughly 3500 dipole traps available. Traps are counted if their maximum intensity is at least 35 percent compared to the spot with highest intensity (Main array: 1197 traps; Auxiliary array 1: 1083 traps; Auxiliary array 2: 1229 traps). The image of each individual light field was acquired separately and merged later (see text for details). Single dark traps result from non-removable dust particles or imperfections on the substrate. Image acquired during [149].

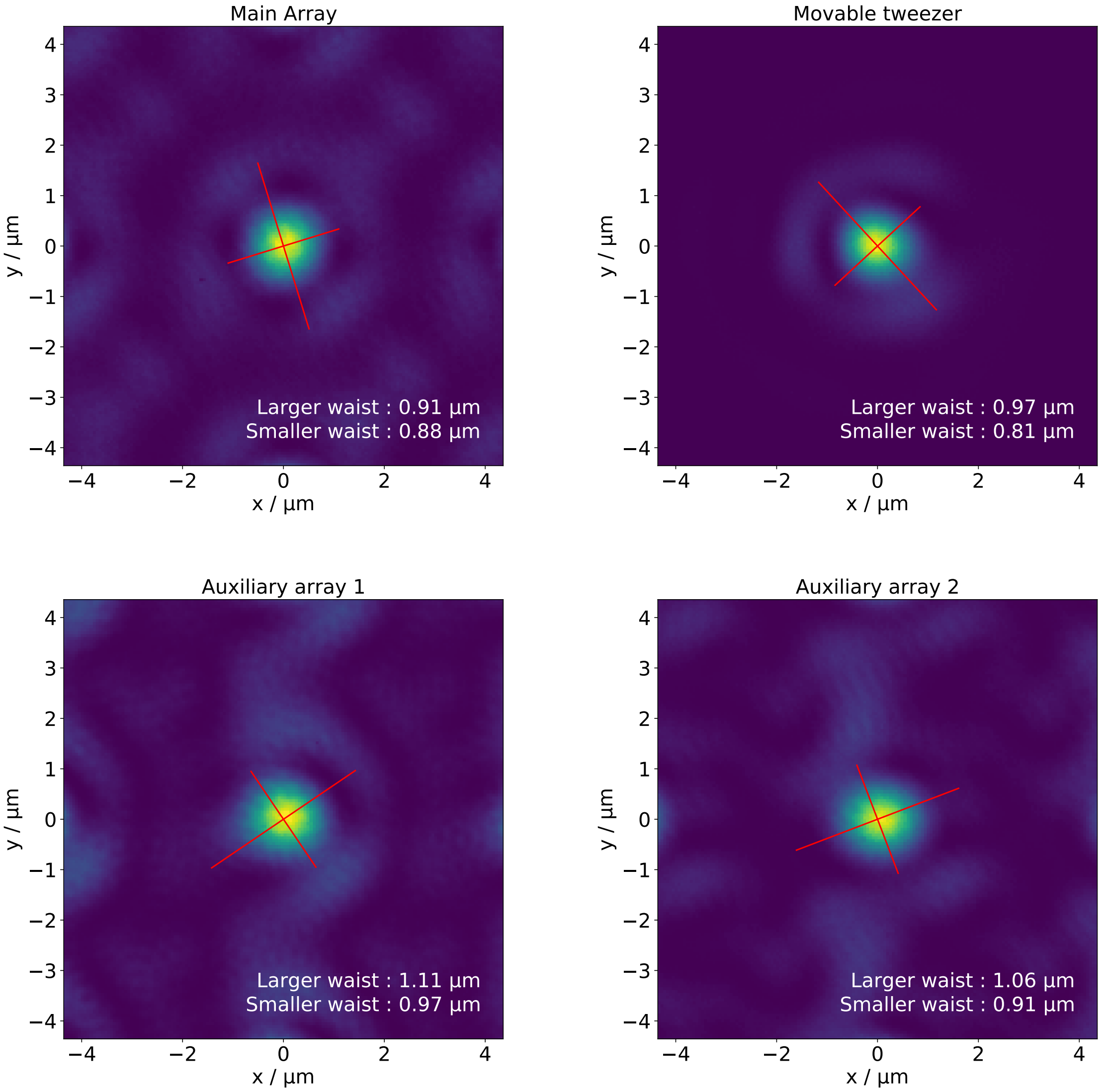

Fig. 5.10.: Image of the spots with highest intensity of each individual array as well as for the movable tweezer. Long and short axis of the spots are visualized by red lines and the corresponding spot waist along this axis is given. Spot analysis based on [148]; Measurement done during [149].

analyzed and the results are given in Tab. 5.3. The spot with highest intensity from each array is shown in Fig. 5.10. For each spot, the long and short axis as well as the corresponding waists are depicted. The main array creates the smallest and most symmetric traps with an average pitch of 5.16(1) µm due to the straight alignment. The measured pitch matches well with the results from the simulation as given in Tab. 5.2. The average spot size is with 0.90(2) µm slightly larger than expected from the simulation which can be caused by aberrations of the system. However, the spot size is in very good agreement with to the best possible spots seen in similar setups [127, 147]. In all setups, the SSC is significantly higher as expected from the simulations and a SSC lower than 0.10 has never been achieved. It is assumed that the increased side structures result from aberrations inside the objective due to variations of the lens surface from the simulated shape or due to slight misalignments of lenses relative to each other, which have not been modeled in the simulation. The spots of the auxiliary arrays show stronger deformations along the x-direction. This increases the average spot size, the aspect ratio as well as the side structures. As expected from the simulation, there is no measurable change in the pitch. The size of the movable tweezer is slightly larger than the spot of the main array and slightly smaller compared to the auxiliary arrays such that it is well suited for sorting atoms within single arrays as well as between arrays. Furthermore, in Tab. 5.3 the number of detected spots is given. Spots are detected by an automatic peak detection algorithm as described in [127] using a threshold value relative to the maximum intensity pixel. If a higher number of spots is detected, this can be an evidence for more traps having a sufficiently high intensity for atom trapping.

During testing and optimizing the setup, the following challenges for aligning became apparent. First of all, it is difficult to simultaneously position the microscope objective relative to the vacuum window and the optical beam relative to the microscope objective which unavoidably results in spot deformations. Therefore, the optical beam path was first aligned perpendicular to the vacuum window and later on the microscope objective is mounted such that the beam axis remains unchanged. With this procedure, a perpendicular alignment of the optical axis of the microscope objective relative to the vacuum window shall be achieved. Furthermore, the tilt of the two auxiliary beams shifts the beam center on the objective by 13.2 mm resulting in a reduction of the transmission from 70 % to 53 % as the laser beam is strongly truncated on one side. Due to this shift, strong Fourier components of the beam are close to the aperture of the microscope objective as shown in Fig. 5.11, such that due to small misalignments additional Fourier components are blocked leading to an increase of the spot size on this axis. Experimentally it has been observed, that a misalignment of 1 mm to 2 mm results in an increase of the spot size by a factor of 20 % to 30 % along the corresponding axis [147]. This underlines the demand for perfect alignment of the optical setup which is best possible with the mount without TTR stage in Fig. 5.4.

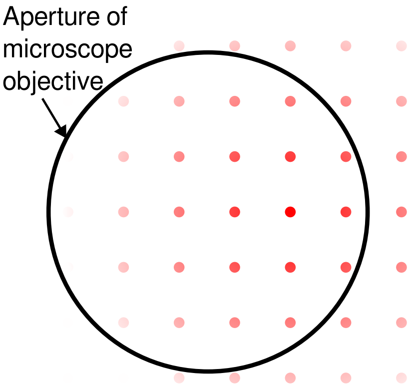

Fig. 5.11.: Schematic illustrating the laser intensity distribution on the microscope objective when illuminating the MLA with a laser beam tilted in horizontal direction with respect to the axis of normal incidence.

This challenge becomes even more evident when reimaging the spot structure inside the vacuum chamber onto a CCD camera. Ideally, the objectives as well as the vacuum windows have to be aligned perfectly to each other which is very challenging in practice. Different alignments of the reimaging objective have led to a significant spread of measured spot sizes behind the vacuum chamber such that these spot size measurements are not trustworthy. It is therefore assumed that the spot size inside the vacuum chamber is, based on our experience in aligning the offline setup, 10 % larger than in the offline setup resulting in an assumed spot size of $w_0 = 1.0(1)$ µm for the main array and the movable tweezer as well as $w_0 = 1.1(1)$ µm for the auxiliary arrays.

5.2. Trapping individual neutral atoms in interleaved trap arrays

The optical setup was then integrated into the experiment and used to characterize the performance in trapping single atoms for each individual array. Furthermore, measurements have been performed to demonstrate the interleaved operation of multiple trap arrays. Finally, the limitations and perspectives of the current setup are discussed.

5.2.1. Characterization of the individual dipole-trap arrays

To characterize the created dipole-trap arrays, several measurements have been performed. At first, the trap frequency as well as the trap depths have been determined to gain further insight into the trapping potential. Furthermore, the atom temperature has been measured using a release-and-recapture technique. The lifetime of the atoms inside the trap has been analyzed and the total number of atoms which can be loaded into a single trap array has been compared between the individual arrays.

Trap frequency

Measuring the optical power of the laser beam at the MLA, in front or behind the vacuum chamber allows to deduce the losses in the optical beam path due to different apertures and anti-reflection coatings. However, calculating the exact laser power illuminating a single microlens and therefrom deducing the trap depths usually results in large uncertainties. It is therefore beneficial to directly measure the trap frequency to deduce quantities such as the trap depth from it. Measuring the trap frequency can be done by resonantly exciting the atoms and detecting the occurring atom loss due to heating [150]. If the excitation frequency equals twice the trap frequency, the atoms are parametrically excited and will be lost. Also for excitation at the resonance frequency itself atom loss is detected. To excite the atoms, the laser power coupled into the trapping-light fiber was intensity modulated. One method was to directly modulate the radio frequency power of the AOM which is usually used for switching the laser on and off. The other method was to modulate the drive frequency of the AOM such that the deflection angle at the AOM changed and the coupling efficiency to the fiber was modulated. The second method was necessary for high modulation frequencies above 100 kHz as no synthesizer with amplitude modulation was available for this frequency range. Both methods resulted in the same measured trap frequencies within the uncertainty of the measurement. In the following, data from a typical measurement of the radial trap frequency of the main array will be introduced and the results for all trap frequencies from the different arrays will be summarized.

Figure 5.12 shows the measurement of the radial trap frequency for the main array in the range were the principle radial trap frequency is expected. The relative atom number is plotted versus the excitation frequency in the range from 40 kHz to 100 kHz. As the laser power within the trap array is radially symmetric due to the Gaussian beam profile of the

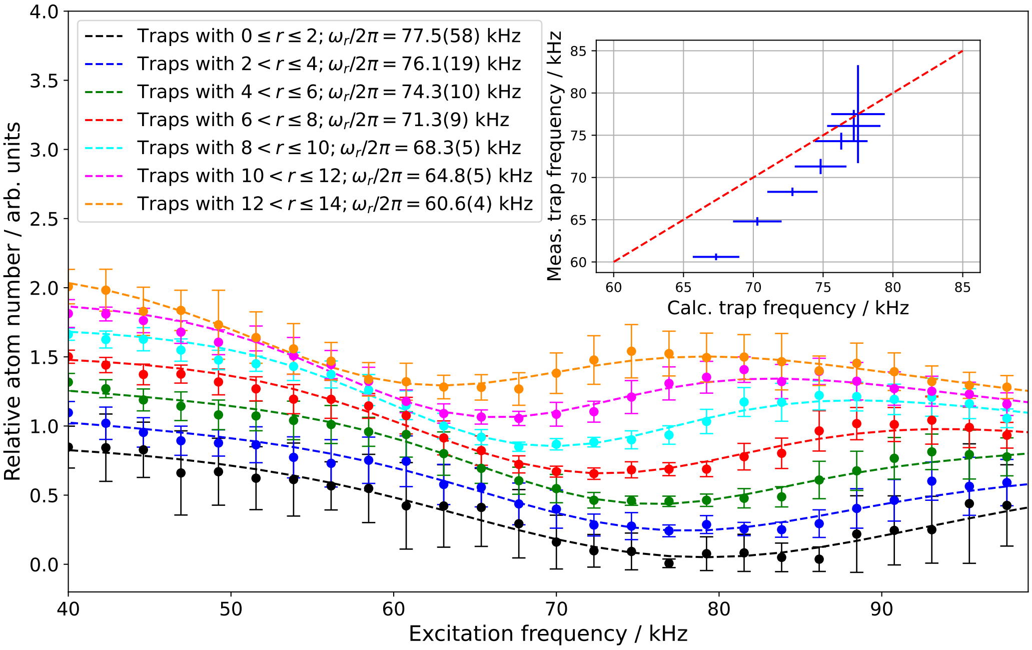

Fig. 5.12.: Measurement of the relative number of remaining atoms after parametric heating of the atoms at a certain excitation frequency. The atom loss is evaluated for rings of traps around the center of the trap array. The corresponding results are plotted with an increasing shift along the y-axis for better visibility. Using the approximation of the data points to the sum of two Gaussian distributions (principle and doubled trap frequency) the radial trap frequency ω_{r} is determined. **Inset:** Measured trap frequency for different r plotted versus the calculated radial trap frequency normalized to the radial trap frequency of the deepest trap ($\omega_{\mathrm{r}\leq 2} = 2\pi \times 77.5(58)\,\mathrm{kHz}$) and the Gaussian intensity distribution of the laser beam incident on the MLA.

laser beam illuminating the microlenses, the atom loss has been evaluated for rings of traps with a width of two trap pitches and the resulting relative atom numbers have been plotted with an increasing offset along the y-axis for better visibility. All curves are evaluated by approximating the sum of two Gaussian distributions to the data points to find the minimum of the principle trap frequency in the range between 60 kHz and 80 kHz and also take into account the doubled trap frequency in the range between 120 kHz and 160 kHz. Looking at the lowermost curve ($0 \leq r \leq 2$) showing the results for the innermost traps, a minimum at 77.5(58) kHz is found for the number of remaining atoms. For traps further away from the center, the trap frequency is lower as the incident laser power illuminating the microlens and correspondingly the trap depth of the trap is reduced. For the uppermost data curves (i.e. largest distance from the center) the second minimum corresponding to the doubled trap frequency is visible for frequencies above 90 kHz. Based on the beam radius of the laser beam illuminating the microlens array, the expected reduction of the trap frequency can be compared to the measured trap frequency. The result is shown in the inset of Fig. 5.12 where the measured trap frequency is plotted against the expected (calculated) radially dependent trap frequency. To calculate the expected radial trap frequency, the measured trap frequency ω_{r} is taken to determine the trap depth of the innermost traps ($0 \leq r \leq 2$) based on Eq. (2.42). Calculating the radial-symmetric reduction of the trap depth, the expected trap frequency of the traps farther away from the center is determined.

It can be seen that the measured trap frequencies are lower than expected from the radial distance of these traps to the beam center. One possible explanation could be that due to a relatively high atom temperature the harmonic approximation applied in Eq. (2.42) is not valid. To check this assumption, the average temperature of the atoms has been determined with measurements described in the next section.

Based on several of these measurements for a frequency range from 1 kHz to 500 kHz the trap frequencies for all arrays as well as the movable tweezer were measured and are summarized in Tab. 5.4. The laser power $P_{0,\mathrm{trap}}$ of a single trap inside the vacuum chamber and the detuning used for the auxiliary arrays were different to those of the main array resulting in a lower trap depth during this measurement. Based on the laser power used and the measured losses at optical surfaces, the expected trap depth of the deepest individual trap potential (innermost trap) is calculated and given as $U_{0,\mathrm{calc}}/k_{\mathrm{B}}$. It is not taking into account that due to diffraction not the full laser power of the single focus is concentrated in the inner focal spot meaning that laser power in side structures does not contribute to the trap depths. Furthermore, the measured radial and longitudinal trap frequencies are given. Assuming a spot size of $w_0 = 1.0(1)$ µm (main array and movable tweezer) or $w_0 = 1.1(1)$ µm (auxiliary arrays), the resulting trap depth was calculated based on Eq. (2.42). Using the corresponding radial trap frequency and Eq. (2.51), the expected longitudinal trap frequency resulting from illumination with a plane wave can be calculated and is given in the last column of Tab. 5.4. The results underline, that for a correct calculation of the longitudinal trap frequency, the illumination with a plane wave has to be taken into account. Comparing the calculated trap depth with the trap depth derived from the trap frequency measurement, it is obvious that neglecting the real intensity distribution of the focal spot leads to an overestimation of the trap depth. For a SSC of roughly 0.2 the ratio of laser power concentrated in the focal spot compared to the total laser power illuminating one lens was determined for several measured spots to be roughly 0.6. This means that only 60 % of the laser power inside the vacuum chamber related to a single microlens contribute to the trap depth, not taking any losses due to apertures or optical coatings into account. This matches relatively well to the results given in Tab. 5.4 where the calculated trap depth is determined from the estimated total laser power inside the vacuum chamber of the microlens, hereby taking all optical losses but not the real intensity distribution in the focal plane into account. For the movable tweezer however, the measured trap depth is only 0.4 of the expected value which indicates stronger aberrations

Tab. 5.4.: Measured radial and longitudinal trap frequencies for all arrays as well as for the movable tweezer. Based on the measured radial trap frequency and assuming $w_0 = 1.0(1)$ µm for the main array and the movable tweezer as well as $w_0 = 1.1(1)$ µm for the auxiliary arrays, the trap depth is calculated. Using the radial frequency and the derived trap depth, the longitudinal trap frequency is deduced assuming a plane wave illumination of the microlens.

	λ in nm	$P_{0,\mathrm{trap}}$ in µW	$U_{0,\mathrm{calc}}/k_{\mathrm{B}}$ in µK	$U_{0,\mathrm{meas}}/k_{\mathrm{B}}$ in kHz	$\omega_{\mathrm{r,meas}}/2\pi$ in kHz	$\omega_{\mathrm{z,meas}}/2\pi$ in µK	$\omega_{\mathrm{z,calc}}/2\pi$ in kHz
Main	798	350	910	610(75)	77.5(58)	8.3(2)	8.0(17)
Aux. 1	796.5	195	735	390(35)	56.6(14)	7.4(2)	5.8(12)
Aux. 2	796.5	190	725	375(35)	55.4(15)	6.3(3)	5.7(12)
Tweezer	798	340	895	345(35)	58.6(8)	6.5(1)	6.1(12)

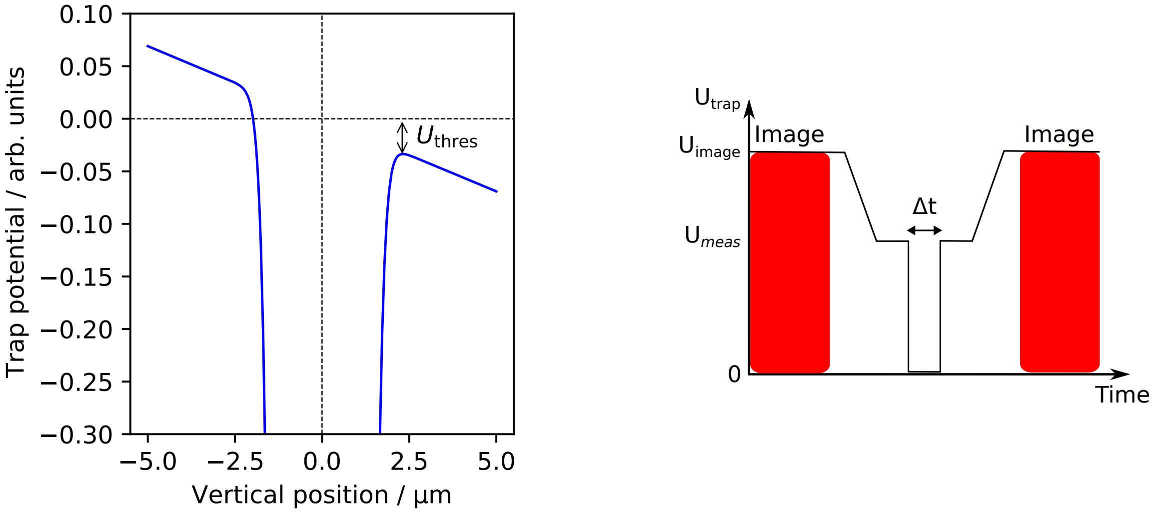

Fig. 5.13.: **Left:** Trapping potential modified due to gravity. **Right:** Time sequence for determining the average temperature of the atoms using a release-and-recapture measurement. The trap depth for imaging is given by U_{image} whereas the trap depth at which the atom temperature is determined is given by U_{meas}. a.u.: arbitrary units.

of the focal spot. A summary of the optical losses along the laser beam path can be found in appendix E.

Atom temperature

The knowledge of the trap parameters such as the trap frequency, the trap depth, and the trap size are the basis for the determination of the atom temperature inside the traps. For single atoms, the temperature is associated with the kinetic energy of an individual atom averaged over several realizations. To determine the temperature of single atoms in a trap array, a simple technique has been demonstrated in [151] which is based on turning off the trap for a defined duration Δt as shown in Fig. 5.13. Depending on the energy distribution, e.g. the average temperature of the atom in the trap, the recapture rate for a given Δt will change. In simple terms: The slower the atom, the longer the trap can be turned off to still recapture the atom.

For a quantitative analysis, the motion of the atom has to be modeled. As derived in [151], the thermal motion of the trapped atom follows a Maxwell-Boltzmann distribution in position and velocity space. For a given temperature T and an elongated cylindrically symmetric, harmonic trap, the spreads in position (radial ($r = \sqrt{x^2 + y^2}$) and longitudinal (z) direction) and velocity space are given by the standard deviations

$$\Delta r = \sqrt{\frac{k_{\mathrm{B}}T}{m\omega_{\mathrm{r}}^2}} \qquad \Delta z = \sqrt{\frac{k_{\mathrm{B}}T}{m\omega_{\mathrm{z}}^2}} \qquad \Delta v = \sqrt{\frac{k_{\mathrm{B}}T}{m}} \tag{5.6}$$

with radial and longitudinal trap frequencies ω_{r} and ω_{z}. This motion is modeled using a Monte Carlo simulation with random start positions $(x_{\mathrm{i}}, y_{\mathrm{i}}, z_{\mathrm{i}})$ and initial velocities $(v_{\mathrm{x,i}}, v_{\mathrm{y,i}}, v_{\mathrm{z,i}})$. When the trap is turned off, the atom propagates under the influence of gravity, which acts along one of the radial trap axes as it is the case in the experiment. After the time Δt, the trap is turned on again and the atom is recaptured if the total energy of the atom at the new

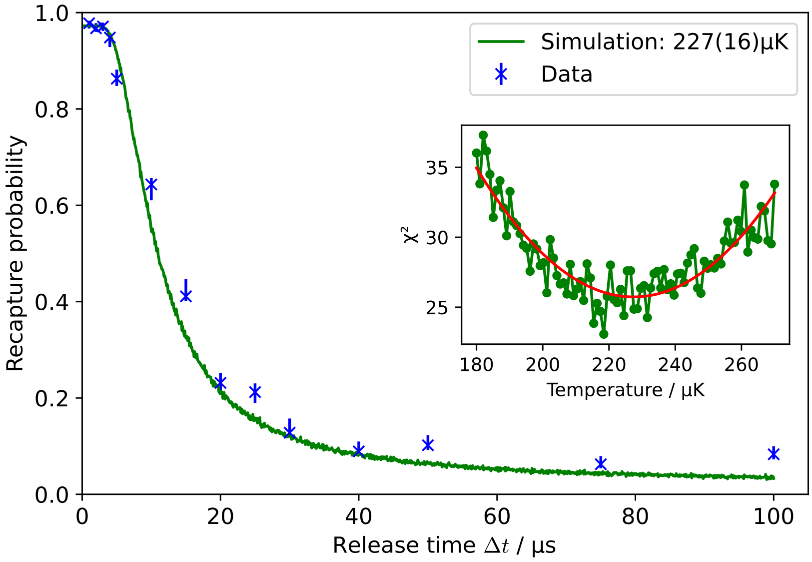

Fig. 5.14.: Recapture probability for the innermost traps with radial distance $0 \leq r \leq 2$ to the center of the trap array. The measurement data (blue data points) are shown together with the best matching Monte Carlo simulation revealing an atom temperature of $227(15)$ µK. The best matching simulation is found by minimizing the least-square deviation χ^2 using a harmonic approximation as shown in the inset.

position is smaller than the depth of the trap potential (see Fig. 5.13 for the gravity-modified potential with reduced threshold energy U_{thres}). To minimize fluctuations due to the Monte Carlo simulation, N=10000 initial starting situations have been used.

This measurement technique will result in a relative atom loss depending on the duration while the trap is switched off as shown in Fig. 5.14. The blue data points show the measured recapture probability in relation to the time Δt. In order to determine the best matching temperature based on the model described above, several Monte Carlo simulations for different average temperatures of the atoms are performed and the resulting recapture probability is compared to the measurement by calculating the least-square deviation χ^2 as shown in the inset of Fig. 5.14. Minimizing χ^2 yields an average temperature of $227(15)$ µK for which the modeled recapture probability according to the Monte Carlo simulation is shown as green curve in Fig. 5.14. The results are given for the innermost traps of the array with radius $0 \leq r \leq 2$ and a trap depth of $U_{\text{meas}}/k_{\text{B}} = 550(70)$ µK. Evaluating the temperature radial-symmetrically with the same radii used in the previous section reveals that the temperature in traps further away from the center decreases as shown in Fig. 5.15. The average ratio between the atom temperature and the trap depth is 0.41(5) which is high compared to other measurements where ratios around 0.2 have been determined [113]. Temperature measurements in the two auxiliary arrays have given the same results as for the main array within the uncertainty of the measurement. This indicates that the cooling process of the atoms inside the dipole traps has to be improved and possible sources of atom heating have to be reduced. A simple solution for more homogeneous cooling in all phases of the experiment would be to use diagonal MOT-beams at 795 nm also during the imaging phase. This enables cooling in all dimensions during imaging while circumventing stray light on the EMCCD camera.

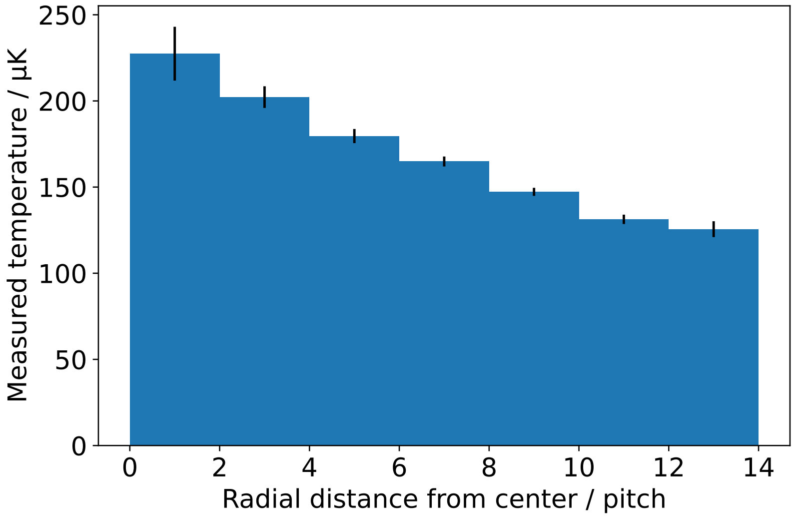

Fig. 5.15.: Dependence of the atom temperature of single atoms in the main array as a function of the trap position relative to the central trap. Traps are evaluated in rings with a width of two trap pitches and the results are shown as bars between the corresponding distances to the central trap.

Time constant for atom loss in the dipole-trap arrays

Due to heating effects as described in section 2.1.3, the atom temperature is related to the time constant for atom loss in a dipole trap: The lower the initial atom temperature relative to the potential depth and the lower the heating rate, the longer the time constant for atom loss. In order to analyze the trapping lifetime of the atoms in the different arrays, two types of measurements have been performed. Type 1 are measurements were the waiting time t_{wait} between the images is fixed for a single measurement but a series of images is taken to determine the atom loss for long time scales while repeatedly detecting the trap occupation and thereby cooling the atoms. For Type-2-measurements, two images with a variable temporal separation t_{wait} between their acquisition are compared and the atom loss relative to t_{wait} is determined. Several measurements of type 2 with different t_{wait} are performed to determine the long-term trapping lifetime of the atoms.

In Fig. 5.16 several type 1 measurements for the main array are shown. For short waiting times t_{wait}, the ratio between waiting time and imaging time (50 ms) is 1 resulting in a long trapping lifetime as during imaging the atoms are cooled. Assuming that heating effects are compensated by repeatedly cooling the atoms, the remaining losses are due to background gas collisions with room temperature atoms. The lifetime for this process is given by Eq. (2.28) and for a vacuum pressure of $1.0(5)\times10^{-9}$ mbar as given in section 3.1 is determined to be $\tau_{\text{back}} = 6(3)$ s due to the large uncertainty in the vacuum pressure. Comparing the theoretical estimation with the measured results, the assumption of the value for the vacuum pressure is plausible.

For longer waiting times t_{wait}, the time constant for atom loss decreases. This is especially apparent for measurements of type 2. Figure 5.17 shows the type-2-measurement for the main array. The atom survival probability is depicted on a log-scale versus the total cycle time $t_{\text{cycle}} = t_{\text{wait}} + t_{\text{img}}$ including the wait time t_{wait} and the imaging time t_{img} for one image.

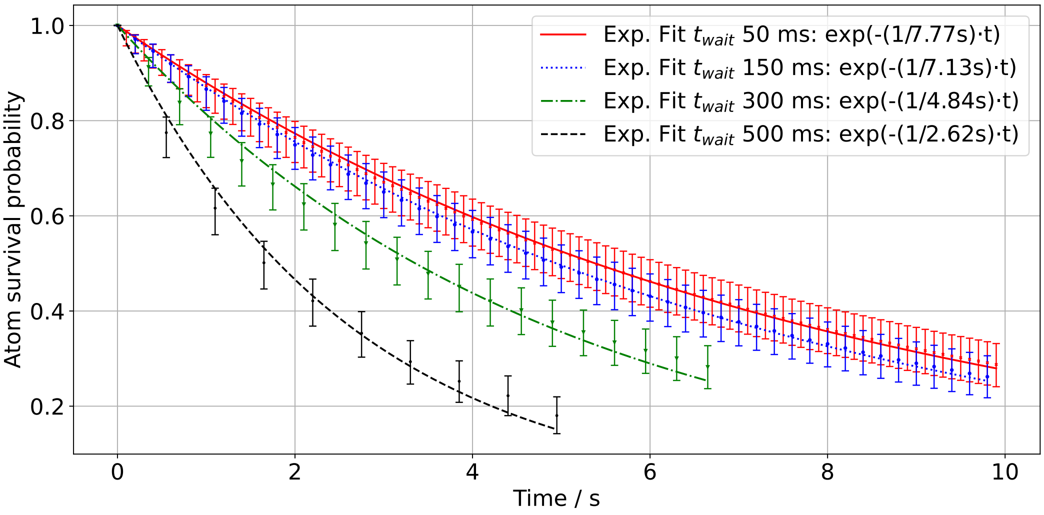

Fig. 5.16.: Type 1 measurements of the time constant for atom loss based on an image series with constant waiting time between subsequent images. To each measurement, an exponential decay curve is approximated to determine the 1/e time constant for atom loss.

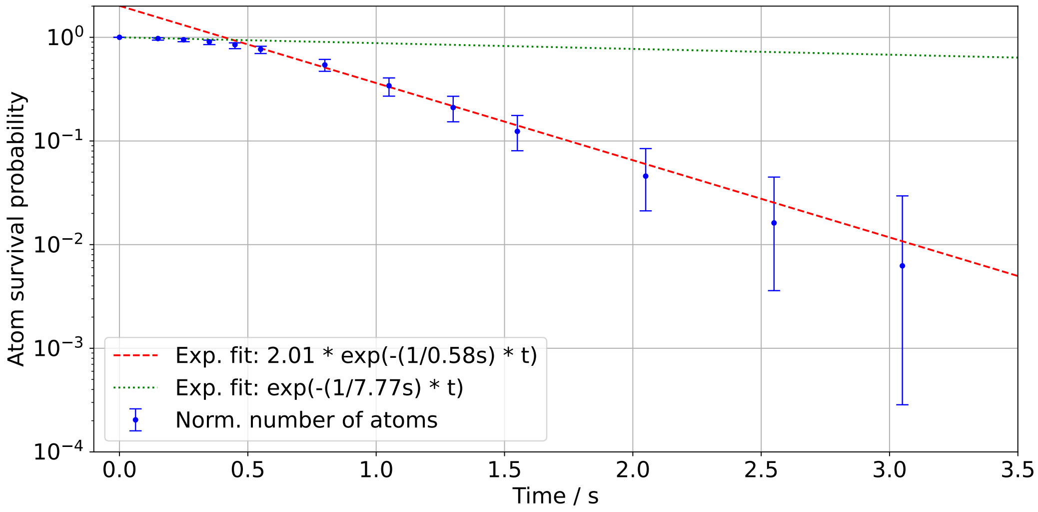

Fig. 5.17.: Type 2 measurement of the time constant for atom loss based on two images with variable waiting time between both images. The last seven data points are approximated with an exponential decay curve to determine the decay constant without subsequent imaging for short wait times, the exponential decay as determined for $t_{\mathrm{wait}} = 100\,\mathrm{ms}$ in Fig. 5.16 is shown.

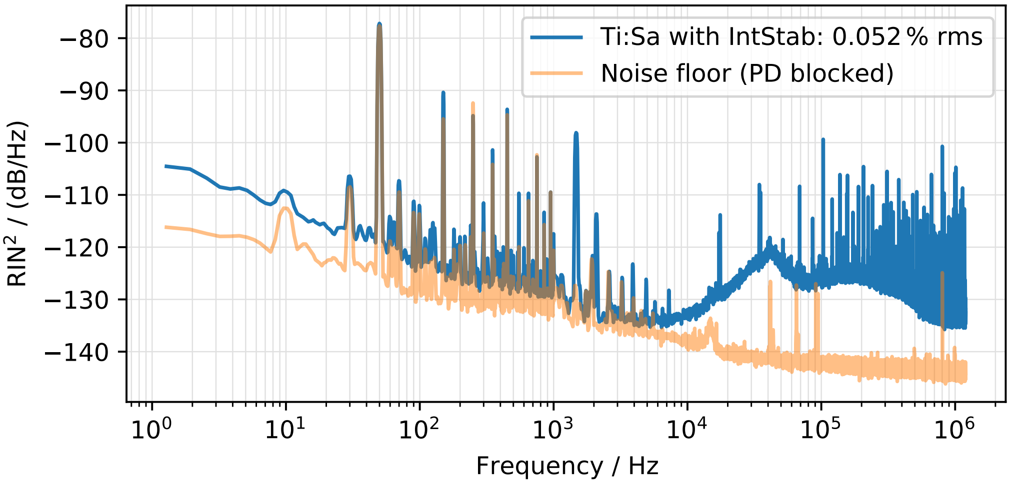

Fig. 5.18.: Relative intensity noise of the main-array laser beam used for dipole trapping with intensity stabilization (Ti:Sa with SN: 221330). Measurement adopted with permission from Tilman Preuschoff.

Tab. 5.5.: Time constants for atom loss in dipole traps with cooling due to repeated imaging (τ_0) and without cooling (τ_1). (*) For auxiliary array 1 a second measurement at 798 nm has been performed where no corresponding trap frequency measurement is available. The laser power was therefore chosen such that the calculated trap depth is equal within the range of the measurement uncertainty.

	λ in nm	$U_{0,\text{meas}}/k_B$ in µK	τ_0 in s	τ_1 in s
Main array	798	610(75)	7.8	0.58
Auxiliary array 1	796.5	390(35)	2.8	0.16
Auxiliary array 1	798	390(35)*	10	0.43
Auxiliary array 2	796.5	375(35)	3.7	0.19

As revealed in the measurement of type 1, the trapping lifetime decreases with increasing wait time. However, due to the logarithmic scale it is apparent, that for long enough t_wait, the trapping lifetime is given by the time constant τ_1 determined by approximating the last seven data points with an exponential decay function $N(t) = \exp\left(t_\text{cycle}/\tau_\text{i}\right)$. The trapping lifetime for short $t_\text{wait} = 100\,\text{ms}$ was determined with the type 1 measurement and the corresponding exponential decay rate is depicted as a green, dotted line with time constant τ_0. The time constants for all arrays are summarized in Tab. 5.5 for measurements with different detuning.

For long waiting times, heating mechanisms due to technical noise and photon recoil heating have to be added to the heating rate due to background gas collisions. Based on Eq. (2.27) the expected heating rate due to technical noise is estimated for the radial axis assuming a constant power spectral intensity noise $S(2\nu) = -120\,\text{dB/Hz}$ based on the measurement shown in Fig. 5.18. Heating along the longitudinal axis, where a weak trapping results in a small trap frequency ν, is neglected as $S(2\nu) < -130\,\text{dB/Hz}$ and following Eq. (2.27) $\Gamma_\text{noise} \propto \nu^2$.

Using $w_\mathrm{r} = 1.0\,\mu\mathrm{m}$, $U_0/k_\mathrm{B} = 550\,\mu\mathrm{K}$ and $E_\mathrm{init}/k_\mathrm{B} = 250\,\mu\mathrm{K}$ the time constant resulting from technical noise is estimated to be $\tau_\mathrm{noise} \approx 15\,\mathrm{s}$. It has to be noted that effects such as heating due to pointing instabilities have not been considered here [61].

For photon recoil heating, the time constant, given by Eq. (2.24), is approximated to $\tau_\mathrm{rec} \approx 1.7\,\mathrm{s}$ using a calculated scattering rate $\Gamma_\mathrm{SC} = 230\,\mathrm{s}^{-1}$ from the detuning and measured trap depth given for the main array in Tab. 5.4. Adding the effect of all heating mechanisms together, results in a total time constant $\tau_\mathrm{tot} \approx 1.2\,\mathrm{s}$ for the main array which is a factor of two larger than the measurement. As for many of these factors, several estimations and approximations have been used, a precise quantitative analysis is beyond the scope of this thesis. However, the estimate reveals which factor contributes most to the current heating. It is therefore obvious that the photon scattering rate either has to be reduced or improved cooling has to be established to reduce atom loss. First tests using continuous cooling have not been successful and pulsed cooling as used during alternating waiting and imaging phases as used for the measurements in this section has been best. A reason for this effect can be that due to continuous cooling, a dilute molasses created from slow atoms from the source or lost from the dipole traps is always present in the surrounding of the trap array. If any of these atoms are recaptured in an occupied trap, light-assisted collisions will result in atom loss as described in [152].

Loading efficiency and total atom number

The last but not least important measure to characterize the different trap arrays is their capability to trap atoms. This can be quantified in terms of the loading efficiency for the individual traps or in terms of the total atom number that can be trapped within the trap structure generated by a single MLA. As the number of illuminated traps for all three arrays is almost identical due to the equal beam sizes illuminating the MLAs, both measures are comparable in the context of this setup. In preparation for simultaneous loading into interleaved trap arrays, the loading efficiency was determined for all three MLAs using laser power parameters such that all MLAs can be operated in parallel. This requires a trapping wavelength of 796.5 nm for the auxiliary arrays while a trapping wavelength of 798 nm can be used for the main array. Laser powers are chosen as for the above mentioned measurements. For each array a grid of 48×48 trapping sites is evaluated containing all traps capable of trapping atoms. For the inner trap region with a radius of 16 trap pitches, the histograms are evaluated, as described in section 3.4.2, using a Gaussian approximation to determine the optimal threshold value to distinguish between an occupied and an unoccupied trap. For traps outside of this area, a fixed threshold is chosen. Based on the threshold value, the loading efficiencies for all traps are determined and depicted in the top row of Fig. 5.19 where each pixel corresponds to a single trap and the color represents the loading efficiency. As expected from theory, there is a plateau in the center of the array where traps are deep enough to achieve a loading efficiency of 0.5 to 0.6. Outside of this plateau, the trap depth is too low for efficient atom loading such that the loading efficiency decreases.

From the Gaussian approximation and the corresponding threshold in the inner traps, the fidelity can be evaluated in traps where, due to higher laser intensities, atoms in intermediate structures cause a higher background signal. The determined fidelity gives a lower bound for the whole array, as in outer traps the zero-atom and one-atom peaks are further separated which increases the fidelity. The bottom row of Fig. 5.19 shows the distribution of the fidelity for all three arrays. Again, each pixel of the image corresponds to one trapping site and the color represents the associated fidelity. A similar radial-symmetric behavior as for the loading

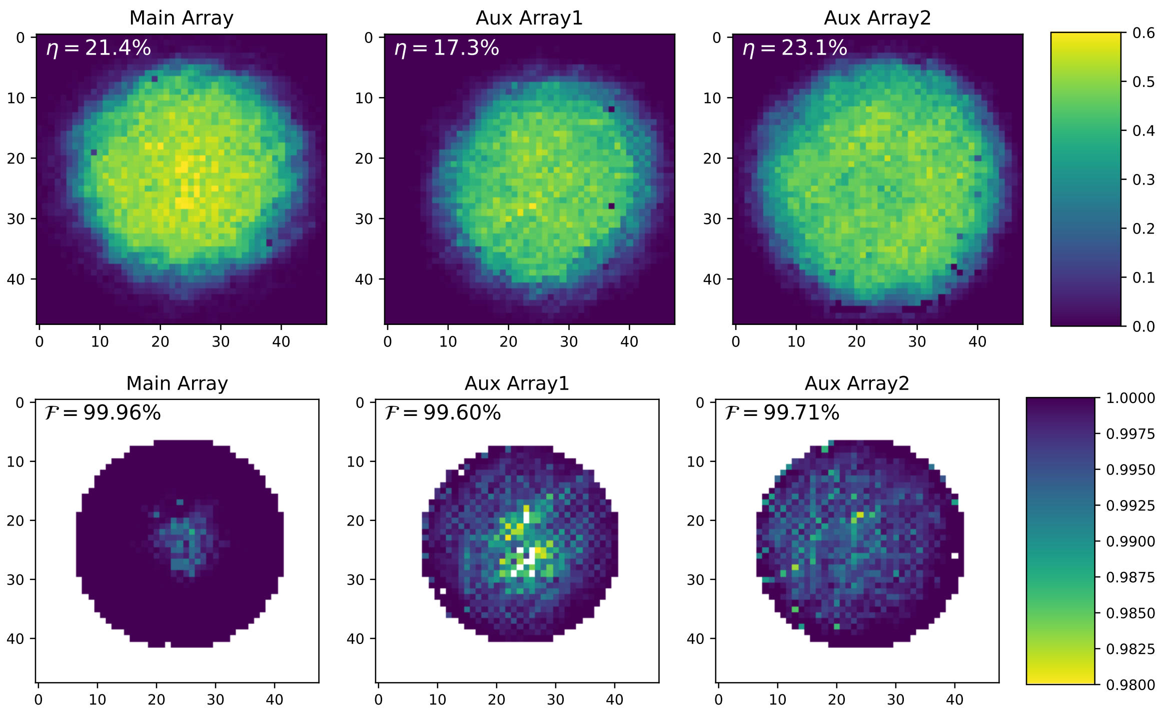

Fig. 5.19.: Load efficiency η (top) and detection fidelity $\mathcal{F}$ (bottom) of the three arrays in comparison evaluated on 48×48 sites for all three MLA. The fidelity is only evaluated in the center where zero- and one-atom peaks can robustly be approximated by a Gaussian distribution.

efficiency is found for the fidelity which is adversely influenced from high potential depths as explained above.

The data is based on 400 experimental repetitions such that, based on the threshold data determined from all shots, the atom number in each individual shot is determined. The average atom number as well as its standard deviation are given in Tab. 5.6 together with a summary of the loading efficiencies and the fidelities. From the distribution of the loading efficiency in Fig. 5.19 it can be seen that the auxiliary array 1 has a smaller area were atoms are efficiently trapped. This could be compensated by the use of more laser power. However, increasing the laser power is still not possible in the case of this array as the side structures in the center of the array get so deep that atoms can be trapped. This results in atoms at intermediate positions and an increased background signal which is detrimental for interleaved trapping with several arrays. The main array as well as the auxiliary array 2 have a more homogeneous loading-efficiency distribution and a larger area were atoms are trapped. The auxiliary array in this measurement has an even wider plateau than the main array which allows to trap more atoms. However, comparing the fidelity distribution of the main array with the ones from the auxiliary arrays, it is also apparent that the background signal, which decreases the fidelity of single-atom detection, is in these measurements better for the main array allowing to increase the used laser power.

Based on these results, it was tested, if two or even three arrays can be used simultaneously to increase the number of trapped atoms. It was ascertained that the trap structure of auxiliary array 1 is not good enough for interleaved trapping. Using two arrays adds up the side structures such that atom trapping in intermediate structures happens more frequently than with a single

Tab. 5.6.: Average atom number, loading efficiency, as well as detection fidelity for the three arrays used with similar trap depths.

	Atom number	Loading Efficiency (48×48)	Fidelity
Main array	499(22)	21.4 %	99.96 %
Auxiliary array 1	400(43)	17.3 %	99.60 %
Auxiliary array 2	538(39)	23.1 %	99.71 %

array. Therefore, the experimental parameters were improved to use the main array together with auxiliary array 2. This meant in addition that auxiliary array 2 was the only array supplied by the second Ti:Sa laser system.

5.2.2. Characterization of interleaved trapping

Using one laser for every array allows for increasing the detuning for auxiliary array 2 by using a trapping wavelength of 798 nm. Furthermore, several experimental parameters such as the dispenser current and the laser power as well as the timings for different phases of the loading cycle were slightly optimized to achieve optimal loading while ensuring good discrimination between zero- and one-atom events. The dispenser current is set to 3.5 A and a loading time of 10 s is used to start with an atom number of roughly $1.2{\times}10^5$ atoms in the MOT (see Fig. 3.11).The maximal central trap depth for the main array as well as for the auxiliary array was slightly reduced. Based on the laser power, the calculated trap depths are $U_{0,\mathrm{calc,main}}/k_\mathrm{B} = 810\,\mu\mathrm{K}$ and $U_{0,\mathrm{calc,aux2}}/k_\mathrm{B} = 632\,\mu\mathrm{K}$ and following the trap frequency

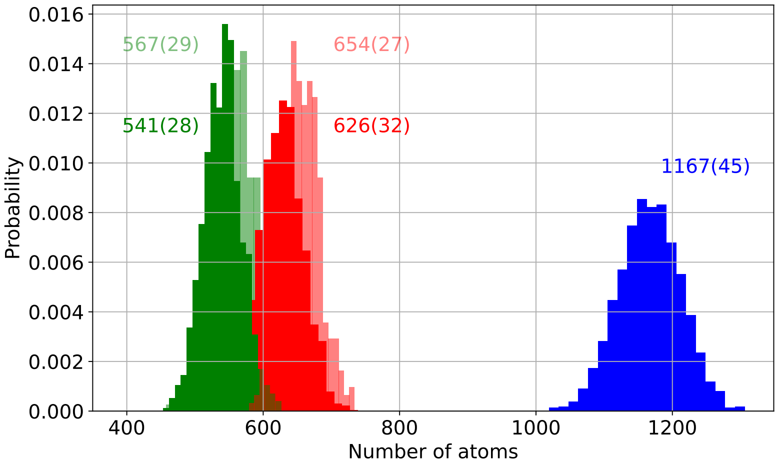

Fig. 5.20.: Histogram of atom number probability of a single shot. The light histograms show the atom number distribution when using only the main array (red) or only the auxiliary array 2 (green). The dark histograms show the atom number distribution for interleaved trapping. Red: Only the main array traps are evaluated; Green: Only the auxiliary array 2 traps are evaluated; Blue: All traps are evaluated. Data represents the measurement for highest atom numbers as described in section 5.2.2.

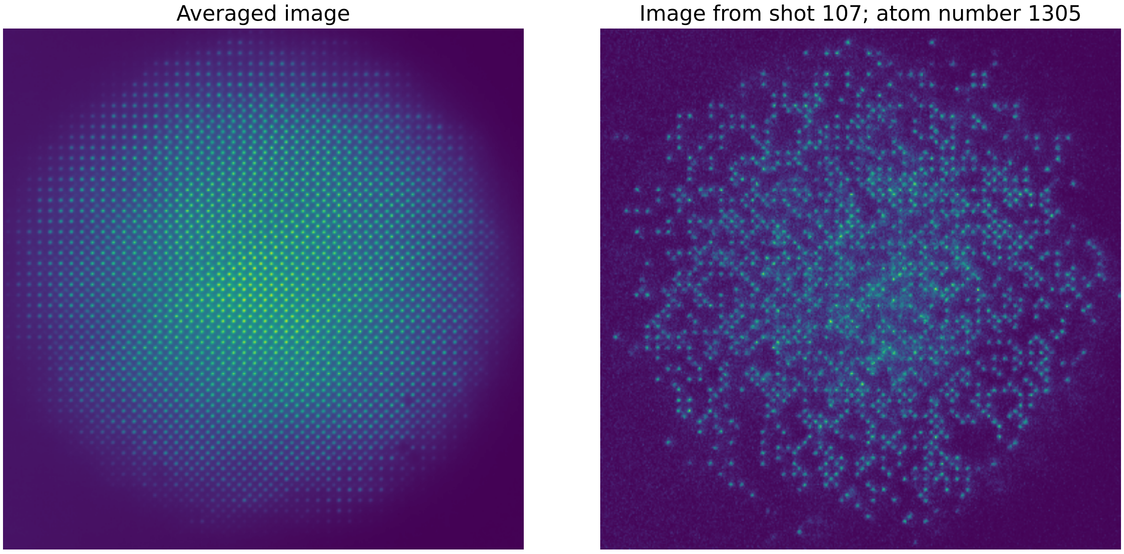

Fig. 5.21.: **Left:** Averaged fluorescence image of the interleaved trap structure. **Right:** Fluorescence image of a single shot with the highest number of detected individual atoms.

measurements as described in section 5.2.1 the corresponding measured trap frequencies are $U_{0,\mathrm{meas,main}}/k_\mathrm{B} = 542(55)$ µK and $U_{0,\mathrm{meas,aux2}}/k_\mathrm{B} = 335(35)$ µK. Furthermore, the cleaning of the Talbot planes as well as the intermediate structures is optimized and reduced in time such that less correctly trapped atoms are lost.

With these settings, it has been possible to trap 1167(45) atoms on average in an interleaved setting of the main array and auxiliary array 2 for an experimental cycle with 2000 executions. In the main array 626(32) atoms are trapped whereas 541(28) atoms are trapped in auxiliary array 2 showing that especially the main array offered further potential in increasing the atom number. Figure 5.20 shows the histograms of both arrays (Main array: red; Auxiliary array 2: green) as well as the histogram of the total atom number (blue) in dark colors. The corresponding histogram when loading atoms only into a single array (the other array being turned off) is shown in light colors. Trapping 654(27) atoms in the main array and 567(29) atoms in the auxiliary array shows that a slight improvement compared to the measurements in the previous section was possible for the auxiliary array while a significant improvement of more than 100 atoms was possible for the main array. Furthermore, the increase in the atom number as compared to the simultaneous loading is roughly 5 %. The reason probably is that the atom density for interleaved trapping is a bit too low and that neighboring traps compete for atoms.

In Fig. 5.21, the averaged fluorescence signal as well as the fluorescence signal of a single shot are depicted. In the outer edge of the trapping area the averaged fluorescence image shows a few dark traps resulting from dust or imperfections on the MLA substrate.

5.2.3. Limitations and perspectives of the current setup

The results presented in the previous sections show the extreme capability of microlens-based dipole-trap potentials in terms of scalability. The robust structure and easy setup of the microlens reimaging enables structures of several thousand trapping sites with high quality. Increasing the number of trapped atoms above 1000 also reveals the limitations of the current setup on the way to trap several thousand individual atoms which shall be discussed together with the next step following the presented results: Sorting the atoms.

Towards several thousand individual trapped atoms

The current setup revealed already in its offline testing phase an intrinsic limitation due to the angled beams used to illuminate the MLA for the auxiliary arrays. This makes beam alignment challenging and error-prone resulting in one array which cannot be used in combination with the others. For the scope of testing the consequences in a real experiment it was desired to test how well beams with non-normal incidence can be handled and due to the multitude of beams available, it would have been easy to rearrange the setup to just use two straight beams if both auxiliary arrays would have been non-optimal. For future setups the deviation from perpendicular incidence should however be reduced for easier alignment. This can either be done by using other Talbot planes or by using two straight beams directly as two interleaved arrays already allow for very small trap separations and due to the achievable spot size an even further reduction of the trap separation is questionable. Straight alignment would also facilitate the positioning of the objective and thereby improving the imaging quality.

The trap frequency measurements showed that the atoms are only weakly confined along the z-axis. For atom sorting as well as for coherent excitation of atoms into the Rydberg state this is disadvantageous. Due to their strong motion along the longitudinal axis of the dipole traps, the atoms sense different light intensities depending on their exact position in space resulting, for example, in a variation of the Rabi frequency for excitation processes or a reduced transport efficiency for movable tweezer transport. This can be circumvented by confining the atoms along the z-axis using a one-dimensional optical lattice created by two angled beams as shown in Fig. 5.22. Using a movable mirror M1, the beam position relative to the PBS can be tuned, resulting in a variable beam separation d. The lattice spacing is then given by $s \approx \lambda \cdot f/d$.

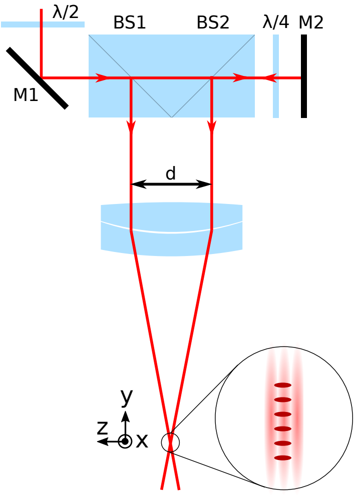

Fig. 5.22.: Proposed setup for spatial confinement of the atoms along the longitudinal direction (z-direction) of the dipole trap array. Idea based on [153].

The biggest limitation to increase the number of trapped atoms right away is the Gaussian beam profile of the laser beam illuminating the MLAs. As demonstrated in [114] it is important to equalize the trapping potential as far as possible to achieve optimal loading efficiencies over the whole array. In the case of microlenses, this can be done by reducing the intensity of the inner traps using a DMD as shown in chapter 4 resulting in a high loss of laser power as excess laser light is reflected out of the beam path by the DMD. It is therefore preferable to redistribute the laser intensity into a flattop intensity-profile to illuminate an MLA. We have tested the feasibility of this concept in an offline setup using an adlOptica flattop beamshaper to illuminate an MLA. Based on MLA2 as used in this chapter with an area of 10 mm×12 mm this allows for several thousand microlenses to be illuminated with an intensity variation of 21.5 % (standard deviation) over the whole array as shown in Fig. 5.23. The shown figure is a reimage of the focal plane taken with an analysis objective. The spot pattern in the focal plane is created with the high-NA microscope objective introduced in section 5.1.1. The field of view of the analysis objective is not as large as of the high-NA objective resulting in slight distortion and

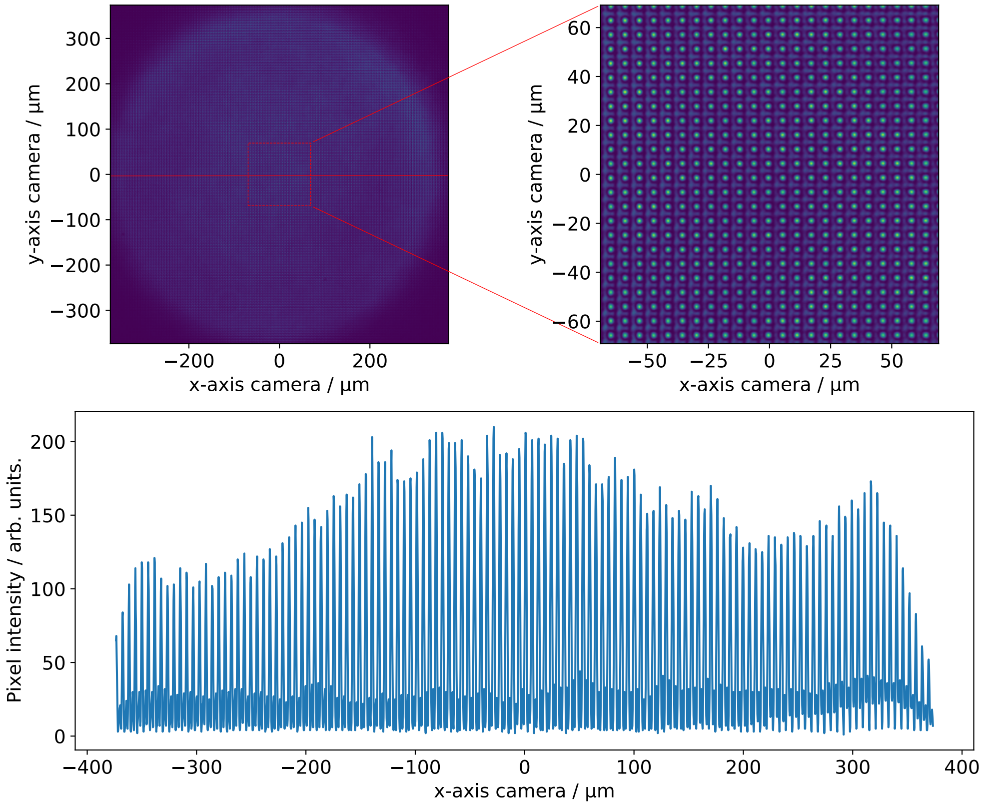

Fig. 5.23.: Light field at the focal plane of the microscope objective created by illuminating an MLA with a flattop beam profile. In the bottom, a cross-section along one line of focal spots(red horizontal line) is shown. Measurement adopted with permission from Tim Gollerthan.

out-of-plane imaging in the outer regions of the image. This reduces the intensity of the outer focal spots and increases the intensity variation. Imaging the flat-top profile directly with a camera before illuminating the microlens array yields an intensity variation of 12.5 % which is a good indication for the achievable intensity variation. Using two lasers as for the experiments described above, each providing roughly 5 W of laser power coupled out of the fiber, several thousand traps are readily available.

Deterministic assembly of individual-atom patterns

Overcoming the limitations just described paves the way to quantum computing with several thousand qubits. For this to be possible, deterministic assembly for creating defect-free structures is necessary. In the context of the QUIPS experiments, a heuristic sorting algorithm has been implemented and described in [113]. It is based on a shortest-move algorithm as presented in [24] and shall be compared to other sorting algorithms introduced in [140] to evaluate if our current algorithm is adequate to be used for sorting on large arrays. To introduce the currently used algorithm and compare it with others, the following assumptions are made:

- There are always more atoms available than necessary for the targeted defect-free structure.
- Only compact, quadratic target structures are taken into account, meaning there are no empty sites within the boundaries of the target structure.
- Moves are performed on the grid lines and not in between traps.
- There is no atom loss occurring.

In the currently used algorithm, at first the trap occupation is analyzed and compared with the target structure yielding a list of overoccupied traps (source traps) as well as underoccupied traps (target traps). The list of underoccupied traps is sorted by their distance $d = \sqrt{(\Delta x)^2 + (\Delta y)^2}$ (Δx and Δy are the traveled distances along columns and rows respectively) from the center of mass of the target structure ensuring that the target structure is filled from the inside out. This is an important improvement compared to [24] which has later on been introduced in a similar way as a compression algorithm, filling the array layer-by-layer from the inside out, in [140, 154]. For the first underoccupied trap in the list, the overoccupied trap with the smallest distance d is determined and the path with least obstacles for this pair is found. Paths are hereby restricted to movements with only a single change in direction meaning that either the path first follows the column of the overoccupied trap until the row of the underoccupied trap is reached and then move along the corresponding row or vice versa. If there is an obstacle, e.g. an atom, along the path, this atom is used to fill the target trap and the now empty site is refilled from the source trap. The aim is to only have paths without obstacles. Each obstacle increases the number of paths which is why it is important to find a method for assigning tuples of source and target traps with a lower number of obstacles or with very short moves were obstacles are directly omitted. Introducing a travel distance $l = \Delta x + \Delta y$ as a cost function for each move, finding short moves is an application of the linear sum assignment problem (LSAP) and was introduced in [140] as a way to reduce the number of moves compared to their compression algorithm. The authors propose two algorithms using slightly different cost functions. Algorithm LSAP1 uses the cost function $\sum_{\text{moves } i} l_i$ whereas algorithm LSAP2 uses $\sum_{\text{moves } i} l_i^2$ thereby favoring shorter paths. As this is only a more elaborate way of finding tuples of source and target traps without taking obstacles into account, the resulting paths have to be post-processed as detailed in [140]. This post processing mainly removes obstacles for LSAP1 as described above or rearranges the order of paths for LSAP2 thereby first making moves without obstacles.

In order to evaluate how these new algorithms perform with respect to the QUIPS-algorithm, the number of moves for different algorithms was compared. It is important to note, that with a *move*, the linear movement of an atom without any changes in direction is meant. This means that an obstacle-free path as described above can consist of one move if either start and end row or start and end column are equal, otherwise the path consists of two moves. This distinction is made as for changing direction, the atom has to be slowed down and accelerated again potentially resulting in atom loss. In Fig. 5.24, the number of moves of the different algorithms for sorting atoms into a staggered (triangles) or a compact (crosses) target structure mentioned above is depicted. The evaluation shows that our algorithm behaves very similar to the compression algorithm. The LSAP2-algorithm is, within the uncertainty of the simulation,

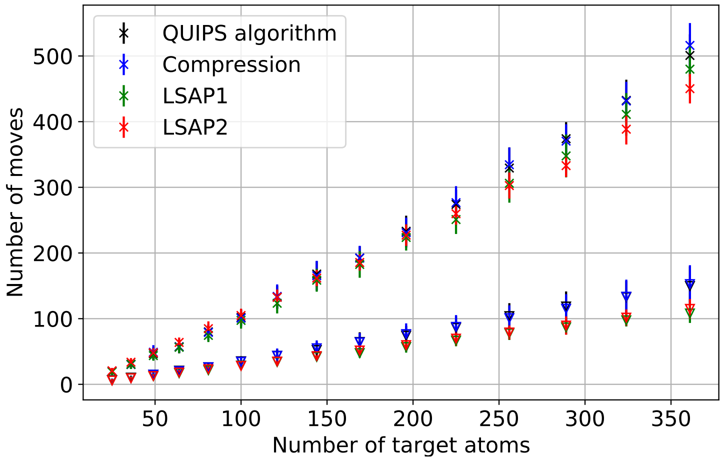

Fig. 5.24.: Comparing the sorting algorithm used in our group (QUIPS algorithm) with the algorithms described in [140]. Triangles represent the number of moves for a staggered target structure whereas crosses represent the number of moves for a compact target structure.

roughly 10 % better than the other algorithms for the compact target structure. For a staggered target structure both LSAP-algorithms outperform the other algorithms by approximately 25 %.

All algorithms with a single movable tweezer have in common that with an average filling fraction of 50 % for a compact target structure with N atoms at least N/2 atoms have to be moved. This results in several hundred moves for the atom number achieved in this section. To overcome this limitation, parallel sorting algorithms moving several atoms at a time have to be used [31, 155–157]. Depending on the degree of parallelism they allow to reduce the number of moves significantly such that scaling as low as $N^{0.388(2)}$ has been demonstrated in [155]. This shows, that for atom numbers below 200 atoms, our current algorithm is compatible with other single-movable-tweezer implementations. However, for large atom numbers above 200 atoms, the number of moves becomes so big that sorting takes too long and parallel sorting needs to be introduced to circumvent extensive atom loss.

5.3. Conclusion

In this chapter, a new high-NA microscope objective was introduced which facilitates spot sizes in the sub-micrometer regime and offers a large enough field of view for high-quality imaging of thousands of dipole traps. Its achromatic optimization will furthermore simplify site-selective Rydberg excitations in future experiments. Based on this new microscope objective, a setup has been introduced which demonstrates the enormous potential of microlens arrays to scale up individual-atom platforms. The potential of interleaving up to three trap arrays was investigated and the created trap arrays were analyzed in detail. Using the two best-performing arrays, on average 1167 individual atoms were trapped simultaneously in two interleaved arrays. To the knowledge of the author this is currently the highest number of individual atoms trapped in a single-site addressable quantum computing platform. Limitations of the current setup as well as possibilities for even larger trap arrays have been discussed. Furthermore, the challenges for defect-free arrangements of the trapped atoms have been outlined.

6. Discussion and future perspectives

In the course of this thesis, a new setup for large-scale individual-atom experiments has been designed and built. It features versatile optical access for state-of-the-art Rydberg experiments, stable magneto-optical trap (MOT) operation and a new, high-NA microscope objective for submicrometer trap waists allowing a new level of large-scale neutral-atom quantum experiments. Related to the new setup, the experimental control system and its extensions towards conditional, in-shot control as well as low-cost, triggered frequency shifting has been introduced, thereby extending the applications of the open-source `labscript` platform. In combination with a variety of improved laser systems, this new setup has been used in this work for novel implementations towards continuously operated large-scale neutral-atom quantum platforms.

Using a large dipole trap filled with laser-cooled atoms as atom reservoir, the deterministic preparation of individual atoms and their subsequent defect-free arrangement in hexagonal target structures has been demonstrated. This was achieved by separating the process of deterministic single-atom loading into functional modules allowing for parallelized operation. Using a movable tweezer for interconnecting the different modules allows us to overcome the typical limitation of state-of-the-art individual-atom tweezer platforms, where quantum operations within the trap arrays have to be alternated with phases of reloading laser-cooled atoms from an optical molasses compensating for atom loss. This novel technique paves the way to a continuous supply of individual atoms if combined with an existing method for long-distance transport or continuous supply of laser-cooled atoms to the reservoir [141, 142]. For future experiments, continuous supply of neutral atoms will be a key technology to enhance the data rate of a quantum processor as currently the reloading of atoms from a MOT takes several 100 ms to several seconds depending on the explicit setup. For comparison, gate operations are performed on the microsecond timescale. Furthermore, utilizing microlens-based parallelization allows us to scale up the small setup used in this work, enlarging both the number of sites in the trap array as well as the number of atom reservoirs.

Scaling the size of a neutral-atom quantum platform is usually limited by the available laser power. Therefore, enlarging the size of the trap array has been addressed by utilizing the superposition of several microlens-based trap arrays in combination with a high-NA microscope objective to create several thousand dipole traps. The novel setup facilitated the use of independent laser sources for different beam paths allows us to significantly shift the power limitations. The dipole potentials created by these huge trap arrays as well as their capabilities in trapping single atoms have been investigated. As a result, the tweezer-array superposition enabled the creation of interleaved trap arrays capable of reliably providing more than 1000 individual atoms. This is an unprecedented large number of single atoms trapped in a site-selectively addressable tweezer array, demonstrating the advantages of trap creation using passive, micro-fabricated platforms. Using techniques at hand, the new setup constitutes a sustainable basis towards the preparation of defect-free arrays of several hundred as well as the trapping of several thousand individual atoms in the near future. Gray-molasses loading will even allow us to push the atom number without increasing the size of the trap array [27]. Furthermore, the inherently limited flexibility of passive platforms, such as microlens arrays,

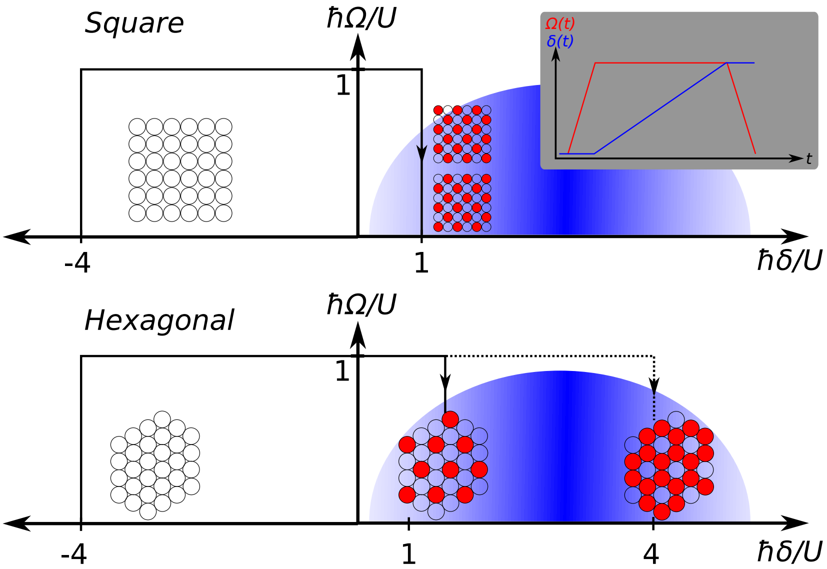

Fig. 6.1.: Sketched phase diagram for square and hexagonal arrays. The sweeps of Rabi frequency Ω and detuning δ shown in the inset are used to prepare the different phases by following the paths depicted in the phase diagram. Image adapted from [32].

to change the interatomic distance is partly overcome due to the adjustable spacing between neighboring traps created by the two distinct microlens arrays as used in this work.

Based on the new setup and the corresponding technological progress presented in this work new quantum technologies can be investigated and developed in future. The predominant aim is therefore to combine this new quantum processing platform with the Rydberg laser system already available in our group or with a new laser system currently set up, enabling two-photon transitions both via the rubidium $\left|5P_{3/2}\right\rangle$ and $\left|6P_{3/2}\right\rangle$ states. This makes a multitude of quantum simulation and quantum computation experiments accessible of which two recently demonstrated examples shall be discussed in further detail.

In quantum simulation, progress has been made in recent years demonstrating, for example, quantum phase transitions from a paramagnetic to an anti-ferromagnetic phase [31, 32]. Utilizing the van der Waals interaction between Rydberg atoms, the system can be described by the Ising Hamiltonian

$$H_{\mathrm{Ryd}} = \sum_{i<j} U_{ij} n_i n_j + \frac{\hbar\Omega}{2} \sum_i \sigma_i^x - \hbar\delta \sum_i n_i \tag{6.1}$$

where the ground and Rydberg states are mapped onto the corresponding spin states $|g\rangle = |{\downarrow}\rangle$ and $|r\rangle = |{\uparrow}\rangle$. $U_{ij} = {}^{C_6}/_{r_{ij}^6}$ is the van der Waals interaction with van der Waals coefficient C_6 and distance r_{ij} between atoms i and j, $n_i = |{\uparrow}\rangle\langle{\uparrow}|_i$ and Pauli matrix $\sigma^x = |{\uparrow}\rangle\langle{\downarrow}| + |{\downarrow}\rangle\langle{\uparrow}|$. The ground and Rydberg states, representing the two spin states, are coupled via a laser field with Rabi frequency Ω and detuning δ to the Rydberg state. The van der Waals interaction prevents simultaneous interaction of atoms into a Rydberg state within the blockade radius $R_b = \sqrt[6]{U/(\hbar\Omega)}$, thus giving rise to antiferromagnetic ordering in the system. Sweeping Ω and δ over time allows to transfer the system from the initial ground state into the antiferromagnetic state as shown in Fig. 6.1. Depending on the geometry, i.e. square or hexagonal, for a fixed ratio between the interatomic spacing a and the blockade radius R_b one or two distinct phases can be established. By increasing the blockade radius relative to the interatomic spacing, there are even more phases obtainable due to Rydberg blockade of more atoms than only the nearest neighbor [158]. In our setup this can be achieved using different Rydberg states since a constant interatomic spacing is given by the used MLA.

In the field of quantum computation, recent progress has been achieved utilizing the two-photon transition via the $\left|6P_{3/2}\right\rangle$ state to implement parallelized, high-fidelity multi-qubit gates in one dimension [105]. Therefore a chain of neutral-atom pairs has been arranged. Utilizing two or three interleaved trap arrays allows to extend these methods to two dimensions by slightly shifting the arrays with respect to each other such that a two-dimensional grid of compact two- or three-atom structures is created.

Another important aspect in quantum computing is that operations with single physical qubits underlie errors. Therefore methods for quantum error correction need to be implemented. One possibility for neutral atoms in two-dimensional structures are surface codes, where one logical qubit is constructed from several physical qubits [159]. The lower the intrinsic fidelity of the gate-operation, the more physical qubits are necessary to achieve an error-tolerant logical qubit. This makes scalability as demonstrated within this work inevitable.

A. Properties of rubidium-85

A detailed compilation of physical and optical properties of ^{85}Rb is given by D. Steck in [46]. In Tab. A.1 the properties relevant for the QUIPS-C experiment are given and in Fig. A.1 the energy level scheme of ^{85}Rb including the $5\mathrm{S}_{1/2}$ ground state as well as the $5\mathrm{P}$ excited states is shown.

Tab. A.1.: Properties of ^{85}Rb relevant for this work. Data taken from [46].

Atomic properties of ^{85}Rb		
Atomic number	Z	37
Total nucleons	$Z+N$	85
Atomic mass	m	$1.409\,99 \times 10^{-25}\,\mathrm{kg}$
Nuclear spin	I	$5/2$
Nuclear g-factor	g_I	$-2.936400(6) \cdot 10^{-4}$

Properties of the ^{85}Rb D1 line and the excited state $5^2P_{1/2}$		
Wavelength	λ	$794.979\,014\,933(96)\,\mathrm{nm}$
Transition frequency	ω_0	$2\pi \cdot 377.107\,385\,690(46)\,\mathrm{THz}$
Natural linewidth	Γ	$2\pi \cdot 5.7500(56)\,\mathrm{MHz}$

Properties of the ^{85}Rb D2 line and the excited state $5^2P_{3/2}$		
Wavelength	λ	$780.241\,368\,271(27)\,\mathrm{nm}$
Transition frequency	ω_0	$2\pi \cdot 384.230\,406\,373(14)\,\mathrm{THz}$
Natural linewidth	Γ	$2\pi \cdot 6.0666(18)\,\mathrm{MHz}$
Saturation intensity	I_0	$1.669\,32(35)\,\mathrm{mW/cm^2}$
Doppler temperature	T_D	$145.57\,\mu\mathrm{K}$
Recoil temperature	T_R	$370.47\,\mathrm{nK}$

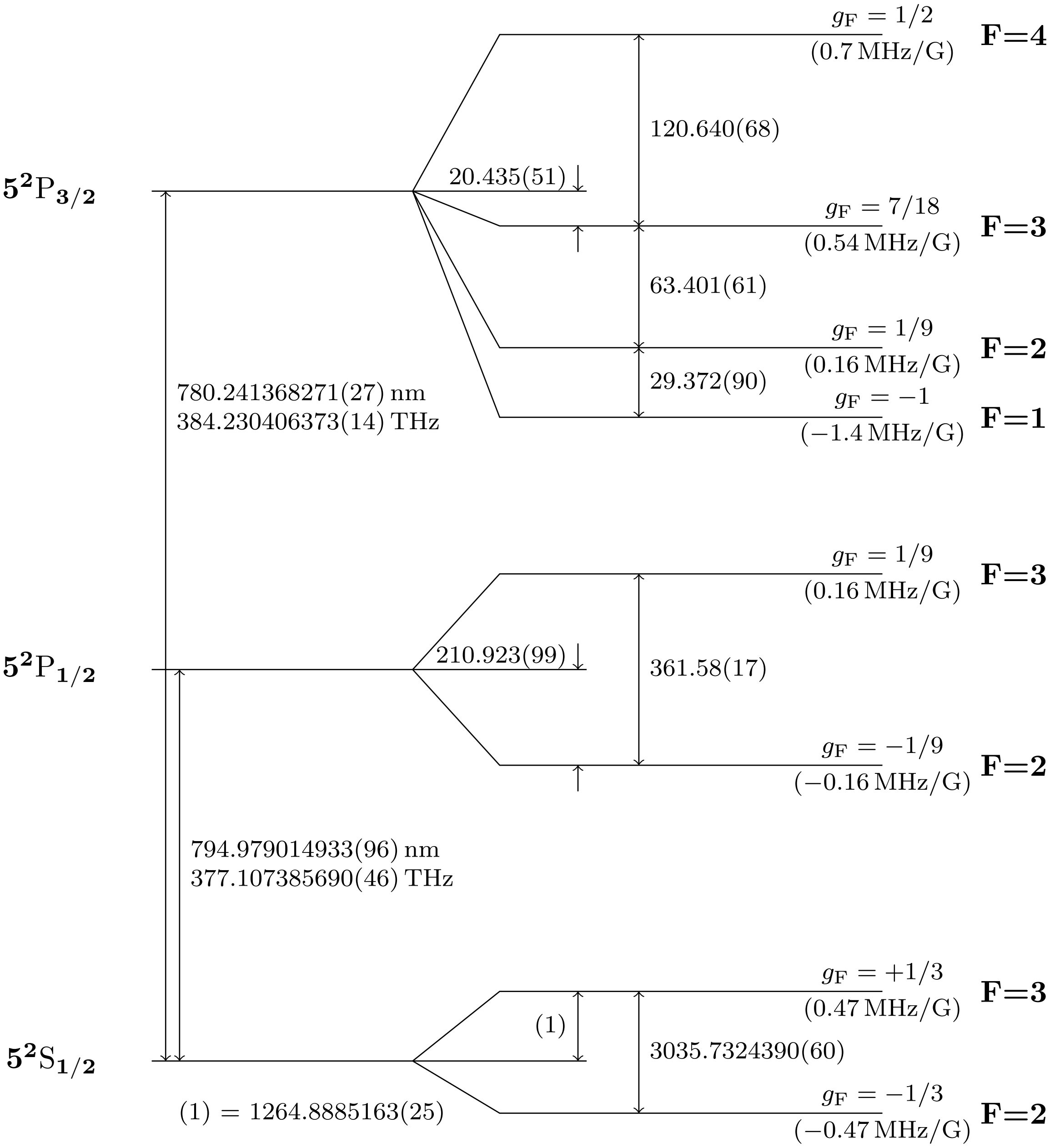

Fig. A.1.: Energy level scheme of the ^{85}Rb D1 and D2 line. The hyperfine structure splittings are given in MHz. The Landé g_F-factors are given with the corresponding Zeeman splittings of the m_F substates.

B. Measured and calculated magnetic fields

In section 3.1.3 the development process of the magnetic field coils attached to the vacuum chamber is described. Here, a more detailed summary of the magnetic fields including drawings of the magnetic field coils assembled around the vacuum chamber and measurements of the magnetic fields is given. In Tab. B.1 information on the field coils for compensation and bias fields is given and in Tab. B.2 information on the gradient field is given. Figures B.1, B.2, and B.3 show a detailed view of the coils and the corresponding dimensions.

Tab. B.1.: Magnetic field strength for compensation and bias field coils attached to the vacuum chamber. The coordinate system definition is shown in Fig. 3.1. All resistances have been measured at a current of 1 A. The used currents for compensation fields were predetermined from measurements with a hall sensor on both sides of the vacuum chamber. Tuning of the compensation fields has been used to position the MOT relative to the trap arrays for optimal loading. A measurement of the residual magnetic field based on a two-photon Raman process as described in [119] has not yet been performed. For the z-axis coil, thermally conductive epoxy (Electrolube ER2220) has been used to glue a frameless coil. The other two compensation coils are fixed on their holders. All compensation coils are made from enameled copper wire with a thickness of 1 mm.

Coil pair (windings)	B-field (meas.) in G/A	B-field (calc.) in G/A	Resistance in Ω	Current I used in Exp. in A
Comp. x (19)	1.6(1)	1.61	0.8	0.68
Bias x (59)	4.8(1)	4.86	2.4	not used
Comp. y (17)	1.8(1)	1.79	0.5	0.0
Bias y (64)	6.65(10)	6.74	1.5	not used
Comp. z (19)	2.2(1)	2.11	0,7	0.23
Bias z (59)	6.3(1)	6.29	2.0	not used

Tab. B.2.: Magnetic field strength and other properties for the gradient field. The coil has been covered in thermally conductive epoxy (Electrolube ER2220). The gradient field coils are made from enameled copper wire with a thickness of 1.25 mm.

Property	Value
Windings	165
Gradient (meas.) along symmetry axis	4.45(5) G/(A cm)
Gradient (calc.) along symmetry axis	4.36 G/(A cm)
Gradient (meas.) perpendicular to symmetry axis	2.18(5) G/(A cm)
Gradient (meas.) perpendicular to symmetry axis	2.17 G/(A cm)
Resistance at 1 A	1.22(2) Ω
Resistance at 5 A	1.28(2) Ω

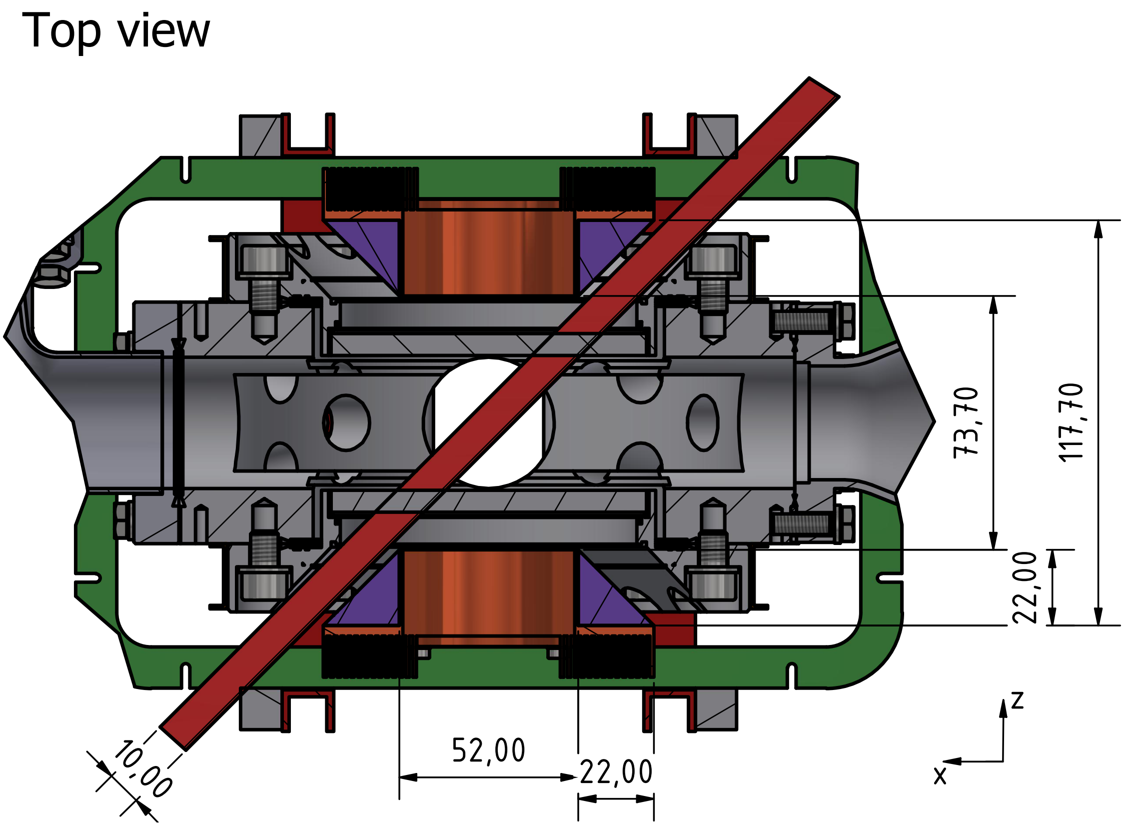

Fig. B.1.: Cut through the vacuum chamber with dimensions given for the gradient field coil as well as for some compensation and bias field coils.

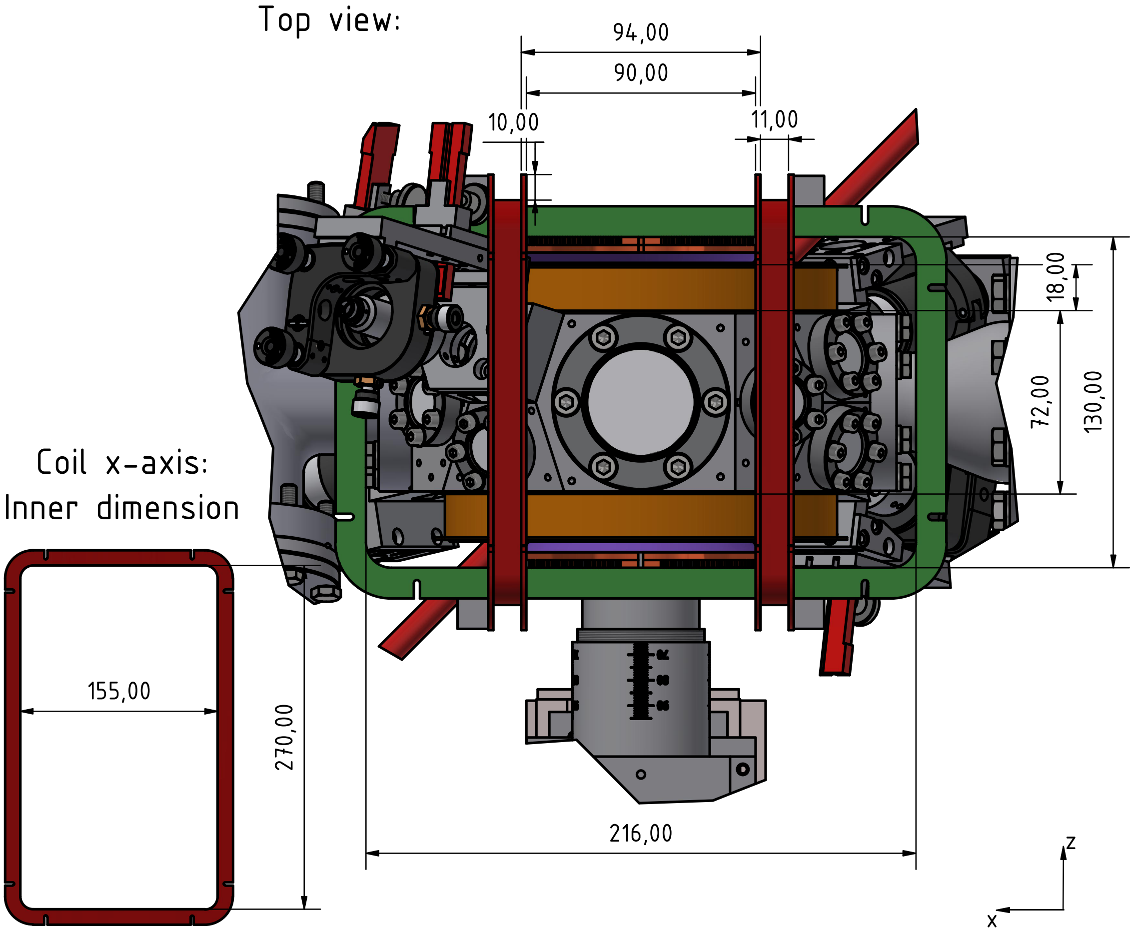

Fig. B.2.: Drawing showing the top view onto the vacuum chamber giving further dimensions for the compensation and bias field coils. In addition, the inner dimensions of the coil for a homogeneous field along the x-axis (red in all drawings) are given.

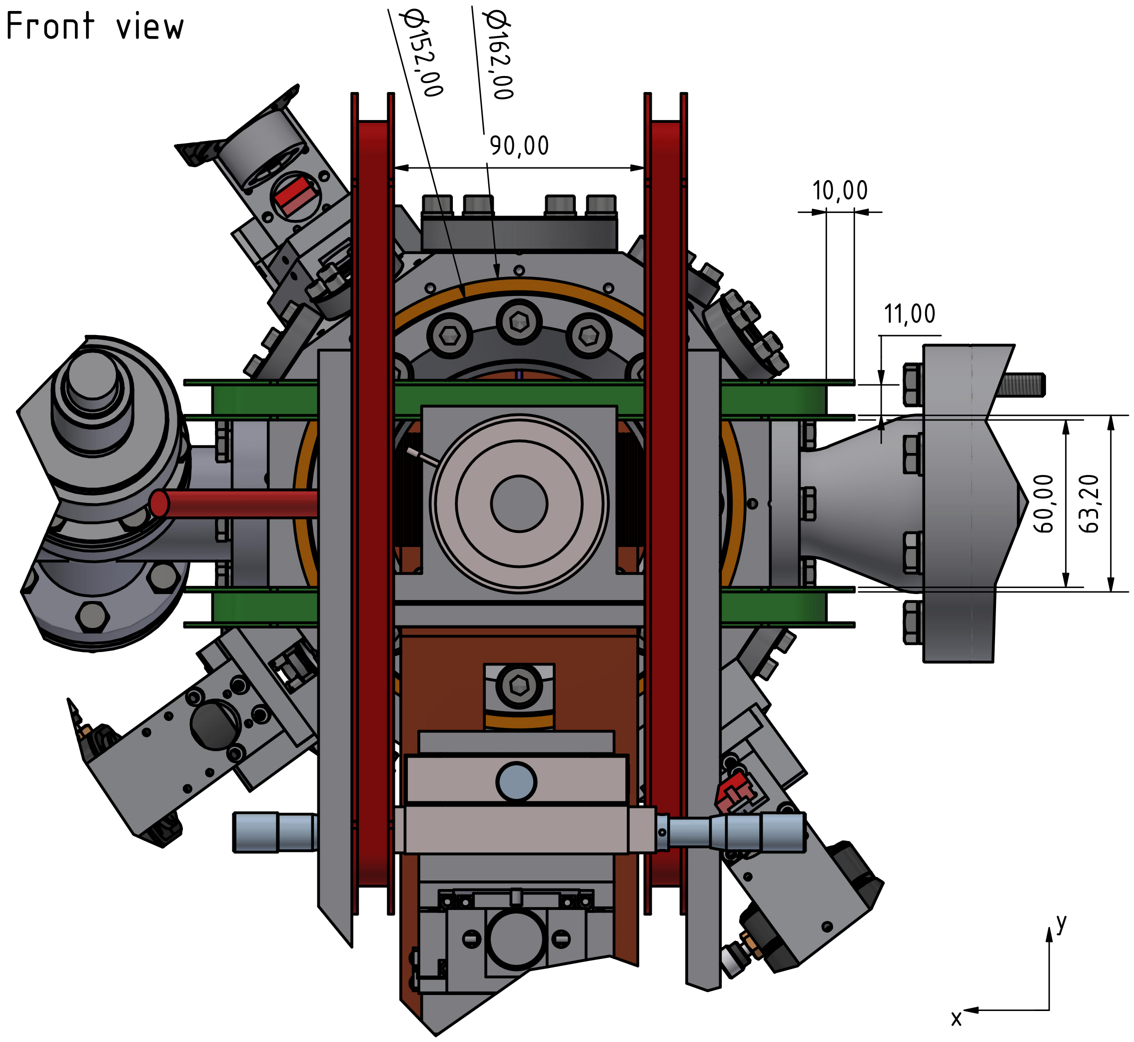

Fig. B.3.: Drawing showing the front view of the vacuum chamber giving further dimensions for the compensation and bias field coils.

The corresponding measured and calculated data for a current of $I = 1\,\mathrm{A}$ are shown in the following Figs. B.4, B.5, B.6, and B.7. All measurements were done using a Teslameter FM220 (Projekt Elektronik Mess- und Regelungstechnik GmbH).

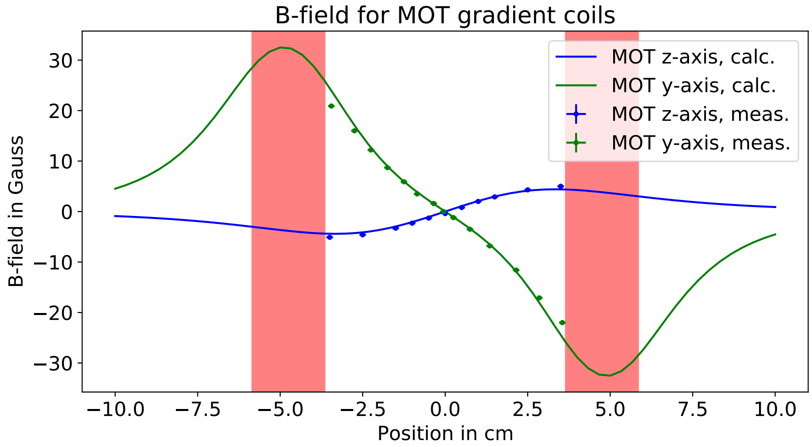

Fig. B.4.: Magnetic field of the MOT gradient coils. The coil position is shown in red for the plot along the y-axis of the vacuum chamber following the definition in Fig. 3.1. The gradient field perpendicular to the coils axis is shown exemplarily for the z-axis in the same plot. As expected, the gradient is inverted and half the size of the on-axis gradient. The magnetic field as calculated theoretically based on the description in section 3.1.3 is shown as solid line.

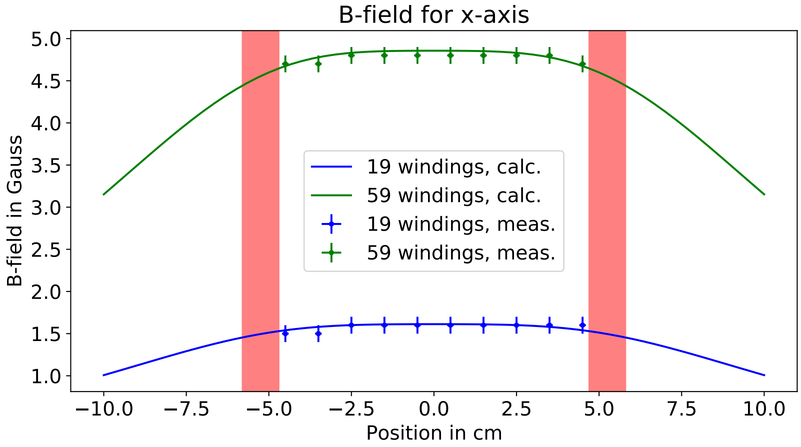

Fig. B.5.: Magnetic field along the x-axis (vacuum axis) of the vacuum chamber following the definition in Fig. 3.1 for both the compensation coil (19 windings) and the bias field coil (59 windings). The magnetic field as calculated theoretically based on the description in section 3.1.3 is shown as solid line.

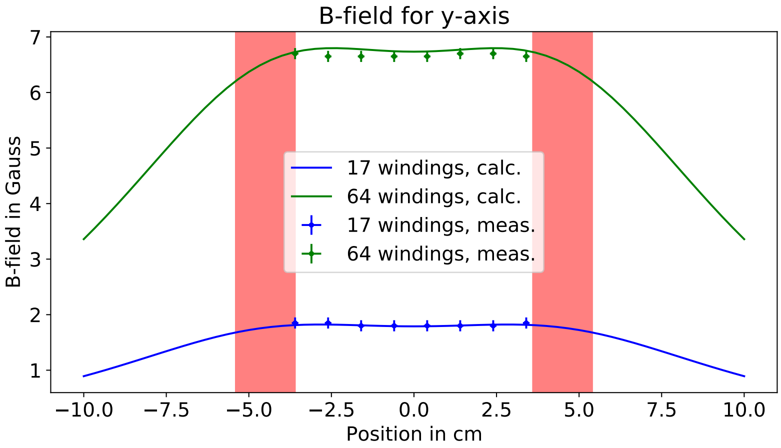

Fig. B.6.: Magnetic field along the y-axis (dipol axis) of the vacuum chamber following the definition in Fig. 3.1 for both the compensation coil (17 windings) and the bias field coil (64 windings). The magnetic field as calculated theoretically based on the description in section 3.1.3 is shown as solid line.

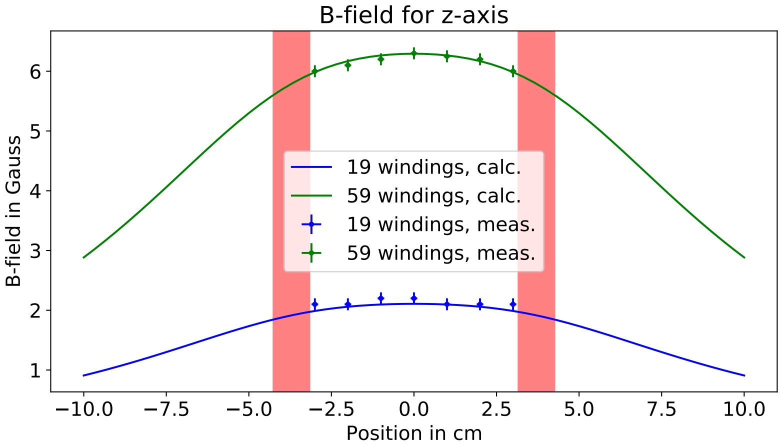

Fig. B.7.: Magnetic field along the z-axis (vertical axis) of the vacuum chamber following the definition in Fig. 3.1 for both the compensation coil (19 windings) and the bias field coil (59 windings). The magnetic field as calculated theoretically based on the description in section 3.1.3 is shown as solid line.

C. Characterization measurements for optical components

For the used optics in our experiments a defined transmission and reflection for the corresponding application is important. In particular the vacuum viewports as well as the dichroic mirror have special, custom-made coatings as detailed in sections 3.1.2 and 3.4.2. In the following sections the curves of the dielectric coatings are given. Furthermore some test measurements are shown and discussed.

As the dichroic mirror is operated at angle of incidence of roughly 22.5° and the CF100 viewports of the vacuum chamber are used together with a high-NA objective as well as MOT beams under an angle of roughly 48°, some notes on polarization-dependence of optical coatings are important. At first, features of optical coatings at wavelength λ_0 shift, assuming small angle changes, with the angle of incidence θ as

$$\lambda(\theta) = \frac{\lambda_0}{n_{\text{eff}}} \sqrt{n_{\text{eff}}^2 - \sin^2 \theta} \tag{C.1}$$

where n_{eff} is the effective refractive index of the coating [160, Chap. 11]. So larger angles shift the features to smaller wavelengths. Furthermore, under angles of incidence larger than 0°, reflection and transmission for s- and p-polarization are different as described by Fresnel's equations (see for example [65, Chap. 4]). Therefore, polarization states different from pure s- and p-polarization change when reflected by or transmitted through an optical element.

C.1. Data for vacuum viewports

For the vacuum viewports a high transmission is important. As we use high-NA objectives and MOT beams under an angle of roughly 48°, transmission is not only important for a normal angle of incidence but also under an angle of incidence of up to 48°. The coating was therefore ordered accordingly and the coating curves for transmission under an angle of 0°, 30°, and 45° as measured by the company are shown in Fig. C.1. A general behavior as described by Equ. C.1 is clearly visible.

The transmission of the coatings has been checked for s- and p-polarization under normal incidence as well as for an angle of roughly 48° for the wavelength range 780 nm to 795 nm. For all measurements the total transmission through both vacuum windows was measured (including four surfaces). Due to a measurement uncertainty of $\pm 1\,\%$ the measurement was not sensitive enough to detect any wavelength dependence in the corresponding wavelength range. The results are given in Tab. C.1 for the complete wavelength range 780 nm to 795 nm. From these results it is apparent that circular polarization will not be maintained for large angles of incidence. This affects both the diagonal MOT beams, which will have elliptical polarization, and strongly focused laser beams. Therefore fine-tuning fine-tuning is at best done using polarization dependent state preparation of atoms.

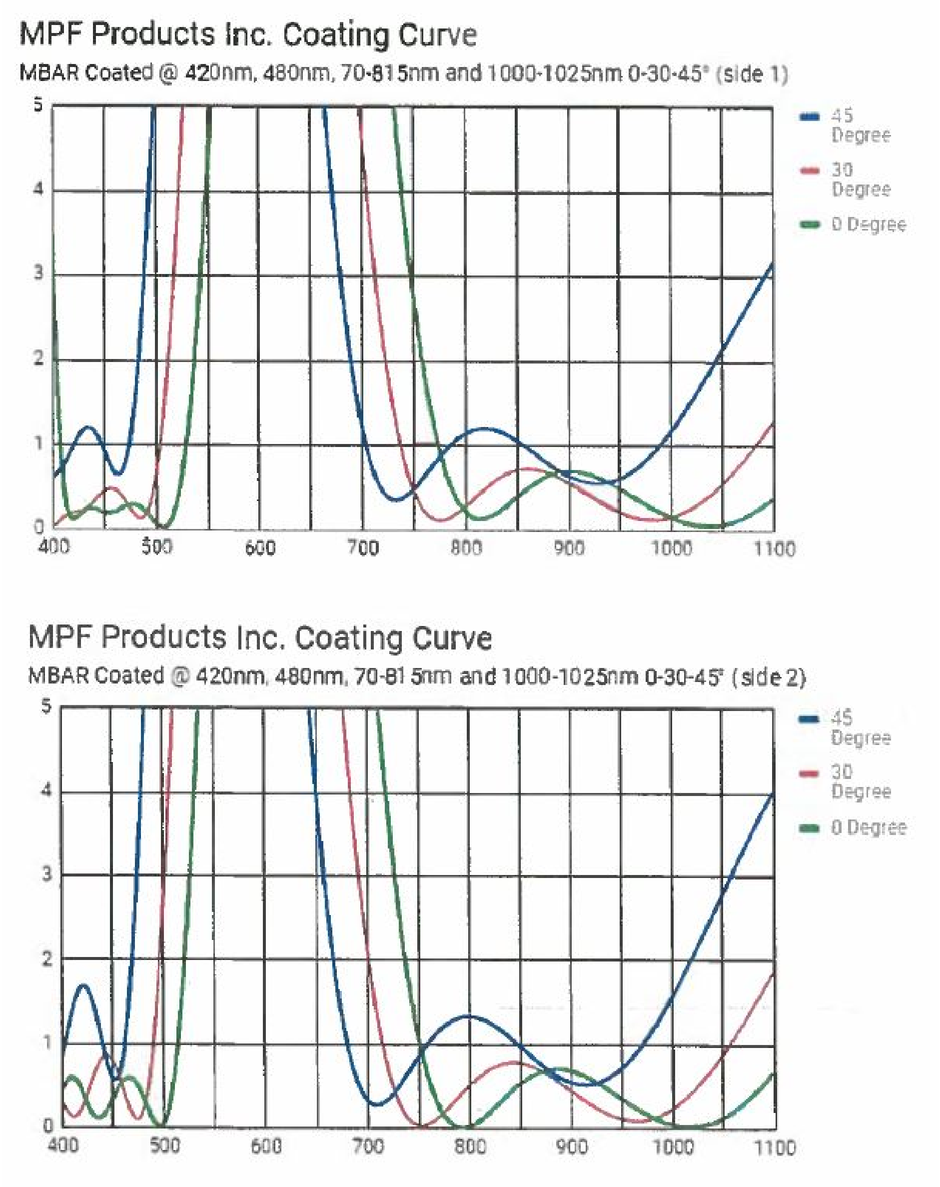

Fig. C.1.: Coating curves for the CF100 viewports as mounted on the vacuum chamber.

Tab. C.1.: Transmission for 780 nm to 795 nm at angles of incidence of 0° and 48° given for a transmission through both vacuum windows (i.e. four surfaces).

	0°	48°
s-polarization	99(1) %	89(1) %
p-polarization	99(1) %	98.5(10) %

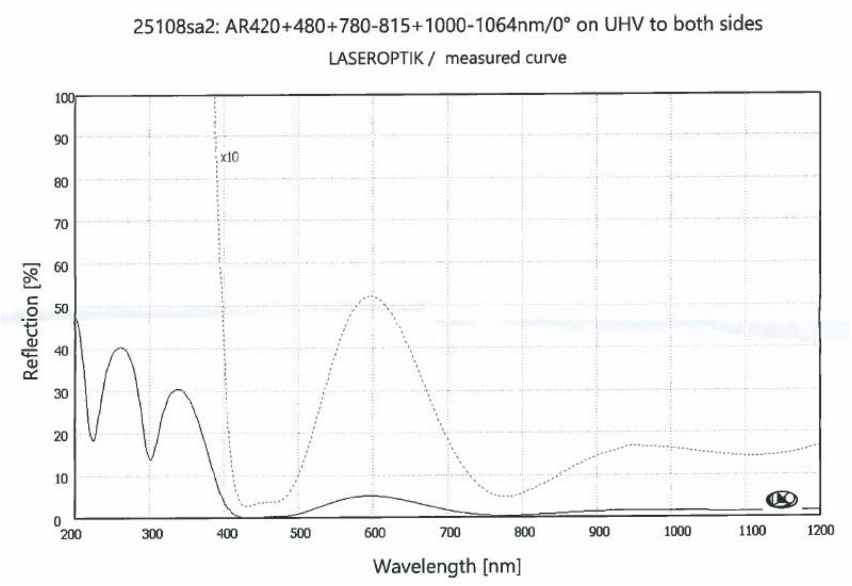

Fig. C.2.: Coating curves for the coated CF16 and CF40 viewports mounted onto the vacuum chamber.

To confirm the effect on circular polarization, a circularly polarized beam was prepared using a quarter wave-plate such that the transmission through a rotatable PBS (rotation axis = beam propagation axis) was as constant as possible for all angles of rotation. This beam was sent through the vacuum chamber at an angle of 0° and 48° and analyzed again behind the vacuum chamber. The results of the measurement, shown in Fig. C.3, verify the above mentioned expectations. For an angle of incidence of 0° only small changes in polarization are measurable. It has to be noted however, that there is a measurable effect such that circularly polarized light will be elliptical inside the vacuum chamber. The reason can be that stress in the window caused from the air pressure outside the vacuum chamber and from tightening the flange bolts causes birefringence both in the glass itself as well as in the coating [161].

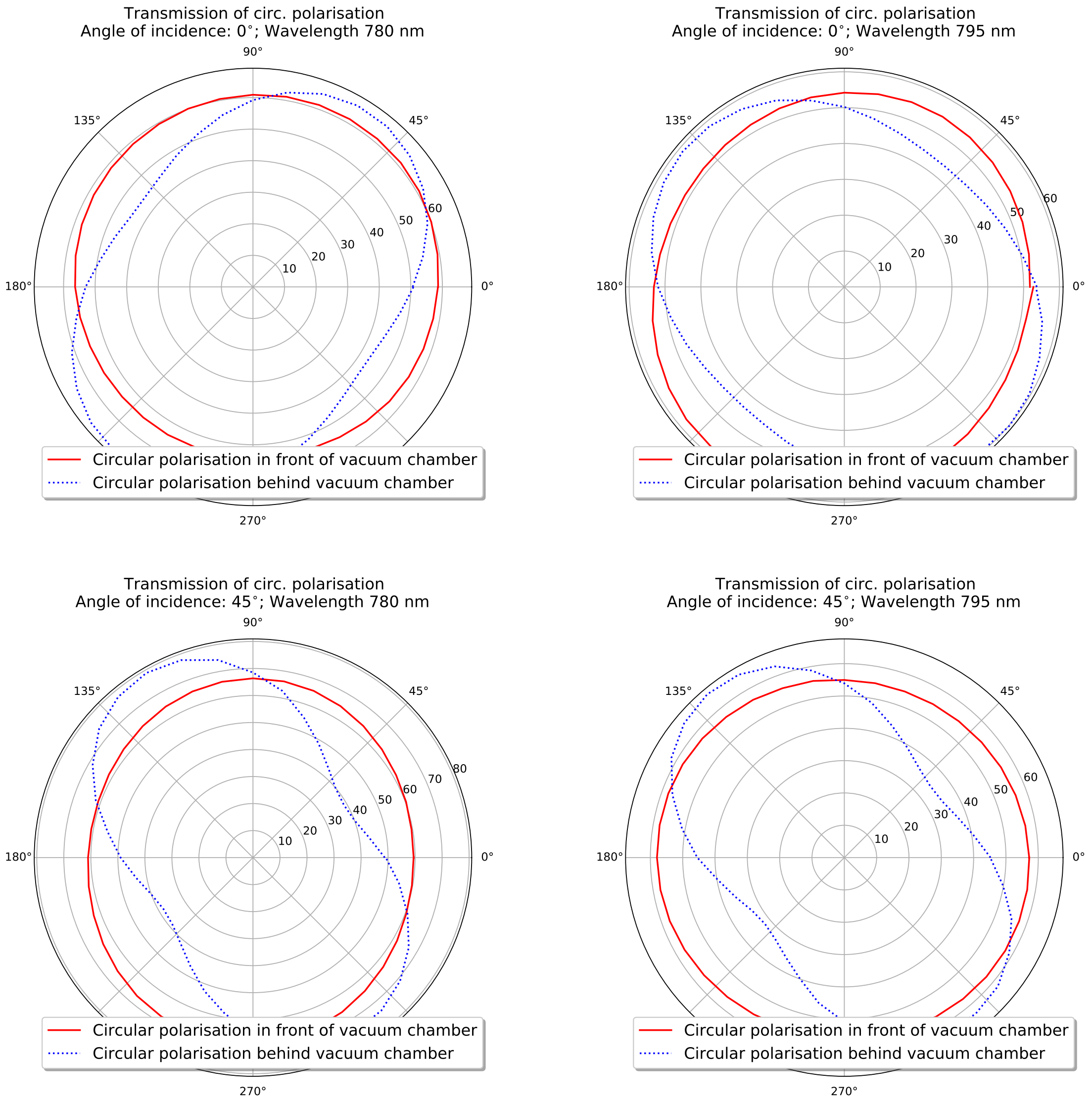
Transmission of circ. polarisation
Angle of incidence: 0°; Wavelength 780 nm

Transmission of circ. polarisation
Angle of incidence: 0°; Wavelength 795 nm

Transmission of circ. polarisation
Angle of incidence: 45°; Wavelength 780 nm

Transmission of circ. polarisation
Angle of incidence: 45°; Wavelength 795 nm

Fig. C.3.: Testing the transmission of circularly polarized light through the CF100 viewports of the vacuum chamber for angles of incidence of 0° and 48°. The radial distance from the center give the measured power in arbitrary units.

C.2. Data for dichroic mirror

For the dichroic mirror the coating curve from the manufacturer Laseroptik to achieve the desired performance as described in section 3.4.2 is shown in Fig. C.4, measured together with the anti-reflection coating on the second side of the substrate. The measurement of the anti-reflection coating is shown in Fig. C.5.

For the wavelength range of 775 nm to 805 nm, the behavior of the coating for the transition from reflection to transmission was measured for s- and p-polarization in the center of the substrate and compared to measured data for unpolarized light as given by Laseroptik. The measured transmission data is shown in Fig. C.6. The measurement reveals the expected deviation between s- and p-polarized light for 775 nm to 790 nm while the average of both curves matches well with the unpolarized data. However, for wavelengths between 790 nm to 800 nm the curves deviate. At first it was assumed that this results from intensity fluctuations of the laser which are possibly the reason for the strong variations of the p-polarization at 795 nm. Several control measurements at 796.9 nm confirmed a transmission of 90(2) % for p-polarization and 88(2) % for s-polarization in accordance with the data shown in Fig. C.4. It is therefore assumed that the transmission between 790 nm to 800 nm is slightly lower than expected.

Furthermore, as the dichroic mirror will be used under an angle of 22.5° in transmission and possibly also in reflection for laser beams, e.g. for state preparation, whose use is polarization sensitive, its effect on linearly polarized light was investigated. For the measurement, linearly polarized light in s-, p- and 45° polarization was prepared and its linearity was tested before and after the dichroic mirror. As the plane of incidence is parallel to the optical table, in this special case, s-polarization corresponds to vertical polarization and p-polarization corresponds to horizontal polarization. From the measurement in 45° polarization, information can be drawn how the phase of s- and p-polarization is shifted relative to each other which would cause circularly polarized light to become elliptical. The results for reflection and transmission are shown in Fig. C.7

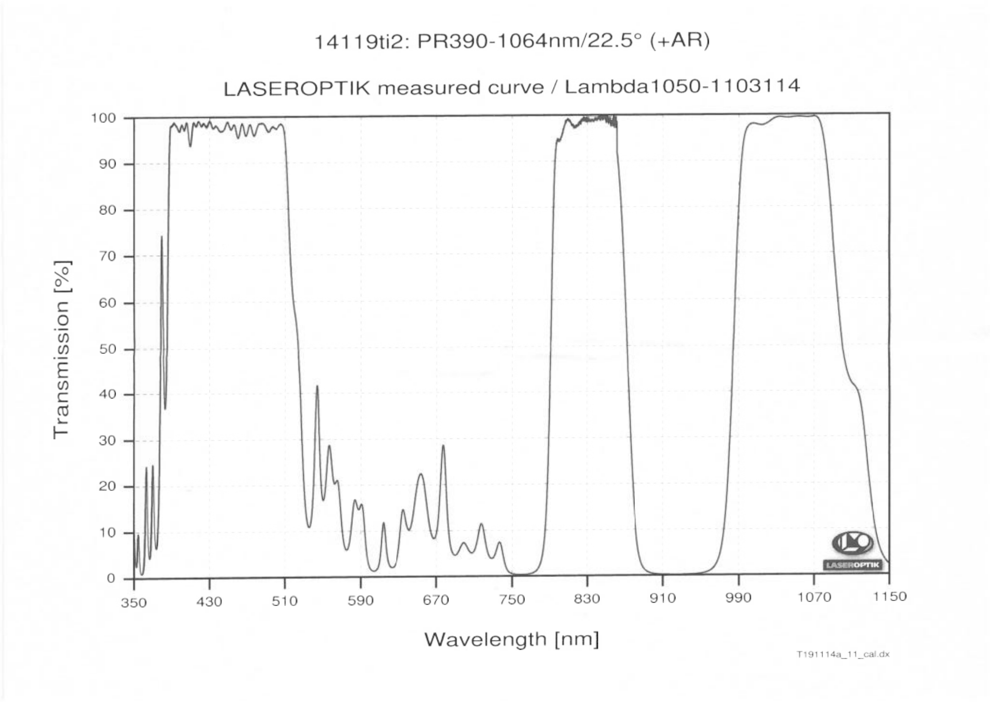

Fig. C.4.: Partially reflective coating curve for the dichroic mirror.

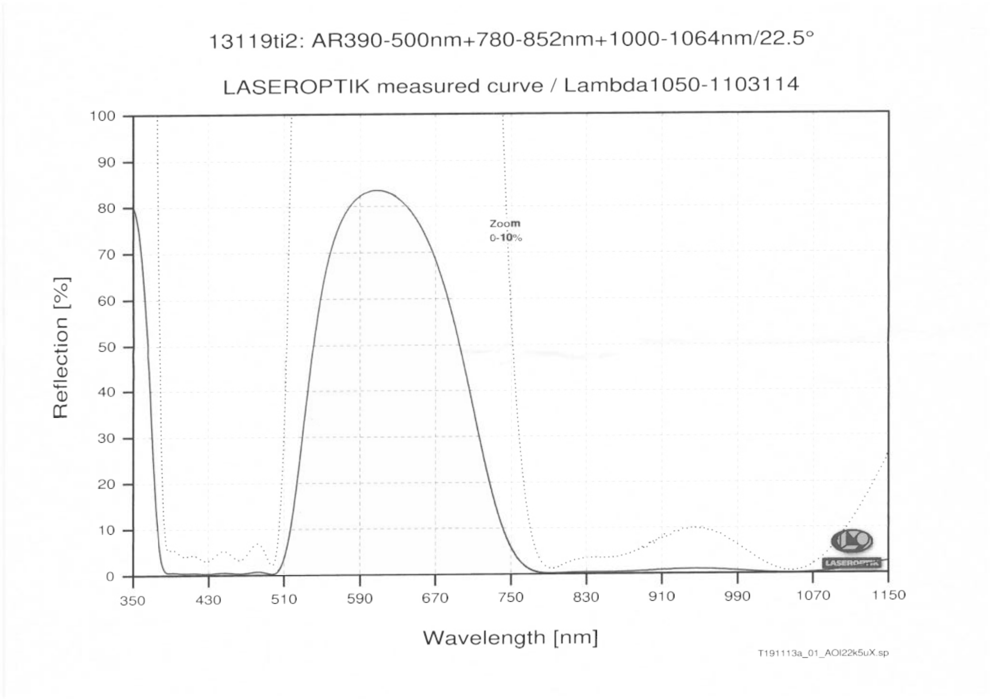

Fig. C.5.: Anti-reflection coating curve for the dichroic mirror.

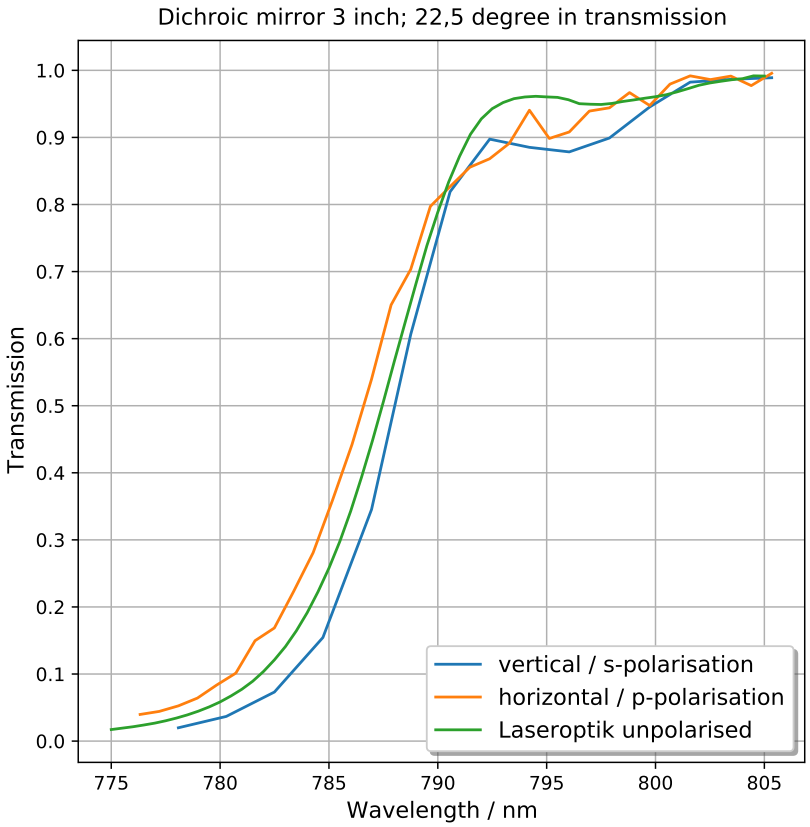

Fig. C.6.: Transmission measured for s- and p-polarization and compared with the unpolarized measurement from Laseroptik. For the measurement no intensity-stabilized laser was available resulting in an uncertainty of up to 5 % in the transmission value. For discussion of the deviations from the unpolarized data, see text.

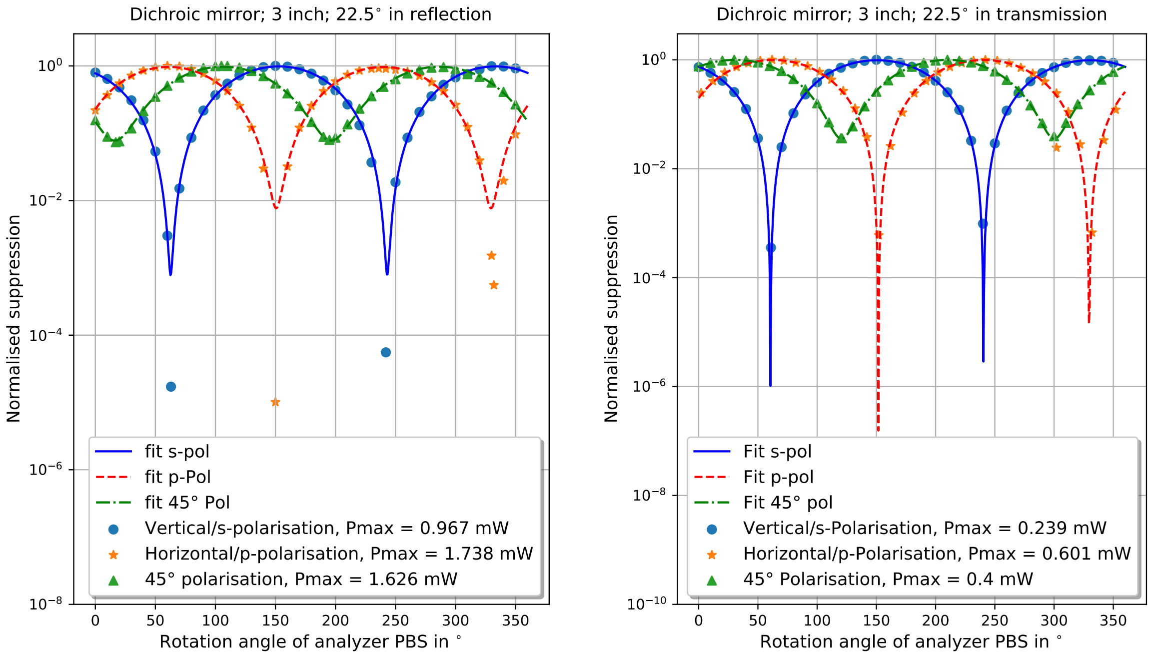

Fig. C.7.: Characterization measurement of linearly polarized light reflected from (left) or transmitted through (right) the dichroic mirror used in the optical setups of chapters 4 and 5.

D. Optical filter suppressing near-resonant light at 780 nm from spontaneous Raman scattering

During the installation of both the microlens setup as well as the reservoir trap described in chapter 4, trapping light was detected on the EMCCD camera. For the reservoir trap this is in general not totally unexpected as the laser beam points directly onto the EMCCD camera. Therefore extreme care was taken to slowly increase the laser intensity during installation in order to avoid overexposure of the camera. However, when inspecting the beam path in detail, only 5 % to 10 % (see appendix C.2) of light around 797 nm is reflected by the dichroic mirror and thus incident onto the EMCCD camera. Furthermore in front of the camera, the two installed laser line filters LL01-780-25 (*Semrock*) have a transmission below 10^{-7} each for a wavelength of 797(1) nm. From measuring the photon count of a 6 mW laser beam at 796.5 nm coupled into a 10 m single-mode fiber (SMF) with an EMCCD camera, the photon rate is calculated to be on the order of 1×10^5 photons/s. Including all losses by the filters this would correspond to a laser power of 50 W coupled out of the fiber, contradicting the measured laser power coupled into the fiber. For the MLA and the movable tweezer using trapping light of a Ti:Sa laser, a similar phenomenon was observed. Here, a reflection on the first surface of the microscope objective (assumed reflectivity of 1(1) %) was visible on the camera.

Possible explanations for this observation can be that the filters have a higher transmission than specified at 795nm or that there is near-resonant light at 780 nm which is not blocked by the filters. To test this, a LL01-808-25 (Semrock) filter was used. At 0° angle of incidence, it has a transmission wavelength of 808.0(15) nm. Changing the angle to approximately 21° changes the center wavelength to the regime of the used trapping wavelength around 797(1) nm. At this angle no light is detected with the EMCCD camera. However, the trapping light is detected again when changing the filter angle to 34°, where the transmission wavelength is approximately 780.0(15) nm. Furthermore, this near-resonant light at 780 nm can only be suppressed by using a filter after the optical fiber (PM780-HP from Thorlabs). When installing the filter in front of the optical fiber, near-resonant light at 780 nm is still visible thus it is created inside the fiber. Including losses for light at 780 nm in the beam path a rate of 2×10^6 photons/s or roughly 0.5 pW of laser power is expected to be emitted from the fiber at 780.0(15) nm.

As stimulated Brillouin scattering (acoustical phonons), which is limiting the transmittable laser power in the used fibers, is only shifting the frequency on the order of 10 GHz ($\Delta\lambda \approx$ 21 pm), this cannot be the reason for the observed behavior. However, Raman scattering (optical phonons) can cause the noticed effect. Usually Raman scattering in fibers is known from the use of stimulated Raman scattering in Raman fiber amplifiers [162]. However also spontaneous Raman scattering is possible, in this case especially anti-Stokes Raman scattering. Therefore the expected anti-Stokes power in an optical single-mode fiber was estimated.

D.1. Estimated power of spontaneous Raman scattering in a single-mode fiber

In reference [163], the authors derive how the total Stokes and Anti-Stokes power due to spontaneous Raman scattering in different types of fibers can be calculated. Based on this derivation, the expected anti-Stokes power radiated along a SMF shall be derived for a wavelength of 797 nm, a transmitted power P_{out} and a fiber of length l.

The power $\mathrm{d}P'$ emitted into a SMF of length $\mathrm{d}z$ is for Stokes (i=S) and anti-Stokes (i=AS) scattering given by

$$\mathrm{d}P'_{\text{i,SMF}} = \mathcal{P}_{\text{i}}\Gamma_{\text{i,SMF}}P_0\mathrm{d}z \tag{D.1}$$

with phonon probability distribution $\mathcal{P}_{\text{i}}$, Raman capture coefficient $\Gamma_{\text{i,SMF}}$ of the SMF and laser power P_0. The laser power along the fiber is reduced during transmission due to scattering effects such as Brillouin, Rayleigh and Raman scattering. Therefore, P_0 is in general not constant. To estimate the spontaneous Raman scattering in a SMF as in our lab ($l = 10\,\text{m}$), it is valid to approximate the power in the fiber by the fixed laser power coupled out of the fiber P_{out} as the loss along the fiber is very low. The phonon probability distribution according to the underlying Bose-Einstein statistics is given by

$$\mathcal{P}_{\text{S}} = \frac{1}{1-\exp(-\Delta E_{\text{S}}/k_{\text{B}}T)} \quad \text{and} \quad \mathcal{P}_{\text{AS}} = \frac{\exp(-\Delta E_{\text{AS}}/k_{\text{B}}T)}{1-\exp(-\Delta E_{\text{AS}}/k_{\text{B}}T)} \tag{D.2}$$

with $\Delta E_{\text{S}} = \hbar(\omega_0 - \omega_{\text{S}})$ and $\Delta E_{\text{AS}} = \hbar(\omega_{\text{AS}} - \omega_0)$ where ω_0 is the angular frequency of the incoming light and ω_{i} the angular frequency of the Stokes/anti-Stokes transition.

The Raman-anti-Stokes capture coefficient $\Gamma_{\text{AS,SMF}}$ is dependent on the properties of the fiber, especially the refractive index of core and cladding (n_{co} and n_{cl}) and the concentration of GeO_2. A higher concentration of GeO_2 will increase the scattered power as the scattering cross section of GeO_2 is roughly a factor of five higher than of SiO_2. To estimate a lower bound of the scattered light power a pure SiO_2-fiber is assumed, thus simplifying $\Gamma_{\text{AS,SMF}}$. The Raman anti-Stokes capture coefficient is then given by

$$\Gamma_{\text{AS,SMF}} = \frac{4\pi c^2}{\omega_{AS,0}^2 r_{\text{eff}}^2 n_{\text{co}}^2}\frac{N\cdot \mathrm{d}\sigma_{\text{SiO}_2}}{\mathrm{d}\Omega}\left(\frac{\pi}{2},\omega_{AS,0}^2\right) \tag{D.3}$$

with the effective core radius r_{eff}, center angular frequency $\omega_{AS,0}$ and molecule density N of the doped fiber. The parameter

$$\frac{N\cdot \mathrm{d}\sigma_{\text{SiO}_2}}{\mathrm{d}\Omega}\left(\frac{\pi}{2},\omega_{AS,0}^2\right) \tag{D.4}$$

is the total differential Raman scattering cross section per unit of $\Delta f/c$ (wavenumber) for which values can be found in a graph in [163]. Based on the data from the LL01-780 optical filter in front of the EMCCD camera, the transmission band is assumed to have a width of 3 nm or 50 cm^{-1} (rectangular transmission assumed). Furthermore, the anti-Stokes frequency shift from 797 nm to 780 nm corresponds to a shift of 8 THz or 270 cm^{-1}. Reading from the graph in [163] or a similar graph in [164], the scattering cross section is approximately half the peak cross section of SiO_2 resulting in a value of 0.2×10^{-8} m sr cm^{-1}. Combined with the transmission window of the filter, the total scattering cross-section is

$$\Gamma_{\text{AS,SMF}} = 8\times10^{-10}/\text{m} \tag{D.5}$$

matching the values given for telecommunication wavelength in reference [163]. A mode-field radius of 3.3 µm calculated from a measured NA of 0.075 and a core refractive index $n_{\mathrm{co}} = 1.46$ (value received from the manufacturer upon request) were used. Assuming a temperature of 293 K it follows that $\mathcal{P}_{\mathrm{AS}} = 0.36$. For a laser power of $P_0 = 6$ mW and a fiber length of $l = 10$ m, an anti-Stokes power of 17 pW is calculated. This is roughly a factor of 30 higher than observed. However, there are some factors of uncertainty present, e.g. gain aging, the exact transmission window of the individual filter, as well as the fiber parameters. Especially the real gain factor of the camera due to gain aging (factor of 1000 was assumed) is not known, such that a reduced gain of the camera can result in an underestimation of the detected power. Furthermore, the real fiber parameters of a polarization-maintaining pandas-type fiber as compared to the assumed radial symmetric single-mode fiber can change the expected anti-Stokes power. However, the result of this estimation is that spontaneous Raman scattering can be expected to be the reason for the observed stray light. Therefore, a long-pass filter LP02-808RE-25 (Semrock) was included into the setup directly after each fiber collimator to suppress light below a wavelength of 796 nm.

E. Optical losses in the beam paths of the optical setup described in chapter 5

To determine the laser power inside the vacuum chamber, a calibration between the reference voltage used for intensity stabilization and the total laser power of the beam behind the vacuum chamber (after the second microscope objective) is used. This assumes, that losses due to the aperture of the first microscope objectives are mainly due to the aperture of the first objective and that the transmission through the second microscope objective is close to unity. The calibration values are given in Tab. E.1. The relative power corresponding to the central trap is $5.9 \cdot 10^{-4} \cdot P_{\text{chamber,tot}}$ based on the square area of the central trap and $0.785 \cdot 5.9 \cdot 10^{-4} \cdot P_{\text{chamber,tot}} = 4.6 \cdot P_{\text{chamber,tot}}$ taking the circular aperture $(\pi r_{\text{lens}}^2/(2 \cdot r_{\text{lens}})^2 = 0.785)$ of a single microlens into account.

Tab. E.1.: Calibration factor between intensity stabilization and total power inside the vacuum chamber. The values for the movable tweezer were determined for the center frequencies $f_{\text{hor}} = 100.5$ MHz and $f_{\text{vert}} = 104$ MHz

	Power inside the vacuum chamber in mW/V
Main array	128
Auxiliary array 1	89
Auxiliary array 2	128
Movable tweezer	5.3

The losses along the beam path have been mainly determined for the beam path of the main array but some values have also been measured for auxiliary array 2. The results are given in Tab. E.2.

---

[1] The transmission behind these components was due to the large beam size measured with an aspheric lens with a focal length of 40 mm and an aperture of approximately 48 mm.

Tab. E.2.: Loss factors for different parts of the beam path as well as the combined total loss. Minor losses from highly reflective mirrors or anti-reflection coated surfaces are included in the loss from nearby components. AC: achromatic lens

	Main array, relative loss	Auxiliary array 2, relative loss
MLA	0.71(1)	0.70(1)
PBS	0.90(1)	0.90(1)
AC [1]	0.74(1)	0.63(1)
Two NPBS and dichroic mirror [1]	0.68(1)	0.53(1)
Microscope obj. and vacuum chamber	0.98(1)	
Total loss η_{loss}	0.32(1)	0.21(1)

Using the values introduced above, the power $P_{\text{central,tot}}$ inside the vacuum chamber for the central trap can be approximated from the stabilized laser power P_{out} coupled out of the fiber and measured behind the pick-off for intensity stabilization. It holds that

$$P_{\text{central,tot}} = 5.9 \cdot 10^{-4} \cdot \eta_{\text{loss}} \cdot P_{\text{out}} \tag{E.1}$$

as the geometric factor of 0.785 is already included in η_{loss}. Following the explanation in section 5.2.1, due to the side structures of the focal spot, there is a difference between the total power of the central trap $P_{\text{central,tot}}$ and the power within the central region of the focal spot $P_{\text{central,trap}}$ which determines the real trap depth. It holds that

$$P_{\text{central,trap}} = \eta_{\text{SSC}} \cdot P_{\text{central,tot}} \tag{E.2}$$

with η_{SSC} being the relative power contributing to the trap depth. η_{SSC} depends on the intensity distribution of the focal spot and is on the order of 0.4 to 0.6 as described in section 5.2.1.

F. Arduino Due-based programmable and triggerable DDS-device AD9910

For neutral-atom experiments, it is often necessary to set frequencies in the range of a few MHz up to a few thousand MHz based on a trigger event. This is the case for

- AOMs working in DP configuration changing the frequency offset of the corresponding laser.
- The reference frequency for an offset-stabilized laser as it is the case for the cooling and repump laser described in section 3.3.
- AODs used for site-selective addressing of trapped atoms or atom rearrangement.
- the offset frequency of an electro-optical modulator (EOM)-shifted laser locked to a high-finesse cavity as it is the case in most Rydberg laser systems.

Based on the broad range for fields of application, different demands in terms of the addressable frequency range as well as the achievable switching speed result. For EOMs used to shift the laser frequency of a laser relative to the transmission fringes of a high-finesse cavity, usually a frequency range of up to 2 GHz is necessary where as for atom rearrangement frequency switching on the nanosecond timescale is necessary. For most of these applications, direct digital synthesis (DDS) is a suitable way to generate the desired frequency. DDS-devices offer different ways to change between the output frequencies such as pre-programmed profiles, on-the-fly programming via a serial peripheral interface (SPI) or via a parallel-port programming interface. Combined with e.g. an FPGA this allows for nanosecond switching times as used for atom rearrangement [113, 119]. As FPGA-programming introduces quite a significant overhead for most applications, programming can also be done based on Arduino controllers [165, 166]. The commercially available version [165] is extremely useful as standalone device offering a small display to program single frequencies as well as different forms of frequency sweeps and ramps. It is however not usable as a triggered device within our labscript framework for experiment control and due to the Arduino Mega attached to it, it would be relatively slow. Furthermore, the Arduino Mega platform works on a 5 V standard while the AD9910 works on a 3.3 V standard. This makes a lot of level shifters necessary on the printed circuit board (PCB).

The aim was therefore to find a device which offers a faster clock than the Arduino Mega (16 MHz). A better alternative was found in the Arduino Due (84 MHz clock) for which a simple library was already available [166]. This library offers functions using SPI-commands to pre-program different profiles of the AD9910. As the AD9910 offers a lot of different possibilities to program amplitude, frequency and phase, some of the possibilities shall be described in the following. The discussions will be limited to options changing the frequency as the interest is mainly in frequency switching for our experiments. All details about the AD9910, especially for programming, can be found in the manual [167].

To switch frequencies generated by the DDS, there are mainly three possibilities which have been studied: Pre-programmed profiles, RAM modulation mode and parallel-port programming.

The AD9910 offers the possibility to program phase, frequency and amplitude for 8 profiles via SPI. Using three pins, representing 3 bits, one can address each individual profile. By connecting the profile pins to the Arduino it is possible to switch between the profiles by setting the voltage at the corresponding pins to high/low according to the bit representation of the profile. As the profiles are pre-programmed, switching times are limited by the response of the Arduino to an external trigger which will be addressed later on. The second method is the RAM modulation mode offered by the DDS. The internal RAM of the AD9910 can hold 1024 frequency values which are stepped through by a programmable timer. If the timing is known in advance, this method can be utilized in the experiment but for most use cases it is not flexible enough. The third option is the parallel-port programming functionality which offers to program a frequency directly onto the AD9910 by using a 16-bit frequency tuning word. Choosing the correct settings within the DDS the 16-bit frequency word encodes the highest 16 bits of the frequency programmed into the DDS. The 16 bits can be transferred directly onto the DDS in parallel (therefore the naming) by setting 16 pins of the DDS to high or low according to the bit values of the frequency tuning word. This is the fastest method to program arbitrarily many frequencies onto the DDS if the corresponding frequency tuning words can be provided, e.g. the corresponding pins can be set fast enough. This method is already used with an FPGA for atom rearrangement as described in [113, 119, 123]. For the use with an Arduino this is also the most flexible method and the main question is if and how fast the pins of the Arduino can be set to program the DDS. In principle, setting 16 pins to either a high or a low level is possible with most Arduinos but setting each individual pin is quite slow. However, data on the Arduino is also saved in terms of some n-bit values depending on the architecture of the Arduino. An Arduino such as the Arduino Due uses a 32-bit architecture. In simple terms this means that on an Arduino Due data as large as 32-bit can be processed in parallel. Processing 32 bits in parallel has an important advantage as each frequency tuning word can be saved in one 32-bit data block whereas on an Arduino Mega (8-bit) two data blocks would be necessary for a 16-bit frequency tuning word. This is useful as pins can then be addressed in parallel using so-called ports. For an 8-bit Arduino, one port corresponds to 8 pins while for a 32-bit Arduino one port corresponds to 32 pins although not all pins are always accessible[1]. It is therefore possible to write a frequency tuning word with a single command to the specific output port and processing of this command within the central processing unit (CPU) is relatively fast. By optimizing the Arduino code using inline functions, it was possible to detect an external trigger signal and load the next frequency value from memory onto the DDS (including processing by the DDS) within 640(30) ns as shown in Fig. F.1.

With serial programming, setting a new frequency takes roughly 100 µs for comparison. Although updating the frequency with less than 1 µs delay is possible, a stable update rate (tested with more than 8000 frequency values) of only 750 kHz is achieved as the Arduino has to be capable of detecting all input triggers. Therefore additional time is necessary to ensure that the CPU is in the state to wait for the next trigger event. The full code, which can be loaded onto the Arduino, is available on GitHub [168]. To be able to use the AD9910 as triggered frequency synthesizer within the experiment, communication with labscript was implemented. It is now possible to load up to 20000 frequency values via USB serial programming onto the Arduino memory and step through this memory based on digital triggers from the pulse blaster or any other digital trigger device from labscript. Care has to be taken that only 3.3 V triggers

---

[1] From computer programming there is also a feature known called direct memory access (DMA), which allows data transfer from the memory to some other device of the computer without processing through the central processing unit (CPU). This is both extremely fast and saves CPU capabilities. However on the Arduino Due this is not available in combination with the ports necessary for triggered parallel programming of the AD9910.

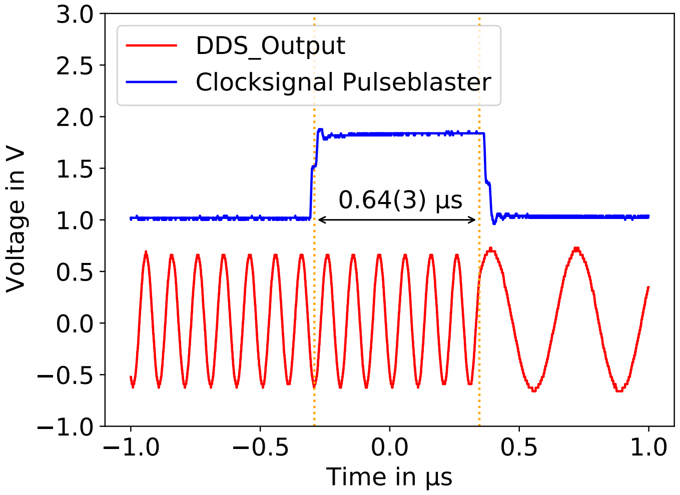

Fig. F.1.: Measurement of the timing between a trigger signal received from the pulse blaster (our currently used pseudoclock in the experiment control system; see section 3.2) and the frequency change at the output of the DDS AD9910. The Arduino due detects rising edges of the trigger signal. Due to internal processing of the Arduino as well as the DDS, the response to the trigger signal takes 640(30) ns. That the length of the pulse from the blaster has a similar length as the response is only because the maximal trigger rate is 750 kHz and pulses from the pulse blaster are symmetric.

are allowed to be used with the Arduino Due. The corresponding labscript device is currently a private user device in our group and can be made available upon request.

G. List of publications

L. Pause, L. Sturm, S. Amann, T. Preuschoff, M. Schlosser, and G. Birkl, *High-performance 2D tweezer arrays with more than 1000 atomic qubits*, in preparation

L. Pause, T. Preuschoff, D. Schäffner, M. Schlosser, and G. Birkl, *Reservoir-based deterministic loading of single-atom tweezer arrays*, Phys. Rev. Research **5**, L032009 (2023)

M. Schlosser, D. Ohl de Mello, D. Schäffner, T. Preuschoff, L. Kohfahl*, and G. Birkl, *Assembled arrays of Rydberg-interacting atoms*, Journal of Physics B: Atomic, Molecular and Optical Physics **53**, 144001 (2020)

D. Ohl de Mello, D. Schäffner, J. Werkmann, T. Preuschoff, L. Kohfahl*, M. Schlosser, and G. Birkl, *Defect-Free Assembly of 2D Clusters of More Than 100 Single-Atom Quantum Systems*, Phys. Rev. Lett. **122**, 203601 (2019)

T. Preuschoff, S. Ristok, D. Schäffner, L. Brozio, D. Ohl de Mello, L. Kohfahl*, M. Schlosser, H. Giessen and G. Birkl, *Micro-optical systems for quantum technologies with laser-trapped neutral atoms based on rapid prototyping by 3D direct laser writing*, In DGaO-Proceedings 2019, p. B016 (DGAO, 2019)

* These papers were published under my birth name Lars Kohfahl.

H. Supervised theses and other work

Bachelor theses

Maxim Hanselowski
Python-based Application for Handling FLIR Cameras and Analyzing Laser Beam Profiles
July 2022

Eric Bossert
Phase-Frequency Stabilization of a Diode Laser at 795 nm
March 2022

Marcel Mittenbühler
Conditional Control for Cold Atom Experiments using Labscript
April 2022

Yannik Atzbach
Setup of a One-Dimensional Optical Lattice to Confine Neutral Atoms in Dipole Trap Arrays
June 2021

Tim Philipp Strohauer
Setup and Characterisation of a Reservoir Dipole Trap for Neutral Rubidium Atoms
February 2021

Lukas Günther
Simulation of the Optical Properties of a new Lens System and a new Microlens Setup
November 2020

Lukas Sturm
Characterization of Mechanical Shutters using a new Optical Setup
August 2020

Master thesis

Lukas Sturm
Neutral Atoms in Large Interleavable Dipole Trap Arrays
January 2023

Stephan Amann
Optical Setup for Interleaved Dipol Trap Arrays with Reduced Trap Waist and Pitch
December 2021

Yannik Wolf
Trapping of Atoms in Hexagonal Dipole Trap Arrays
August 2020

Research interns

Nikita Cernomazov
Optimierung des FP-Versuchs zur magneto-optischen Falle
September 2018

Eric Bossert
Characterisation and integration testing of the PrawnBlaster
September 2021

Marcel Mittenbühler
Migration der FP-MOT Steuerung zu Labscript
Oktober 2021

Research assistants

Yannik Atzbach, Simon Bickel, Marietta Coelle, Lukas Günther, Marcel Mittenbühler, Pascal Sauer, Lukas Sturm, Lukas Walther

References

[1] J. P. Dowling und G. J. Milburn, *Quantum technology: the second quantum revolution*, Philosophical Transactions of the Royal Society of London. Series A: Mathematical, Physical and Engineering Sciences **361,** 1655 (2003).

[2] A. Acín et al., *The quantum technologies roadmap: a European community view*, New Journal of Physics **20,** 080201 (2018).

[3] L. Henriet, L. Beguin, A. Signoles, T. Lahaye, A. Browaeys, G.-O. Reymond und C. Jurczak, *Quantum computing with neutral atoms*, Quantum **4,** 327 (2020).

[4] I. Bloch, J. Dalibard und S. Nascimbene, *Quantum simulations with ultracold quantum gases*, Nature Physics **8,** 267 (2012).

[5] T. Xin, B.-X. Wang, K.-R. Li, X.-Y. Kong, S.-J. Wei, T. Wang, D. Ruan und G.-L. Long, *Nuclear magnetic resonance for quantum computing: Techniques and recent achievements*, Chinese Physics B **27,** 020308 (2018).

[6] R. Blatt und C. F. Roos, *Quantum simulations with trapped ions*, Nature Physics **8,** 277 (2012).

[7] M. J. Hartmann, *Quantum simulation with interacting photons*, Journal of Optics **18,** 104005 (2016).

[8] M. Kjaergaard, M. E. Schwartz, J. Braumüller, P. Krantz, J. I.-J. Wang, S. Gustavsson und W. D. Oliver, *Superconducting qubits: Current state of play*, Annual Review of Condensed Matter Physics **11,** 369 (2020).

[9] C. Kloeffel und D. Loss, *Prospects for spin-based quantum computing in quantum dots*, Annu. Rev. Condens. Matter Phys. **4,** 51 (2013).

[10] J. Weber, W. Koehl, J. Varley, A. Janotti, B. Buckley, C. Van de Walle und D. D. Awschalom, *Quantum computing with defects*, Proceedings of the National Academy of Sciences **107,** 8513 (2010).

[11] P. Shor, *Algorithms for quantum computation: discrete logarithms and factoring*, In *Proceedings 35th Annual Symposium on Foundations of Computer Science*, pp. 124–134 (1994).

[12] L. K. Grover, *Quantum mechanics helps in searching for a needle in a haystack*, Physical review letters **79,** 325 (1997).

[13] J. A. Jones, M. Mosca und R. H. Hansen, *Implementation of a quantum search algorithm on a quantum computer*, Nature **393,** 344 (1998).

[14] L. M. Vandersypen, M. Steffen, G. Breyta, C. S. Yannoni, M. H. Sherwood und I. L. Chuang, *Experimental realization of Shor's quantum factoring algorithm using nuclear magnetic resonance*, Nature **414,** 883 (2001).

[15] D. P. DiVincenzo, *The Physical Implementation of Quantum Computation*, Fortschritte der Physik **48,** 771 (2000).

[16] J. I. Cirac und P. Zoller, *Goals and opportunities in quantum simulation*, Nature physics **8,** 264 (2012).

[17] M. Morgado und S. Whitlock, *Quantum simulation and computing with Rydberg-interacting qubits*, AVS Quantum Science **3,** 023501 (2021).

[18] S. Chu, *Nobel Lecture: The manipulation of neutral particles*, Rev. Mod. Phys. **70,** 685 (1998).

[19] C. N. Cohen-Tannoudji, *Nobel Lecture: Manipulating atoms with photons*, Rev. Mod. Phys. **70,** 707 (1998).

[20] W. D. Phillips, *Nobel Lecture: Laser cooling and trapping of neutral atoms*, Rev. Mod. Phys. **70,** 721 (1998).

[21] W. Ketterle, *Nobel lecture: When atoms behave as waves: Bose-Einstein condensation and the atom laser*, Rev. Mod. Phys. **74,** 1131 (2002).

[22] M. Greiner, O. Mandel, T. Esslinger, T. W. Hänsch und I. Bloch, *Quantum phase transition from a superfluid to a Mott insulator in a gas of ultracold atoms*, Nature **415,** 39 (2002).

[23] M. Endres, H. Bernien, A. Keesling, H. Levine, E. R. Anschuetz, A. Krajenbrink, C. Senko, V. Vuletic, M. Greiner und M. D. Lukin, *Atom-by-atom assembly of defect-free one-dimensional cold atom arrays*, Science **354,** 1024 (2016).

[24] D. Barredo, S. de Léséleuc, V. Lienhard, T. Lahaye und A. Browaeys, *An atom-by-atom assembler of defect-free arbitrary two-dimensional atomic arrays*, Science **354,** 1021 (2016).

[25] D. Ohl de Mello, D. Schäffner, J. Werkmann, T. Preuschoff, L. Kohfahl, M. Schlosser und G. Birkl, *Defect-Free Assembly of 2D Clusters of More Than 100 Single-Atom Quantum Systems*, Phys. Rev. Lett. **122,** 203601 (2019).

[26] H. Kim, W. Lee, H.-g. Lee, H. Jo, Y. Song und J. Ahn, *In situ single-atom array synthesis using dynamic holographic optical tweezers*, Nature communications **7,** 13317 (2016).

[27] M. O. Brown, T. Thiele, C. Kiehl, T.-W. Hsu und C. A. Regal, *Gray-Molasses Optical-Tweezer Loading: Controlling Collisions for Scaling Atom-Array Assembly*, Phys. Rev. X **9,** 011057 (2019).

[28] C. S. Adams, J. D. Pritchard und J. P. Shaffer, *Rydberg atom quantum technologies*, J. Phys. B: At. Mol. Opt. Phys. **53,** 012002 (2019).

[29] A. Browaeys und T. Lahaye, *Many-body physics with individually controlled Rydberg atoms*, Nature Physics **16,** 132 (2020).

[30] Y. Wang, S. Shevate, T. M. Wintermantel, M. Morgado, G. Lochead und S. Whitlock, *Preparation of hundreds of microscopic atomic ensembles in optical tweezer arrays*, npj Quantum Information **6,** 54 (2020).

[31] S. Ebadi et al., *Quantum phases of matter on a 256-atom programmable quantum simulator*, Nature **595,** 227 (2021).

[32] P. Scholl et al., *Quantum simulation of 2D antiferromagnets with hundreds of Rydberg atoms*, Nature **595,** 233 (2021).

[33] P. Huft, Y. Song, T. M. Graham, K. Jooya, S. Deshpande, C. Fang, M. Kats und M. Saffman, *Simple, passive design for large optical trap arrays for single atoms*, Phys. Rev. A **105,** 063111 (2022).

[34] T. M. Graham, M. Kwon, B. Grinkemeyer, Z. Marra, X. Jiang, M. T. Lichtman, Y. Sun, M. Ebert und M. Saffman, *Rydberg-Mediated Entanglement in a Two-Dimensional Neutral Atom Qubit Array*, Phys. Rev. Lett. **123,** 230501 (2019).

[35] M. J. Piotrowicz, M. Lichtman, K. Maller, G. Li, S. Zhang, L. Isenhower und M. Saffman, *Two-dimensional lattice of blue-detuned atom traps using a projected Gaussian beam array*, Phys. Rev. A **88,** 013420 (2013).

[36] A. M. Kaufman und K.-K. Ni, *Quantum science with optical tweezer arrays of ultracold atoms and molecules*, Nature Physics **17,** 1324 (2021).

[37] C. Gross und I. Bloch, *Quantum simulations with ultracold atoms in optical lattices*, Science **357,** 995 (2017).

[38] R. Löw, H. Weimer, J. Nipper, J. B. Balewski, B. Butscher, H. P. Büchler und T. Pfau, *An experimental and theoretical guide to strongly interacting Rydberg gases*, Journal of Physics B: Atomic, Molecular and Optical Physics **45,** 113001 (2012).

[39] L. Isenhower, E. Urban, X. L. Zhang, A. T. Gill, T. Henage, T. A. Johnson, T. G. Walker und M. Saffman, *Demonstration of a Neutral Atom Controlled-NOT Quantum Gate*, Phys. Rev. Lett. **104,** 010503 (2010).

[40] J. Simon, W. S. Bakr, R. Ma, M. E. Tai, P. M. Preiss und M. Greiner, *Quantum simulation of antiferromagnetic spin chains in an optical lattice*, Nature **472,** 307 (2011).

[41] S. De Léséleuc, V. Lienhard, P. Scholl, D. Barredo, S. Weber, N. Lang, H. P. Büchler, T. Lahaye und A. Browaeys, *Observation of a symmetry-protected topological phase of interacting bosons with Rydberg atoms*, Science **365,** 775 (2019).

[42] D. Bluvstein et al., *A quantum processor based on coherent transport of entangled atom arrays*, Nature **604,** 451 (2022).

[43] H. J. Metcalf und P. Van der Straten, *Laser cooling and trapping* (Springer, 1999).

[44] D. A. Steck, *Quantum and Atom Optics*, 2016.

[45] R. Grimm, M. Weidemüller und Y. B. Ovchinnikov, *Optical dipole traps for neutral atoms*, Advances in atomic, molecular, and optical physics **42,** 95 (2000).

[46] D. A. Steck, *Rubidium 85 D Line Data*, Technical report, University of Oregon (2013) .

[47] M. Schlosser, *Bereitstellung und kohärente Kontrolle von Einzel-Atom-Quantensystemen in zweidimensionalen Quantenregistern*, Phd thesis, TU Darmstadt, (2013).

[48] J. Dalibard, S. Reynaud und C. Cohen-Tannoudji, *Proposals of stable optical traps for neutral atoms*, Optics communications **47,** 395 (1983).

[49] E. L. Raab, M. Prentiss, A. Cable, S. Chu und D. E. Pritchard, *Trapping of Neutral Sodium Atoms with Radiation Pressure*, Phys. Rev. Lett. **59,** 2631 (1987).

[50] J. Dalibard und C. Cohen-Tannoudji, *Laser cooling below the Doppler limit by polarization gradients: simple theoretical models*, JOSA B **6,** 2023 (1989).

[51] N. Schlosser, G. Reymond, I. Protsenko und P. Grangier, *Sub-poissonian loading of single atoms in a microscopic dipole trap*, Nature **411,** 1024 (2001).

[52] N. Schlosser, G. Reymond und P. Grangier, *Collisional Blockade in Microscopic Optical Dipole Traps*, Phys. Rev. Lett. **89,** 023005 (2002).

[53] S. J. M. Kuppens, K. L. Corwin, K. W. Miller, T. E. Chupp und C. E. Wieman, *Loading an optical dipole trap*, Phys. Rev. A **62,** 013406 (2000).

[54] J. Kruse, *Neutral Atoms in a Dipole-Trap Array for Quantum Information Processing*, Phd thesis, TU Darmstadt, (2010).

[55] L. Pause und T. Strohauer, *Code for Monte-Carlo Simulations of atom loss processes in optical dipole traps*, Github repository, *https://github.com/TU-Darmstadt-APQ/CollBlockadeMonteCarlo.git*, 2023.

[56] Y. R. P. Sortais, A. Fuhrmanek, R. Bourgain und A. Browaeys, *Sub-Poissonian atom-number fluctuations using light-assisted collisions*, Phys. Rev. A **85,** 035403 (2012).

[57] Y. Fung und M. Andersen, *Efficient collisional blockade loading of a single atom into a tight microtrap*, New Journal of Physics **17,** 073011 (2015).

[58] T. Grünzweig, A. Hilliard, M. McGovern und M. Andersen, *Near-deterministic preparation of a single atom in an optical microtrap*, Nature Physics **6,** 951 (2010).

[59] B. J. Lester, N. Luick, A. M. Kaufman, C. M. Reynolds und C. A. Regal, *Rapid Production of Uniformly Filled Arrays of Neutral Atoms*, Phys. Rev. Lett. **115,** 073003 (2015).

[60] J. P. Gordon und A. Ashkin, *Motion of atoms in a radiation trap*, Phys. Rev. A **21,** 1606 (1980).

[61] T. Savard, K. O'hara und J. Thomas, *Laser-noise-induced heating in far-off resonance optical traps*, Physical Review A **56,** R1095 (1997).

[62] J. He, B.-d. Yang, Y.-j. Cheng, T.-c. Zhang und J.-m. Wang, *Extending the trapping lifetime of single atom in a microscopic far-off-resonance optical dipole trap*, Frontiers of Physics **6,** 262 (2011).

[63] A. Steane, M. Chowdhury und C. Foot, *Radiation force in the magneto-optical trap*, JOSA B **9,** 2142 (1992).

[64] S. Bali, K. O'Hara, M. Gehm, S. Granade und J. Thomas, *Quantum-diffractive background gas collisions in atom-trap heating and loss*, Physical Review A **60,** R29 (1999).

[65] E. Hecht, *Optik* (Walter de Gruyter GmbH & Co KG, 2018).

[66] H. Gross, *Handbook of Optical Systems* (Wiley Online Library, 2005).

[67] S. A. Self, *Focusing of spherical Gaussian beams*, Applied optics **22,** 658 (1983).

[68] B. E. Saleh und M. C. Teich, *Fundamentals of photonics* (John Wiley & Sons, 2019).

[69] M. Born und E. Wolf, *Principles of optics: electromagnetic theory of propagation, interference and diffraction of light* (Elsevier, 2013).

[70] A. Lengwenus, *Manipulation der internen und externen Freiheitsgrade neutraler Atome in optischen Mikropotentialen*, Phd thesis, Technische Universität, (2008).

[71] Y. Li und E. Wolf, *Focal shifts in diffracted converging spherical waves*, Optics communications **39,** 211 (1981).

[72] Y. Li und H. Platzer, *An experimental investigation of diffraction patterns in low-Fresnel-number focusing systems*, Optica Acta: International Journal of Optics **30,** 1621 (1983).

[73] P. Ruffieux, T. Scharf, H. P. Herzig, R. Völkel und K. J. Weible, *On the chromatic aberration of microlenses*, Optics express **14,** 4687 (2006).

[74] *Zemax OpticStudio 22.2.1 User Manual*.

[75] J. Wen, Y. Zhang und M. Xiao, *The Talbot effect: recent advances in classical optics, nonlinear optics, and quantum optics*, Advances in optics and photonics **5,** 83 (2013).

[76] L. Rayleigh, *XXV. On copying diffraction-gratings, and on some phenomena connected therewith*, The London, Edinburgh, and Dublin Philosophical Magazine and Journal of Science **11,** 196 (1881).

[77] J. T. Winthrop und C. R. Worthington, *Theory of Fresnel images. I. Plane periodic objects in monochromatic light*, JOSA **55,** 373 (1965).

[78] B. Besold und N. Lindlein, *Fractional Talbot effect for periodic microlens arrays*, Optical Engineering **36,** 1099 (1997).

[79] M. Schlosser, S. Tichelmann, D. Schäffner, D. O. de Mello, M. Hambach und G. Birkl, *Large-scale multilayer architecture of single-atom arrays with individual addressability*, arXiv preprint arXiv:1902.05424 (2019).

[80] P. Memmolo, L. Miccio, F. Merola und P. Ferraro, *Talbot effect in self-assembled red blood cells investigated by digital holography*, Journal of Physics: Photonics (2020).

[81] P. Memmolo, C. Distante, M. Paturzo, A. Finizio, P. Ferraro und B. Javidi, *Automatic focusing in digital holography and its application to stretched holograms*, Optics letters **36,** 1945 (2011).

[82] W. Alt, *An objective lens for efficient fluorescence detection of single atoms*, Optik–International Journal for Light and Electron Optics **113,** 142 (2002).

[83] T. F. Gallagher, *Rydberg atoms* (Cambridge University Press, 2005), Vol. 3.

[84] J. Rydberg, *XXXIV. On the structure of the line-spectra of the chemical elements*, The London, Edinburgh, and Dublin philosophical magazine and journal of science **29,** 331 (1890).

[85] W. Demtröder, *Experimentalphysik 3: Atome, Moleküle und Festkörper*, 4. ed. (Springer, 2010).

[86] C.-J. Lorenzen und K. Niemax, *Quantum Defects of the $n^2P_{1/2,3/2}$ Levels in ^{39}K and ^{85}Rb*, Physica Scripta **27,** 300 (1983).

[87] N. Šibalić, J. D. Pritchard, C. S. Adams und K. J. Weatherill, *ARC: An open-source library for calculating properties of alkali Rydberg atoms*, Computer Physics Communications **220,** 319 (2017).

[88] I. Beterov, I. Ryabtsev, D. Tretyakov und V. Entin, *Quasiclassical calculations of blackbody-radiation-induced depopulation rates and effective lifetimes of Rydberg n S, n P, and n D alkali-metal atoms with $n \leq 80$*, Physical Review A **79,** 052504 (2009).

[89] C. Glaser, F. Karlewski, J. Kluge, J. Grimmel, M. Kaiser, A. Günther, H. Hattermann, M. Krutzik und J. Fortágh, *Absolute frequency measurement of rubidium 5 S- 6 P transitions*, Physical Review A **102,** 012804 (2020).

[90] P. Thoumany, T. Hänsch, G. Stania, L. Urbonas und T. Becker, *Optical spectroscopy of rubidium Rydberg atoms with a 297 nm frequency-doubled dye laser*, Optics letters **34,** 1621 (2009).

[91] J. Zeiher, R. Van Bijnen, P. Schauß, S. Hild, J.-y. Choi, T. Pohl, I. Bloch und C. Gross, *Many-body interferometry of a Rydberg-dressed spin lattice*, Nature Physics **12,** 1095 (2016).

[92] I. Ryabtsev, I. Beterov, D. Tretyakov, V. Entin und E. Yakshina, *Doppler-and recoil-free laser excitation of Rydberg states via three-photon transitions*, Physical Review A **84,** 053409 (2011).

[93] A. Hankin, Y.-Y. Jau, L. Parazzoli, C. Chou, D. Armstrong, A. Landahl und G. Biedermann, *Two-atom Rydberg blockade using direct 6 S to n P excitation*, Physical Review A **89,** 033416 (2014).

[94] T. G. Walker und M. Saffman, *Entanglement of two atoms using Rydberg blockade*, in *Advances in Atomic, Molecular, and Optical Physics* (Elsevier, 2012), Vol. 61, pp. 81–115.

[95] B. W. Shore, *Coherent manipulations of atoms using laser light*, Acta Phys. Slovaca **58,** 243 (2008).

[96] J. Deiglmayr, M. Reetz-Lamour, T. Amthor, S. Westermann, A. De Oliveira und M. Weidemüller, *Coherent excitation of Rydberg atoms in an ultracold gas*, Optics communications **264,** 293 (2006).

[97] Y. Miroshnychenko, A. Gaëtan, C. Evellin, P. Grangier, D. Comparat, P. Pillet, T. Wilk und A. Browaeys, *Coherent excitation of a single atom to a Rydberg state*, Phys. Rev. A **82,** 013405 (2010).

[98] P. Thoumany, T. Germann, T. Hänsch, G. Stania, L. Urbonas und T. Becker, *Spectroscopy of rubidium Rydberg states with three diode lasers*, Journal of Modern Optics **56,** 2055 (2009).

[99] D. P. Fahey und M. W. Noel, *Excitation of Rydberg states in rubidium with near infrared diode lasers*, Optics express **19,** 17002 (2011).

[100] K. M. Maller, M. T. Lichtman, T. Xia, Y. Sun, M. J. Piotrowicz, A. W. Carr, L. Isenhower und M. Saffman, *Rydberg-blockade controlled-not gate and entanglement in a two-dimensional array of neutral-atom qubits*, Phys. Rev. A **92,** 022336 (2015).

[101] Y.-Y. Jau, A. Hankin, T. Keating, I. H. Deutsch und G. Biedermann, *Entangling atomic spins with a Rydberg-dressed spin-flip blockade*, Nature Physics **12,** 71 (2016).

[102] Y. Zeng, P. Xu, X. He, Y. Liu, M. Liu, J. Wang, D. J. Papoular, G. V. Shlyapnikov und M. Zhan, *Entangling Two Individual Atoms of Different Isotopes via Rydberg Blockade*, Phys. Rev. Lett. **119,** 160502 (2017).

[103] C. Picken, R. Legaie, K. McDonnell und J. Pritchard, *Entanglement of neutral-atom qubits with long ground-Rydberg coherence times*, Quantum Science and Technology **4,** 015011 (2018).

[104] H. Levine, A. Keesling, A. Omran, H. Bernien, S. Schwartz, A. S. Zibrov, M. Endres, M. Greiner, V. Vuletić und M. D. Lukin, *High-Fidelity Control and Entanglement of Rydberg-Atom Qubits*, Phys. Rev. Lett. **121,** 123603 (2018).

[105] H. Levine et al., *Parallel Implementation of High-Fidelity Multiqubit Gates with Neutral Atoms*, Phys. Rev. Lett. **123,** 170503 (2019).

[106] A. Omran et al., *Generation and manipulation of Schrödinger cat states in Rydberg atom arrays*, Science **365,** 570 (2019).

[107] P. Schauß, J. Zeiher, T. Fukuhara, S. Hild, M. Cheneau, T. Macrì, T. Pohl, I. Bloch und C. Groß, *Crystallization in Ising quantum magnets*, Science **347,** 1455 (2015).

[108] V. Lienhard, S. de Léséleuc, D. Barredo, T. Lahaye, A. Browaeys, M. Schuler, L.-P. Henry und A. M. Läuchli, *Observing the Space- and Time-Dependent Growth of Correlations in Dynamically Tuned Synthetic Ising Models with Antiferromagnetic Interactions*, Phys. Rev. X **8,** 021070 (2018).

[109] S. de Léséleuc, S. Weber, V. Lienhard, D. Barredo, H. P. Büchler, T. Lahaye und A. Browaeys, *Accurate Mapping of Multilevel Rydberg Atoms on Interacting Spin-*$1/2$ *Particles for the Quantum Simulation of Ising Models*, Phys. Rev. Lett. **120,** 113602 (2018).

[110] P. Schauss, *Quantum simulation of transverse Ising models with Rydberg atoms*, Quantum Science and Technology **3,** 023001 (2018).

[111] D. Barredo, H. Labuhn, S. Ravets, T. Lahaye, A. Browaeys und C. S. Adams, *Coherent excitation transfer in a spin chain of three Rydberg atoms*, Physical review letters **114,** 113002 (2015).

[112] R. Dumke, M. Volk, T. Müther, F. B. J. Buchkremer, G. Birkl und W. Ertmer, *Micro-optical Realization of Arrays of Selectively Addressable Dipole Traps: A Scalable Configuration for Quantum Computation with Atomic Qubits*, Phys. Rev. Lett. **89,** 097903 (2002).

[113] D. Ohl de Mello, *Rydberg interactions in a defect-free array of single-atom quantum systems*, Phd thesis, Technical University of Darmstadt, (2020).

[114] K.-N. Schymik, B. Ximenez, E. Bloch, D. Dreon, A. Signoles, F. Nogrette, D. Barredo, A. Browaeys und T. Lahaye, *In situ equalization of single-atom loading in large-scale optical tweezer arrays*, Phys. Rev. A **106,** 022611 (2022).

[115] M. Saffman, *Quantum computing with atomic qubits and Rydberg interactions: progress and challenges*, Journal of Physics B: Atomic, Molecular and Optical Physics **49,** 202001 (2016).

[116] W. Demtröder, *Experimentalphysik 2: Elektrizität und Optik*, 4. ed. (Springer, 2006).

[117] K. Krzysztof et al., *Magneto-optical trap: fundamentals and realization*, CMST pp. 115–129 (2010).

[118] *Website for magnetic field data on earth*, *https://www.ngdc.noaa.gov/geomag/calculators/magcalc.shtml*, 2023.

[119] D. Schäffner, *Interacting Neutral Atoms in a Scalable Platform of Optical Tweezers for Quantum Computation and Sensing*, Phd thesis, Technical University of Darmstadt, (2021).

[120] P. Starkey, C. Billington, S. Johnstone, M. Jasperse, K. Helmerson, L. Turner und R. Anderson, *A scripted control system for autonomous hardware-timed experiments*, Review of Scientific Instruments **84,** 085111 (2013).

[121] P. T. Starkey, *A software framework for control and automation of precisely timed experiments*, Phd thesis, Monash University, (2019).

[122] APQ group, *Labscript-devices folder forked from mainline labscript repository*, *https://github.com/TU-Darmstadt-APQ/labscript-devices.git*, 2023.

[123] J. Werkmann, *Control Systems and Optical Tweezers for Quantum Information Processing*, Master Thesis, 2018.

[124] ARTIQ development team, *ARTIQ (Advanced Real-Time Infrastructure for Quantum physics)*, *https://m-labs.hk/experiment-control/artiq/*, 2023.

[125] G. Kasprowicz et al., *ARTIQ and Sinara: Open Software and Hardware Stacks for Quantum Physics*, In *OSA Quantum 2.0 Conference*, p. QTu8B.14 (Optica Publishing Group, 2020).

[126] M. Mittenbühler, *Conditional Control for Cold Atom Experiments using Labscript*, Bachelor's thesis, 2022.

[127] T. Preuschoff, *Laser Technologies for Applications in Quantum Information Science*, Phd thesis, Technical University of Darmstadt, (2023).

[128] T. Preuschoff, M. Schlosser und G. Birkl, *Optimization strategies for modulation transfer spectroscopy applied to laser stabilization*, Optics Express **26,** 24010 (2018).

[129] X. Baillard, A. Gauguet, S. Bize, P. Lemonde, P. Laurent, A. Clairon und P. Rosenbusch, *Interference-filter-stabilized external-cavity diode lasers*, Optics Communications **266,** 609 (2006).

[130] T. Preuschoff, M. Schlosser und G. Birkl, *Digital laser frequency and intensity stabilization based on the STEMlab platform (originally Red Pitaya)*, Review of Scientific Instruments **91,** 083001 (2020).

[131] G. Gattobigio, T. Pohl, G. Labeyrie und R. Kaiser, *Scaling laws for large magneto-optical traps*, Physica Scripta **81,** 025301 (2010).

[132] T. M. Brzozowski, M. Maczynska, M. Zawada, J. Zachorowski und W. Gawlik, *Time-of-flight measurement of the temperature of cold atoms for short trap-probe beam distances*, Journal of Optics B: Quantum and Semiclassical Optics **4,** 62 (2002).

[133] W. D. Phillips und J. V. Prodanf, *Cooling atoms with a frequency chirped laser*, In *Coherence and Quantum Optics V: Proceedings of the Fifth Rochester Conference on Coherence and Quantum Optics held at the University of Rochester, June 13–15, 1983*, pp. 15–22 (1984).

[134] F. Schmaltz, *Bose-Einstein-Kondensate in dynamischen Dipolpotentialen aus konischer Refraktion*, Phd thesis, Technichal University of Darmstadt, (2019).

[135] A. Franzen, *Component Library*, *http://www.gwoptics.org/ComponentLibrary/*, 2006.

[136] A. L. Shaw, P. Scholl, R. Finklestein, I. S. Madjarov, B. Grinkemeyer und M. Endres, *Dark-state enhanced loading of an optical tweezer array*, arXiv preprint arXiv:2302.10855 (2023).

[137] A. Jenkins, J. W. Lis, A. Senoo, W. F. McGrew und A. M. Kaufman, *Ytterbium Nuclear-Spin Qubits in an Optical Tweezer Array*, Phys. Rev. X **12,** 021027 (2022).

[138] D. Schäffner, T. Preuschoff, S. Ristok, L. Brozio, M. Schlosser, H. Giessen und G. Birkl, *Arrays of individually controllable optical tweezers based on 3D-printed microlens arrays*, Optics express **28,** 8640 (2020).

[139] L. Pause, T. Preuschoff, D. Schäffer, M. Schlosser und G. Birkl, *Reservoir-based deterministic loading of single-atom tweezer arrays*, arXiv preprint arXiv:2302.12730 (2023).

[140] K.-N. Schymik, V. Lienhard, D. Barredo, P. Scholl, H. Williams, A. Browaeys und T. Lahaye, *Enhanced atom-by-atom assembly of arbitrary tweezer arrays*, Phys. Rev. A **102,** 063107 (2020).

[141] T. Klostermann, C. R. Cabrera, H. von Raven, J. F. Wienand, C. Schweizer, I. Bloch und M. Aidelsburger, *Fast long-distance transport of cold cesium atoms*, Phys. Rev. A **105,** 043319 (2022).

[142] C.-C. Chen, R. González Escudero, J. Minář, B. Pasquiou, S. Bennetts und F. Schreck, *Continuous Bose–Einstein condensation*, Nature pp. 1–5 (2022).

[143] T. Graham et al., *Multi-qubit entanglement and algorithms on a neutral-atom quantum computer*, Nature **604,** 457 (2022).

[144] G. S. Kino und T. R. Corle, *Confocal scanning optical microscopy and related imaging systems* (Academic Press, 1996).

[145] H. Ottevaere und H. Thienpont, *Refractive optical microlenses: an introduction to nomenclature and characterization techniques*, in *Encyclopedia of Modern Optics (edited by RD Guenther, DG Steel, L. Bayvel), Elsevier, Oxford, Vol. 4, pp. 21-43, 2004, n invited* (2004).

[146] L. Günther, *Simulation of the optical properties of a new lens system and a new microlens setup*, Bachelor's thesis, 2020.

[147] S. Amann, *Optical Setup for Interleaved Dipole Trap Arrays with Reduced Trap Waist and Pitch*, Master's thesis, 2021.

[148] T. Preuschoff, J. Werkmann, L. Pause, S. Amann, L. Brozio und L. Sturm, *Python code for evaluation of periodic light fields*, Github repository, 2023.

[149] L. Sturm, *Neutral Atoms in Large Interleavable Dipole Trap Arrays*, Master's thesis, 2023.

[150] S. Friebel, C. D'Andrea, J. Walz, M. Weitz und T. Hänsch, *CO 2-laser optical lattice with cold rubidium atoms*, Physical Review A **57,** R20 (1998).

[151] C. Tuchendler, A. M. Lance, A. Browaeys, Y. R. Sortais und P. Grangier, *Energy distribution and cooling of a single atom in an optical tweezer*, Physical Review A **78,** 033425 (2008).

[152] K.-N. Schymik, S. Pancaldi, F. Nogrette, D. Barredo, J. Paris, A. Browaeys und T. Lahaye, *Single Atoms with 6000-Second Trapping Lifetimes in Optical-Tweezer Arrays at Cryogenic Temperatures*, Phys. Rev. Applied **16,** 034013 (2021).

[153] L. Amico, D. Aghamalyan, F. Auksztol, H. Crepaz, R. Dumke und L. C. Kwek, *Superfluid qubit systems with ring shaped optical lattices*, Scientific reports **4,** 1 (2014).

[154] C. Sheng, J. Hou, X. He, P. Xu, K. Wang, J. Zhuang, X. Li, M. Liu, J. Wang und M. Zhan, *Efficient preparation of two-dimensional defect-free atom arrays with near-fewest sorting-atom moves*, Phys. Rev. Research **3,** 023008 (2021).

[155] W. Tian, W. J. Wee, A. Qu, B. J. M. Lim, P. R. Datla, V. P. W. Koh und H. Loh, *Parallel Assembly of Arbitrary Defect-Free Atom Arrays with a Multitweezer Algorithm*, Phys. Rev. Appl. **19,** 034048 (2023).

[156] S. Zhu, Y. Long, M. Pu und X. Luo, *Parallel compression algorithm for fast preparation of defect-free atom arrays*, arXiv preprint arXiv:2212.03047 (2022).

[157] S. Wang, W. Zhang, T. Zhang, S. Mei, Y. Wang, J. Hu und W. Chen, *Accelerating the assembly of defect-free atomic arrays with maximum parallelisms*, arXiv preprint arXiv:2210.10364 (2022).

[158] R. Samajdar, W. W. Ho, H. Pichler, M. D. Lukin und S. Sachdev, *Complex Density Wave Orders and Quantum Phase Transitions in a Model of Square-Lattice Rydberg Atom Arrays*, Phys. Rev. Lett. **124,** 103601 (2020).

[159] A. G. Fowler, M. Mariantoni, J. M. Martinis und A. N. Cleland, *Surface codes: Towards practical large-scale quantum computation*, Phys. Rev. A **86,** 032324 (2012).

[160] W. J. Smith, *Modern optical engineering: the design of optical systems* (McGraw-Hill Education, 2008).

[161] R. Priestley, *Birefringence dispersion in fused silica for DUV lithography*, In *Optical Microlithography XIV*, **4346,** 1300 (2001).

[162] L. Sirleto und M. A. Ferrara, *Fiber amplifiers and fiber lasers based on stimulated Raman scattering: a review*, Micromachines **11,** 247 (2020).

[163] M. A. Farahani und T. Gogolla, *Spontaneous Raman scattering in optical fibers with modulated probe light for distributed temperature Raman remote sensing*, Journal of Lightwave Technology **17,** 1379 (1999).

[164] I. Mandelbaum, M. Bolshtyansky, T. F. Heinz und A. R. H. Walker, *Method for measuring the Raman gain tensor in optical fibers*, JOSA B **23,** 621 (2006).

[165] A. Formin, *Arduino Mega combined with AD9910*, Github repository, *https://gra-afch.com/catalog/rf-units/dds-ad9910-arduino-shield/*, 2023.

[166] N. Pisenti, D. Barker und B. Reschovsky, *AD9910 arduino library*, Github repository, *https://github.com/JQIamo/AD9910-arduino*, 2023.

[167] Analog Devices, *AD9910 manual*, Datasheet, *https://www.analog.com/media/en/technical-documentation/data-sheets/ad9910.pdf*, 2023.

[168] L. Pause, *AD9910 library for arduino due*, Github repository, *https://github.com/TU-Darmstadt-APQ/AD9910-arduino.git*, 2023.

Acknowledgments

Am Ende dieser Arbeit möchte ich noch all denjenigen Dank sagen, ohne die diese Arbeit nicht möglich gewesen wäre und die mich auf meinem Weg begleitet haben. Ich habe in den letzten Jahren und ganz besonders in den letzten, stressigen Monaten vielfältige Unterstützung erfahren, für die ich sehr dankbar bin.

Zuallererst danke ich Ihnen, Herr Prof. Dr. Birkl, für die ausgezeichnete Betreuung während meiner Zeit in Ihrer Arbeitsgruppe. Seit dem Beginn meiner Forschungsarbeit habe ich in Ihrer Gruppe immer ein anregendes Arbeitsumfeld vorgefunden, in dem ich viel lernen und auch ausprobieren konnte. Bei Fragen und Anregungen hatten Sie immer ein offenes Ohr und haben mit einer Vielzahl konstruktiver Diskussionen die Projekte bereichert. Ein herzlicher Dank gilt auch Herrn Prof. Dr. Walther für die Übernahme des Zweitgutachtens sowie die tolle Zusammenarbeit und Kooperation, die ich insbesondere während der Promotion mit Ihnen und Ihrer Arbeitsgruppe hatte. Herrn Prof. Dr. Walser und Herrn Prof. Dr. Enders ein herzliches Dankschön für die Beteiligung an meiner Prüfungskommision.

Zum tollen Arbeitsumfeld während meiner Zeit am Institut für Angewandte Physik haben auch die vielen Mitglieder der Arbeitsgruppe Atome-Photonen-Quanten und viele weitere Mitarbeitende des Instituts beigetragen. Besonderer Dank gilt Tilman, mit dem ich die Ehre hatte, ein komplett neues Experiment aufzubauen und Stück für Stück zu einer großen, vielseitigen Maschine zu entwickeln, wie ich sie in dieser Arbeit präsentieren konnte. Es war eine große Bereicherung mit dir zusammenzuarbeiten. Daniel und Dominik, ihr habt das Nachbarexperiment betrieben, an dem ich meine Masterarbeit durchgeführt habe und auch danach konnte ich immer auf eure Hilfe und Erfahrung zählen. Vielen Dank für die tolle Zusammenarbeit im und auch außerhalb des Labors. Ein großer Dank gilt auch Malte, der bei Fragen aller Art immer mit Rat und Tat zur Seite stand und der zusammen mit Sascha während meiner Bachelorzeit bei mir die Faszination für dieses Experiment geweckt hat. Besonders bedanken möchte ich mich auch bei allen Bachelor- und Masterstudenten, mit denen ich während meiner Promotion zusammenarbeiten durfte. Tobias, wir haben zusammen angefangen das Experiment aufzubauen und ich erinnere mich noch gerne an das gemeinsame Spulenwickeln zurück. Inzwischen hast du von Daniel und Dominik das Experiment übernommen und ich wünsche dir dabei ganz viel Erfolg. Stephan und Yannik, danke für die Unterstützung am Experiment, es war toll mit euch den Aufbau weiterzuentwickeln. Lukas, dir gilt ein besonderer Dank. Seit du deine Bachelorarbeit bei mir angefangen hast, war es immer eine tolle Zusammenarbeit und ich lege mit Freude und großer Zuversicht den QUIPS-C-Staffelstab in deine Hände. Das Experiment ist nun deines und ich weiß, dass es bei dir sehr gut aufgehoben ist. Dank auch an Maxim, Eric, Marcel, Yannik, Simon, Tim und Lukas. Ihr habt als Bachelorstudenten mit vielen Projekten unser Experiment weitergebracht und teilweise auch noch drüber hinaus als Masterstudent oder Hiwi das Experiment unterstützt. Ein großer Dank gilt auch den Kollegen an den anderen Experimenten. Patrick, du hast mir bei Software- und Elektronikfragen immer unterstützend zur Seite gestanden und für ein allzeit stabiles Laborklima gesorgt. Dank auch an das ATOMICS-Team um Felix, Dominik und Ludwig für die tolle Zusammenarbeit und Unterstützung. Eine stete Stütze war auch unser Sektretariat. Gabi und Nathalie, ihr habt die Bürokratie so erträglich wie möglich gemacht und uns abseits des Labors immer unterstützt.

Ein ganz besonderer Dank geht an das Team von Herrn Weick in der Feinmechanischen Werkstatt. Ihr hattet immer ein offenes Ohr, wenn ich Fragen bei mechanischen Konstruktionen hatte und habt insbesondere meine Kontruktionen Wirklichkeit werden lassen. Egal ob kleine oder große Bauteile, bei euch konnte man immer sicher sein, dass am Ende das optimale Ergebnis herauskommt.

Zu guter Letzt danke ich meiner Familie für die Hilfe und Förderung auf meinem bisherigen Weg. Ihr habt mir immer zur Seite gestanden, wenn es nötig war, und mich machen lassen, wenn ich mich ausprobieren wollte. Ganz besonders danke ich meiner Frau Isabelle. Du hast mich in den letzten Jahren unglaublich unterstützt, vor allem in schwierigen und stressigen Phasen und hattest Geduld, wenn die Uni mal wieder zeitweise zu meinem Wohnzimmer wurde.

Curriculum Vitae

The CV is not included in the online version for reasons of data protection.

Erklärungen laut Promotionsordnung

§8 Abs. 1 lit. c PromO

Ich versichere hiermit, dass die elektronische Version meiner Dissertation mit der schriftlichen Version übereinstimmt.

§8 Abs. 1 lit. d PromO

Ich versichere hiermit, dass zu einem vorherigen Zeitpunkt noch keine Promotion versucht wurde. In diesem Fall sind nähere Angaben über Zeitpunkt, Hochschule, Dissertationsthema und Ergebnis dieses Versuchs mitzuteilen.

§9 Abs. 1 PromO

Ich versichere hiermit, dass die vorliegende Dissertation selbstständig und nur unter Verwendung der angegebenen Quellen verfasst wurde.

§9 Abs. 2 PromO

Die Arbeit hat bisher noch nicht zu Prüfungszwecken gedient.

Darmstadt, 8. Mai 2023

L. Pause